Surface Freezing in Surfactant/Alkane/Water Systems

ASH, PHILIP,ANDREW

Surface Freezing in Surfactant/Alkane/Water Systems

A thesis submitted in partial fulfilment of the requirements for the degree of Doctor of Philosophy in the University of Durham by,

Philip Ash

Department of Chemistry and Ustinov College

University of Durham

September 2010

Surface Freezing in Surfactant/Alkane/Water Systems

A thesis submitted in partial fulfilment of the requirements for the degree of Doctor of Philosophy in the University of Durham by

Philip Ash

Department of Chemistry and Ustinov College

Surface freezing transitions in mixed monolayers of a homologous series of cationic surfactants, the alkyltrimethyl ammonium bromides (C_nTAB where n = 12, 14, 16, 18), as well as a range of non-ionic, zwitterionic and biological surfactants, have been investigated ellipsometrically with a range of *n*-alkanes (C_m where m = 12 – 20, 28). Two distinct solid phases are observed depending upon the chain length difference between surfactant and *n*-alkane. Type I solid phases consist of a surface frozen mixed monolayer and are formed when this difference is small. Type II solid phases are bilayer structures with a frozen layer of neat *n*-alkane above a liquid-like mixed monolayer. Type II freezing was thought to occur *via* wetting of surface frozen *n*-alkane, as previously reported type II transitions took place in the presence of surface frozen *n*-alkanes. Thermodynamically stable type II solid phases have now been found in the presence of *n*-alkanes that do not show surface freezing at the air/alkane interface, however, and so this picture is incomplete. In the presence of pentadecane, for example, the biological surfactant *lyso*-OPC forms a stable type II solid phase 6.5 °C above the *n*-alkane bulk melting point. Such a large surface freezing range is unprecedented for a type II system.

Studies using external reflection FTIR (ER-FTIRS) and vibrational sum-frequency spectroscopies (VSFS) have been used to probe these novel behaviours. Results were fully consistent with the proposed structures of both type I and type II surface frozen layers. 2D correlation analysis of ER-FTIR spectra as a function of temperature showed that type II frozen layer formation does not proceed *via* a simple wetting transition, with the formation of a transient intermediate implied. Evidence for such an intermediate was provided by dynamic ellipsometry measurements on the type II C_{18}TAB/*n*-eicosane system.

Acknowledgements

My deepest thanks go to my Supervisor, Professor Colin Bain, whose support and patience have been invaluable in researching and preparing this thesis. Special thanks also go to Dr. Eric Tyrode for letting me play with his spectrometer in Sweden, beating me at squash and teaching me how to clean a kitchen sink.

It is said that if an infinite number of monkeys were given an infinite number of typewriters, they would eventually write the complete works of Shakespeare. This thesis may not hit such heady heights, but I've had some great cage-mates along the way. Thanks go to all members of the Bain group, past and present, who have never failed to keep me entertained with pies, cake, bowling, barbecues, crosswords and the occasional bit of science.

Throughout my time in Durham I have had the support of no less than three brass bands. The massed ranks of Chester-le-Street, DUBB and Trimdon never lost faith in me throughout my studies, and for that I am grateful. As well as for the trips to Blackpool, London and, er, Peterlee leisure centre of course.

To EMH
Surveyor of turtles and teacher of Zambians.

Glossary of Common Abbreviations and Symbols

Surfactants

C_{18}TAB	octadecyltrimethylammonium bromide
C_{16}TAB	hexadecyltrimethylammonium bromide
C_{14}TAB	tetradecyltrimethylammonium bromide
C_{12}TAB	dodecyltrimethylammonium bromide
lyso-PPC	*lyso*-palmitoylphosphatidylcholine
lyso-OPC	*lyso*-oleylphosphatidylcholine
$C_{16}E_8$	octaethyleneglcol hexadecyl ether
$C_{16}E_6$	hexaethyleneglcol hexadecyl ether
$C_{14}E_8$	octaethyleneglcol tetradecyl ether
C_{14}DAPS	tetradecyltrimethylammonio-1-propanesulfonate
C_{16}DAPS	hexadecyltrimethylammonio-1-propanesulfonate
C_{12}mal	β-n-dodecyl D-maltoside
C_{14}mal	β-n-tetradecyl D-maltoside

Techniques

ER-FTIRS	external reflection Fourier transform infrared spectroscopy
IRRAS	infrared reflection-absorption spectroscopy
RAIRS	reflection-absorption infrared spectroscopy
PM-IRRAS	polarisation-modulation infrared spectroscopy
VSFS	vibrational sum frequency spectroscopy
BAM	Brewster angle microscopy
SAXS	small angle x-ray scattering

Symbols

r_x	Fresnel reflection coefficient
t_x	Fresnel transmission coefficient
R_{123}	reflectivity of a thin film between two bulk media
$\overline{\rho}$	coefficient of ellipticity
η	ellipsometric thickness
d	interfacial film thickness
ΔT	difference between bulk and surface freezing points
ϕ_x	volume fraction of component x
R_m	molar refractivity
V_m	molar volume
Φ	synchronous correlation spectrum
Ψ	asynchronous correlation spectrum

Table of Contents

Chapter 1

Introduction

1.1 Research Objectives

Oil and water do not mix. They do, however, interact with each other both at and across interfaces. Such interactions are of vital importance to various biological functions and play pivotal roles in many industrial applications. A thorough understanding of the molecular-level structures formed at the oil/water interface and the air/water interface in the presence of oil is therefore of great importance as a first step towards the full elucidation of processes as diverse as microemulsion formation, cellular transport, detergency and solubilisation.

The objective of this thesis is to investigate solid-liquid phase transitions in mixed monolayers of surfactant and alkane at the air/water interface, known as surface freezing transitions. A combination of ellipsometry, exquisitely sensitive to changes in interfacial density, and two spectroscopic techniques, external reflection FTIR spectroscopy (ER-FTIRS) and vibrational sum-frequency spectroscopy (VSFS) are employed to assess the generality of surface freezing and to characterise the resultant solid phases.

In the current chapter, an overview of relevant concepts of surface chemistry is presented, followed by an introduction to the formation of mixed monolayers at the air/water interface by wetting phenomena. The chapter concludes with a discussion of recent advances in the understanding of surface freezing including a more detailed discussion of the aims of this work.

1.2 Surfactants

1.2.1 Surfactants at Aqueous Interfaces

The modification of interfacial properties by surfactants constitutes a large and important field of interest, both academically and industrially, with implications for processes as disparate as oil recovery,[1] detergency,[2] coating technologies,[3] ice cream manufacture[4] and biological functions such as breathing.[5] This affinity for action at interfaces arises due to the amphiphilic nature of surfactant molecules, with the overall balance between hydrophilic (headgroup) and

hydrophobic (tailgroup) regions determining the properties of the molecule as a whole (figure 1.1).

Initial studies of surfactant monolayers focused on the spreading of polar oils on water. Pockels[6] measured how the surface tension of these monolayers changed as they were compressed, and noticed two different states of oil – one in which compression altered the surface tension and one in which compression had no effect. Rayleigh[7] interpreted these results in terms of compression of a single layer of molecules (i.e. a monolayer) on the surface of the water. Langmuir further developed these techniques and deduced that the polar headgroups of oils were in contact with the water surface, whilst the chains were tilted at a steep angle to the surface plane.[8] Langmuir later stated that the monolayers existed in solid, liquid and gaseous phases which were directly analogous to the related bulk phases, except for a difference in dimensionality.[9] As a result of his pioneering work, monolayers of surfactants that are effectively insoluble on the timescale of the experiment have become known as Langmuir monolayers.

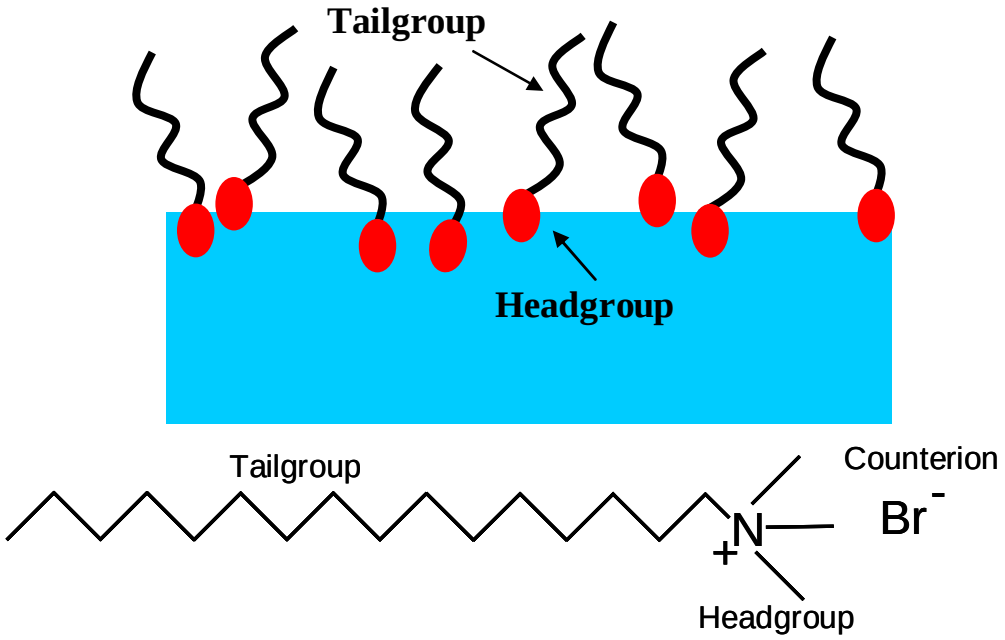

Figure 1.1 Top, schematic illustration of a surfactant monolayer at the air/water interface, showing hydrophobic tailgroup and hydrophillic headgroup regions of the surfactant molecules. Bottom, structure of C_{16}TAB. The C_nTABs are the principal series of surfactants studied in this thesis. For the structure of other surfactants used, see Chapter 3.

This study focuses on Gibbs monolayers: monolayers of soluble surfactants which are spontaneously transferred to an interface from solution via a process

termed “adsorption”. The reverse (“desorption”) also occurs, and when the rates of the two processes are equal the monolayer is at equilibrium. It should be noted that, in the case of Gibbs monolayers, the term monolayer refers to the monomolecular layer formed at an interface as a result of surfactant adsorption regardless of the extent of the adsorption – i.e. whether saturation coverage has been reached or not.

Adsorption is driven by the differing thermodynamic interactions between solvent and surfactant molecules. The “hydrophobic effect”[10, 11] describes these interactions in terms of the free energy for the process of adsorption, which has both enthalpic and entropic contributions. Enthalpic stabilisation of the adsorbed monolayer arises due to the increased van der Waals interactions between surfactant tailgroups that are confined to an interface, as well as through the resulting increase in hydrogen-bonding accompanying the removal of tailgroups from the aqueous phase. These effects are only minor however, and the dominant factor behind adsorption is entropic in origin, arising from an increase in orientational degrees of freedom of water molecules as the hydrophobic surfactant tails are removed from solution. Thus, monolayer formation is driven by the expulsion of molecules from bulk solution rather than any favourable interaction between the tailgroups and air.

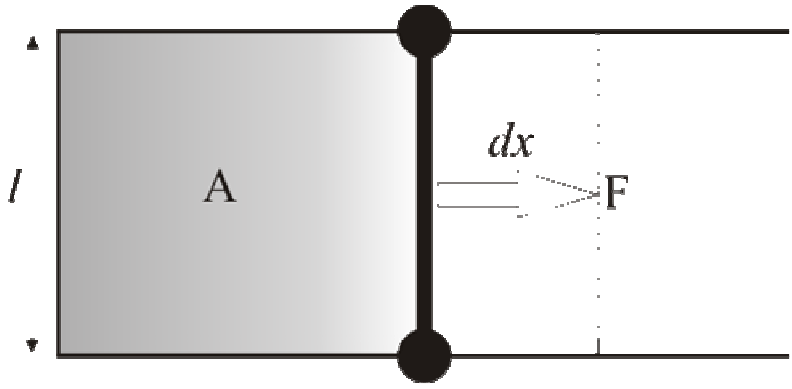

Figure 1.2 Increasing the area, A, of a thin film by moving a barrier through a small distance dx.

A result of the adsorption of surfactants to an interface is the reduction of the interfacial tension. Interfacial tension arises due to uncompensated forces at the surface of a fluid relative to its bulk, and hence substances displaying the highest interfacial tensions are those in which the greatest cohesive interactions exist between constituents (for example water [72.8 $mN\,m^{-1}$] and mercury [425.4

$mN\,m^{-1}$]][12]). Although normally expressed in terms of a force per unit length, interfacial tension can equivalently be described in terms of the reversible work required to create unit area of the interface, in units of $mJ\,m^{-2}$. Aside from the obvious equivalence of these two sets of units (work done = force applied x distance) this relation is readily demonstrated by considering the example of a liquid film that is stretched across a wire frame by a moveable barrier to create two interfaces of total area *A* (figure 1.2).[13] The work done when the barrier is moved an infinitesimal amount, leading to an increase in surface area *dA*, is equal to

$$dw = \gamma dA \tag{1.1}$$

which can also be expressed in terms of the force applied in moving the barrier as

$$dw = Fdx = \gamma 2ldx = \gamma dA \tag{1.2}$$

and it is seen that the two approaches are equivalent.

Interfacial tension can be related to the adsorbed amount of surfactant through use of the Gibbs adsorption isotherm,[2]

$$d\gamma = -\sum_i \Gamma_i d\mu_i \tag{1.3}$$

where $d\gamma$ is the change in interfacial tension in an *i*-component system (including solvents), Γ_i is the surface excess concentration (in units of $mol\,m^{-2}$) of component *i*, and $d\mu_i$ is the change in chemical potential of component *i* resulting from an infinitesimal change in composition of the system.

For a fluid/fluid interface it is hard to define the interfacial plane as there exists a certain surface roughness leading to an interfacial region in which the density changes gradually between that of the two bulk phases. A convenient choice of dividing surface therefore is to define a plane such that the surface excess of the solvent(s) is zero, which reduces the number of terms required in the analysis of the Gibbs adsorption isotherm solely to those arising from any solutes present

(surfactants, co-ions etc.). In the example of a single aqueous surfactant at the air-water interface, equation 1.3 can be written

$$d\gamma = -\sum_n \Gamma_n d\mu_n \tag{1.4}$$

where n is the number of adsorbing species present (for example, n = 2 for a 1:1 ionic surfactant, as both the surfactant ion and counterion must adsorb in order to maintain local electroneutrality). The change in chemical potential of a component can be defined in terms of the activity of that component as

$$d\mu_i = RTd\ln a_i \tag{1.5}$$

where R is the gas constant, T is temperature and a is the activity of component i. Applying the condition for equality of chemical potential of each component in all phases at equilibrium the sum in equation 1.4 can be further simplified (equation 1.6).

$$d\gamma = -nRT\Gamma d\ln a \tag{1.6}$$

In the limit of an ideal dilute solution the activity can be replaced by the concentration of the surfactant ($a = c/c^{\phi}$ where c^{ϕ} is the one molal standard state concentration), and rearranging in terms of surface excess gives the Gibbs equation for adsorption (equation 1.7).

$$\Gamma = -\frac{1}{nRT}\left(\frac{d\gamma}{d\ln c}\right)_{T,p} \tag{1.7}$$

Due to the finite size of and interactions between surfactant molecules, there is a maximum obtainable surface excess. This is referred to as the "limiting surface excess", Γ_∞, and is reached at infinite surfactant activity. In practice this point cannot be reached and the maximum obtainable surface excess, Γ_{max}, occurs at a bulk concentration roughly equal to the Critical Micelle Concentration (CMC). At and above the CMC surfactant monomers spontaneously form micellar aggregates (see section 1.2.2), limiting the activity of the surfactant in bulk solution. As a result, the interfacial tension also reaches a minimum value above the CMC (although this is also due to the constancy of the subsurface monomeric surfactant concentration above the CMC).

The effectiveness and efficiency of a surfactant can be described in terms of its interfacial tension reducing capability. An effective surfactant is one which is capable of producing a low minimum interfacial tension (i.e. a high maximum surface pressure since $\pi_{max} = \gamma_0 - \gamma_{max}$, where γ_0 is the interfacial tension of the neat interface). More effective surfactants generally have more than one hydrophobic chain, such as gemini, surfynol or polymeric surfactants. A high concentration may be required to reach this maximum adsorption, however, and so the efficiency of a surfactant is measured as the concentration required to lower the interfacial tension by $20\,mN\,m^{-1}$, where this concentration is lower for a more efficient surfactant.

1.2.2 Surfactants in Solution

The hydrophobic effect is not only manifested by the process of adsorption. The unfavourable ordering of solvent molecules around surfactant tailgroups can also be reduced by the aggregation of surfactant in solution in such a way that the tailgroups are effectively shielded from the solvent by the headgroups. The aggregates formed are called micelles, and their formation occurs spontaneously above the CMC. The environment within the micelles is fluid-like due to thermal motion of the surfactant tailgroups. The specific geometry of the surfactant determines such parameters as micellar shape, size and the average number of molecules per micelle (the "aggregation number"). Factors such as concentration and temperature can also have an effect. Figure 1.3 shows some examples of micellar structure.

The CMC of a surfactant varies in a predictable way with certain structural features.[2] For example, non-ionic surfactants generally have lower CMCs than ionic surfactants with a similar overall hydrophobicity. This is due to the reduced electrostatic repulsion between headgroups in the case of non-ionic surfactants. As a rule of thumb, factors that increase the hydrophobic nature of the tailgroup decrease the CMC, so within a homologous series of surfactants CMC decreases with increasing tailgroup length. The addition of background electrolyte to a solution of an ionic surfactant depresses the CMC as the

increased ionic strength of the solution serves to reduce the effect of electrostatic repulsions between headgroups.

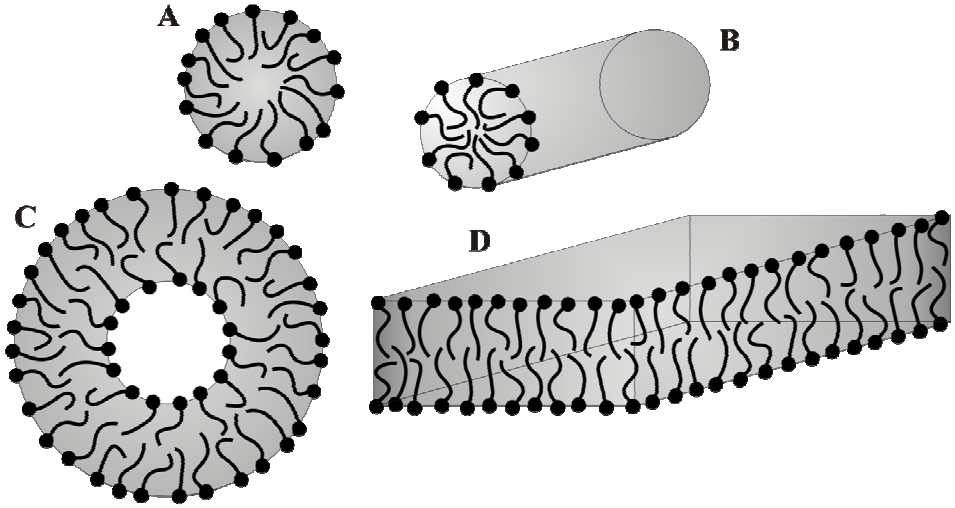

Figure 1.3 Examples of aggregates formed in solution by surfactants: (A) spherical, (B) cylindrical, (C) vesicle, (D) lamellar sheets.

The temperature dependence of the CMC is generally very weak, since the enthalpy of solution for a typical hydrocarbon surfactant is small and therefore the van't Hoff isochore tells us that its solubility product is relatively insensitive to temperature. Non-ionic surfactants based around polyoxyethylene units are an exception to this rule as the CMC decreases markedly with increasing temperature, due largely to the decreasing solubility of these surfactants as the temperature is raised. This decrease in solubility is caused by dehydration of the headgroups at higher temperatures. In fact, at a certain temperature the level of dehydration becomes sufficient to render these surfactants insoluble. This temperature is called the cloud point due to the opaque nature of the resulting suspensions. A related phenomenon occurs with ionic surfactants, although in this instance the solubility decreases markedly as the temperature is lowered below a certain point, called the Krafft temperature. The Krafft temperature represents the point at which the solubility limit of the surfactant is equal to its CMC – i.e. micelles do not form below the Krafft temperature. The marked decrease in overall solubility is caused by the relative insensitivity of the CMC to temperature, as below the CMC solubility is limited by the absolute solubility of the individual surfactant molecules. This is in contrast to the situation at surfactant concentrations above the CMC, where a small increase in the solubility of monomeric surfactant with temperature causes a sharp increase in

the absolute solubility of surfactant (since micelles are soluble even in the hypothetical situation when the concentration of monomeric surfactant in solution is zero). The Krafft temperature of a surfactant reflects not only its CMC but also the free energy difference between hydrated crystals and fully solvated ions.[14]

The ability of surfactants to form soluble aggregates with a hydrophobic interior has led to numerous applications in industry and their appearance in a number of biological systems.[1, 15] The hugely technologically important process of detergency relies upon the ability of surfactants to solubilise oily dirt particles, either within micelles or through the formation of microemulsions. Other applications include the solubilization of drug molecules within microemulsion droplets or vesicles (see figure 1.3), a method which has recently been extended to the search for viable alternatives to viral transfection vectors for the treatment of various genetic disorders.[16]

1.3 Experimental Techniques

1.3.1 Tensiometry

Although many different techniques have been developed for the determination of the interfacial tension between two phases, they can all be grouped into four categories dependent upon the physical principles they exploit:

1. Force methods, such as the Wilhelmy plate and du Noüy ring, measure the force exerted on an object suspended at the interface of interest. This force is related to the interfacial tension by a set of equations determined by the geometry of the experiment.

2. Capillary wave methods, such as Surface Light Scattering, measure the frequency of light scattered from the thermally excited capillary waves which exist at all fluid/fluid interfaces. The dispersion equation of the waves is related to the interfacial tension, as well as to the viscosity of the two fluid phases.

3. Pressure methods, such as the Maximum Bubble Pressure technique, measure the pressure difference across a curved interface that arises as a consequence of the interfacial tension. This pressure difference is known as the Laplace Pressure.

4. Drop Shape methods, such as pendant/rising and spinning drop techniques, utilise the balance between the gravitational/buoyancy forces which tend to distend the drop and the force due to the interfacial tension which tends to contract the drop into a sphere.

Of these methods the most commonly encountered are those measuring force or drop shape. The force exerted on an object such as a Wilhelmy plate immersed in a solution contains contributions from the surface tension of the solution and the buoyancy of the object. This force can be expressed as

$$F = 2(l_t + l_w)\gamma\cos\theta + l_t l_w \Delta\rho g l_d \qquad (1.8)$$

where l_t, l_w and l_d are the thickness, width and immersion depth of the plate, θ is the contact angle at the three-phase contact line, γ the interfacial tension, $\Delta\rho$ the difference in density between the two phases and g is the acceleration due to gravity. This equation is greatly simplified by experimentally setting the immersion depth to zero (the point of maximum force) and the contact angle to zero (through the use of a highly hydrophilic plate material). The interfacial tension is then simply given by the measured force divided by the plate perimeter.

The pressure difference across a curved interface can be described by the Laplace equation[17]

$$\Delta p = \gamma\left(\frac{1}{R_1} + \frac{1}{R_2}\right) \qquad (1.9)$$

where Δp is the pressure difference across the interface, γ is the interfacial tension and R_1 and R_2 are the principal radii of curvature of the drop.

For an axi-symmetric drop this pressure difference may also be expressed as a function of gravity and the difference in densities of the phases on either side of the interface. Equating these two expressions gives the Laplace-Young equation.

$$\Delta\rho gh = \gamma\left(\frac{1}{R_1}+\frac{1}{R_2}\right) \tag{1.10}$$

Here $\Delta\rho$ is the difference of the densities of the two phases, g is the acceleration due to gravity and h is the height within the drop. Drop images are captured and the drop profile is compared to those computed analytically from the Laplace-Young equation. The surface tension is then provided by the profile that best fits the experimental image.

1.3.2 Scattering Techniques

Various scattering or reflectometry techniques can be used to study interfaces, all of which rely upon a few basic properties of electromagnetic radiation (i.e. light) and how it interacts with matter. When light encounters an interface (defined by a discontinuity in refractive index) it is transmitted, reflected and refracted in well defined ways determined by the nature of both the incident and reflecting/transmitting media. The relation between the angles of incidence, reflection, refraction and the refractive index of the two media are given by Snell's law,[18]

$$n_i \sin\theta_i = n_t \sin\theta_t \tag{1.11}$$

where terms are defined in figure 1.4.

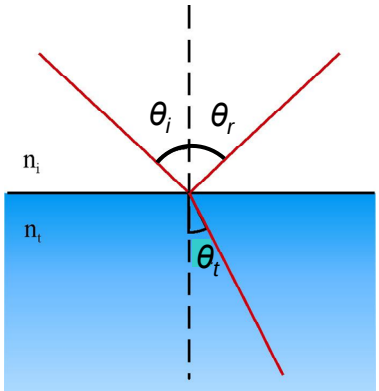

Figure 1.4 Reflection and refraction of a light beam from a planar interface.

The light may be considered as two orthogonal components, with electric field vectors perpendicular (s-polarised) and parallel (p-polarised) to the plane of incidence. The behaviour of these two components upon reflection from (*r*) and transmission through (*t*) an interface is given by the Fresnel equations (1.12).[18]

$$\begin{aligned} r_p &= \frac{n_t \cos\theta_i - n_i \cos\theta_t}{n_i \cos\theta_t + n_t \cos\theta_i}, \quad t_p = \frac{2n_i \cos\theta_i}{n_i \cos\theta_t + n_t \cos\theta_i} \\ r_s &= \frac{n_i \cos\theta_i + n_t \cos\theta_t}{n_i \cos\theta_i - n_t \cos\theta_t}, \quad t_s = \frac{2n_i \cos\theta_i}{n_i \cos\theta_i + n_t \cos\theta_t} \end{aligned} \tag{1.12}$$

Since the p-polarised and s-polarised light behaves differently reflection from an interface generally leads to a change in the polarisation state of the light. This fact is used by the techniques of ellipsometry and Brewster angle microscopy, for example.

Ellipsometry

Ellipsometry measures the changes in polarisation that occur when light is reflected from an interface, specifically the ellipsometric ratio r_p / r_s. If light of a well defined initial state of polarisation is used, it is possible to model these changes and relate them to the dielectric properties of the interface. In this manner, ellipsometry can be used as a way of measuring the dielectric excess at an interface, a quantity intricately related to the adsorbed amount and physical state of any adsorbed material.

The conformation of ellipsometer relevant to the present research is known as a phase modulated ellipsometer, and will be introduced in more detail in chapter 2. The main feature of this implementation is the use of an angle of incidence fixed at the Brewster angle of the interface of interest. The Brewster angle of an interface is the angle at which, for an ideal sharp interface, the reflectivity of p-polarised light falls to zero and is given by

$$\tan\theta_b = \frac{n_t}{n_i} \tag{1.13}$$

For a real interface, r_p / r_s is not zero at the Brewster angle but is purely imaginary, and this imaginary component is called the coefficient of ellipticity, $\overline{\rho}$.

$$\mathrm{Im}(r_p / r_s) = \overline{\rho} \tag{1.14}$$

The coefficient of ellipticity is exquisitely sensitive to changes in the dielectric profile across an interface such as those caused by surface roughness or adsorbed surfactant. Corrections to Fresnel's equations were derived by Drude to take into account smooth changes in permittivity across an interface, given by

$$\overline{\rho} = \frac{\pi}{\lambda} \frac{\sqrt{\varepsilon_i + \varepsilon_t}}{(\varepsilon_i + \varepsilon_t)} \eta \tag{1.15}$$

where ε_x is the relative permittivity of the incident (*i*) or reflecting (*t*) medium, λ is the wavelength of the probing light and η is the ellipsometric thickness of the interfacial layer given, for a uniform isotropic layer, by

$$\eta = \frac{(\varepsilon_m - \varepsilon_i)(\varepsilon_m - \varepsilon_t)}{\varepsilon_m} d \tag{1.16}$$

where ε_m is the dielectric constant of the layer and *d* is its thickness.

Grazing Incidence X-ray and Neutron Scattering

The typical wavelength of a beam of neutrons or x-ray radiation used to study interfaces is of the order of a few Å. If a beam impinges on the surface of a sample at near-grazing incidence then it undergoes total reflection and can give information about any surface layers present.

Figure 1.5 shows the geometry of a typical specular reflectivity experiment. Reflectivity curves are determined with respect to the momentum transfer upon reflection at the interface, generally in the z-direction. This momentum transfer, Q_z, is given by

$$Q_z = \frac{4\pi}{\lambda} \sin \alpha_i \tag{1.17}$$

where terms are defined in figure 1.5.

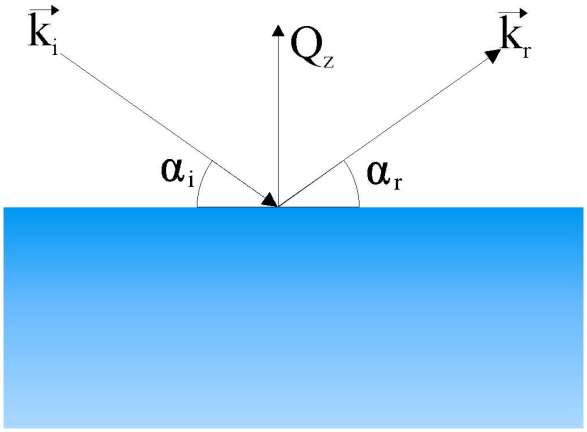

Figure 1.5 Geometry for a specular reflectivity experiment. The angle of incidence, α_i has been exaggerated for clarity.

The specular reflectivity of a sample is dependent upon the scattering length density profile perpendicular to the interface, and hence is a good tool for measuring parameters such as thickness, density or interfacial roughness. In the case of neutrons isotopic substitution can give more detailed information about the structure of the interface as scattering occurs from the nuclei, and so different isotopes of the same element may have markedly different scattering lengths.

Spectroscopic Techniques

Spectroscopic techniques have the advantage of chemical specificity, i.e. they have the potential to be used to distinguish between the various chemical components of a system. In this work External Reflection Fourier Transform Infra-Red Spectroscopy (ER-FTIRS, sometimes referred to as IRRAS – Infra-Red Reflection Absorption Spectroscopy – or RAIRS – Reflection-Absorption IR Spectroscopy – in the literature) is used to study Gibbs monolayers at the air-water interface.

In an ER-FTIRS experiment an IR beam impinges upon the interface being studied at an angle to the surface normal, and only the reflected beam is collected by the detector, thereby giving the technique a good degree of surface specificity.

The Fresnel equations, combined with the relevant complex refractive indices, can be applied to the three-layer system of air, surfactant monolayer and bulk

solution. Both the real and imaginary parts of the complex refractive index vary depending upon the frequency of incident radiation that is used to measure it, with the imaginary part giving information about the absorption of radiation. The refractive indices of the monolayer and the bulk solution will vary differently across the IR frequency range, resulting in a change in the overall reflectivity from the interface, which is determined by the interference of beams reflected from the air-monolayer and monolayer-solution interfaces. Effectively this means that the peaks observed in an ER-FTIR spectrum result not directly from the absorption of specific frequencies of IR radiation, but from the large variation in complex refractive indices in the region of molecular vibrations.

The application of ER-FTIRS to surfactant systems is non-trivial. Difficulties arise in the extraction of monolayer peaks because their magnitude is extremely small and they sit on highly curved baselines caused by bulk water and water vapour in the beam path. Despite the inherent difficulties of the technique, the rewards of applying ER-FTIRS to the surface freezing systems introduced in this chapter are potentially great. Information about the molecular structure of a monolayer can be inferred from the central wavenumber of a peak, which is determined by the electronic environment of a molecule. For example, the frequency of carbonyl stretches in transition metal complexes is heavily dependent upon the presence and position of electron donating or withdrawing groups. More relevant to this research is the fact that the frequency of the CH_2 stretches in hydrocarbon compounds is higher for a chain with many *gauche* defects than for a chain in an all-*trans* conformation. The former is typical of a liquid environment, whilst the latter is indicative of a crystalline environment and hence ER-FTIRS can be used to distinguish between solid and liquid monolayers.

1.4 Phase Transitions in Two Dimensions

Three-dimensional phases and the transitions between them are commonly encountered in everyday life. The use of steam to cook food, ice to cool drinks and the sublimation of dry ice to produce artificial fog are but a few examples. In the same way, two-dimensional systems exhibit a varied phase behaviour which

can be just as important, if less obviously so, than their three-dimensional counterparts.

For example, phase transitions in monolayers of the phospholipid DPPC, a major component of human lung surfactant, enables the attainment of low interfacial tensions on the surface of alveoli which allows us to breathe.[19] Phospholipid bilayers present in cell membranes undergo a fluid-gel transition with changing temperature.[20] The fluid phase occurs at physiological temperature and this allows certain substances that are soluble in the phospholipid tails to pass through the membrane into the cell (drug molecules, for example).

These phospholipids fall into the class of "insoluble" surfactants which form Langmuir monolayers. Langmuir monolayers are possibly the most extensively characterised two-dimensional systems to date, as in general they show rich phase behaviour in comparison to their soluble counterparts.[21] Phase transitions have been reported in Gibbs monolayers, however, and are of potential importance to industry since soluble surfactants are the more widely used class of surfactants.

The following sections introduce the variety of phases and phase transitions that occur in 2D systems, beginning with the classification of phase transitions before moving on to the seemingly trivial concept of spreading oil on water.

1.4.1 Characterisation of Phases and Classification of Phase Transitions

As for the three dimensional case, two dimensional phases are characterised by the translational and orientational order present.[22] Order can be quantified through the use of correlation functions, which consider the environment surrounding an arbitrary point in the sample. For example, a translational correlation function might show how the distance between particles varies with distance from a particular point within the sample. In effect this gives information about the repeatability of the lattice through space, and is related to the density of the sample. The rate at which a correlation function decays denotes whether a phase has long or short-range order with respect to that

particular function. For an ideal crystalline sample the translational correlation function will give regular peaks over infinite distances, indicating long-range order. In reality crystals contain defects, and so the correlation function decays with distance, tending towards the average number density of particles within the crystal. In the case of a liquid sample the translational correlation function decays exponentially with distance, indicative of short-range order.

In systems made up of chain molecules or ellipsoidal particles, such as those found for liquid crystals or the crystalline phases of alkanes, order can also be quantified in terms of the tilt of particles relative to a fixed axis or the rotation of particles about an axis.

In the two-dimensional case a phase cannot exhibit true long-range translational order, due to thermal fluctuations of the mean layer position which destroys long-range ordering. Instead, 2D solids are described as having quasi-long-range order, with an algebraically decaying correlation function. 2D solids do, however, display long-range orientational order (in terms of nearest-neighbour direction, tilt or rotation for example), whereas in the liquid phase both translational and orientational ordering is short-range.

The order of a phase transition depends upon the behaviour of the chemical potential. As classified by Ehrenfest, a transition is first order if there is a discontinuity in $\left(\partial\mu/\partial T\right)_P$.[23] This can be related to a discontinuity in the enthalpy, entropy and molar volume, as well as a singularity in the heat capacity (C_P) through the transition as shown below.

Chemical potential, μ, is defined as the partial molar Gibbs free energy, such that

$$\mu_i = \frac{\partial G}{\partial n_i}\Bigg)_{T,p,n_j(j\neq i)} \tag{1.18}$$

For a multicomponent system, one can write

$$dG = Vdp - SdT + \sum_{i=1}^{k} \mu_i dn_i \tag{1.19}$$

where V and S are the volume and entropy, respectively, p is the pressure and n_i is the number of moles of component i. The change in volume and entropy during a phase transition are therefore given by

$$\begin{aligned}\Delta_{21}S_m &= \left.\frac{\partial G_{m,2}}{\partial T}\right)_{p,n_i} - \left.\frac{\partial G_{m,1}}{\partial T}\right)_{p,n_i} = \sum_i^k \phi_i \Delta_{21} S_{m,i} = -\sum_i^k \phi_i \frac{\Delta_{21} H_{m,i}}{T} \\ \Delta_{21}V_m &= \left.\frac{\partial G_{m,2}}{\partial p}\right)_{T,n_i} - \left.\frac{\partial G_{m,1}}{\partial p}\right)_{T,n_i} = \sum_i^k \phi_i \Delta_{21} V_{m,i}\end{aligned} \tag{1.20}$$

where subscript m denotes a molar quantity and subscript 21 denotes a transition from phase 1 to phase 2. The heat capacity tends to infinity due to the finite enthalpy change.

$$C_p = \left(\frac{\partial H}{\partial T}\right)_{p,n} \tag{1.21}$$

Second order transitions show a discontinuity in the second derivative of the chemical potential, and hence in the first derivatives of enthalpy and volume with respect to temperature (see figure 1.6).

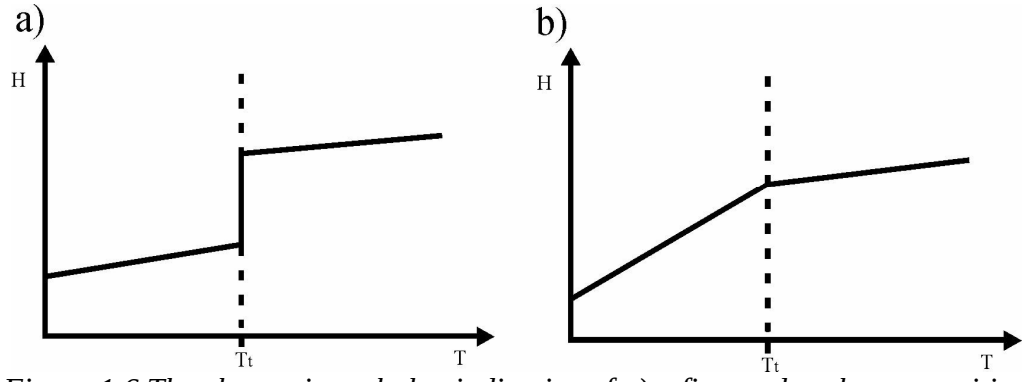

Figure 1.6 The change in enthalpy indicative of a) a first-order phase transition and b) a second-order phase transition.

This analysis applies equally to the two-dimensional case, replacing pressure with surface pressure (Π), and volume with the area per mole at the interface (A). Thus a first-order transition will be associated with a discontinuity in A, and therefore also in the surface excess. In very dilute solution the surface excess is inversely proportional to the area per molecule, $\Gamma \propto 1/A$, as the bulk contribution to the surface concentration can be ignored.

1.4.2 Wetting and Wetting Transitions

Although oil and water do not mix, the appearance of interference colours on the surface of puddles is testament to the fact that complex oils will, in general, spread across a water surface. The spreading of a liquid at a flat surface (itself either solid or liquid) is known as its wetting behaviour, and there are three possible scenarios (figure 1.7). In the case of complete wetting, a liquid drop placed on the surface will spread out to form a uniform film covering the whole surface. At the other extreme the drop may not spread and remain as a lens floating at the surface (in equilibium with a dilute 2D gas as required thermodynamically), a case termed partial wetting. Partial wetting is the situation common to most *n*-alkanes on water; complete wetting is restricted to pentane – heptane[24-26] which is perhaps surprising given how readily other common oils spread on water. The third possibility describes an intermediate wetting state where the drop spreads to form a uniform thin film at the interface in equilibrium with a floating lens of excess oil. This situation is the one most commonly encountered for oil drops at the air/surfactant solution interface, and hence is of most relevance to the present study.

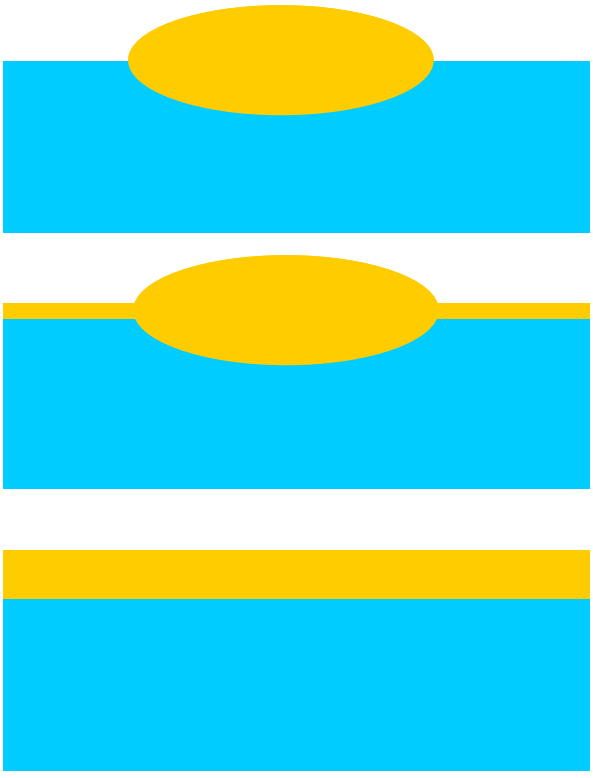

Figure 1.7 Wetting behaviour of an oil drop placed on an aqueous surface. Top, partial wetting. Middle, pseudo-partial wetting. Bottom, complete wetting.

Which of the three possibilities actually occurs is governed by competition between long- and short-range forces across a spread film. The long-range forces are described by the variation in free energy, $F(d)$, with film thickness, d. For a sufficiently thick film the free energy is simply the sum of the interfacial tensions of the air-oil and oil-water interfaces. If the thickness of the film is similar to the range of long-range dispersion forces an additional contribution due to the interaction of water and air across the film must be included, and $F(d)$ can be expressed as,

$$F(d) = \gamma_{ow} + \gamma_{ao} + P(d) = \gamma_{ow} + \gamma_{ao} - \frac{A_{aow}}{12\pi d^2} \qquad (1.22)$$

where γ_{ow} and γ_{ao} are the interfacial tensions of the oil-water and air-water interface, respectively, and the final term ($P(d)$) describes the long-range Van der Waals interaction across the film. The Hamaker constant, A_{aow}, depends upon the dielectric properties of the system as calculated by Lifshitz,[27]

$$A_{aow} \approx \frac{3}{4}kT\left(\frac{\varepsilon_a - \varepsilon_o}{\varepsilon_a + \varepsilon_o}\right)\left(\frac{\varepsilon_w - \varepsilon_o}{\varepsilon_w + \varepsilon_o}\right) + \frac{3h}{4\pi}\int_{\upsilon_1}^{\infty}\left(\frac{\varepsilon_a(i\upsilon) - \varepsilon_o(i\upsilon)}{\varepsilon_a(i\upsilon) + \varepsilon_o(i\upsilon)}\right)\left(\frac{\varepsilon_w(i\upsilon) - \varepsilon_o(i\upsilon)}{\varepsilon_w(i\upsilon) + \varepsilon_o(i\upsilon)}\right)d\upsilon \qquad (1.23)$$

where ε_x is the dielectric constant of medium x and $\varepsilon_x(i\upsilon)$ is its value at the imaginary frequency $i\upsilon$. The first term in equation 1.23 describes van der Waals interactions between permanent dipole – permanent dipole and permanent dipole – induced dipole pairs. The second term takes into account dispersion interactions between instantaneous dipole – induced dipole pairs. This dispersion contribution to the overall Hamaker constant is susceptible to retardation effects at distances greater than about 5 nm (retardation effects occur when the time taken for a pair of dipoles to "communicate" with each other is similar to the timescale of fluctuation of the original dipole; the effect becomes significant at larger distances, or when the separating medium is a condensed phase, such as the oils considered here). An important point regarding the effect of the long-range contribution in equation 1.22 relates to the sign of the Hamaker constant. It can be seen that a negative Hamaker constant leads to a reduction in free energy as the film thickens (favouring complete wetting), whilst a positive

Hamaker constant promotes thinning of the film. In the case of the short *n*-pentane, therefore, the fact that the Hamaker constant is negative (above a certain critical temperature, as discussed later) leads to a net repulsive van der Waals force and complete wetting behaviour. For the higher *n*-alkanes the dispersion contribution to the total Hamaker constant is large and dominant, leading to a net attractive force and the formation of lenses at the air-water interface.

The Hamaker constant for any three medium system can be estimated from the Hamaker constants of the individual media across vacuum, by noting the following combining relations;

$$A_{aow} \approx \sqrt{A_{aoa} A_{wow}} \tag{1.24}$$

$$A_{aoa} \approx A_{aa} - 2A_{ao} + A_{oo} = \left(\sqrt{A_{aa}} - \sqrt{A_{oo}}\right)^2 \tag{1.25}$$

From these two approximations, coupled with the fact that the Hamaker constant of air across a vacuum is essentially zero due to the near identical dielectric constants, an overall expression for the Hamaker constant of the air-oil-water system is given by

$$A_{aow} \approx A_{oo} - A_{wo} \tag{1.26}$$

Short-range contributions to the free energy can be considered from the behaviour of equation 1.22 as film thickness tends to zero. In this limit, the free energy of the system reduces to that of the neat air-water interface.

$$F(d \to 0) = \gamma_{aw} \tag{1.27}$$

Substitution of this result into equation 1.22 gives

$$P(d \to 0) = \gamma_{aw} - (\gamma_{ow} + \gamma_{ao}) = S_i \tag{1.28}$$

In this equation, S_i is known as the initial spreading coefficient. Like the Hamaker constant, the sign of the initial spreading coefficient determines how the free energy of the system behaves in the presence of an oil film. If $S_i < 0$,

the oil will not wet water, whereas if $S_i > 0$ spreading is favoured. In effect these two statements describe a net energy penalty (or gain) upon destruction of an air/water interface and subsequent replacement with air/oil and oil/water interfaces. The example of *n*-pentane can again be used as an illustration of the effect of short range forces on wetting. The relevant surface tensions, and therefore S_i, are temperature dependent. Upon heating past 25 °C S_i changes sign from negative to positive, and a first-order wetting transition from partial to pseudo-partial wetting occurs.[26]

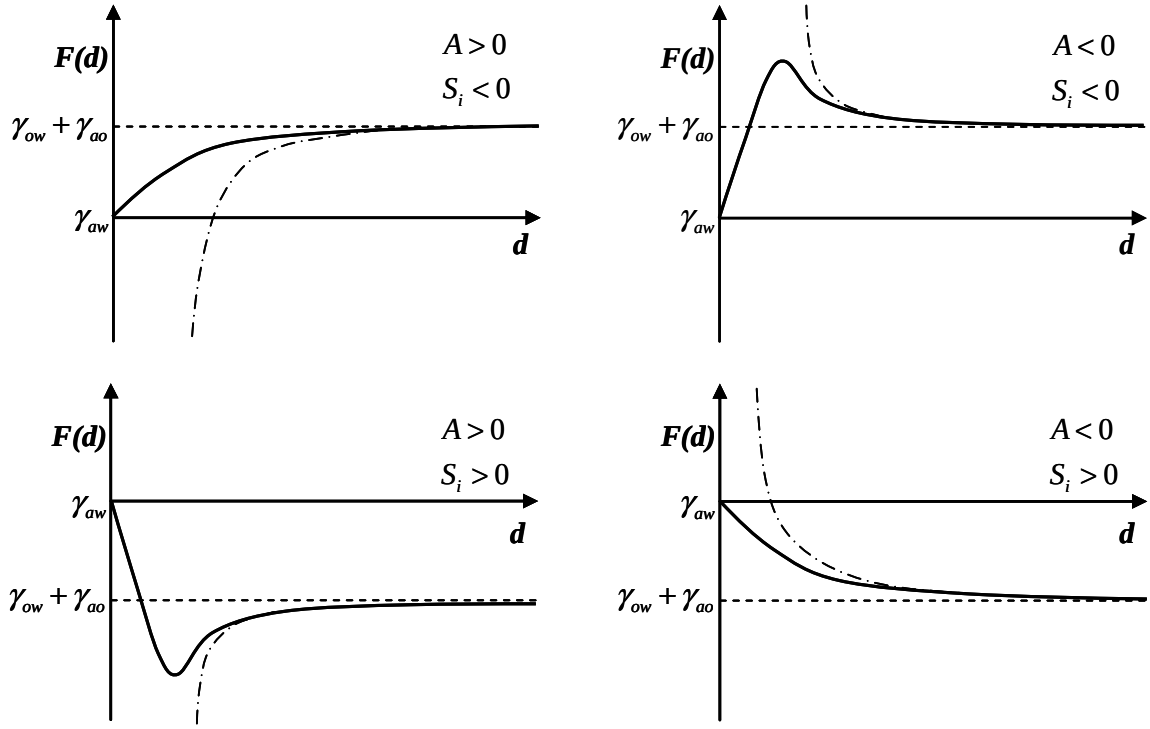

Figure 1.8 The effect of oil film thickness, d, on the free energy, F(d), of the air/water interface. Total free energy shown by a solid line, long-range van der Waals contribution shown by dash-dotted line.

Combining the observations on the behaviour of long- and short-range forces leads to four possible situations, shown graphically in figure 1.8. Partial wetting is favoured when $S_i < 0$, regardless of the sign of the Hamaker constant. Complete wetting occurs when $S_i > 0$ and the Hamaker constant is negative (i.e. when both effects favour spreading/thickening of the film). Finally, when $S_i > 0$ (favouring spreading) and the Hamaker constant is also positive (promoting thinning of the film) pseudo-partial wetting occurs, with excess oil forming a thermodynamically stable lens in equilibrium with a uniform thin film. The thermodynamic stability of two phases (bulk oil and oil in a film) over a single

phase can be seen by imagining a tangent between the minimum in $F(d)$ at finite thickness and a secondary minimum at infinite thickness. At all points this tangent is more negative than $F(d)$, hence the stability of a mixture of two phases.

The overall wetting behaviour of *n*-pentane, as demonstrated by Bonn *et al.*,[26] can now be understood in terms of the possibilities outlined in figure 1.8. As mentioned earlier, complete wetting occurs for *n*-pentane on water, due to a negative Hamaker constant for the system. In fact, this situation only arises above 53 °C, below this temperature the Hamaker constant is positive. Two wetting transitions are therefore observed for *n*-pentane, a first order transition at 25 °C from partial to pseudo-partial wetting caused by a change in sign of the initial spreading coefficient and a second, continuous transition to complete wetting at 53 °C (it should be noted that the boiling point of pentane is 36 °C and these experiments were performed in the presence of a saturated vapour). The first order nature of the lower temperature transition is in line with the theoretical predictions of Cahn, who deduced that below the critical temperature of the spreading oil a wetting transition from partial to complete wetting should be first order (in the case where the transition proceeds via pseudo-partial wetting, the first transition was predicted to be first order, followed by a continuous transition as the Hamaker constant changes sign).[28] At intermediate temperatures the film thickness diverges continuously with increasing temperature. Similar sequences of wetting transitions have been found for hexane and heptane on water,[29] hexane on brine,[25] and heptane on brine, induced by varying the salinity.[24]

Intermediate wetting behaviour has been observed for *n*-octane, where a range of film thicknesses have been observed dependent upon the substrate. A continuous transition from pseudo-partial to complete wetting was induced by increasing glucose concentration in the bulk, resulting in a 70 Å thick film.[30] Similarly thick films were formed at the surface of AOT solutions,[31] whilst thicker films of 100 Å and 200 Å were formed at the air/$C_{10}E_8$ solution interface and at the air-silicon interface,[32] respectively.

Other examples of wetting transitions of *n*-alkanes on silicon have found that a thin film of solid alkane is in equilibrium with a liquid lens. This behaviour was found for chain lengths between 16 and 50 carbons, and in all cases above the surface freezing temperature (see section 1.5) the alkane completely wets the interface.[33] The presence and structure of the solid alkane film was confirmed by x-ray reflectivity, which suggested the presence of a thin layer of chains oriented parallel to the interface underneath a layer of vertically oriented chains.[34] Similarly, at mica surfaces solid films of heptadecane and octadecane were found to coexist with liquid lenses using surface force measurements. Only partial wetting was found for tetradecane and hexadecane, however.[35, 36]

As has been noted, only short chain *n*-alkanes exhibit wetting transitions on a pure water surface. Wetting transitions can be induced, however, if surfactants are introduced into the subphase. Both the initial spreading coefficient and the Hamaker constant vary under the influence of such an external stimulus (in the same way as salinity, temperature etc. change the wetting behaviour of short *n*-alkanes) and a change in sign of either property results in a concurrent wetting transition.

Detailed studies of the mixing of oils with surfactant monolayers have been carried out by both Binks *et al.* and Aratono, Bain *et al.* using a combination of neutron reflectivity, surface tension and contact angle measurements, ellipsometry, line tension and theoretical modelling.

Binks *et al.* demonstrated that the surface excess of oil in mixed monolayers of the cationic surfactant C_{16}TAB and *n*-alkane was dependent upon the alkane chain length, with shorter oils more readily penetrating the surfactant monolayer.[37] Experiments on a range of C_nE_m/*n*-alkane systems revealed two competing behaviours.[38] Almost irrespective of surfactant, shorter alkanes (chain length of nine carbons or less) were found to completely wet the interface with the appearance of interference colours indicating a thick (>100 nm) film. Longer alkanes were found to pseudo-partially wet the interface. Analysis of surface tension data using the Gibbs equation (eqn. 1.7) suggested that alkane adsorption was limited to inclusion into an existing surfactant monolayer, and increased linearly with alkane activity to give an ideal-gas like isotherm. The use of

squalane as a non-adsorbing oil makes the interpretation of this finding questionable, however, as squalane has been shown to pseudo-partially wet solutions of the cationic surfactant C_{12}TAB.[39]

Neutron reflectivity experiments using selectively deuterated surfactant and alkane combinations showed that alkane uptake into cationic C_nTAB monolayers was less effective than into either non-ionic C_nE_m or anionic SDS monolayers, where the alkane was found to overlap more favourably with the surfactant tail.[40-42] In all cases wetting of the air-solution interface was found to cause a thickening of the surface monolayer as a result of a change in average tilt of surfactant tails toward the surface normal. The surface excess of surfactant was found not to change appreciably on adsorption of oil. Measurements of oil adsorption into monolayers of C_nTAB, C_nE_m, AOT and CPC suggested that oils with a variety of different structural features either wet or are close to wetting the air/solution interface, with the equilibrium spreading pressure close to zero for cyclohexane, perfluorooctane and PDMS.[43] It was also found that oil can adsorb into a surfactant monolayer through the vapour phase.

Aratono *et al.* demonstrated that a transition from partial wetting to pseudo-partial wetting occurs coincidentally with the gas-liquid phase transition in mixed monolayers of tetramethylammonium dodecyl sulphate (TMADS) and hexadecane.[44] Moreover, the phase transition was driven to lower surfactant concentration by the presence of the oil. Neumann's equations relate the dihedral angles of an oil lens to the three interfacial tensions (equations 1.29).

$$\begin{aligned} \cos\theta_a &= (\gamma_{ow}{}^2 - \gamma_{ao}{}^2 - \gamma_{aw}{}^2)/2\gamma_{ao}\gamma_{aw} \\ \cos\theta_w &= (\gamma_{ao}{}^2 - \gamma_{aw}{}^2 - \gamma_{ow}{}^2)/2\gamma_{aw}\gamma_{ow} \\ \cos\theta_o &= (\gamma_{aw}{}^2 - \gamma_{ow}{}^2 - \gamma_{ao}{}^2)/2\gamma_{ow}\gamma_{ao} \end{aligned} \qquad (1.29)$$

In order for the lens to be thermodynamically stable, the interfacial tensions must satisfy three inequalities given by equations 1.30. When these relations do not hold, complete wetting is expected.

$$\begin{aligned} \gamma_{ao} &< \gamma_{aw} + \gamma_{ow} \\ \gamma_{aw} &< \gamma_{ow} + \gamma_{ao} \\ \gamma_{ow} &< \gamma_{ao} + \gamma_{aw} \end{aligned} \qquad (1.30)$$

Close to the wetting transition in the TMADS/hexadecane system, however, these Neumann relations do not hold, despite the observation of a thermodynamically stable oil lens and a rigorously verified experimental technique.[45, 46] A similar exception to the Neumann relations was found close to the partial to a pseudo-partial wetting transition observed in monolayers of C_{12}TAB in the presence of hexadecane lenses,[47] where Bain *et al*. used ellipsometry to show unambiguously that the behaviour in the presence and absence of oil was fundamentally different. It was argued that a discontinuity in the coefficient of ellipticity as a function of surfactant concentration in the presence of hexadecane showed inclusion of oil molecules in the surfactant monolayer above a critical bulk concentration; the transition could either be viewed as a first order wetting transition driven by adsorbed surfactant or as a gaseous-liquid expanded transition caused by the presence of hexadecane. Aratono *et* al. measured the line tension of the C_{12}TAB/hexadecane system.[48] The line tension can be thought of as an energy penalty for the creation of a unit length of air-solution-oil contact line, and therefore plays a crucial role in the determination of the relative size of oil lenses. A positive line tension favours the minimisation of contact line through the coalescence of small lenses, whereas a negative line tension favours the creation of contact line by lens deformation or fission. The line tension of the C_{12}TAB/hexadecane system was found to undergo a sudden, discontinuous change of sign at a bulk surfactant concentration very close to the previously observed wetting transition. This finding was argued to be in accord with the theoretical and experimental treatments of Indeku, which predicted and demonstrated a change in sign of line tension approaching a first order transition from partial to complete wetting on solid surfaces.[49]

The generality of the wetting behaviour of oils of various structures on C_{12}TAB solutions and of hexadecane on different surfactant solutions was investigated by Bain *et al*. using a combination of ellipsometry and surface tension measurements.[39] Wetting transitions were found for dodecane, hexadecane and squalane on C_{12}TAB as well as for dodecane and hexadecane on C_{14}TAB and squalane and hexadecane on the local anaesthetic dibucaine hydrochloride. In all cases the mixed layers formed were found to be of monolayer thickness. These

results demonstrated that structure of both oil and surfactant need not be limited to simple linear hydrocarbon structures. Wetting phenomena, although common, were proved not to be universal as no wetting transitions were found for even simple linear alkanes on the surface of AOT solutions.

1.4.3 2D Analogues of Freezing and Condensation

For Langmuir monolayers initial evidence for phase transitions came from kinks and plateaus in surface pressure-area isotherms,[50, 51] although it was not until the use of X-ray diffraction showed that these phases had different structures that this interpretation was widely accepted.[52, 53] Figure 1.9 shows a generic phase diagram for Langmuir monolayers, where some of the phases shown are often divided further based on theoretical and/or experimental studies.

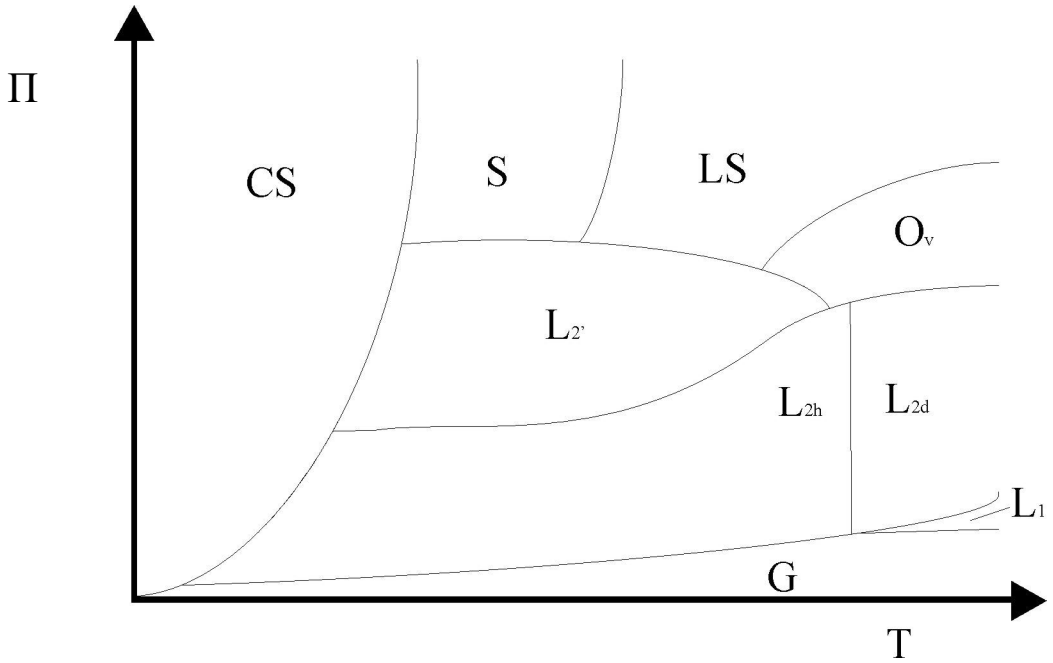

Figure 1.9 Generic phase diagram for Langmuir monolayers, adapted from Petersen et al..[54] The CS phase is a crystalline solid. Both G and L_1 are isotropic fluid phases. All other phases are mesophases- i.e they have short-range translational order but long-range orientational order.

The CS phase and the various mesophases (on a local scale) have hexagonal or distorted-hexagonal close packing, and the different phases can be distinguished by the direction of tilt of the molecules or the direction of compression of the lattice. Whilst both the CS phase and the mesophases exhibit long-range

orientational order, only the CS phase possesses quasi long-range translational order.

The order of transitions between the phases of Langmuir monolayers are still a matter of debate.[55] The transitions between tilted phases are first order, and transitions between tilted and untilted phases are generally continuous, but some studies suggested these should be classed as weakly first order.[56]

This hexagonal packing led to the comparison of Langmuir monolayers with bulk lamellar phases of *n*-alkanes, since both contain layered hydrocarbon chains.[54, 57] It is instructive, therefore, to consider briefly the crystal structures of bulk alkanes and draw correlations with phases of 2D chain molecules.

Many bulk alkanes freeze initially into layered rotator phases with an area per molecule of approximately 19.5 $Å^2$ perpendicular to the chains long axis (the area per molecule in the plane of the layer is modified by any chain tilt, θ, by a factor $\cos\theta^{-1}$).[125] Within each layer the chains are in an all-*trans* conformation, aligned roughly normal to the plane of the layer, and are free to rotate about their long axis. The exact rotator phase entered depends upon the chain length of the alkane. Long chain alkanes ($n \geq 26$) adopt a tilted orientation, taking up an undistorted hexagonal R_{IV} structure. Odd-numbered alkanes with shorter chains ($n < 22$) freeze directly into a distorted hexagonal R_I structure, whereas even-numbered bulk alkanes exhibit no thermodynamically stable rotator phaess. Alkanes with intermediate chain lengths ($22 \leq n \leq 25$) freeze firstly into an untilted and undistorted R_{II} structure, and then undergo a transition to a distorted R_I structure. At lower temperatures three crystalline phases are observed; orthorhombic, triclinic and monoclinic, with odd alkanes typically adopting orthorhombic phases and even alkanes triclinic. In these phases the area per molecule is slightly lower, at around 18.5 $Å^2$. The structures of the various rotator and crystalline phases, as well as their 2D analogues, are shown in figure 1.10.

In a Langmuir monolayer, phase transitions can be induced through compression of the monolayer in a Langmuir trough (in an analogous way to the phase transitions which can be induced, for example, by varying the pressure of a

given number of moles of water at constant temperature). For the case of Gibbs monolayers this method is not possible as compression of the surface will simply lead to desorption of surfactant into the bulk solution, and hence the surface excess concentration (and therefore area per molecule) of the surfactant will remain constant.

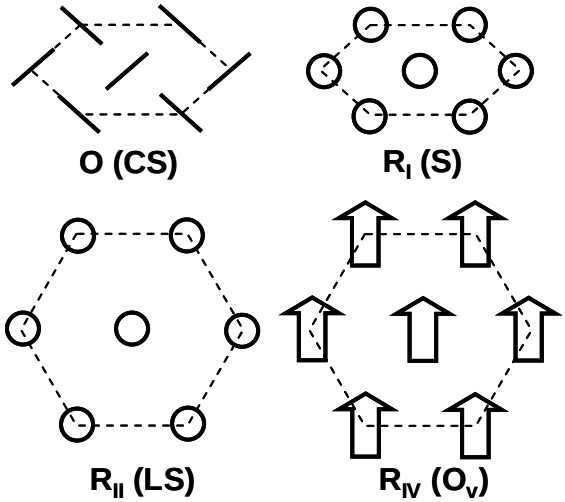

Figure 1.10 The equivalence of the orthorhombic (O) and rotator (R_I, R_{II} and R_{IV}) lamellar phases of bulk n-alkanes with structures found in Langmuir monolayers (CS, S, LS and O_v as shown in brackets). Circles represent chains aligned normal to the plane of the page, arrows denote the direction of tilt. Chains are free to rotate about their long axis with the exception of O (CS), where the line defines the plane of the carbon backbone.

The principal method for studying Gibbs monolayers is surface tensiometry. Tensiometric data can be interpreted in terms of the Gibbs equation, which was introduced in section 1.2.1.

$$\frac{\partial \gamma}{\partial \ln c} = -nRT\Gamma \qquad (1.31)$$

At a first order phase transition there is a discontinuity in the surface excess, and so there will be a kink in the surface tension isotherm.

Transitions described as gas-liquid have been observed in this way for a range of surfactants; decylammonium chloride,[58] dodecylammonium chloride,[59] sodium dodecyl sulphate (SDS),[58] sodium octanoate,[58] decyltrimethylammonium bromide,[59] octanol[58] and decanol,[60] for example.

Evidence to support the first order gas-liquid transition in monolayers of dodecylammonium chloride has been seen in the dynamic properties of the

interface. The damping coefficient of capillary waves (a function of surface tension, elasticity and viscosity) was measured by light scattering[61] and a direct electromechanical probe.[62] Deviations from theoretical predictions were attributed to the occurrence of a phase transition.

Previously such gas-liquid phase transitions were thought to be unobservable, as it was thought that Gibbs monolayers would be above their critical point at room temperature. Measurements on lauric acid monolayers suggested they were supercritical at 15 ˚C,[21] whilst measurements on pentadecanoic acid, an insoluble homologue, had a critical temperature of 50-60 ˚C.[63] On top of this experimental evidence, 2D theoretical van der Waals models give a critical temperature half that of the 3D fluid, suggesting that at room temperature no gas-liquid phase transition should occur.[64]

Unequivocal evidence for the existence of gas-liquid transitions was obtained for decanol monolayers using ellipsometry.[65] Kinks in surface tension isotherms are often small, and so it can be difficult to distinguish between a discontinuity in the surface tension and a rapidly changing gradient. Ellipsometric measurements on the other hand are directly linked to the dielectric excess normal to the interface, and hence are sensitive to changes in the phase of an adsorbed layer where there is a discontinuity in the dielectric excess.

Phase transitions have also been observed by measuring the evolution of surface tension during adsorption. A plateau in the plot of surface pressure, Π, against time is indicative of a first-order transition. Gas-liquid transitions have been observed by this method in monolayers of sodium octanoate[66] and nonanol[67]. This technique has been combined with fluorescence microscopy, a method used to image monolayers, for monolayers of hexaethylene glycol tetradecyl ether[68] and monoethylene glycol tetradecyl ether.[69] These systems clearly show phase coexistence in the plateau region, a key feature of a first-order transition.

Perhaps more elegantly, evidence of phase coexistence have been observed by Brewster Angle Microscopy (BAM) during the adsorption of n-hexadecyl phosphate for both gas-liquid and liquid-solid transitions.[70, 71] Whereas fluorescence microscopy relies upon the differential solubility of a fluorescent

dye in the two phases, BAM does not require the addition of an extra component to the system being studied.

BAM has been used in conjunction with surface tension evolution to directly compare the behaviour of Langmuir and Gibbs monolayers during a liquid-solid transition.[72] Surface pressure-area isotherms were recorded for the insoluble surfactant *N*-(γ-hydroxypropyl)-tetradecanoic acid amide (HTEAA), and surface pressure-time adsorption kinetics were recorded for the slightly soluble *N*-(γ-hydroxypropyl)-tridecanoic acid amide (HTRAA), which were then converted to $\pi - A(t)$ isotherms to allow direct comparison. Much slower and more homogeneous growth of the condensed phase was observed for Gibbs monolayers, implying a more equilibrated state. Gibbs monolayers also showed a greater orientational correlation length, resulting in a lower density of defects in the condensed phase.

BAM has also been used to study a liquid-solid transition in octadecanol at the hexane/water interface.[73] Here phase coexistence was observed over a range of temperatures, suggesting that the transition was not truly first-order. This observation was thought to be due to small amounts of surface active impurity in the monolayer acting to increase the thermodynamic variance of the system.

Berge et al. have reported detailed studies of liquid-solid phase transitions in monolayers of medium chain (8-14 carbons) 1-alcohols. Studies using ellipsometry and simultaneous surface tensiometry[74] indicated some degree of pre-transitional modification of the structure of the liquid phase, and x-ray diffraction[75] showed a hexagonal structure in the solid phase comparable to that of the bulk frozen alcohol. The hexagonal structure was later confirmed, and a large in-plane coherence length (>2500Å) was deduced.[76] X-ray reflectivity has been developed as an independent measure of the thickness of the monolayers. The thickness of the solid phase was found to increase from 13.3 Å for decanol monolayers to 18.0 Å for hexadecanol monolayers.[77] Large changes in the observed thickness below the transition were attributed to a large heat capacity. A more recent study on racemic mixtures of 2-alcohols showed similar behaviour.[78] PM-IRRAS studies on these systems indicated that a high level of gauche defects appeared upon melting of the monolayer, and that in the frozen

monolayers chains were in an all-*trans* confirmation with an almost perpendicular orientation to the interface (to within a few degrees). Again, 2-alcohols showed the same behaviour.[79]

Monolayers of dodecanol have also been seen to undergo liquid-solid phase transitions below 14.5 °C for concentrations greater than 0.20 mM.[65, 80] At 25 °C the solubility of decanol in water is 0.23 mM.[81] Transitions were also observed during adsorption in dodecanol monolayers close to saturation.[82] It is possible that this transition only occurs in the presence of excess surfactant, although this could be a purely kinetic effect.

Liquid-solid phase transitions have also been observed in a number of mixed monolayer systems. Pure solutions of sodium 3,6,9,12-tetraoxa-octacosanoate (TOOCNa) and sodium 3,6,9,12-tetraoxa-triacontanoate (TOTCNa) do not undergo liquid-solid transitions. When either is present in a mixed monolayer with 2-hydroxyethyl laurate (2-HEL), however, the transition does occur.[83] It was suggested that the shorter headgroup of 2-HEL lowered the overall headgroup repulsion, allowing the chains in the monolayer to reach greater densities. Similarly, a liquid-solid transition was observed in mixed monolayers of TOOCNa and $C_{12}E_1$.[84]

Initial reports of liquid-solid transitions in monolayers of pure SDS[85] were shown to be due to the presence of a more surface active impurity, dodecanol.[86] Casson et al. showed that the transition temperature increased with the concentration of dodecanol, and that only 0.1% dodecanol was needed to induce the phase transition. The explanation for this was increased total adsorption in the mixed monolayer system due to the reduction of average headgroup repulsion by the dodecanol, leading to a higher surface excess than for pure SDS.

1.5 Surface Freezing

In the case of freezing of a liquid, it is generally the less ordered surface which coexists with the more ordered bulk (figure 1.11). That is, the surface melts at a lower temperature than the bulk. This phenomenon of surface-melting has been

observed in most cases studied.[87, 88] The behaviour is easily understood due to the reduced confinement and hence higher entropy of a molecule at the surface relative to the bulk.[89] The opposite behaviour, surface freezing, is much less common although several instances have been reported in the literature, with the most important class of molecules displaying this behaviour being the *n*-alkanes.

Surface-freezing of alkanes and alkane mixtures has been widely studied.[90] Linear alkanes between 16 and 50 carbons in length have surface transition temperatures up to 3 °C above the bulk melting point. X-ray diffraction and reflection measurements have shown the existence of three condensed phases dependent upon the chain length of the alkane.[91] A rotator phase of upright chains is observed for chains between 16 and 29 carbons in length, 30-43 carbon-long chains have a tilted rotator phase with the tilt angle increasing from C_{30} to C_{43}. The rotator phase has long-range translational and tilt-orientational order, but the molecules are free to rotate about their principal (long) axes. Chains longer than 43 carbons show a crystalline phase with no rotation. The thickness of the solid layer remains constant until the bulk freezing point is reached, indicating that the surface-frozen layer only partially wets the bulk phase. Ellipsometry[92] and sum frequency spectroscopy[93] have also been used to study the transitions.

In the case of binary mixtures of alkanes phase behaviour depends upon the relative proportions of the two components and the difference between their chain lengths.[94] For large chain length differences segregation of the two components has been observed leading to discontinuous changes in structure as the composition is varied. This is due to competition between the surface enthalpy and the entropy of mixing. The latter favours a mixed monolayer, but the effect of the former is dependent upon chain length differences. For large differences the enthalpy becomes dominant and segregation occurs in the solid phase. For small chain length differences the enthalpy is no longer dominant and a smooth variation in structure of the frozen surface with composition occurs.

Surface-freezing of alkanes has also been observed at solid interfaces. At the SiO_2 interface, transitions have been observed by X-ray reflectivity for a range of n-alkanes.[33] Here the solid-liquid transition of the monolayer seems to

coincide with a wetting transition of the bulk. Above the surface transition temperature the alkane completely wets the SiO_2 surface, whilst below the transition a surface-frozen monolayer is in equilibrium with a liquid alkane lens. X-ray reflectivity studies are suggestive of a perpendicular arrangement of alkane chains relative to the surface in the frozen layer,[95] and ellipsometric data implies the presence of a thin layer of molecules aligned parallel to the surface underneath this.[34] An incomplete film of triacontane has also been shown to freeze to islands of a rotator phase at the air-SiO_2 interface, with the freezing temperature of the film coincident with a wetting transition temperature of the bulk alkane.[96]

Transitions also occur at the graphite interface, where short *n*-alkanes (chain lengths of less than 15 carbon atoms) were seen to form solid monolayers at temperatures above the bulk melting point.[97, 98] These alkanes do not undergo surface freezing at the air/alkane interface. Multilayer formation through a process of layer-by-layer freezing was shown through a combination of DSC and neutron scattering at the graphite-alcohol interface.[99] Freezing transitions have also been observed at the Au(111)/alkane interface.[100] The transition temperatures were found to be surprisingly insensitive to alkane chain length. Longer chain alkanes were found to undergo a surface-induced reorganisation to a mesophase templated by the Au(110) plane.

Surface frozen monolayers have been used to template the formation of metastable rotator phases that are not observed, or are only transiently stable, in the bulk alkane.[101, 102] Surface freezing transitions of microencapsulated alkane were detected using DSC, followed by unusual bulk freezing behaviour. X-ray diffraction and FTIR spectra in the CH_2 rocking region showed that surface frozen octadecane could template a transition to a crystalline triclinic phase via a metastable R_I phase that is not observed in the bulk alkane. Likewise, a novel R_{II} phase was found to be templated by surface frozen nonadecane.

Alkyl side-chain polymer melts exhibit interesting surface freezing behaviour.[103, 104] The alkyl side-chains surface freeze at much higher temperatures than in bulk alkane, and a number of interesting additional effects have been seen. Mixtures of polymers with different side-chain lengths show mixing at temperatures above

the surface freezing point of the longer chain component, whilst at lower temperatures the surface is completely dominated by the longer side-chain polymer.[105] This is in complete contrast to the situation with bulk alkane mixtures, where both species are present at the interface in the liquid and solid phases, and in fact the surface is slightly richer in the more "surface active" (shorter) alkane. Also in contrast to bulk alkanes, the surface freezing range of alkyl side-chain polymers decreases with increasing alkyl side-chain length. This has been attributed to the formation of an intrinsically less ordered surface frozen layer, with up to nine methylene units closest to the polymer backbone remaining disordered in the solid phase; a situation unheard of in the untethered chains.[106]

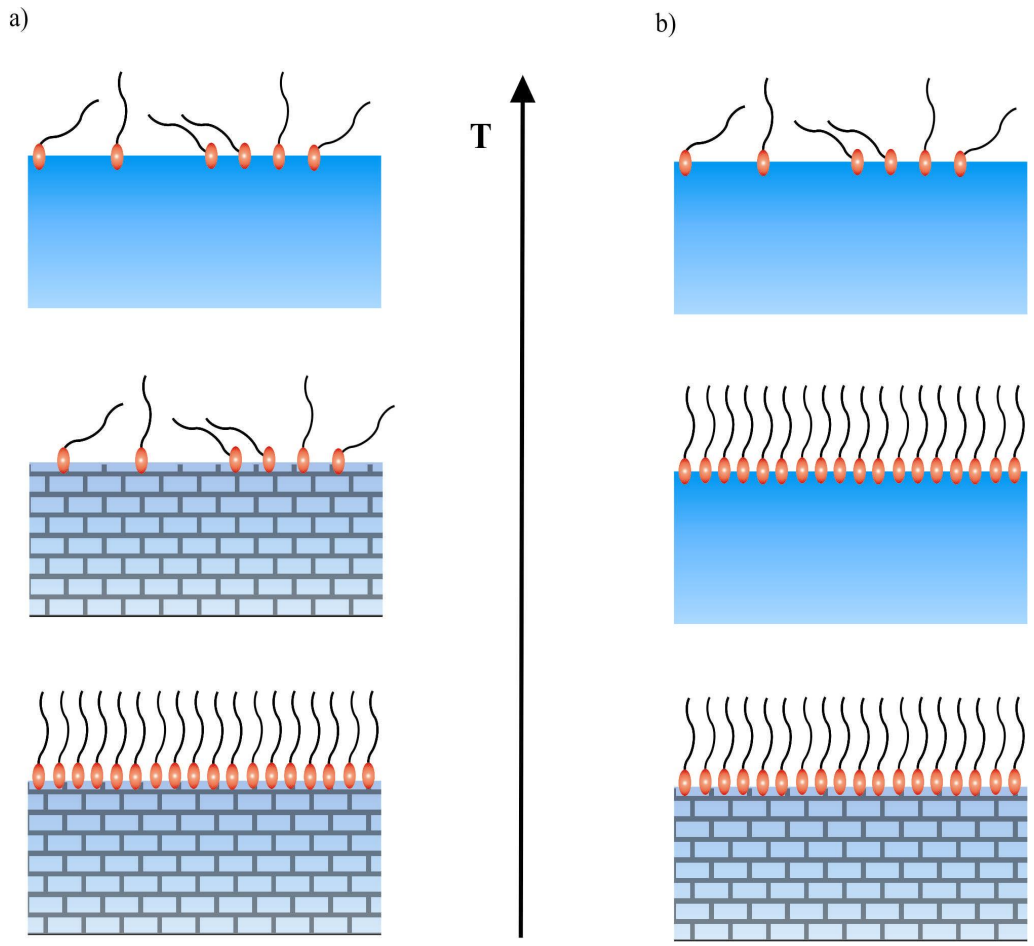

Figure 1.11 Schematic illustration of a) surface-melting and b) surface-freezing. The brick pattern denotes a crystalline bulk phase. Un-patterned substrate denotes liquid bulk.

Grazing-incidence X-ray reflectivity and diffraction studies have also shown surface-freezing effects in gallium-rich eutectics of Tl in Ga and Pb in Ga.[107, 108] Surface-freezing has been observed in some alkenes, notably α-eicosene.[109] The

surface frozen layer in this case was found to be stable over a large temperature range. This was rationalised in terms of the entropy gain associated with inversion of the molecules, since the presence of a double bond breaks the symmetry of the chain molecule about its centre of mass. 1-alcohols have also been shown to undergo surface-freezing.[110] Bilayer formation was observed due to the existence of hydrogen bonding between the headgroups. In the presence of a saturated water atmosphere the bilayers were observed to swell by 3%, independent of chain length of alcohol, perpendicular to the surface.[111] This was interpreted as the intercalation of water into the centre of the bilayer. Intercalation of diols was also observed.[112]

Surface freezing is not generally observed at the liquid/liquid interface.[113] A surface freezing transition can be induced by the addition of surfactant to the water phase of an alkane-water system, as has been demonstrated at the water/tetradecane interface.[114] The cationic surfactant C_{16}TAB was added to the aqueous phase, and ellipsometric measurements were taken as a function of temperature. A step change in the coefficient of ellipticity was observed at a temperature above the bulk melting point of tetradecane. This was indicative of a first-order solid-liquid transition. The transition temperature observed was found to vary linearly with surface excess of surfactant, and by extrapolation it was deduced that the mole fraction of surfactant required to induce surface freezing was less than 0.1.

Surface freezing has also been observed at the air/water interface in mixed monolayers of C_{16}TAB and alkane.[115] These transitions can be thought of in two ways. Either the presence of surfactant induces surface-freezing in the spread alkane monolayer, or the penetration of alkane chains into the adsorbed surfactant monolayer raises the surface excess of chains so that the density at the surface is sufficient for a liquid-solid phase transition to occur.

A recent systematic study of solid-liquid transitions in mixed monolayers at the air/water interface has been carried out using sum frequency spectroscopy (VSFS) and ellipsometry.[116] Phase transitions were observed for a range of *n*-alkanes, undecane-heptadecane, by placing a lens of liquid alkane on the surface of a C_{16}TAB solution. The temperature was then varied in discrete steps and the

coefficient of ellipticity recorded. Transition temperatures were obtained from a discontinuity in the coefficient of ellipticity at the transition temperature (see figure 1.12). VSFS results showed that both the surfactant and alkane chains became ordered during the transition. The transition temperatures were found to increase with alkane chain length, as would be expected from a consideration of van der Waals forces within the monolayer. ΔT was found to decrease with alkane chain length, although when the bulk freezing point was taken as the mean of the alkane and surfactant tailgroup freezing points, the variation in ΔT was much less pronounced, as illustrated in figure 1.13.

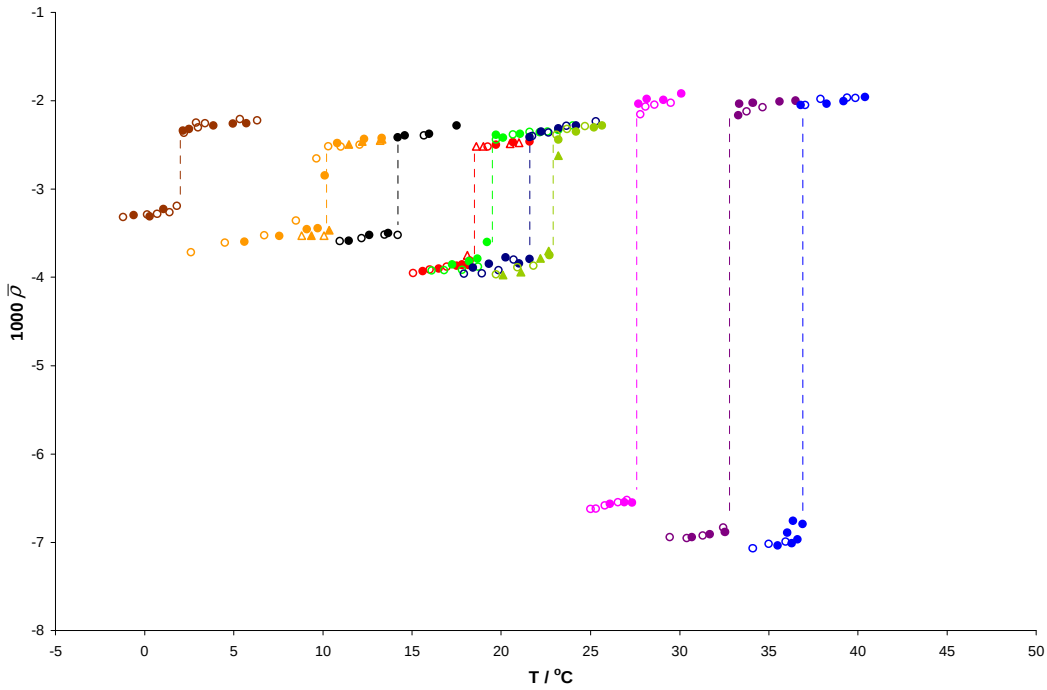

Figure 1.12 Coefficient of ellipticity as a function of temperature at the air-C_{16}TAB solution interface with floating alkane lens for alkane chain lengths between 11(left) and 20 (right). Taken from Wilkinson et al..[116]

Sloutskin *et al.* carried out surface tension and x-ray reflectivity measurements on mixed monolayers of C_{16}TAB and the series of *n*-alkanes, undecane-heptadecane.[117] A monolayer thickness of 8 Å was found for the disordered air/C_{16}TAB solution interface, which thickened slightly upon addition of alkane in the liquid phase. Fits to reflectivity curves in the solid phase gave a thickness of 20.4 Å for a solid C_{16}TAB/hexadecane mixed monolayer, in excellent agreement with modelled thicknesses obtained from ellipsometry measurements previously,[116] and very close to the expected length of a fully extended C_{16} alkyl chain. Grazing incidence diffraction measurements revealed untilted hexagonal

packing in the solid monolayer with a $4.785x4.785\sqrt{3}$ Å^2 unit cell and a molecular area of 19.83 Å^2 (with two molecules per unit cell), in good agreement with structures previously observed for surface frozen *n*-alkane melts. Entropy changes calculated from surface tension measurements were very similar to those found for surface freezing of alkane melts, suggesting that the thermodynamics are the same in both cases. Whilst the thickness of the liquid-phase monolayers remained roughly constant, the thickness of the surface frozen monolayers increased with *n*-alkane chain length.

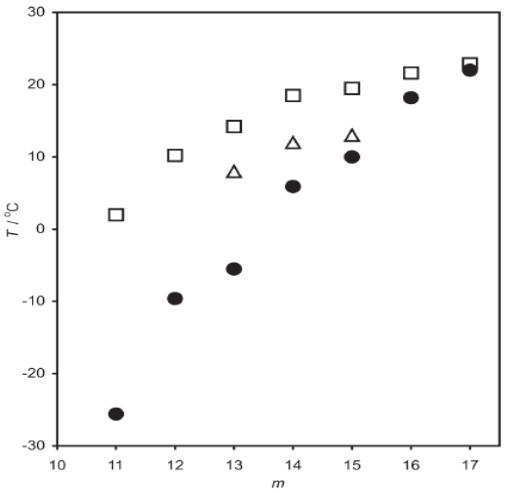

Figure 1.13 Comparison of the surface phase transition temperatures of mixed C_{16}TAB + Cm monolayers at the air–solution interface, T_s (open squares) with the melting points of the bulk alkanes, T_b (filled circles) and the surface freezing temperatures at the interface between C_{16}TAB solutions and bulk alkanes (open triangles).[116]

Figure 1.12 also shows the variation in coefficient of ellipticity with temperature for mixed monolayers of surfactant with octadecane, nonadecane and eicosane. These systems show a different type of behaviour, characterised by a much larger change in the ellipticity at the transition temperature. These two distinct kinds of transition have been termed type I (short alkanes, indicated by a small change in ellipticity) and type II (long alkanes, indicated by a large change in ellipticity). Type II behaviour (octadecane, nonadecane and eicosane) gave a modelled thickness of the solid phase similar to the extended length of the surfactant tailgroup plus the alkane chain, suggestive of an unprecedented bilayer structure; again the thickness modelled from x-ray reflectivity curves agreed with the ellipsometry data, yielding a surface frozen layer thickness of 39.4 Å.[118] In this instance, however, the upper and lower leaflets of the bilayer

have fundamentally different structures. The upper layer corresponds to a fully extended, upright layer containing only *n*-alkane and the lower layer remains a disordered liquid-like mixed monolayer. The unit cell and molecular area for the solid alkane layer show an identical structure to type I frozen monolayers.

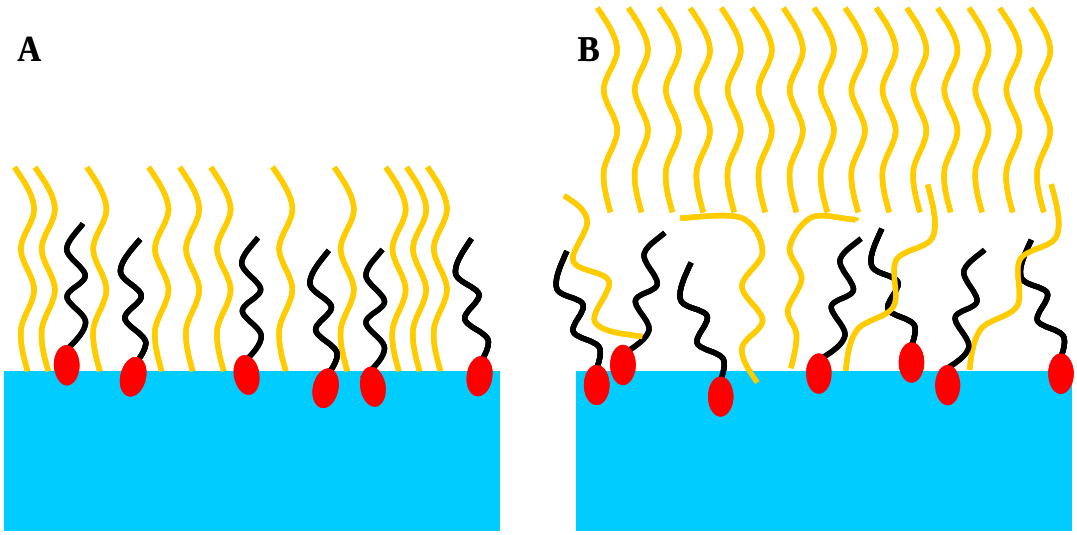

Figure 1.14 Schematic diagram of the possible formation of a bilayer in type II systems. A) Formation of type I frozen layers is unfavourable due to the excess length of the alkane chains. B) The surface of the liquid phase mixed monolayer mimics the air/alkane interface due to the high number of gauche defects, and so wetting can occur.

The transition temperatures of the type II systems lie very close to the bulk melting points of the alkanes. In addition, the air/alkane interface undergoes surface freezing at a higher temperature than the air/solution interface. It is possible, therefore, that this surface frozen layer could wet the mixed monolayer at the air/solution interface, in effect treating the monolayer as if it were bulk alkane. The liquid-like nature of the mixed monolayer leads to a high proportion of *gauche* defects at the air/chain interface, and so the air/solution interface will indeed closely resemble the air/alkane interface. Therefore, a surface frozen layer at the surface of the alkane lens could interact in a similar fashion with the air/solution interface as with bulk alkane, and so wetting may become favourable. Type I freezing is disfavoured by the greater length of the alkane chain over the surfactant tail, which would lead to protrusion of the alkane above the surface of a type I frozen monolayer (figure 1.14), leading to unfavourable van der Waals interactions.

Type II behaviour has also been observed in mixed monolayers of C_{12}TAB and hexadecane. Matsubara *et al*. (although a special mention for the patience of E. Ohtomi is well deserved) located the triple point of the C_{12}TAB/hexadecane system by recording the coefficient of ellipticity as a function of temperature for numerous bulk surfactant concentrations.[119] The triple point occurred at a temperature of 17.3 °C, and a surfactant molality of 0.75 mmol kg^{-1}. The liquid-solid phase boundary was found to be extremely flat with respect to bulk surfactant concentration, lending support to the view of type II transitions as wetting transitions in which the lower monolayer plays no part. The surface excess of C_{12}TAB was found to decrease during the transition, however, although this decrease was not significant (approximately 3 % of a saturated monolayer). A gas-solid phase boundary was also identified, the slope of which changes when the hexadecane lens freezes, becoming almost vertical. It is likely that this does not represent the true thermodynamics of the system, as transfer kinetics between a frozen lens and a frozen film will most likely be extremely slow. Furthermore, in the case where both lens and layer are frozen, the entropy change of the gas-solid transition should be positive, and as a result the gas-solid phase boundary would be expected to be negative by application of the Clapeyron equation. Nevertheless, the phase diagram of the C_{12}TAB/hexadecane/water system gives a solid thermodynamic backing to the wetting mechanism of type II transitions.

As was the case with Langmuir monolayers, the phases of these mixed monolayers have inevitably been compared to the phases present in bulk alkanes. The comparison is perhaps slightly more justified in the case of Gibbs monolayers, since the molecules in the monolayer are free to exchange with molecules in the bulk solution (as is the case at the surface of an alkane), whereas no exchange is possible in the case of Langmuir monolayers.

Theoretical models have been proposed to explain why some chain molecules exhibit surface freezing. An expression for the difference in transition temperature of the surface and the bulk ($\Delta T = T_s - T_b$) for alkanes has been derived by Ocko et al.[91] The surface tension per molecule is equal to the excess

free energy of a molecule at the surface relative to the bulk. So, at the surface transition temperature

$$\gamma(T_s) = (H_s^l - T_s S_s^l) - (H_b^l - T_s S_b^l) \tag{1.32}$$

where *l* denotes liquid phase and *s* and *b* refer to surface and bulk, respectively.

At the transition temperature, the free energy of the liquid surface is equal to the free energy of the frozen surface *(f)*, and so this can be rewritten

$$\gamma(T_s) = (H_s^f - T_s S_s^f) - (H_b^l - T_s S_b^l) \tag{1.33}$$

A similar expression can be derived for $\gamma(T_b)$, and combining this with equation 1.32 gives

$$\Delta T = \frac{\gamma(T_s) - \gamma(T_b)}{\Delta S_s} \tag{1.34}$$

where ΔS_s is the entropy change of the surface on melting.

A form for $\Delta T(n)$, where *n* is the number of carbons in the alkyl chain, was deduced from experimental data for a range of alkanes. It was found that for $n<16$ the energy penalty for surface-freezing was too great, in agreement with experimental evidence. A high *n* limit was also found, occurring due to increasing ΔS_s (and hence decreasing ΔT) as *n* increases.

The lower density of CH_3 end groups is argued to give them a higher surface activity, leading to a preferred vertical alignment which ultimately favours the formation of a more ordered surface layer. An entropic stabilisation due to the length of the molecules has also been suggested.[120] It was proposed that the surface possessed an additional source of entropy relative to the bulk due to fluctuations normal to the plane of the surface. These fluctuations would be damped in the bulk by the presence of neighbouring layers of molecules. Lindemann's criterion for crystal melting[121] states that any such fluctuations must have an amplitude less than 10% of the lattice spacing for the surface to remain frozen. Provided this criterion is met, fluctuations could serve to give entropic stabilisation to the frozen layer. The high and low chain length cut-offs

for surface freezing were explained by considering two different kinds of mismatch effects within the frozen layer, both occurring as a result of the relative shifts of neighbouring chains. End of chain mismatch is dependent only upon the magnitude of these shifts, whereas internal mismatch is an additive function of the number of mismatched CH_2 units. Hence, above a certain chain length the energy penalty due to internal mismatch of chains becomes dominant and surface-freezing is disfavoured.

This fluctuation based approach has been contested, however, and Sirota *et al.* maintain that surface freezing is to be expected purely on the basis of the interfacial tensions alone.[122, 123] The crux of the argument hangs around the relative values of the various solid/liquid and solid/vapour interfacial tensions within the system, which are both hard to define and hard to measure. As a result, there still exists considerable doubt over what causes surface freezing to be favoured for certain chain molecules.

1.6 Implications of Surface-Freezing

A study by Sloutskin *et al.*[124] on the behaviour of the interfacial tension at the C_{18}TAB solution/hexadecane interface showed the novel effect of vanishing interfacial tension as the temperature was lowered. The opposite effect is common, occurring for example at the critical point of a liquid. A positive slope in the surface tension isopleth is induced by a change in the surface excess entropy, S^{γ}, upon surface-freezing. The surface excess entropy is related to the slope of the isopleth by the Maxwell relation

$$S^{\gamma} = -\left(\frac{d\gamma}{dT}\right)_{A,c} \tag{1.35}$$

The surface excess entropy of surface frozen layers has been shown to be negative, and hence the interfacial tension of these systems tends towards zero as the temperature is lowered, unless the effect is pre-empted by freezing of the bulk. For low surfactant concentrations the interfacial tension at the transition temperature is relatively high, and so the onset of bulk freezing does indeed pre-empt the vanishing of interfacial tension. In the system studied by Sloutskin *et al*. the vanishing surface tension could be observed due to the marked reduction

in interfacial tension caused by large concentrations of C_{18}TAB in the water phase. Vanishing interfacial tension was found for C_{18}TAB concentrations greater than 0.17 mM, and for concentrations greater than 0.2 mM the onset of vanishing interfacial tension appeared to be concentration independent. The CMC of C_{18}TAB at the Krafft temperature was estimated to be ~0.21 mM, and the Krafft temperature is 37 °C. All data taken during this study were taken below the Krafft temperature, and so it was suggested that the C_{18}TAB solutions used were, to some extent, metastable and hence supersaturated. This was possible due to a high kinetic barrier against crystal nucleation preventing precipitation, and hence a solution which mimics behaviour above the Krafft temperature could be prepared.

When the interfacial tension of a system is zero, thermal diffusion leads to the mixing of phases on either side of the interface, resulting in the formation of a single homogeneous phase. In the surface-freezing induced case, however, the interfacial tension only vanishes in the presence of the frozen monolayer. The only way that a single uniform phase can be produced in this instance is through the formation of a microemulsion of oil droplets coated by surfactant molecules. Such a microemulsion will be stable with regard to coalescence since there is no free energy gain to counteract the decrease in entropy concomitant with coalescence.

The phenomenon of vanishing interfacial tension has implications for enhanced oil recovery.[2, 15] If a thermodynamically stable microemulsion can be formed then the amount of oil which can be solubilised will be maximised. The microemulsion can either be thought of as a single phase micellar solution in which the micelles are swollen by solubilised oil, or as a dispersion of oil droplets in water. In either case, the necessity for a low interfacial tension is clear. In the first case, no oil water interface exists (provided that the micelles solubilise the oil much more efficiently than they solubilise water), and in the second case the system has such a large interfacial area that the energy cost of creating the interface would be too great if the interfacial tension were not ultra-low. In addition, the interfacial region needs to be relatively labile in order to surround the oil molecules, and again ultra-low surface tension is a prerequisite.

1.7 Aims and Outline

This thesis focuses on the determination and characterisation of surface freezing transitions in mixed monolayers of surfactant and alkane at the air/solution interface. The aims are threefold:

1. To elucidate fully the dependence of surface freezing temperature on the relative chain lengths of surfactant and alkane in C_nTAB/C_m mixed monolayers. Ellipsometry measurements are presented in chapter 2 for alkanes ranging from dodecane (C_{12}) to eicosane (C_{20}).

2. To assess the generality of the surface freezing phenomenon by experimenting with an expanded range of surfactants and oil systems. Chapter 3 contains ellipsometric studies utilising cationic, anionic, non-ionic, zwitterionic and biological surfactants, in addition to alkane mixtures.

3. To gain explicit, chemically specific information regarding the molecular level differences between type I and type II freezing transitions through the application of ER-FTIR spectroscopy and VSFS. ER-FTIR data are presented in chapter 4 for both type I and type II freezing transitions, taking advantage of a novel analytical technique, 2D-IR correlation analysis. VSFS data on the same systems are presented in chapter 5, alongside spectra of a novel non-ionic surfactant system.

Concepts from all the experimental chapters are brought together and set in the context of existing knowledge to conclude in chapter 6.

1.8 References

1. Porter, M. R., *Handbook of Surfactants*. 2nd ed.; Kluwer: 1994.

2. Rosen, M. J., *Surfactants and Interfacial Phenomena*. 3rd ed.; Wiley-Interscience: 2004.

3. Adams, J. W., In *Surface Phenomena and Additives in Water-Based Coatings and Printing Technology*, Sharma, M. K., Ed. Plenum Press, NY: 1991; p 73.

4. Goff, H. D., *International Dairy Journal* **1997,** 7, 363.

5. Lipp, M.; Lee, K.; Waring, A.; Zasadzinski, J., *Science* **1996,** 273, 1196.

6. Pockels, A., *Nature* **1891,** 43, 437.

7. Rayleigh, L., *Phil. Mag.* **1899,** 48, 321.

8. Langmuir, I., *Journal of the American Chemical Society* **1917,** 39, 1848.

9. Langmuir, I., *Science* **1936,** 84, 379.

10. Tanford, C., *The Hydrophobic Effect: Formation of Micelles and Biological Membranes*. 2nd ed.; Wiley: New York, 1980.

11. Chandler, D., *Nature* **2005,** 437, 640.

12. *C. R. C. Handbook of Chemistry and Physics*. 74th ed.; CRC Press Inc.: Boca Raton, 1993.

13. Hamley, I. W., *Introduction to Soft Matter*. 1st ed.; Wiley: Chichester, 2000.

14. Moroi, Y., *Micelles: Theoretical and Applied Aspects*. Plenum: New York, 1992.

15. Schramm, L. L.; Stasiuk, E. N.; Marangoni, D. G., *Annual Reports of Progress in Chemistry, Section C* **2003,** 99, 3.

16. Kirby, A. J.; Camilleri, P.; Engberts, J. B. F. N.; Feiters, M. C.; Nolte, R. J. M.; Soderman, O.; Bergsma, M.; Bell, P. C.; Fielden, M. L.; Garcia Rodriguez, C. L.; Guidat, P.; Kremer, A.; McGregor, C.; Perrin, C.; Ronsin, G.; van Eijk, M. C. P., *Angewandte Chemie International Edition* **2003,** 42, 1448.

17. Adamson, A. W., *Physical Chemistry of Surfaces*. 5th ed.; Wiley: New York, 1990.

18. Hecht, E., *Optics*. 2nd ed.; Addison-Wesley Publishing Company: 1987.

19. Pastrana-Rios, B.; Flach, C. R.; Brauner, J. W.; Mautone, A. J.; Mendelsohn, R., *Biochemistry* **1994,** 33, 5121.

20. Taylor, K. M. G.; Morris, R. M., *Thermochimica Acta* **1995,** 248, 289.

21. Gaines, G. L., *Insoluble Monolayers at the Liquid-Gas Interface*. Wiley and Sons: New York, 1966.

22. Strandburg, K. J., *Reviews of Modern Physics* **1988,** 60, 161.

23. Atkins, P. W., *Physical Chemistry*. 6th ed.; OUP: Oxford, 1998.

24. Bertrand, E.; Dobbs, H.; Broseta, D.; Indekeu, J. O.; Bonn, D.; Meunier, J., *Physical Review Letters* **2000,** 85, 1282.

25. Bonn, D.; Pauchard, L.; Shahidzadeh, N.; Meunier, J., *Physica* **1999,** 263, 78.

26. Ragil, K.; Meunier, J.; Broseta, D.; Indekeu, J. O.; Bonn, D., *Physical Review Letters* **1996,** 77, 1532-1535.

27. Israelachvili, J., *Intermolecular and Surface Forces*. 2nd ed.; Academic Press: 1991.

28. Cahn, J. W., *Journal of Chemical Physics* **1977,** 66, 3667.

29. Pfohl, T.; Mohwald, H.; Riegler, H., *Langmuir* **1998,** 14, 5285.

30. Pfohl, T.; Riegler, H., *Physical Review Letters* **1999,** 82, 783.

31. Kellay, H.; Binks, B. P.; Hendrikx, Y.; Lee, L. T.; Meunier, J., *Advances in Colloid and Interface Science* **1994,** 49, 85.

32. Esibov, L.; Sarkisov, D.; Jeng, U. S.; Crow, M. L.; Steyerl, A., *Physica B* **1997,** 241, 1077.

33. Merkl, C.; Pfohl, T.; Riegler, H., *Physical Review Letters* **1997,** 79, 4625.

34. Volkmann, U. G.; Pino, M.; Altamirano, L. A.; Taub, H.; Hansen, F. Y., *Journal of Chemical Physics* **2002,** 116, 2107.

35. Maeda, N.; Kohonen, M. M.; Christenson, H. K., *Physical Review E* **2000,** 61, 7239.

36. Maeda, N.; Yaminsky, V. V., *International Journal of Modern Physics B.* **2001,** 15, 3055.

37. Aveyard, R.; Binks, B. P.; Cooper, P.; Fletcher, D. I., *Progress in Colloid and Polymer Science* **1990,** 81, 36-40.

38. Aveyard, R.; Binks, B. P.; Fletcher, D. I.; MacNab, J. R., *Langmuir* **1995,** 11, 2515-2524.

39. Wilkinson, K. M.; Bain, C. D.; Matsubara, H.; Aratono, M., *ChemPhysChem* **2005,** 6, 547-555.

40. Lu, J. R.; Li, Z. X.; Thomas, R. K.; Binks, B. P.; Crichton, D.; Fletcher, P. D. I.; McNab, J. R., *Journal of Physical Chemistry B* **1998,** 102, 5785-5793.

41. Lu, J. R.; Thomas, R. K.; Aveyard, R.; Binks, B. P.; Cooper, P.; Fletcher, P. D. I.; Sokolowski, A.; Penfold, J., *Journal of Physical Chemistry* **1992,** 96, 10971.

42. Lu, J. R.; Thomas, R. K.; Binks, B. P.; Fletcher, P. D. I.; Penfold, J., *Journal of Physical Chemistry* **1995,** 99, 4113.

43. Binks, B. P.; Crichton, D.; Fletcher, P. D. I.; MacNab, J. R.; Li, Z. X.; Thomas, R. K.; Penfold, J., *Colloids and Surfaces A: Physiochemical and Engineering Aspects* **1999,** 146, 299-313.

44. Aratono, M.; Kawagoe, H.; Toyomasu, T.; Ikeda, N.; Takiue, T.; Matsubara, H., *Langmuir* **2001,** 17, 7344-7349.

45. Aratono, M.; Toyomasu, T.; Shinoda, T.; Ikeda, N., *Langmuir* **1997,** 13, 2158-2163.

46. Toyomasu, T.; Takiue, T.; Ikeda, N.; Aratono, M., *Langmuir* **1998,** 14, 7313-7320.

47. Matsubara, H.; Ikeda, N.; Takiue, T.; Aratono, M.; Bain, C. D., *Langmuir* **2003,** 19, 2249-2253.

48. Takata, Y.; Matsubara, H.; Kikuchi, Y.; Ikeda, N.; Matsuda, T.; Takiue, T.; Aratono, M., *Langmuir* **2005,** 21, 8594-8596.

49. Indeku, J. O., *Physica A* **1992,** 183, 439.

50. Ställberg-Stenhagen, S.; Stenhagen, E., *Nature* **1945,** 156, 239.

51. Lundquist, M., *Chemica Scripta* **1971,** 1, 5.

52. Kjaer, K.; Als-Nielsen, J.; Helm, C. A.; Laxhuber, L. A.; Möhwald, H., *Physical Review Letters* **1987,** 58, 2224.

53. Dutta, P.; Peng, J. B.; Lin, B.; Ketterson, J. B.; Prakash, M.; Georgepoulos, P.; Elrich, S., *Physical Review Letters* **1987,** 58, 2228.

54. Petersen, I. R.; Kenn, R. M., *Langmuir* **1994,** 10, 4645.

55. Kaganer, V. M.; Möhwald, H.; Dutta, P., *Reviews of Modern Physics* **1999,** 71, 779.

56. Rivière, S.; Hénon, S.; Meunier, J.; Schwartz, M.; Tsao, W.; Knobler, C. M., *Journal of Chemical Physics* **1994,** 101, 10045.

57. Sirota, E. B., *Langmuir* **1997,** 13, 3849.

58. Aratono, M.; Uryu, S.; Hayami, Y.; Motomura, K.; Matuura, R., *Journal of Colloid and Interface Science* **1984,** 98, 33.

59. Matsuki, H.; Aratono, M.; Kaneshina, S.; Motomura, K., *Journal of Colloid and Interface Science* **1997,** 191, 120.

60. Lin, S.-Y.; Hwang, W.-B.; Lu, T.-L., *Colloids and Surfaces A: Physiochemical and Engineering Aspects* **1996,** 114, 143.

61. Kizling, J.; Stenius, P.; Erikson, J. C.; Ljunggren, S., *Journal of Colloid and Interface Science* **1995,** 171, 162.

62. Noskov., *Colloids and Surfaces A: Physiochemical and Engineering Aspects* **1993,** 71, 99.

63. Pallas, N. R.; Pethica, B. A., *Journal of the Chemical Society, Faraday Transactions 1* **1987,** 83, 585.

64. Hill, T. L., *Introduction to Statistical Thermodynamics*. Dover: New York, 1960.

65. Casson, B. D.; Bain, C. D., *Journal of the American Chemical Society* **1999,** 121, 2615.

66. Colthrop, K. A.; Franses, E. I., *Colloids and Surfaces A: Physiochemical and Engineering Aspects* **1996,** 108, 225.

67. Lee, Y.-C.; Liou, Y.-B.; Miller, R.; Liu, H.-S.; Lin, S.-Y., *Langmuir* **2002,** 18, 2686.

68. Subramanyam, R.; Maldarelli, C., *Journal of Colloid and Interface Science* **2002,** 253, 377.

69. Pollard, M. L.; Pan, R.; Steiner, C.; Maldarelli, C., *Langmuir* **1998,** 14, 7222.

70. Hossain, M. M.; Suzuki, T.; Kato, T., *Langmuir* **2000,** 16, 9109.

71. Hossain, M. M.; Suzuki, T.; Kato, T., *Langmuir* **2000,** 16, 10175.

72. Melzer, V.; Volhardt, D.; Brezesinski, G.; Möhwald, H., *Journal of Physical Chemistry B* **1998,** 102, 591.

73. Uredat, S.; Findenegg, G. H., *Langmuir* **1999,** 15, 1108.

74. Berge, B.; Renault, A., *Europhysics Letters* **1993,** 21, 73.

75. Renault, A.; Legrand, J. F.; Goldmann, M.; Berge, B., *Journal de Physique II France* **1993,** 3, 761.

76. Legrand, J. F.; Renault, A.; Konovalov, O.; Chevigny, E.; Als-Nielsen, J.; Grübel, G.; Berge, B., *Thin Solid Films* **1994,** 248, 95.

77. Rieu, J. P.; Legrand, J. F.; Renault, A.; Berge, B.; Ocko, B. M.; Wu, X. Z.; Deutsch, M., *Journal de Physique II France* **1995,** 5, 607.

78. Renault, A.; Alonso, C.; Artzner, F.; Berge, B.; Goldmann, M.; Zakiri, C., *European Physical Journal B* **1998,** 1, 189.

79. Alonso, C.; Blaudez, D.; Desbat, B.; Artzner, F.; Berge, B.; Renault, A., *Chemical Physics Letters* **1998,** 284, 446.

80. Casson, B. D.; Braun, R.; Bain, C. D., *Faraday Discussions* **1996,** 104, 209.

81. Reulle, P.; Kesserling, U. W., *Journal of Pharmaceutical Sciences* **1997,** 86, 179.

82. Volhardt, D.; Emrich, G.; Fainerman, V. B., *Journal of Physical Chemistry B* **2000,** 104, 5744.

83. Hossain, M. M.; Islam, M. N.; Okano, T.; Kato, T., *Colloids and Surfaces A: Physiochemical and Engineering Aspects* **2002,** 205, 249.

84. Islam, M. N.; Okano, T.; Kato, T., *Langmuir* **2002,** 18, 10068.

85. Berge, B.; Faucheux, L.; Schwab, K.; Libchaber, A., *Nature* **1991,** 350, 322.

86. Casson, B. D.; Bain, C. D., *Journal of Physical Chemistry B* **1998,** 102, 7434.

87. Frenken, J. W. M.; van der Veen, J. F., *Physical Review Letters* **1985,** 54, 134.

88. Chandavarkar, S.; Geertman, R. M.; de Jeu, W. H., *Physical Review Letters* **1992,** 69, 2384.

89. Penfold, J., *Reports on Progress in Physics* **2001,** 64, 777.

90. Lang, P., *Journal of Physics - Condensed Matter* **2004,** 16, R699.

91. Ocko, B. M.; Wu, X. Z.; Sirota, E. B.; Sinha, S. K.; Gang, O.; Deutsch, M., *Physical Review E* **1997,** 55, 3164.

92. Pfohl, T.; Beaglehole, D.; Riegler, H., *Chemical Physics Letters* **1996,** 260, 82.

93. Sefler, G. A.; Du, Q.; Miranda, P. B.; Shen, Y. R., *Chemical Physics Letters* **1995,** 235, 347.

94. Sloutskin, E.; Wu, X. Z.; Peterson, T. B.; Gang, O.; Ocko, B. M.; Sirota, E. B.; Deutsch, M., *Phyical Review E* **2003,** 68, 031065/1.

95. Mo, H.; Taub, H.; Volkmann, U. G.; Pino, M.; Ehrlich, S. N.; Hansen, F. Y.; Lu, E.; Miceli, P., *Chemical Physics Letters* **2003,** 377, 99.

96. Schollmeyer, H.; Ocko, B. M.; Riegler, H., *Langmuir* **2002,** 18, 4351-4355.

97. Arnold, T.; Thomas, R. K.; Castro, M. A.; Clarke, S. M.; Messe, L.; Inaba, A., *Physical Chemistry Chemical Physics* **2002,** 4, 345.

98. Arnold, T.; Dong, C. C.; Thomas, R. K.; Castro, M. A.; Perdigan, A.; Clarke, S. M.; Inaba, A., *Physical Chemistry Chemical Physics* **2002,** 4, 3430.

99. Messe, L.; Perdigan, A.; Clarke, S. M.; Castro, M. A.; Inaba, A., *Journal of Colloid and Interface Science* **2003,** 266, 19-27.

100. Cousty, J.; Marchenko, A., *Surface Science* **2002,** 520, 128-136.

101. Xie, B.; Shi, H.; Jiang, S.; Zhao, Y.; Han, C. C.; Xu, D.; Wang, D., *Journal of Physical Chemistry B* **2006,** 110, 14279-14282.

102. Xie, B.; Liu, G.; Jiang, S.; Zhao, Y.; Wang, D., *Journal of Physical Chemistry B* **2008,** 112, 13310-13315.

103. Gautam, K. S.; Dhinojwala, A., *Physical Review Letters* **2002,** 88, 145501/1-4.

104. Prasad, S.; Hanne, L.; Dhinojwala, A., *Macromolecules* **2005,** 38, 2541-2543.

105. Prasad, S.; Hanne, L.; Dhinojwala, A., *Macromolecules* **2006,** 39, 7467-7470.

106. Prasad, S.; Jiang, Z.; Sinha, S. K.; Dhinojwala, A., *Physical Review Letters* **2008,** 101, 065505.

107. Yang, B.; Li, D.; Huang, Z.; Rice, S. A., *Physical Review B* **2000,** 62, 13111.

108. Yang, B.; Li, D.; Rice, S. A., *Physical Review B* **2003,** 67, 212103.

109. Gang, H.; Gang, O.; Shao, H. H.; Wu, X. Z.; Patel, J.; Hsu, C. S.; Deutsch, M.; Ocko, B. M.; Sirota, E. B., *Journal of Physical Chemistry B* **1998,** 102, 2754.

110. Deutsch, M.; Wu, X. Z.; Sirota, E. B.; Sinha, S. K.; Ocko, B. M.; Magnussen, O. M., *Europhysics Letters* **1995,** 30, 283.

111. Gang, O.; Ocko, B. M.; Wu, X. Z.; Sirota, E. B.; Deutsch, M., *Physical Review Letters* **1998,** 80, 1264.

112. Gang, O.; Ocko, B. M.; Wu, X. Z.; Sirota, E. B.; Deutsch, M., *Physical Review Letters* **1999,** 82, 588.

113. Tikhonov, A. M.; Mitrinovic, D. M.; Li, M.; Huang, Z.; Schlossman, M. L., *Journal of Physical Chemistry B* **2000,** 104, 6336.

114. Lei, Q.; Bain, C. D., *Physical Review Letters* **2004,** 92, 176103.

115. Mckenna, C. E.; Knock, M. M.; Bain, C. D., *Langmuir* **2000,** 16, 5853.

116. Wilkinson, K. M.; Lei, Q.; Bain, C. D., *Soft Matter* **2006,** 2, 66-76.

117. Sloutskin, E.; Sapir, Z.; Tamam, L.; Ocko, B. M.; Bain, C. D.; Deutsch, M., *Thin Solid Films* **2007,** 515, 5664-5668.

118. Sloutskin, E.; Sapir, Z.; Lei, Q.; Wilkinson, K. M.; Tamam, L.; Deutsch, M.; Ocko, B. M., *Physical Review Letters* **2007,** 99, 136102.

119. Matsubara, H.; Ohtomi, E.; Aratono, M.; Bain, C. D., *Journal of Physical Chemistry B* **2008,** 112, 11664.

120. Tkachenko, A.; Rabin, Y., *Physical Review Letters* **1996,** 76, 2527.

121. Lindemann, F. A., *Physik A* **1910,** 76, 609.

122. Sirota, E. B.; Wu, X. Z.; Ocko, B. M.; Deutsch, M., *Physical Review Letters* **1997,** 79, 531.

123. Tkachenko, A.; Rabin, Y., *Physical Review Letters* **1997,** 79, 532.

124. Sloutskin, E.; Bain, C. D.; Ocko, B. M.; Deutsch, M., *Faraday Discussions* **2005,** 129, 1.

125. Small, D. M., *The Physical Chemistry of Lipids: From Alkanes to Phospholipids.* Plenum Press: New York, 1986.

Chapter 2

Ellipsometric Study of Surface Freezing in Mixed Monolayers of C_nTAB and *n*-alkane

2.1 Introduction

Mixed monolayers of cationic surfactant and *n*-alkane at the air-water interface have been shown to undergo two distinct type of surface freezing transition dependent upon the difference in chain length of alkane and surfactant tail.[1-3] Type I frozen monolayers consist of a single layer of frozen mixed chains, whilst type II frozen layers contain a liquid-like mixed monolayer beneath a layer of surface frozen alkane. Type I freezing occurs when the chain length mismatch is small. Figure 2.1 shows the coefficient of ellipticity as a function of temperature for mixed monolayers of C_{16}TAB and a range of *n*-alkanes ($11 \le n \le 20$), and the two distinct behaviours can be clearly seen.

The purpose of this chapter is to explore the relation between transition type and chain length mismatch in order to understand this novel behaviour.

2.2 Ellipsometry

2.2.1 Polarisation and Propagation of Light

A beam of light can be described by an electric vector, $\vec{E}(z,t)$, which describes the electric field at time *t* and position *z* along the beam axis. For the special case where the direction of $\vec{E}$ lies in a single plane at all points along the beam the light is said to be linearly polarized and can be expressed by the equation[4]

$$\vec{E}_x(z,t) = \hat{i}E_0 \cos(\vec{k}z - \omega t) \qquad (2.1)$$

where E_0 represents the amplitude of the wave, $\hat{i}$ is a unit vector in the *x* direction, *k* the magnitude of the wavevector and ω the frequency of the wave, which is travelling in the positive z direction.

If the light has a constant amplitude, E_0, but time-dependent direction, $\vec{E}$, then the electric field vector will rotate in a circular fashion about the direction of propagation and it is said to be circularly polarised. Linear and circular polarisation

are really limiting cases of elliptically polarised light, where both direction and amplitude of the electric field vector change with time.

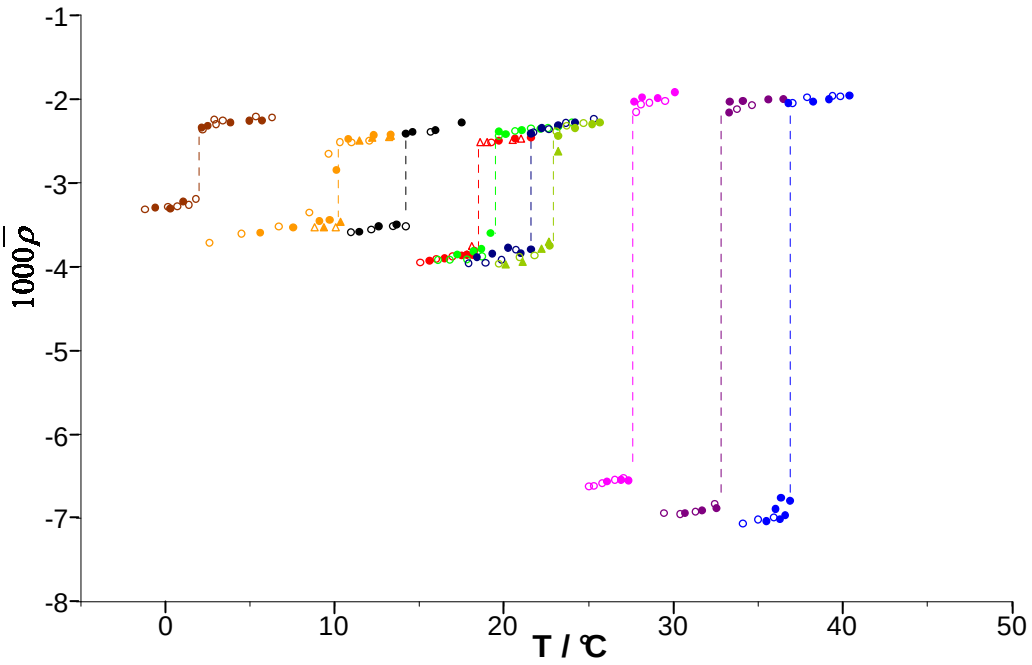

Figure 2.1 Coefficient of ellipticity as a function of temperature for mixed monolayers of 0.6 mM C_{16}TAB and the n-alkanes C_{11} (left) to C_{20} (right).

Light of any arbitrary state of polarisation can be expressed in terms of two orthogonal, linearly polarised waves. The Jones vector representation utilises this fact to express the electric field vector in matrix form

$$\vec{E} = \begin{bmatrix} |E_{0x}|e^{i\delta_x} \\ |E_{0y}|e^{i\delta_y} \end{bmatrix} = \begin{bmatrix} E_x \\ E_y \end{bmatrix} \tag{2.2}$$

where δ_x and δ_y are the phases of the two components.

When electromagnetic radiation encounters matter (i.e. when it is not propagating through vacuum) it is transmitted, reflected and refracted in well defined ways determined by the nature of that matter. In essence all of these macroscopic properties arise due to scattering processes occurring at the atomic level, via the absorption and re-emission of photons by the electron clouds of atoms and molecules within the relevant media. Incident radiation drives the electron clouds into resonance and each atom or molecule illuminated can be thought of as emitting scattered wavelets which propagate in all directions. Since the number of atoms or

molecules illuminated by the radiation is large what we observe is a superposition of all these scattered wavelets with the incident radiation, resulting in a redistribution of energy from regions of destructive interference into regions of constructive interference.

Propagation through a homogeneous medium can be thought of as a sequence of scattering events, each of which causes some shift in the phase of the overall electromagnetic field. This is manifested as a change in the velocity of the beam which is quantified by the refractive index, n, of the medium[4]

$$n = \frac{c}{v} \tag{2.3}$$

where *c* is the speed of light in vacuum and *v* its speed in the medium. An important point to note is that the refractive index is dependent upon the frequency of the incident radiation. This effect is of relevance to the spectroscopic properties of matter, and is discussed further in chapter 4.

At an interface between two media there is a discontinuity in the refractive index and the incident beam splits into two components, a reflected wave and a transmitted wave, whose properties are dependent on both the angle of incidence and the refractive indices of the two media. The laws of reflection (2.4) and refraction (2.5) describe the behaviour of the two beams, where terms are defined in figure 2.2.

$$\theta_i = \theta_r \tag{2.4}$$

$$n_i \sin\theta_i = n_t \sin\theta_t \tag{2.5}$$

The orientation of the electric field of the orthogonal, linearly polarised waves introduced in eqn. 2.2 can now be described as either parallel (*p*-polarised) or perpendicular to the plane of incidence (*s*-polarised). The behaviour of these two component waves can be treated independently, *via* the amplitude reflection and amplitude transmission coefficients (*r* and *t*, respectively). Combining this separability with the boundary condition that components of both the electric and magnetic field vectors tangential to the interface must be continuous, Fresnel

calculated *r* and *t* for both *s*- and *p*-polarised light impinging on an ideal (non-absorbing) flat interface (eqns. 2.6).[5]

$$r_p = \frac{n_t \cos\theta_i - n_i \cos\theta_t}{n_i \cos\theta_t + n_t \cos\theta_i}, t_p = \frac{2n_i \cos\theta_i}{n_i \cos\theta_t + n_t \cos\theta_i}$$

$$r_s = \frac{n_i \cos\theta_i + n_t \cos\theta_t}{n_i \cos\theta_i - n_t \cos\theta_t}, t_s = \frac{2n_i \cos\theta_i}{n_i \cos\theta_i + n_t \cos\theta_t} \quad (2.6)$$

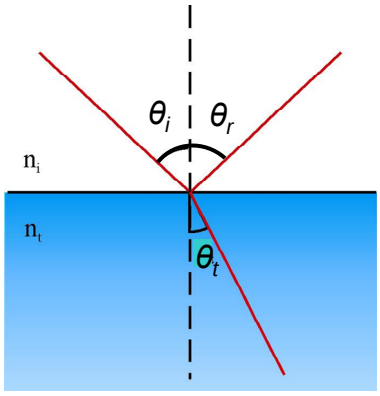

Figure 2.2 Specular reflection of a light beam from a planar interface.

Figure 2.3 shows the schematic variation of r_s and r_p with angle of inceidence. The angle for which $r_p = 0$ is called the Brewster angle, θ_B, and occurs when $\theta_i + \theta_t = 90°$. This effect is also illustrated in figure 2.3, where the angle of incidence is such that the direction of propagation of the reflected wave makes a small angle, α, with the induced dipolar axis in the transmission medium. The amplitude reflectivity, r_p, in this instance will be low, and in the case where $\alpha = 0$ there will be no reflected *p*-polarised wave. Since the transmitted wave always propagates in a direction perpendicular to the dipolar axis this situation will occur when $\theta_i + \theta_t = 90°$.

2.2.2 Ellipsometry

The above example illustrates the extreme case of polarisation by reflection. In general, reflection induces a change in polarisation state of light due to the difference in reflectivity of *s*- and *p*-polarised light. Ellipsometry measures these changes in polarisation through the ratio r_p/r_s, known as the ellipticity, ρ.[6] For reflection from an ideal interface at the Brewster angle this ratio is exactly zero. Real interfaces have an

associated roughness and thickness which cause the dielectric profile perpendicular to the interface to deviate from a step function. The ratio then contains both real and imaginary components (eqn 2.7).

$$\rho = \mathrm{Re}(r_p / r_s) + \mathrm{Im}(r_p / r_s) \tag{2.7}$$

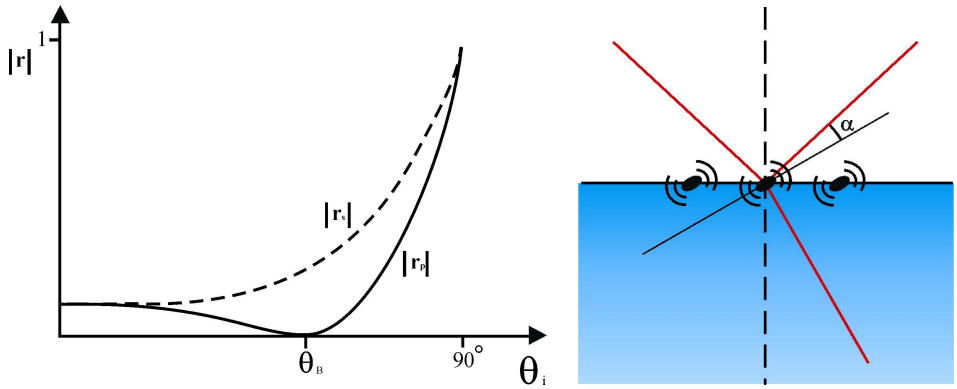

Figure 2.3 Left, variation of amplitude reflectivity coefficients with angle of incidence. Right, schematic illustration of polarisation by reflection, adapted from Hecht.[4]

The Brewster angle is defined as the angle at which the real part of eqn. 2.7 is equal to zero. In the case of an ideal interface the imaginary part is also zero. For imperfect interfaces the real part has a minimum at the Brewster angle and the non-zero imaginary part is known as the coefficient of ellipticity, $\overline{\rho}$, which provides a measure of the imperfection of the interface and hence is closely linked to the physical nature of any layer adsorbed at the interface.

In the thin film limit the coefficient of ellipticity can be expressed in terms of the wavelength of the incident light and the dielectric constants of the incident and transmission media using the Drude equation (eqn. 2.8).[7]

$$\overline{\rho} = \frac{\pi}{\lambda} \frac{\sqrt{\varepsilon_i + \varepsilon_r}}{\varepsilon_i - \varepsilon_r} \eta \tag{2.8}$$

The parameter η is termed the ellipsometric thickness, and can be split into contributions from both the roughness of the interface and the thickness of any adsorbed layer (this component may be further broken down to account for contributions from surfactant headgroups and tailgroups, for example) to allow the experimentally measured coefficient of ellipticity to be modelled.

The effect of interfacial roughness can be analysed by considering capillary waves which modulate the shape of an infinitesimally thin interface. Meunier has discussed the effect of such capillary waves on the coefficient of ellipticity at the Brewster angle, and found that the roughness contribution is dependent upon the inverse square root of the surface tension.[8] In this model, non-zero reflectivity of *p*-polarised light at the Brewster angle results from multiple scattering of the incident light beam which leads to some reflected intensity in the specular direction.

The roughness contribution to the coefficient of ellipticity is typically small, and so the dominant contribution generally comes from the adsorbed layer. In the presence of an adsorbed layer with a single value of dielectric constant normal to the interface, the ellipsometric thickness is given by

$$\eta = \int \frac{(\varepsilon - \varepsilon_i)(\varepsilon - \varepsilon_r)}{\varepsilon} dz \tag{2.9}$$

The ellipsometric thickness of a uniform, isotropic layer of thickness *d* is then given by eqn. 2.10. This provides a good model for a disordered surface layer.

$$\eta = \frac{(\varepsilon - \varepsilon_i)(\varepsilon - \varepsilon_r)}{\varepsilon} d \tag{2.10}$$

In the same way that individual molecules can possess different polarisabilities along different axes, bulk materials can have different dielectric constants in different directions governed by molecular orientation and alignment. For an anisotropic surface layer, therefore, an additional contribution to the ellipsometric thickness is needed. In general the 'isotropic' (calculated normal to the interface as in eqn.2.10) and anisotropic contributions are additive, and so the anisotropic ellipsometric thickness can be either larger or smaller than the isotropic ellipsometric thickness. When surface molecules are aligned with the same orientation the layer is uniaxially anisotropic and the ellipsometric thickness is given by

$$\eta = \eta_i + (\varepsilon_e - \varepsilon_o) d \tag{2.11}$$

where ε_e and ε_o are the dielectric constants perpendicular and parallel to the interface, respectively, and η_i is the ellipsometric thickness calculated from eqn.

2.10. Monolayers containing ordered, vertically aligned chains can be modelled in this way. Ordered monolayers with tilted chains can also be modelled as uniaxially anisotropic, provided that the domain size within the monolayer is much smaller than the measurement area.

2.3 Experimental Methods and Materials

2.3.1 Phase Modulated Ellipsometry

The ellipsometric method used in this chapter is known as phase modulated ellipsometry. It was initially devised by Jasperson and Schnatterly[9] and later applied to liquid surfaces by Beaglehole.[7] A phase modulated ellipsometer consists of a laser, polariser, neutral density filter and birefringence modulator placed in front of the sample, and an analyser and PMT placed after the sample. The optical components are arranged as shown in figure 2.4. The plane of reference for optical alignment is the *s*-direction relative to the sample surface.

The birefringence modulator introduces a periodic phase shift between *s*- and *p*-polarised light using the photoelastic effect. An isotropic fused silica block is mounted between two quartz crystals. The quartz crystals are driven into oscillation electrically *via* the piezoelectric effect, and this oscillation in turn drives longitudinal resonance in the silica block at its natural frequency, ω. This longitudinal resonance leads to a periodic variation in refractive index for light polarised parallel and perpendicular to the longitudinal axis, and hence to a phase shift between the two polarisations of $\delta(\omega) = \delta_0 \sin(\omega t)$. Equal amplitudes of *s*- and *p*-polarised light are ensured by setting the polariser at 45˚. The analyser is oriented either parallel or perpendicular to the polariser and measurements contain information gathered from both positions, allowing the effect of stray birefringence introduced by optical components and the sample cell to be minimised.

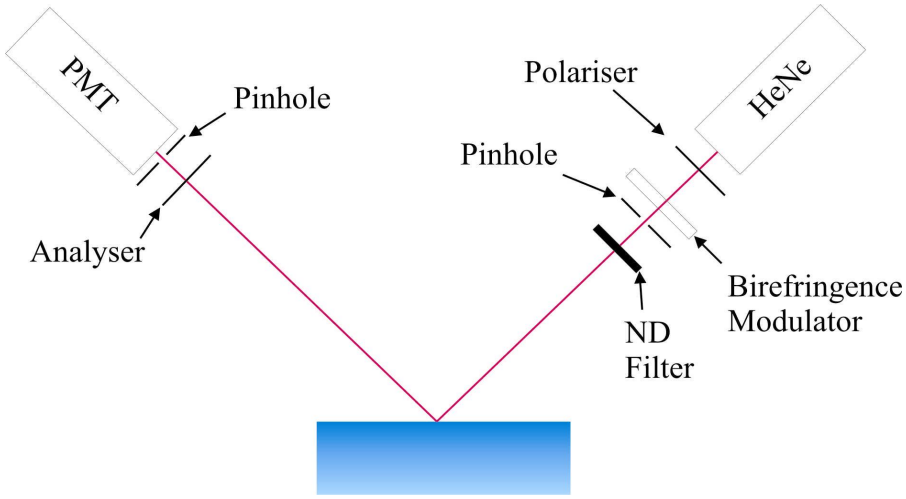

Figure 2.4 Optical layout of the phase modulated ellipsometer.

The intensity of light impinging upon the PMT is given by[10]

$$I = I_0 \rho_s^{\,2} \cos^2 A \cos^2 P (1 + \rho'^2 + 2\rho' \cos(\Delta + \delta)) \tag{2.12}$$

where

$$\rho' = \tan A \tan P \rho_s \tag{2.13}$$

$$\rho_s^{\,2} = \mathrm{Re}(r)^2 + \mathrm{Im}(r)^2 \tag{2.14}$$

The terms P and A in eqn. 2.12 refer to the orientations of the polariser and analyser, respectively, δ is the strain induced birefringence and Δ is the phase shift between *p*- and *s*-polarised light induced by reflection from the interface. Expansion of the $\cos(\Delta + \delta)$ term results in three components to the detected signal; two modulated signal of frequency ω and 2ω, and a non-modulated dc signal. The dc signal allows normalisation of the modulated signals to take into account fluctuations in laser intensity. When $A = P = 45^\circ$, the detected signals are

$$\begin{aligned} Y &= \frac{S_\omega}{S_{dc}} = -g_y \frac{4J_1(\delta_0)\,\mathrm{Im}(r)}{1 + \rho^2 + 2J_0(\delta_0)\,\mathrm{Re}(r)} \\ X &= \frac{S_{2\omega}}{S_{dc}} = -g_x \frac{4J_2(\delta_0)\,\mathrm{Re}(r)}{1 + \rho^2 + 2J_0(\delta_0)\,\mathrm{Re}(r)} \end{aligned} \tag{2.15}$$

where g_y and g_x are gain factors of the system and J_n are nth order Bessel functions. Through calibration of the birefringence modulator, δ_o can be adjusted such that J_0 is

zero and J_1 and J_2 are constant. This removes the effect of Re(r) from the denominator in eqns. 2.15, and allows $J_1(\delta_0)$ and $J_2(\delta_0)$ to be combined with g_y and g_x to give instrumental gain factors G_y and G_x. Making these substitutions, and the fact that $\rho_s^{\,2} = \mathrm{Re}(r)^2 + \mathrm{Im}(r)^2$ leads to the experimentally measured parameters x and y (eqns. 2.16).

$$y = \frac{Y}{G_y} = \mathrm{Im}(r)\frac{2}{1+\mathrm{Re}(r)^2+\mathrm{Im}(r)^2}$$
$$x = \frac{X}{G_x} = \mathrm{Re}(r)\frac{2}{1+\mathrm{Re}(r)^2+\mathrm{Im}(r)^2} \qquad (2.16)$$

Thus, the signal at ω is related to Im(r) and the signal at 2ω is related to Re(r). Moreover, since at the Brewster angle Re(r) is minimal and Im(r) is typically small for aqueous interfaces, the coefficient of ellipticity is given directly as $\overline{\rho} = \mathrm{Im}(r) = y/2$.

The Picometer Ellipsometer

Measurements presented in this thesis were taken using a Picometer Ellipsometer (Beaglehole Instruments, NZ). The light source was a He-Ne laser (632.9 nm), the polariser and analyser positions were computer controlled and set to 45˚ and ±45˚, respectively, and the birefringence modulator oscillated at 50 kHz (ω). The sample was placed in a 7 cm diameter Petri dish within a sealed, temperature controlled cell, thermostated to ±0.1 ˚C (designed by KMW[1]). The sample surface was positioned such that the reflected beam passed through a pinhole mounted on the front of the PMT, minimising the amount of stray light reaching the detector. The signals at ω (50 kHz) and 2ω (100 kHz) are extracted by lock-in amplifiers, and the dc component is detected using a low-pass filter. G_x and G_y were calibrated at the beginning of each experiment by recording the maximum throughput of the instrument with the laser, birefringence modulator, analyser and PMT in a 'straight-through' configuration. A phase difference of π/2 was introduced between *s*- and *p*-polarised light, allowing the maximum signal at 2ω to be measured as the laser is unattenuated.

2.3.2 Experimental Materials

All glassware was soaked in dilute alkaline detergent (Borer 15PF, Borer Chemie) for several hours and rinsed copiously before use. All cleaning and solution preparation used Milli-Q ultrapure water (Millipore).

The Surfactants C_{12}TAB (Alfa, >99%), C_{14}TAB (Sigma, >99%), C_{16}TAB (Sigma, >99%) and C_{18}TAB (Fluka, >99%) were recrystallised three times from a mixture of acetone and ethanol before use.

The *n*-alkanes tetradecane (Sigma, 99%), pentadecane (Sigma, 99%), hexadecane (Acros Organics, 99%), heptadecane (Sigma, 99%), octadecane (Sigma, 99%), nonadecane (Sigma, 99%) and eicosane (Sigma, 99%) were purified by passing through a column of activated basic alumina (Sigma).

2.4 Results

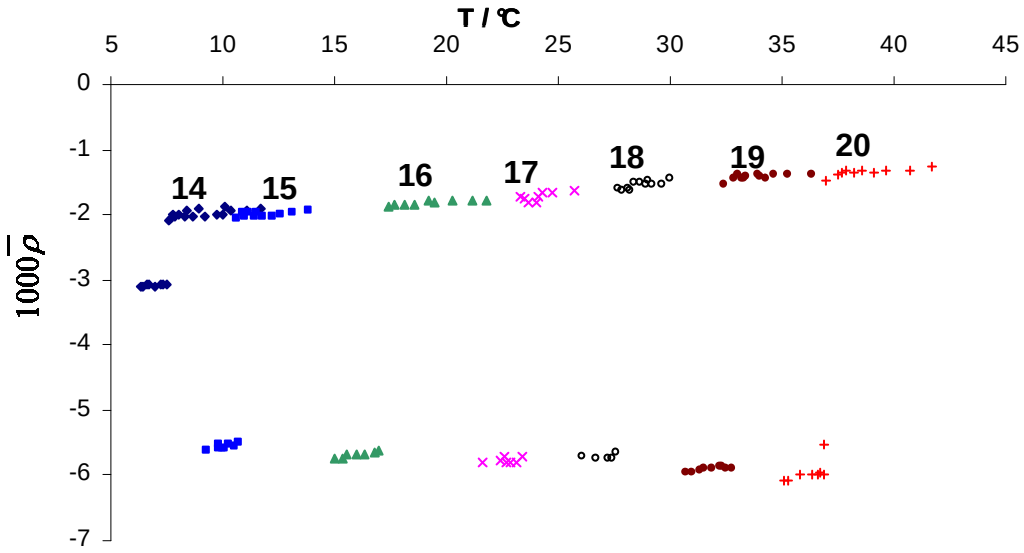

Figure 2.5 Coefficient of Ellipticity as a function of temperature about the surface freezing transitions in mixed monolayers of 1.2 mM C_{14}TAB and C_n, where $14 \le n \le 20$, at the air-water interface. Data shown were taken during both heating and cooling cycles. For examples of heating and cooling cycles, see figure 2.8.

The coefficient of ellipticity as a function of temperature for mixed monolayers of *n*-alkane (C_n, where $12 \le n \le 20$) and C_mTAB ($m = 12$, 14 and 18) are shown in figures 2.5 – 2.7, data for C_{16}TAB in the presence of C_n were shown in figure 2.1. The data shown are representative examples, with each experiment carried out at least three

times. In all cases studied a discontinuity in the plot indicates a first-order phase transition. The data were acquired upon both heating and cooling of the sample, and transition temperatures were found to be free of hysteresis (examples shown in figure 2.8), and typically reproducible to within 0.2 °C. The marked decrease in the coefficient of ellipticity on freezing of the monolayers is a result of the increase in thickness and/or adsorption density that accompanies the surface freezing transitions.

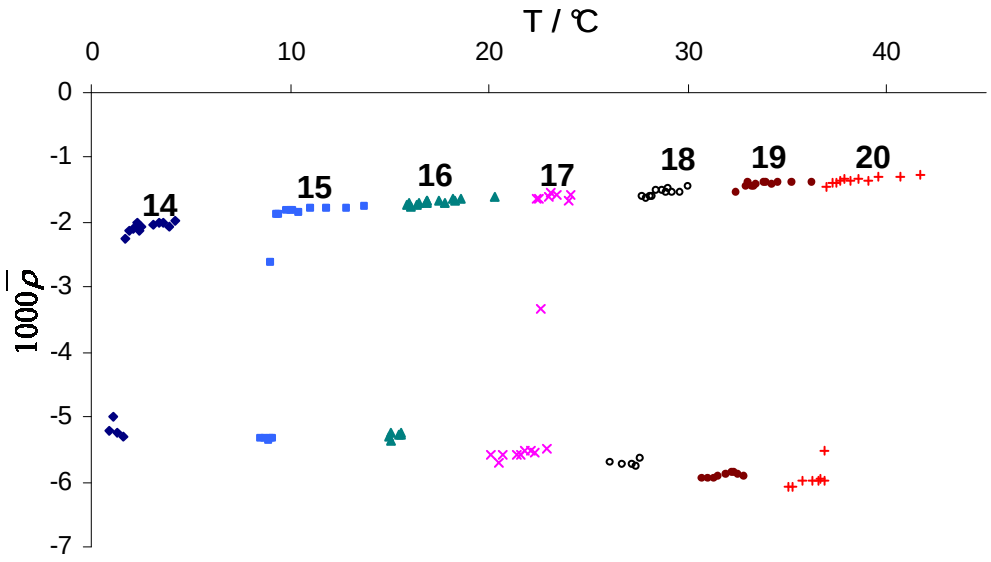

Figure 2.6 Coefficient of Ellipticity as a function of temperature about the surface freezing transitions in mixed monolayers of 11 mM C_{12}TAB and C_n, where $14 \le n \le 20$, at *the air-water interface.*

In order to ensure the ellipsometric data presented in this thesis was compatible with previous studies[1, 3, 11-13] measurements were taken of surface freezing in mixed monolayers of C_{16}TAB and hexadecane. These data are shown in figure 2.9, along with previous data collected by Katherine Wilkinson.[1] The datasets agree to within $10^{-4}\,\bar{\rho}$, well within the repeatability of ellipsometric calibration procedures.

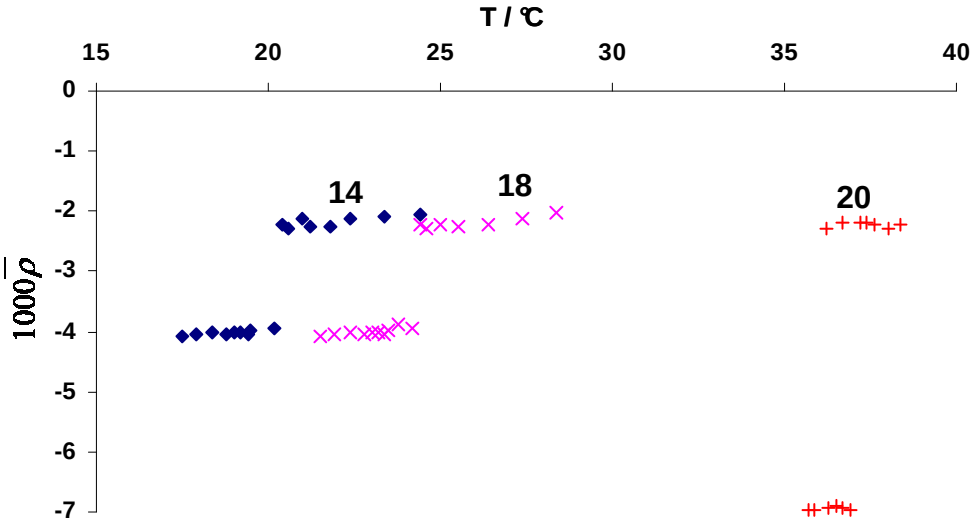

Figure 2.6 Coefficient of Ellipticity as a function of temperature about the surface freezing transitions in mixed monolayers of 0.8 mM C_{18}TAB and C_n, where n = 14, 18, 20, at the air/water interface.

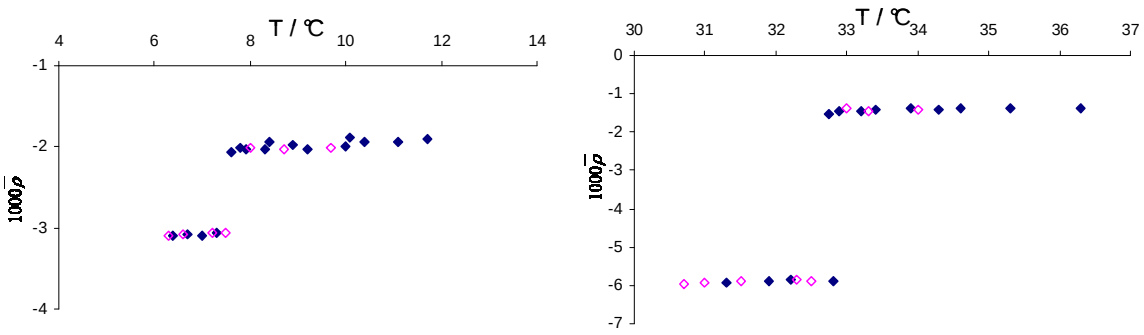

Figure 2.8 Left, surface freezing of C_{14}TAB/C_{14} type I mixed monolayer. Right, surface freezing of C_{12}TAB/C_{19} type II mixed monolayer. Open symbols denote a heating cycle, closed symbols denote a cooling cycle.

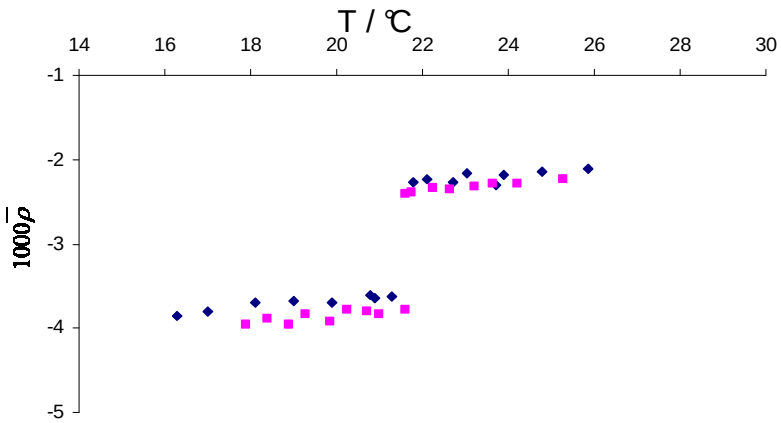

Figure 2.9 Coefficient of Ellipticity as a function of temperature of a mixed monolayer of 0.6 mM C_{16}TAB and hexadecane. Comparison of current (squares) and previous[1] (diamonds) data.

In addition to static measurements of the ellipticity as a function of temperature, data were recorded as a function of time during thermal equilibration of the sample. The behaviour of the coefficient of ellipticity in the transition region is dependent upon both the rate at which the transition takes place and the size of the solid domains formed during growth of the surface frozen phase. For a true first-order phase transition, the only observable coefficients of ellipticity should correspond to either the pure solid or pure liquid phase values. At the phase transition temperature, however, both phases coexist and so the experimentally observed ellipticity may be stable and intermediate between the solid and liquid phase values if the domain size is smaller than the measurement area. In this instance the observed ellipticity is weighted according to the fractional surface coverage of each phase. If the domain size is sufficiently large fluctuations will be observed as thermal motion causes domains to pass through the measurement area. Examples of both behaviours have been observed, as illustrated figure 2.10, where it can be seen that regardless of the precise behaviour of the ellipticity the temperature range in which the transition takes place is always small (typically less than 0.05 °C) as would be expected from a first order phase transition.

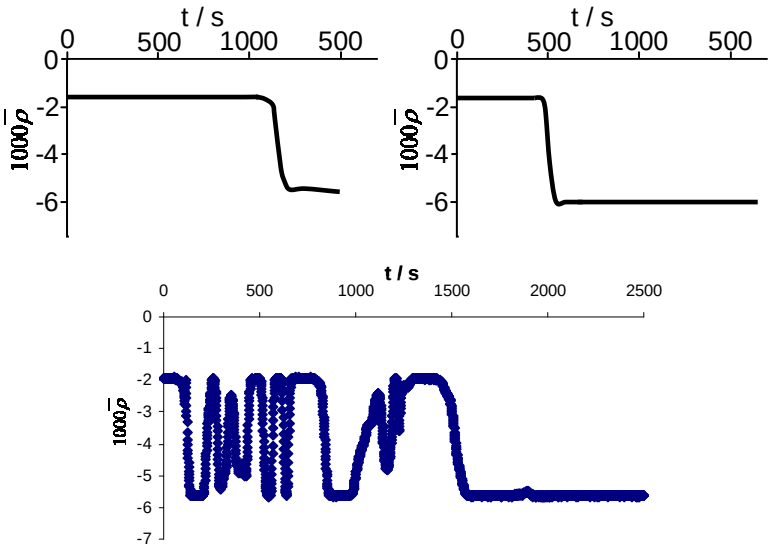

Figure 2.10 Coefficient of Ellipticity as a function of time for C_{12}TAB/C_{18} (upper left), C_{12}TAB/C_{19} (upper right) and C_{14}TAB/C_{16} mixed monolayers as the temperature is lowered through the transition temperature at a rate of 0.02 °C/min..

Comparison of figures 2.5 – 2.7 with the previous data from C_{16}TAB/C_n mixed monolayers shown earlier (figure 2.1) suggests that all surface freezing transitions

for the C_mTAB/C_n system can be categorised as either type I (frozen monolayer) or type II (bilayer structure in the frozen phase). These two distinct behaviours are characterised by a drop in ellipticity of either $1.5 - 2\times10^{-3}$ for a type I transition or more than double this (roughly $2.5 - 4\times10^{-3}$) for a type II transition. The absolute magnitude of the drop is influenced by the difference in thickness between the liquid and solid monolayers, and hence upon the length of the chains involved in both the surfactant tailgroup and *n*-alkane chain. These effects can be considered in detail by modelling the coefficient of ellipticity in both phases, at the transition temperature. Such models have been constructed previously[3, 14] and are briefly described here.

2.4.1 Modelling the Coefficient of Ellipticity

In order to estimate the thickness of the chain region of a monolayer, the coefficient of ellipticity can be separated into contributions from interfacial roughness, surfactant headgroups, counterions and the chain region itself (incorporating both surfactant and alkane chains) as introduced in section 2.2.2. These individual contributions can be modelled using the Drude equation (eqn. 2.8), modified to account for anisotropy in the chain layer in the case of the frozen phase. The chain contribution can then be obtained by subtraction of counterion, headgroup and roughness contributions from experimentally measured values and compared with the model (eqn. 2.17).

$$\overline{\rho}_c = \overline{\rho}_{\text{exp}} - \overline{\rho}_r - \overline{\rho}_h - \overline{\rho}_i \qquad (2.17)$$

Here a subscript *c* represents the chain layer, exp the experimental value, *r* the roughness, *h* the headgroup layer and *i* the counterion layer.

The dielectric constant of water at each transition temperature was estimated from a third-order polynomial fit to literature values in the range 0 – 100 °C,[15] eqn. 2.18.

$$\varepsilon_{H_2O}(T) = 3.715\times10^{-8}(T/^{\circ}C)^3 - 7.803\times10^{-6}(T/^{\circ}C)^2 + 4.996\times10^{-5}(T/^{\circ}C) + 1.776 \qquad (2.18)$$

The roughness contribution can be modelled based on a capillary wave approach as derived by Meunier.[8] For a neat air-liquid interface the roughness contribution is

governed by the proportionality shown in eqn. 2.19. A constant of proportionality can then be estimated using the measured ellipticity of pure water at 25 °C. Roughness contributions were calculated according to eqn. 2.20.

$$\overline{\rho}_r \propto \sqrt{\frac{T}{\gamma}} \tag{2.19}$$

$$\overline{\rho}_r = 0.4\times10^{-3}\sqrt{\frac{T/K}{273}\frac{72}{\gamma/mNm^{-1}}} \tag{2.20}$$

The surface tension values used were based on measurements taken from C_{12}TAB/C_{16} monolayers (43 mNm^{-1}, Aratono *et al.*[16]), C_{14}TAB/C_{12} monolayers (43 mNm^{-1}, Thomas *et al.*[17]) and C_{18}TAB/C_{16} monolayers (43 mNm^{-1}, measured using Wilhelmy plate) all at 25 °C. More accurate values are not necessary as the roughness contribution is typically very small and so has little effect on the final modelled chain layer thickness (an error in surface tension of 20 mNm^{-1} translates to a change of roughly 1 Å in the modelled solid layer thickness, an error of less than 3% for a type II system). In addition, it has been shown that the surface tension is continuous at the phase transition temperature and therefore surface roughness makes no contribution to $\overline{\rho}_{s,\exp} - \overline{\rho}_{l,\exp}$,[11] although this interpretation assumes the bending modulus of the interface does not change at the phase transition. The bending modulus acts to suppress capillary waves at the interface and hence reduce $\overline{\rho}_r$. Unpublished dynamic light scattering experiments (performed by D. Sharpe, Bristol) on dodecanol monolayers at the air/water interface showed independently that the surface roughness does not change upon surface freezing, and so the above assumption is valid.

The headgroup contribution was modelled based on the formation of an isotropic layer in water 8 Å thick, taken from neutron measurements by Thomas *et al.*[18-20] of a C_{16}TAB monolayer at the air/water interface. The dielectric constant of this layer was calculated using the Lorentz-Lorenz effective medium approximation

$$\frac{\varepsilon-1}{\varepsilon+2} = \left(\frac{\varepsilon_1-1}{\varepsilon_1+2}\right)\phi_1 + \left(\frac{\varepsilon_2-1}{\varepsilon_2+2}\right)\phi_2 \tag{2.21}$$

where ε_1 and ε_2 are the dielectric constants of the two media being mixed and ϕ_1 and ϕ_2 are their volume fractions. The volume fractions are easily calculated from the molar volume of the C_{16}TAB headgroup ($62.3\,cm^3mol^{-1}$) calculated by Thomas *et al.* and the surface excess, according to eqn. 2.22. The surface excess of the surfactants were presumed to be the same in the mixed monolayers as in the absence of oil, and are summarised in table 2.1. This assumption has been shown to be reasonable by Thomas *et al*. in the case of SDS, $C_{12}E_5$ and C_{12}TAB in the presence of dodecane.[21-23]

$$\phi_h = 0.623(\Gamma / \mu mol\,m^{-3}) \tag{2.22}$$

The molar volume also allows calculation of a dielectric constant for the headgroup using the relation

$$\frac{\varepsilon - 1}{\varepsilon + 2} = \frac{R_m}{V_m} \tag{2.23}$$

where V_m is the molar volume and R_m the molar refractivity calculated as a sum of the bond refractivities of the constituent C-H and C-N bonds within the headgroup. Table 2.2 shows the refractivities used and calculated within this chapter.

Table 2.1 Surface excess concentrations of surfactants used in this chapter

Surfactant	**Surface excess / µmol m^{-2}**
C_{12}TAB	3.1[16]
C_{14}TAB	2.7[17]
C_{16}TAB	3.4[24]
C_{18}TAB	3.3 (calculated based upon Battal *et al*.)[25]

Modelling of the counterion contribution also utilises the Lorentz-Lorenz effective medium approximation. The surface excess of counterions must be the same as that of the chains in order to preserve charge neutrality, and the layer was assumed to have a thickness equal to the Debye length of the solution (~100 Å, calculated from the surfactant concentration), although the ellipticity of the layer is insensitive to the

absolute thickness chosen. The volume fraction of Br^- can then be calculated from its ionic radius (196 pm,[26] to give a molar volume of 19 cm^3 mol^{-1}) and molar refractivity, leading to an estimated dielectric constant of 6.29 based on eqn. 2.21.

Table 2.2 Summary of molar refractivities used in this chapter.[26]

Bond/Species	**Molar refractivity / cm^3 mol^{-1}**
C-H	1.65
C-N	1.66
Trimethylammonium [$N^+(CH_3)_3$]	19.6
Br^-	12.12

The chain layer is modelled differently in the liquid and solid phases, since the ellipticity is sensitive to anisotropy present in the monolayer. In the liquid phase, the Drude equation can be rearranged directly to give the thickness of the monolayer as

$$d_{c,liq.} = \overline{\rho}_{c,liq.} \Bigg/ \left(\frac{\lambda}{\pi} \frac{\varepsilon_a - \varepsilon_w}{\sqrt{\varepsilon_a + \varepsilon_w}} \right) \left(\frac{(\varepsilon_c - \varepsilon_a)(\varepsilon_c - \varepsilon_w)}{\varepsilon_c} \right) \tag{2.24}$$

where ε_c is the dielectric constant of the chain layer and other terms are as previously defined. An effective medium approximation was used to estimate ε_c, based upon a 1:1 mixture of alkane and surfactant in the monolayer. The surface excess of alkane in the monolayer is actually chain-length dependent,[23, 27] with shorter alkanes adsorbing to a greater extent. The volume fractions, however, remain fairly constant. In addition the dielectric constant of *n*-alkanes, at their melting points, is relatively insensitive to chain length, and so an effective medium approximation based on a constant 1:1 mixture in the monolayer introduces little error into the calculation. The tailgroups were assumed to have the same refractive index as the corresponding *n*-alkane. Values of ε_c calculated in this way fell in the range 2.03 – 2.07 for all mixed monolayers studied.

In the solid phase, a modified Drude equation must be used to account for optical anisotropy and the chain layer must be modelled using two orthogonal dielectric constants, ε_e and ε_o. Casson *et al.*,[14, 28] Wilkinson *et al.*[1, 3] and Sefler *et al.*[29] have shown that surface frozen mixed monolayers, alkanes and alcohol monolayers have similar structures and optical properties. Casson *et al.* calculated values of $\varepsilon_e = 2.23$ and $\varepsilon_o = 2.12$ for surface frozen dodecanol monlayers at a molecular area of 20.9 Å^2. Based on X-ray diffraction data, Riegler *et al.*[30] used multiple-angle ellipsometry to measure values of $\varepsilon_e = 2.37$ and $\varepsilon_o = 2.16$ for a behenic acid monolayer at a molecular area of 19.3 Å^2, assuming a layer thickness of 27.5 Å for a fully extended $C_{21}H_{43}$ chain, and 2.5 Å for the acid headgroup. Deutsche *et al*. have measured the area per chain in surface frozen C_{16}TAB/C_n mixed monolayers to be 19.8 Å^2, insensitive of alkane chain length, and therefore the measurements of Riegler *et al*. were chosen for use in the present modelling as the area per chain provides the closest match (although in principle dielectric constants can be scaled to account for differences in monolayer density, discrepancies in both relative anisotropy and absolute value are accentuated by the interconversion, as demonstrated by Casson[14]). Assuming the area per chain in the solid phase is similarly insensitive to the length of the surfactant tail, modified values for the dielectric constants can be calculated as $\varepsilon_e = 2.32$ and $\varepsilon_o = 2.16$. These values can then be used to calculate the thickness of a solid layer of chains *via*. eqn. 2.25.

$$d_{c,sol.} = \overline{\rho}_{c,sol.} \Bigg/ \left(\frac{\lambda}{\pi} \frac{\varepsilon_a - \varepsilon_w}{\sqrt{\varepsilon_a + \varepsilon_w}} \right) \left(\frac{(\varepsilon_e - \varepsilon_a)(\varepsilon_e - \varepsilon_w)}{\varepsilon_e} + (\varepsilon_e - \varepsilon_o) \right) \tag{2.25}$$

Type II frozen monolayers have been shown to consist of two layers.[3, 31] The upper leaflet is a layer of frozen alkane chains with a thickness equal to the fully extended alkane chain length, and the lower leaflet a liquid-like mixed monolayer. The total thickness of a type II frozen layer can therefore be calculated using a two layer model. The thickness of the upper leaflet is known (from x-ray reflectivity measurements) and so its contribution to the ellipticity of the solid phase can be

estimated by rearranging eqn 2.25 in terms of $\overline{\rho}_{c,sol.}$. Subtraction of this value from the experimental solid phase ellipticity then gives the coefficient of ellipticity of the lower liquid-like layer, the thickness of which can be calculated using eqn. 2.24.

2.4.2 Modelled Layer Thicknesses

The liquid and solid monolayer thicknesses calculated in this way for the range of C_mTAB/C_n mixed monolayer systems studied are summarised in figures 2.11, 2.12 and table 2.3. The surface excess of surfactant is assumed to remain constant during the transition.

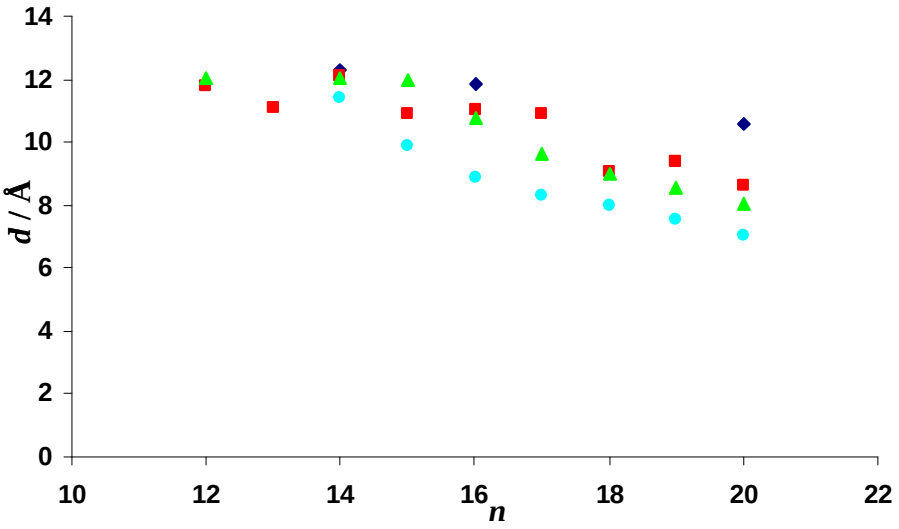

Figure 2.11 Variation in modelled liquid layer thickness with n-alkane chain length in mixed monolayers containing C_{12}TAB (circles), C_{14}TAB (triangles), C_{16}TAB (squares) and C_{18}TAB (diamonds). Note that for n=14, the thicknesses of the C_{12}TAB, C_{14}TAB, C_{16}TAB and C_{18}TAB monolayers are approximately equal and the C_{18}TAB data has been offset within error for clarity.

In the case of the liquid monolayers (figure 2.11), the monolayer thickness decreases with increasing chain length of alkane for a given surfactant. This is to be expected, since it has been shown by Binks *et al.* that alkane uptake into surfactant monolayers is chain length dependent, with the extent of adsorption decreasing as alkane chain length increases.[23, 27] In general, monolayer thickness increases with surfactant tailgroup length for a given alkane showing that in the liquid phase it is the surfactant, as the dominant species at the interface, which determines the monolayer thickness. For C_{14}TAB and C_{16}TAB, the thickness tends toward a plateau for short alkanes. Despite the enhanced adsorption of these shorter alkanes, the excess length

of the surfactant tail places an upper limit on the monolayer thickness as Thomas *et al.* have shown the alkane does not extend beyond the surfactant tails in liquid-like mixed monolayers.[22, 23] C_{12}TAB exhibits no such plateau, since even the shortest alkane studied (tetradecane) contained an alkyl chain longer than the surfactant tail.

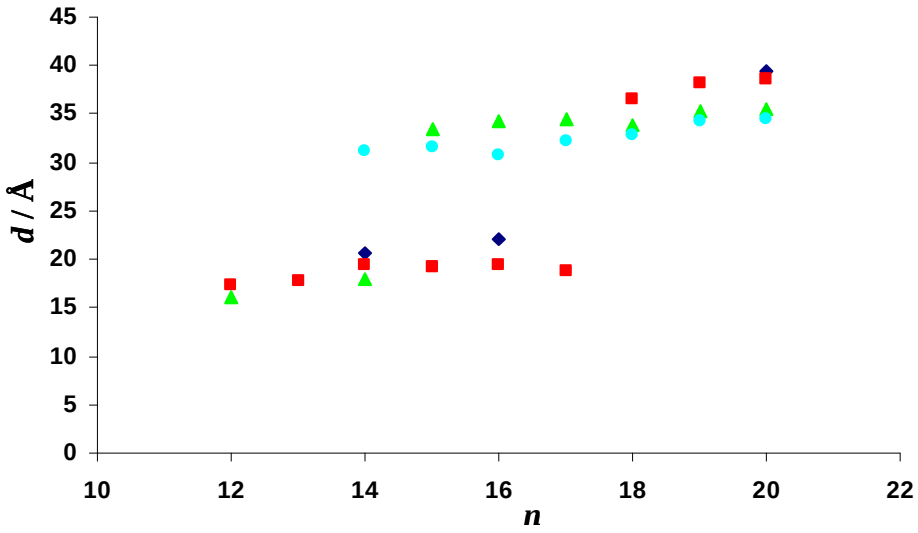

Figure 2.12 Variation in modelled solid layer thickness with n-alkane chain length in mixed monolayers containing C_{12}TAB (circles), C_{14}TAB (triangles), C_{16}TAB (squares) and C_{18}TAB (diamonds).

Similar trends are observed in the solid monolayers (figure 2.12), although the effect of alkane on monolayer thickness is reversed. For a given alkane the thickness increases with the surfactant tail length, and for a given surfactant the thickness increases with alkane chain length. There are clearly two different regimes of thickness of the solid layers; thin layers, 20 Å or thinner, correspond to the formation of type I frozen monolayers whilst thick layers of 30 Å or greater are type II frozen layers. The thicknesses of the type I layers are close to that of the fully extended surfactant tail, consistent with an upright monolayer of all-*trans* chains. The thickness of the type II layers lies close to, but below, the sum of the extended lengths of the surfactant and alkane chains, consistent with a bilayer structure.

The effect of alkane on the solid layer thickness is weaker than might be expected, however, based on an approximate length of 1.3 Å per CH_2 unit in a fully extended chain.[32] In the case of type I monolayers this is easily reconciled, as the surfactant is either longer than the alkane or the difference in chain length is only slight and therefore the thickness of the solid layer is again controlled by the surfactant. Type II

frozen layers are thought to consist of a liquid-like mixed monolayer beneath a surface frozen layer of alkane chains. Naively, then, the thickness of the type II frozen phase should scale with the corresponding change in thickness of surface frozen alkane at the air-melt interface. This is apparently not the case, as best demonstrated by the C_{12}TAB/C_n frozen phases which all form type II solid layers. The relative insensitivity is perhaps as a result of the competing effects of an increase in surface frozen alkane thickness and a decreasing lower liquid-like layer thickness for longer alkanes (figure 2.13).

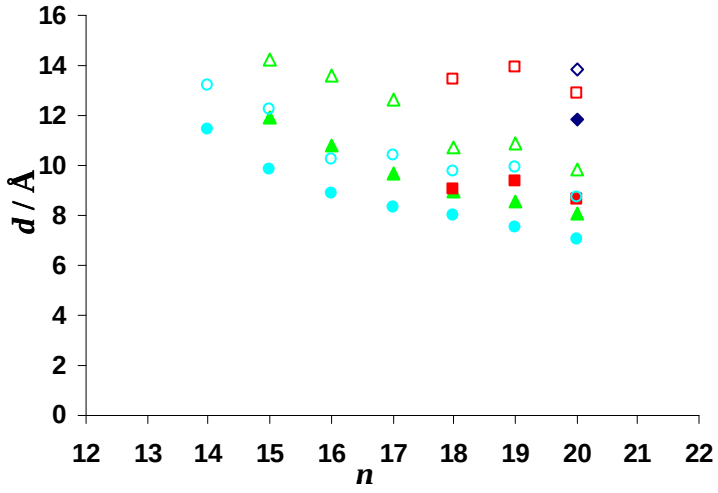

Figure 2.13 Variation in lower liquid-like layer thickness with n-alkane chain length in type II frozen monolayers containing C_{12}TAB (circles), C_{14}TAB (triangles), C_{16}TAB (squares) and C_{18}TAB (diamonds). Open symbols relate to the low temperature phase, with thicknesses in the high temperature phase (closed symbols) included for comparison.

As described in section 2.4.1, if the upper frozen alkane layer of a type II solid phase is assumed to have the same thickness as the corresponding fully extended alkane chain (as shown by Sloutskin *et al*. using X-ray reflectivity[2, 31]) it is possible to calculate the thickness of the lower liquid-like layer. The variation in thickness of the lower liquid-like layer with alkane chain length is shown in figure 2.13 (included for comparison are the corresponding liquid phase monolayer thicknesses). In all cases the thickness of the mixed monolayer appears to increase upon formation of the type II solid phase by roughly 2 – 4 Å. The surface excess of surfactant has been shown to remain constant,[11, 33] so this implies a greater surface excess of alkane in the mixed monolayer in the solid phase.

In order to assess the feasibility of such a change in alkane surface excess, the type II solid phases were also modelled assuming that the lower mixed monolayer thickness remained constant. The difference in ellipticity between the solid and liquid phases is then entirely attributable to a surface frozen layer of alkane, the thickness of which can be calculated directly from equation 2.25. The solid phase alkane layer thicknesses calculated in this way are 2 – 4 Å greater than the extended length of the alkane chains as shown in figure 2.14, calculated using the relation[32] $d = 1.27n + 1.8$ Å modified according to the convention of Riegler *et al.*[30] which ignores the contribution of one terminal H atom to a $C_{21}H_{44}$ alkyl chain (see section 2.4.3). It should be noted that under both sets of assumptions the *total* modelled solid layer thickness remains constant to within 0.1 Å. Therefore the possibility of an increase in surface excess of alkane upon type II freezing seems reasonable, as it seems unlikely that the frozen alkane layer would be thicker than the molecular length of the alkane. An increase in surface excess of alkane can be rationalised in terms of a more bulk alkane-like environment at the interface in the presence of an upper layer of surface frozen alkane. This could lead to a more favourable Hamaker constant in the air/surface frozen alkane/mixed monolayer/water case promoting a thickening of the mixed monolayer *via* an increase in alkane surface excess.

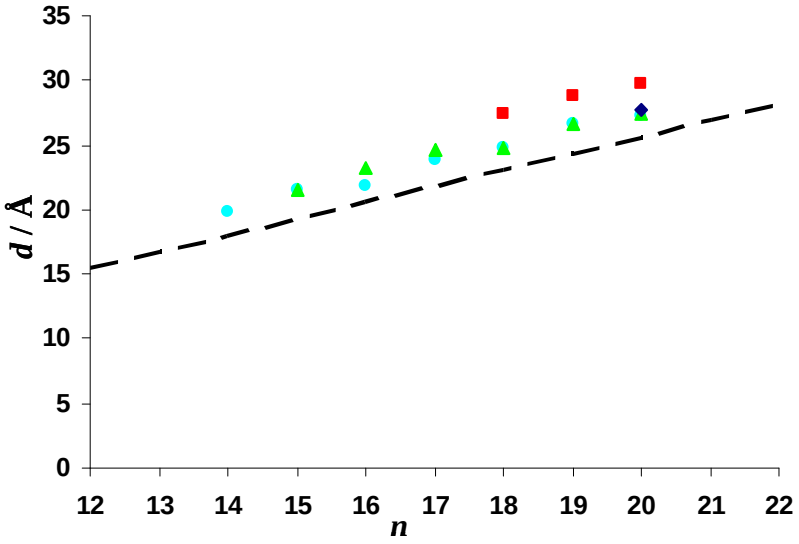

Figure 2.14 Thickness of the upper solid alkane layer, calculated assuming no change in thickness or composition of the lower liquid-like mixed monolayer, in type II frozen monolayers containing C_{12}TAB (circles), C_{14}TAB (triangles), C_{16}TAB (squares) and C_{18}TAB (diamonds). The dashed line corresponds to the fully extended alkane chain length.

2.4.3 Sensitivity of the Modelled Thickness to ε_e and ε_o

Modelling of the type II solid phases using either of the above methods is sensitive to the choice of dielectric constants used. Figure 2.15 shows the sensitivity of the modelled lower layer thicknesses as ε_e and ε_o are varied, assuming that the upper frozen alkane layer thickness is equal to that of a fully extended alkane chain. A decrease in anisotropy of the frozen alkane layer by roughly 20 % (figure 2.15, left) reduces the modelled lower liquid-like layer thickness to within 0.5 Å of the liquid phase mixed monolayer thickness. This corresponds to an error of just 0.02 in the assumed value of ε_e. A decrease of 0.02 in mean permittivity at constant anisotropy (figure 2.15, right) causes the discrepancy between the liquid phase thickness and the lower liquid-like layer thickness in the low temperature phase to increase. Conversely, an increase in the mean permittivity would decrease the discrepancy. However, the calculated thickness is much more sensitive to the anisotropy than to the mean value of ε. Although it is physically reasonable that the lower layer thickness should increase upon surface freezing, the measured change in thickness lies within the uncertainty introduced into the model by the imprecision of ε_e and ε_o.

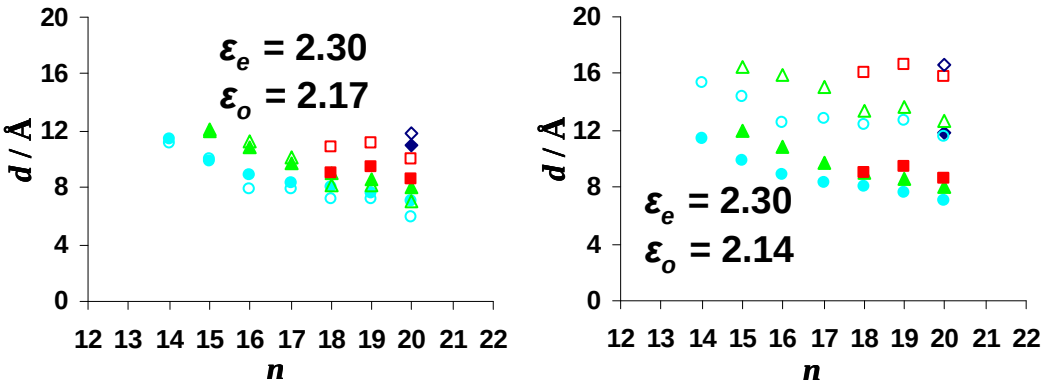

Figure 2.15 Comparison of modelled layer thicknesses for the liquid phase (closed symbols) and lower liquid-like layer thicknesses in the low temperature phase (open symbols), assuming the upper solid layer thickness is equal to the fully extended alkane length. Left, a reduction in upper layer anisotropy. Right, lower polarisability of the upper layer. Dielectric constants as shown, symbols as figures 2.11 – 2.14.

The initial measurement of the dielectric constants requires an assumption about the structure of the layer that was used for the measurement, in particular the layer

thickness. Riegler *et al.* assumed an alkyl chain thickness of 27.5 Å for a fully extended $C_{21}H_{44}$ behenic acid tailgroup at a molecular area of 19.3 $Å^2$. The C-C distance in a fully extended alkyl chain is 1.27 Å, and the terminal H atom has been shown to add a further 0.9 Å to the length of the molecule.[32] The total length of a linear alkane, including two terminal H atoms, can therefore be calculated as $d = 1.27n + 1.8$, where *n* is the number of carbon atoms in the chain. Riegler *et al.* based their chain length assumption on previously reported X-ray reflectivity data,[34] removing the headgroup contribution to the monolayer thickness and therefore effectively modelling a hypothetical alkyl chain with only one terminal H atom. To maintain internal consistency between the assumed alkane chain lengths used in this chapter and the dielectric constants used in modelling the solid phases, the same assumption was made, namely that the extended alkane chain length is given by $d = 1.27n + 0.9$. It is reasonable to assume, therefore, that calculated chain lengths and modelled layer thicknesses presented are comparable.

2.4.4 Variations in Transition Temperature and Type

Type I/Type II Crossover

The nature of the surface frozen layer formed upon cooling is dependent upon the difference in chain length between surfactant and alkane, which affects the degree of stabilisation of a solid mixed monolayer. Sloutskin *et al.*[35-37] have studied surface freezing at the air-melt interface of binary alkane mixtures. Distinct behaviours were found for mixtures with large (10 CH_2 units) and small (2 – 3 CH_2 units) chain length differences between the component alkanes. In the case of a small chain length difference the alkanes co-crystallise to form a uniform surface frozen phase with a composition-dependent transition temperature between that of the component alkanes. This situation is analogous to that found in the bulk, where alkanes with chain length differences of up to about 6 CH_2 units will co-crystallise.[32] For a larger chain length difference the nature of the frozen phase varied with composition as phase separation occurred at the interface. Such phase separation cannot occur in mixed monolayers of surfactant and alkane at the air-water interface and so it is simply not possible to form a solid mixed monolayer when the chain length mismatch is too great; the solid monolayer formed would possess a high degree of

surface roughness, with the portions of alkane chain extending beyond the surfactant tails experiencing a reduced van der Waals interaction and thus destabilising the monolayer. This accounts for the appearance of a high *n*-alkane chain length limit for type I behaviour with any given surfactant.

Table 2.3 Modelled solid layer thicknesses for C_mTAB/C_n mixed monolayers

		Solid Phase Thickness (lower layer thickness for type II systems) / Å			
n-alkane	*n*-alkane length / Å	C_{12}TAB	C_{14}TAB	C_{16}TAB	C_{18}TAB
12	16.1		16.2	17.4	
13	17.4			17.7	
14	18.7	31.5(13.2)	17.9	19.4	20.7
15	20.0	31.8(12.2)	33.8(14.3)	19.3	
16	21.2	31.1(10.3)	34.5(13.6)	19.3	22.2
17	22.5	32.5(10.4)	34.8(12.6)	18.7	
18	23.8	33.1(9.7)	34.1(10.7)	36.8(13.4)	
19	25.0	34.5(9.9)	35.5(10.9)	38.6(13.9)	
20	26.3	34.7(8.8)	35.8(9.8)	38.8(12.9)	39.7(13.8)

The precise *n*-alkane for which the crossover in behaviour takes place turns out to be relatively insensitive to C_mTAB tailgroup length where m = 14, 16 or 18. The crossover in behaviour either occurs for a chain length difference of $n-m=2$, i.e. the alkane chain is longer by 2 CH_2 units, when $m=16,18$ or when $n-m=1$ in the case of C_{14}TAB. Type I monolayers are more tolerant of the opposite chain length difference, i.e. an excess length of surfactant tail, as evidenced by the appearance of type I behaviour in, for example, mixed monolayers of C_{18}TAB and tetradecane or C_{16}TAB and undecane. Molecular models have suggested that the optimum chain length match is found in mixed monolayers of C_{16}TAB and tetradecane.[1] The

surfactant headgroup hinders close approach of the alkane to the monolayer-water interface, and hence alkanes with shorter chains do not create the same level of surface roughness as those with chains longer than the surfactant. With C_{14}TAB as surfactant the potential frozen mixed monolayer is thinner and therefore less tolerant of end-chain roughness, hence the lower alkane chain length crossover to type II freezing. The onset of type II behaviour is, then, caused by a protrusion of roughly 4 alkane CH_2 units above the mixed monolayer, with the ends of the alkane chains tilted away from the surface normal to form a high proportion of *gauche* defects. The greater sensitivity of type I monolayer freezing to chain length difference over the bulk alkane mixtures shows that the balance of free energies is very fine in the mixed monolayers. In a bulk alkane mixture, the effect of mismatch can be reduced by sharing excess CH_2 units between both ends of the molecule, up to a limit of 3 units per chain end, conceptually similar to the type II crossover point observed in mixed monolayers.

C_{12}TAB does not form type I frozen monolayers with any of the *n*-alkanes used, whilst alkanes shorter than tetradecane could not be tested due to the subzero temperatures required. Nevertheless, the fact that type II frozen layers are formed with all alkanes in the range $C_{14} – C_{20}$ is not immediately consistent with the current models for formation of type II layers, as will be discussed later.

Transition Temperatures

Figure 2.16 shows the variation in transition temperature with *n*-alkane for the range of surfactants studied. Within a given surfactant series, the surface freezing temperature, T_s, increases with *n*-alkane chain length due to the increase in attractive Van der Waals forces. For type I systems, T_s increases with surfactant tail length for a given *n*-alkane series for the same reason, although the differences in T_s do not follow the regular pattern that might be expected. For the series of surfactants with tetradecane, there is a large difference in T_s of over 10 °C between C_{14}TAB and C_{16}TAB as surfactant, compared to a difference of only 1.6 °C between C_{16}TAB and C_{18}TAB. A similarly small difference in T_s is observed in the hexadecane series. In addition, a 10 °C difference is also found in mixed monolayers of C_{14}TAB or C_{16}TAB with dodecane.

There are two possible explanations for these observations. The surface excess of C_{14}TAB in a 1.2 mM solution in the presence of dodecane is approximately 2.7 μmol m^{-2}, whereas the surface excesses of C_{16}TAB and C_{18}TAB are slightly higher at 3.4 μmol m^{-2} and 3.3 μmol m^{-2} respectively.[16, 17, 24, 25] The lower surface excess of C_{14}TAB may, therefore, contribute to an excessively low T_s in these systems. The effect of surface excess on transition temperature at the air-water interface is demonstrated by the low T_s of 2 °C found by Wilkinson *et al.*[1, 3] for a mixed monolayer of C_{16}TAB and undecane, where a lower surfactant concentration (0.3 mM, rather than 0.6 mM) had to be used due to the high Krafft point of C_{16}TAB. Alternatively, the smaller increase in T_s in the C_{18}TAB systems could be due to the lower percentage increase in total Van der Waals attraction going from a C_{16} chain to a C_{18} chain.

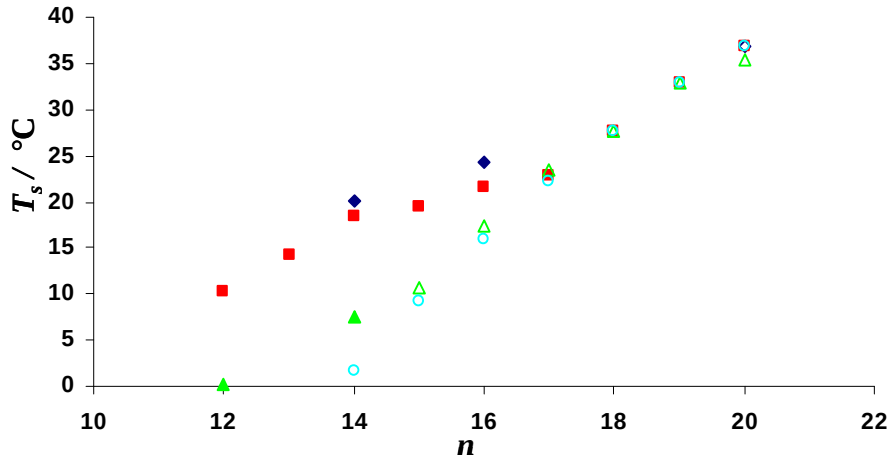

Figure 2.16 Variation in transition temperature, T_s with n-alkane chain length. Monolayers containing C_{12}TAB (circles), C_{14}TAB (triangles), C_{16}TAB (squares) and C_{18}TAB (diamonds). Filled symbols denote type I monolayers, open symbols denote type II monolayers.

Of more interest is the surface freezing range, $\Delta T = T_s - T_b$, plotted in figure 2.17. ΔT decreases with increasing alkane chain length, falling to approximately zero at the crossover between type I and type II behaviour. In the type I regime the same trends as those described above are observed, with longer tail length surfactants providing a larger surface freezing range. In the case of type II freezing with alkanes where $16 \leq n \leq 20$, ΔT falls within the surface freezing range reported for bulk *n*-alkanes (up to 3 °C). The transition temperatures for these alkanes have the same T_s,

within experimental precision, irrespective of surfactant tail length, suggesting that the mixed monolayer takes no part thermodynamically in the transition. However, the appearance of type II freezing for mixed monolayers of pentadecane with C_{12}TAB or C_{14}TAB and tetradecane with C_{12}TAB demonstrates for the first time the formation of a type II frozen layer in the presence of an alkane that does not exhibit surface freezing.

The type II frozen layers were stable and were generally maintained at the interface even if the bulk alkane lens became frozen (although they would not form in the presence of a frozen lens). Freezing of the lens was only observed for tetradecane, pentadecane and hexadecane, implying a supercooling of lenses of the longer alkanes by several degrees. Supercooling of the shorter alkanes must have also taken place to some extent, as any freezing of the lens was only observed below T_s, and several of the ΔT values are negative. The only system that proved to be unstable when the bulk lens froze was C_{12}TAB/tetradecane, reverting to a liquid phase mixed monolayer. From a thermodynamic viewpoint this should be the expected behaviour for all type II frozen monolayers in the presence of a crystalline bulk lens, as at sufficiently low temperatures it becomes favourable to transfer molecules from a 2D surface rotator phase to a 3D bulk crystalline phase. It is possible, therefore, that in the presence of a frozen alkane lens type II monolayers are only kinetically stabilised due to slow transport of alkane when both lens and surface are frozen.

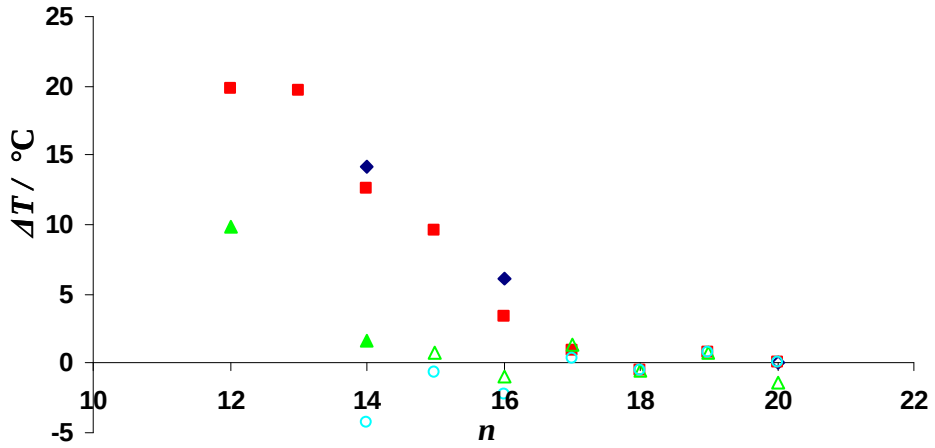

Figure 2.17 Variation in $\Delta T = T_s - T_b$ with n-alkane chain length. Monolayers containing C_{12}TAB (circles), C_{14}TAB (triangles), C_{16}TAB (squares) and C_{18}TAB (diamonds). Filled symbols denote type I monolayers, open symbols denote type II monolayers.

2.4.5 Comparison with Previous Experiments

Surface Freezing at the Alkane-Solution Interface

Surface freezing has only been observed for tridecane, tetradecane and pentadecane at the C_{16}TAB solution-bulk alkane interface,[11] and for hexadecane at the C_{18}TAB solution-bulk alkane interface.[38] The scope of phase behaviour in mixed monolayers of C_mTABs and alkane at the liquid-liquid interface appears much reduced compared to the air-solution interface, although fewer total systems have been studied. This observation can be rationalised in terms of the lower surface freezing range at the liquid-liquid interface (ΔT is typically 5 °C lower than at the air-solution interface) and the fact that no type II behaviour is observed at the liquid-liquid interface. Both these facts indicate that frozen mixed monolayers are more stable at the air-solution interface. The new phase transitions reported in this chapter serve to emphasize this observation.

The increased stability of surface frozen layers at the air-solution interface can be understood in terms of the relative entropy changes taking place at both interfaces. Alkane molecules at the alkane-solution interface are free to exchange with those in the bulk, whereas at the air-solution interface they are not. Surface freezing at the air-solution interface therefore involves the loss of one fewer degree of freedom, resulting in a more favourable, less negative, entropy change than at the alkane-solution interface.

X-ray Reflectivity and Ellipsometry

Sloutskin, Deutsch *et al.* have performed detailed x-ray reflectivity experiments to determine the structure of surface frozen layers at the neat alkane surface,[35, 39] as well as the structure of type I and type II C_{16}TAB/*n*-alkane mixed monolayers at the air-water interface.[2, 31] Grazing incidence diffraction of type I monolayers indicated that in the solid phase chains were upright and hexagonally packed with an area per molecule of 19.8 $Å^2$ and a crystalline coherence length of several hundred Å. The modelled layer thicknesses were found to increase approximately linearly with *n*-alkane chain length from approximately 15.5 Å in the presence of dodecane to 20.3 Å in the presence of hexadecane. These measured thicknesses are in good agreement

with previously modelled ellipsometry data,[1, 3] confirming the validity of comparisons with thicknesses reported in the present chapter (table 2.1). In the case of type I freezing, therefore, it appears that the liquid layer thickness is limited by the ultimate length of the surfactant tail, whereas the thickness of the solid layer is controlled by the alkane. The structures obtained by x-ray reflectivity, and the ellipsometrically modelled layer thicknesses are in excellent agreement with structural parameters previously observed for surface freezing at the neat alkane interface and in small chain length difference mixtures of alkanes,[35, 36] justifying the assertion that type I monolayers freeze to a 2D rotator phase.

Reflectivity experiments on type II C_{16}TAB/*n*-alkane mixed monolayers give equally good agreement with solid layer thicknesses modelled by ellipsometry. For example, the solid phase of a C_{16}TAB/*n*-eicosane mixed monolayer was shown by x-ray reflectivity to have a layer thickness of 39.4 Å,[31] whilst the ellipsometrically modelled thickness is 38.5 Å using similar two layer models.

Type II frozen layers have been proposed to consist of a liquid-like mixed monolayer underneath a surface frozen alkane layer.[1, 31] This conclusion is supported by X-ray data, detailed interpretation of which suggests that the upper solid leaflet of the bilayer has a thickness equivalent to surface frozen alkane (as measured by x-ray reflectivity[39] or calculated using the relation $d = 1.27n + 0.9$ Å as described in section 2.4.3), whilst the lower leaflet consists of a disordered layer of alkane-independent thickness. The modelled ellipsometry data presented in this chapter broadly agrees with this finding, with good agreement between the total layer thicknesses calculated using both techniques. In contrast to X-ray reflectivity data, however, a two layer model of ellipsometry data implies a change in thickness of the lower liquid-like layer upon freezing, and also a dependence upon *n*-alkane chain length (figures. 2.11 – 2.14). This analysis implies a lower leaflet thickness of approximately 13 Å (for C_{16}TAB monolayers, 11 Å for C_{12}TAB, 12 Å for C_{14}TAB), greater than any liquid phase monolayer thickness previously reported using either X-ray reflectivity or ellipsometry. An increase in layer thickness is indicative of a greater surface excess of alkane in the solid phase lower leaflet, a reasonable conclusion given the bulk alkane-like environment provided by the upper surface

frozen layer which will serve to reduce the energy penalty for alkane adsorption to the interface. It was shown in section 2.4.3, however, that the magnitude of this implied change in thickness was within the error of the assumed solid layer dielectric constants. This does not, *a posteriori*, necessarily mean that such a change in thickness does not take place. Section 2.4.3 also showed a high degree of internal consistency between the modelled layer thicknesses and the assumed alkane chain lengths, since the same assumptions about the layer thickness were made as by Rielger *et al.* in the original determination of the dielectric constants. In addition, the liquid phase and solid phase lower leaflet thicknesses could only be made equal in the case where the anisotropy of the upper frozen alkane layer was reduced by at least 20 %. An increase in anisotropy led to an increase in the modelled difference. Since the magnitude of optical anisotropy has been shown to be similar for several ordered chain structures[14, 40-42] it seems unlikely that there is a 20% error in the original anisotropy measured by Riegler *et al.*, although without independent evidence that is less reliant upon small details in the modelling no firm conclusion can be made.

The *n*-alkane and surfactant tail length dependent behaviour presented in this chapter is in full agreement with the existence of only two distinct types of transition, and the excellent agreement between the solid layer thicknesses and the sum of the component chain lengths shows that all the transitions are consistent with either the type I or type II behaviour previously observed.

2.4.6 Unexpected Aspects of Type II Behaviour

Examples were shown earlier following the change in ellipticity as a function of time as a freezing transition took place. Figure 2.18 shows the freezing transition as a mixed monolayer of C_{18}TAB and eicosane was cooled to form a stable type II solid phase. Interestingly in this case the transition appears to proceed stepwise with the appearance of a plateau in the ellipticity. No readings of the plateau value were ever obtained from a fully equilibrated monolayer, despite repeated attempts, and the plateau was only ever observed transiently as the temperature of the sample was changing. The plateau ellipticity is very similar to that of a type I frozen monolayer,

suggesting that a type I phase could be metastable at a temperature just below the transition temperature for this system.

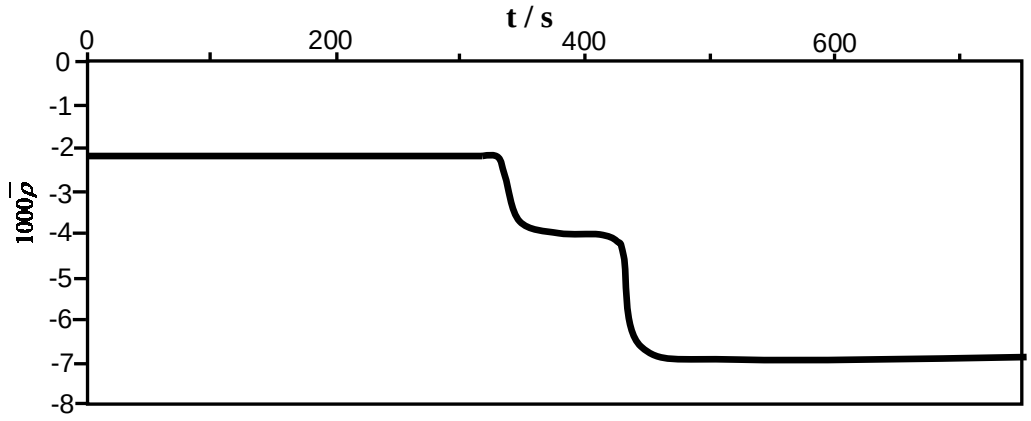

Figure 2.18 Coefficient of ellipticity as a function of time as the temperature of a C_{18}TAB/C_{20} mixed monolayer was lowered through the transition temperature.

The observation of type II behaviour in the presence of alkanes that do not surface freeze at the neat alkane-air interface is novel, as type II layers were believed to form *via* wetting of the interface by surface frozen alkane.[1, 31] The present data do not necessarily contradict this model, however, since the stability of a surface frozen layer of alkane will be different depending on whether the layer is above bulk liquid alkane or a liquid mixed monolayer at the air-water interface. In addition to subtle changes in short-range forces at the interface, the long-range van der Waals interaction across the interface will be different due to the different subphase in both situations. It is therefore possible that a surface frozen layer of tetradecane or pentadecane is more stable above a mixed monolayer at the air-solution interface than at the air-alkane interface.

Although the appearance of type II behaviour in the presence of tetradecane and pentadecane can be rationalised within the framework of the current model, doubt as to how alkane is transported into the frozen monolayer remains. Direct spreading of a frozen layer would require the presence of surface frozen alkane. The fact that surface frozen alkane seems not to be a prerequisite therefore suggests a more complicated mechanism.

2.4.7 Conclusion

The data presented in this chapter are consistent with the current structural models of both type I and type II frozen monolayers. The mechanism of formation of type II monolayers is in doubt, however, as shown by the existence of several new, unexpected type II systems in the presence of non-surface freezing alkanes. Unusual behaviour during the type II transition of the C_{18}TAB/C_{20} system may provide clues as to the mechanism of type II frozen monolayer formation. These findings will be discussed further in chapter 6 along with additional ellipsometric and spectroscopic evidence.

2.5 References

1. Wilkinson, K. M. Phase Transitions in Monolayers of Soluble Surfactants. University of Oxford, 2004.
2. Sloutskin, E.; Sapir, Z.; Tamam, L.; Ocko, B. M.; Bain, C. D.; Deutsch, M., *Thin Solid Films* **2007,** 515, 5664-5668.
3. Wilkinson, K. M.; Lei, Q.; Bain, C. D., *Soft Matter* **2006,** 2, 66-76.
4. Hecht, E., *Optics*. 2nd ed.; Addison-Wesley Publishing Company: 1987.
5. Born, M.; Wolf, E., *Principles of Optics*. 6th ed.; Pergamon Press: Oxford, 1989.
6. Möbius, D.; Miller, R., In *Novel Methods to Study Interfacial Layers*, Elsevier: 2001; Vol. 11.
7. Beaglehole, D., *Physica B* **1980,** 100, 163.
8. Meunier, J., *Journal de Physique II France* **1987**, (48), 1819.
9. Jasperson, S. N.; Schnatterly, S. E., *Review of Scientific Intruments* **1969,** 40, 761.
10. *Picometer Ellipsometer Manual*. Beaglehole Instruments: Wellington, 2008.
11. Lei, Q.; Bain, C. D., *Physical Review Letters* **2004,** 92, 176103.
12. Casson, B. D.; Braun, R.; Bain, C. D., *Faraday Discussions* **1996,** 104, 209.
13. Casson, B. D.; Bain, C. D., *Journal of Physical Chemistry B* **1998,** 102, 7434.
14. Casson, B. D. Phase Transitions in Surfactant Monolayers. University of Oxford, 1998.
15. Lide, D. R., *CRC Handbook of Chemistry and Physics*. 74th ed.; CRC Press: Boca Raton: 1993.
16. Matsubara, H.; Ikeda, N.; Takiue, T.; Aratono, M.; Bain, C. D., *Langmuir* **2003,** 19, 2249.
17. Lu, J. R.; Thomas, R. K.; Aveyard, R.; Binks, B. P.; Cooper, P.; Fletcher, P. D. I.; Stokolowski, A.; Penfold, J., *Journal of Physical Chemistry* **1992,** 96, 10971.
18. Lu, J. R.; Hromadova, M.; Simister, E. A.; Thomas, R. K.; Penfold, J., *Physica B* **1994,** 198, 120.

19. Lu, J. R.; Li, Z. X.; Smallwood, J.; Thomas, R. K.; Penfold, J., *Journal of Physical Chemistry* **1995,** 99, 8233.
20. Lu, J. R.; Hromadova, M.; Simister, E. A.; Thomas, R. K.; Penfold, J., *Journal of Physical Chemistry* **1994,** 98, 11519.
21. Lu, J. R.; Li, Z. X.; Thomas, R. K.; Penfold, J., *Journal of the Chemical Society, Faraday Transactions* **1996,** 92, 403.
22. Lu, J. R.; Li, Z. X.; Thomas, R. K.; Binks, B. P.; Crichton, D.; Fletcher, P. D. I., *Journal of Physical Chemistry B* **1998,** 102, 5785.
23. Binks, B. P.; Crichton, D.; Fletcher, P. D. I.; MacNab, J. R.; Li, Z. X.; Thomas, R. K.; Penfold, J., *Colloids and Surfaces A: Physiochemical and Engineering Aspects* **1999,** 146, 299.
24. Manning-Benson, S.; Parker, S. R. W.; Bain, C. D.; Penfold, J., *Langmuir* **1998,** 14, 990.
25. Battal, T.; Shearman, G. C.; Valkovska, D.; Bain, C. D., *Langmuir* **2003,** 19, 1244.
26. Atkins, P. W., *Physical Chemistry*. 6th ed.; OUP: Oxford, 1998.
27. Aveyard, R.; Binks, B. P.; Fletcher, P. D. I., *Progress in Colloid and Polymer Science* **1990,** 81, 36.
28. Casson, B. D.; Bain, C. D., *Langmuir* **1997,** 13, 5465.
29. Sefler, G. A.; Du, Q.; Miranda, P. B.; Shen, Y. R., *Chemical Physics Letters* **1995,** 235, 347.
30. Paudler, M.; Ruths, J.; Riegler, H., *Langmuir* **1992,** 8, 184.
31. Sloutskin, E.; Sapir, Z.; Lei, Q.; Wilkinson, K. M.; Tamam, L.; Deutsch, M.; Ocko, B. M., *Physical Review Letters* **2007,** 99, 136102.
32. Small, D. M., *The Physical Chemistry of Lipids: From Alkanes to Phospholipids*. Plenum Press: New York, 1986.
33. Matsubara, H.; Ohtomi, E.; Aratono, M.; Bain, C. D., *Journal of Physical Chemistry B* **2008,** 112, 11664.
34. Kenn, R. M.; Böhm, C.; Bibo, A. M.; Peterson, I. R.; Möhwald, H., *Journal of Physical Chemistry* **1991,** 95, 2092.
35. Sloutskin, E.; Wu, X. Z.; Peterson, T. B.; Gang, O.; Ocko, B. M.; Sirota, E. B.; Deutsch, M., *Phyical Review E* **2003,** 68, 031065/1.
36. Sloutskin, E.; Sirota, E. B.; Kraak, H.; Ocko, B. M.; Deutsch, M., *Physical Review E* **2001,** 64, 031708.
37. Wu, X. Z.; Ocko, B. M.; Tang, H.; Sirota, E. B.; Sinha, S. K.; Deutsch, M., *Physical Review Letters* **1995,** 75, 1332.
38. Sloutskin, E.; Bain, C. D.; Ocko, B. M.; Deutsch, M., *Faraday Discussions* **2005,** 129, 1.
39. Ocko, B. M.; Wu, X. Z.; Sirota, E. B.; Sinha, S. K.; Gang, O.; Deutsch, M., *Physical Review E* **1997,** 55, 3164.
40. Ducharme, D.; Max, J.; Salesse, C.; Leblanc, R. M., *Journal of Physical Chemistry* **1990,** 94, 1925.
41. Englesen, D. D., *Surface Science* **1976,** 56, 272.
42. Englesen, D. D., *Journal of the Optical Society of America* **1971,** 61, 1460.

Chapter 3

Ellipsometric Survey of Surface Freezing in Novel Surfactant Systems

3.1 Introduction

In general, in order for surface freezing to take place in any given surfactant/alkane system, the alkane must form a mixed monolayer at the air-water interface, i.e. the alkane must pseudo-partially wet the air/water interface (direct gas-solid transitions have been observed in monolayers of C_{12}TAB in the presence of C_{16})[1]. The wetting state is determined by short- and long-range interactions within and across the interfacial film. Short range forces are described by the initial spreading constant, S_i

$$S_i = \gamma_{aw}^0 - (\gamma_{ao} + \gamma_{ow}) \tag{3.1}$$

where γ_{aw}^0 is the surface tension of the air-solution interface in the absence of oil, γ_{ao} is the air-oil interfacial tension and γ_{ow} the oil/water interfacial tension.

Long range forces are dependent on the Hamaker constant of the air/oil/solution system, A_{woa}. The free energy varies with film thickness, D, according to

$$P(D) = \frac{-A_{woa}}{12\pi D^2} \tag{3.2}$$

The balance between these two forces determines the thickness of the interfacial film. Pseudo-partial wetting occurs when $S_i>0$, favouring spreading, and $A_{woa}>0$, favouring thinning of the film. In this regime a mixed monolayer is formed in equilibrium with a bulk alkane lens.

Mixed monolayers of surfactant and oil have been well described in the literature, using a combination of surface tension, ellipsometry and neutron reflectivity data. Mixed monolayer formation was indicated by a reduction in interfacial tension upon addition of medium chain length alkanes for C_{12}TAB[2, 3] and C_nE_m,[4] dodecane on $C_{12}E_5$[5] and hexadecane on tetramethylammonium dodecylsulphate.[6] Unequivocal evidence for the first-order nature of the wetting transitions was provided by ellipsometry from C_nTAB monolayers with hexadecane, dodecane and squalane, as well as the identification of a wetting transition of hexadecane on the anaesthetic

dibucaine hydrochloride.[7] The mixed layers formed were shown to be of monolayer thickness through modelling of both ellipsometry and neutron reflectivity data.[7, 8]

Intermixing of surfactant tails with oil chains was shown using neutron reflection for dodecane on C_nTAB, SDS and C_nE_m.[4, 5, 8] The surfactant tails became more extended on addition of oil, tilting more towards the surface normal. The surface excess of surfactant remained relatively unchanged. The extent of oil adsorption was found to decrease with increasing alkane chain length, and to increase with increasing surfactant tail length.

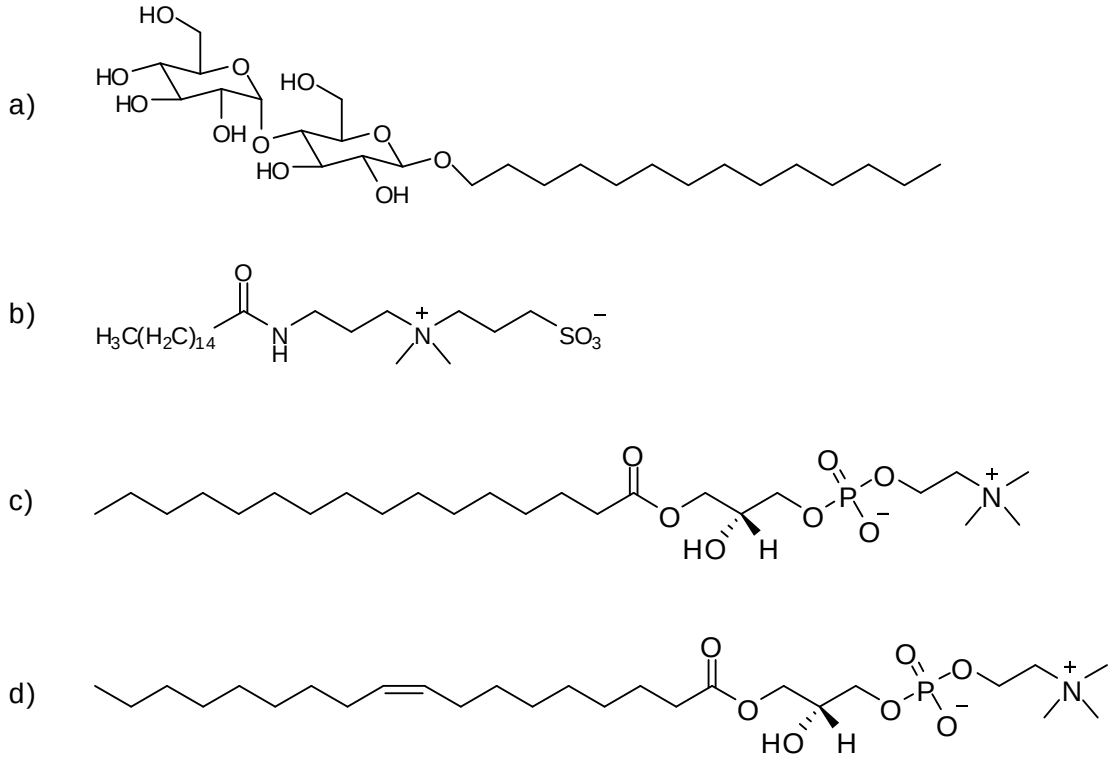

Figure 3.1 Structures of surfactants used in this chapter. C_{14}mal, (a), C_{14}DAPS, (b), lyso-PPC, (c), and lyso-OPC, (d).

Despite the relatively wide range of surfactants that have been shown to form mixed monolayers at the air-water interface in the presence of oil, investigations into surface freezing in such mixed monolayers have so far been restricted to a small subset of systems. Freezing transitions have been found in mixed monolayers of C_nTABs with a range of *n*-alkanes at the air/water interface[9-12] and, to a lesser extent, the oil/water interface.[13, 14] Phase transitions have also been observed in mixed monolayers of C_nTAB,[15] SDS[16] and octanoic acid[17] with dodecanol. A few other

solid-liquid phase transitions in mixed monolayers have been observed,[18-20] although in these cases surfactant/surfactant mixtures were used so the origins of the behaviour is likely to be unique to each system. For example, mixed monolayers of the catanionic surfactants dodecyltrimethylammonium dodecyl sulphate and decyltrimethylammonium decyl sulphate undergo a solid-liquid phase transition as the overall repulsion between headgroups is reduced in the mixed monolayer compared to the individual surfactants.[18]

In this chapter results are presented for a range of ionic, non-ionic, zwitterionic and biological surfactant systems in the presence of alkane. The effect of adding *n*-alkane mixtures to the surface of C_{16}TAB solutions is also investigated to gain a better understanding of the effects of chain length difference and headgroup structure on surface freezing behaviour.

3.2 Experimental Methods and Materials

3.2.1 The Ellipsometer

The coefficient of ellipticity (defined as the imaginary part of the ratio r_p / r_s at the Brewster angle) was measured using a Picometer Ellipsometer (Beaglehole Instruments, Wellington, NZ). Details of the technique and of the ellpsometer were presented in section 2.2.1.

3.2.2 Materials

The surfactants *lyso*-palmitoylphosphatidylcholine (*lyso*-PPC, Avanti Polar Lipids), *lyso*-oleylphosphatidylcholine (*lyso*-OPC, Avanti Polar Lipids), octaethylene glycol monohexadecyl ether ($C_{16}E_8$, Nikko Chemicals), hexaethylene glycol monohexadecyl ether ($C_{16}E_6$, Nikko Chemicals), pentaethylene glycol monotetradecyl ether ($C_{14}E_5$, Sigma Aldrich $\geq 99\%$), *n*-tetradecyl-beta-D-maltopyranoside (C_{14}mal, Sigma $\geq 99.5\%$), Triton X-100 (SigmaUltra) and polysorbate 80 (Tween 80, Sigma) were used as received. The surfactants hexadecyl trimethylammmonium bromide (C_{16}TAB, Sigma $\geq 99.9\%$), (C_{14}DAPS, Sigma) and (C_{12}DAPS, Sigma) were recrystallised three times from an acetone/ethanol mixture

before being dried under vacuum. The structures of some of these surfactants are shown in figure 3.1.

The *n*-alkanes tetradecane (Aldrich $\geq 99\%$), pentadecane (Aldrich $\geq 99\%$), hexadecane (Aldrich $\geq 99\%$), octadecane (Aldrich $\geq 99\%$), nonadecane (Aldrich $\geq 99\%$) and eicosane (Aldrich $\geq 99\%$) were passed though a column of neutral alumina under a flow of dry nitrogen prior to use. *n*-Octacosane was provided by Professor C. D. Bain and was mixed with purified hexane before passing through an alumina column. The hexane was removed under vacuum before use.

All glassware was soaked in alkaline Deconnex detergent (Borer Chemie) and rinsed copiously in ultra high purity water (Millipore). Oil lenses were introduced to the sample surface using a glass syringe. Alkane mixtures were prepared by mixing known masses of each component to give the desired molecule:molecule ratio. Experiments were also carried out by adding a known volume of each alkane to the surface in succession.

The temperature of samples was varied discontinuously with a minimum equilibration time of 40 minutes between each measurement. The evolution of the coefficient of ellipticity was constantly monitored during temperature changes, in order to ensure the surface was fully equilibrated. The temperature was recorded to a precision of 0.1 °C using a thermocouple housed inside a tight-fitting glass capillary.

3.3 Results

3.3.1 Surface Freezing Systems

Lyso-PPC/*n*-alkane Mixed Monolayers

Figure 3.2 shows measurements of the coefficient of ellipticity as a function of temperature for mixed monolayers at the surface of a 0.4 mM *lyso*-PPC solution with added tetradecane, nonadecane and octacosane. Data include both heating and cooling cycles.

Clear discontinuities in the coefficient of ellipticity occurred at 18.2 °C, 32.8 °C and 62.1 °C in the presence of tetradecane, nonadecane and octacosane, respectively. Two distinct behaviours were observed, characterised by changes in the coefficient of ellipticity of different magnitudes, with the octacosane system dropping by over four times more than the shorter alkanes. Superficially these changes in $\overline{\rho}$ seem to support the presence of both type I and type II freezing, although the discontinuities are larger than in similar C_nTAB/alkane mixed monolayers. The layer thicknesses of all the systems presented in this chapter are modelled in section 3.3.3 in order to confirm the solid layer structure.

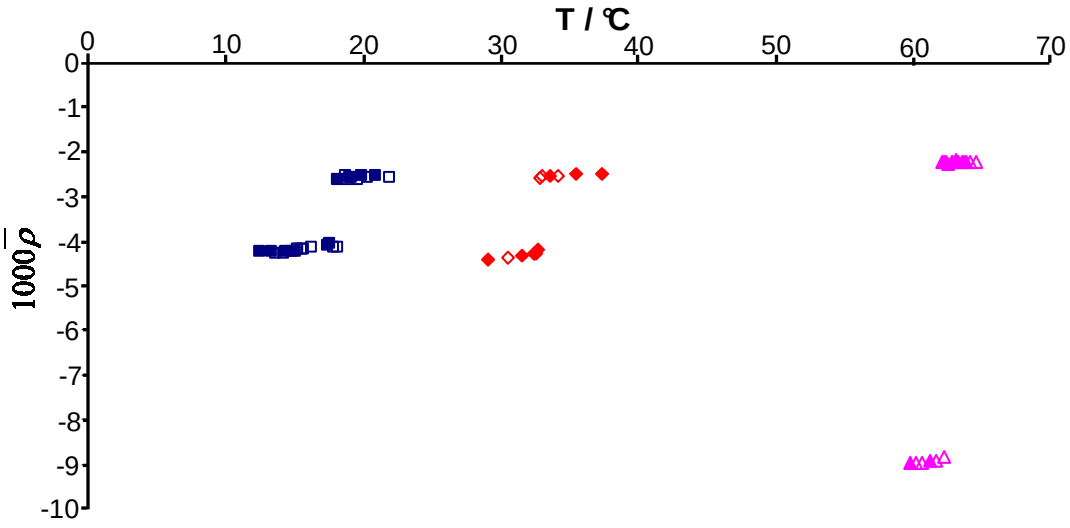

Figure 3.2 Coefficient of ellipticity as a function of temperature for mixed monolayers at the surface of a 0.4 mM lyso-PPC solution in the presence of tetradecane (squares), nonadecane (diamonds) and octacosane (triangles).

Lyso-OPC/_n_-alkane Mixed Monolayers

First order freezing transitions were also found in mixed monolayers of the unsaturated lysolipid *lyso*-OPC with pentadecane and nonadecane, as shown in figure 3.3. In the case of pentadecane the monolayer had to be cooled approximately 5° below the transition temperature, as defined by the heating cycle, before freezing took place.

Transitions occurred at 16.2 °C and 33.2 °C in the presence of pentadecane and nonadecane, respectively. In both cases the change in coefficient of ellipticity is approximately the same, implying the presence of only type II behaviour in these systems. In this respect surface freezing in *lyso*-OPC monolayers has more in

common with the shorter chain C_nTABs, whereas *lyso*-PPC behaves similarly to longer chain C_nTABs.

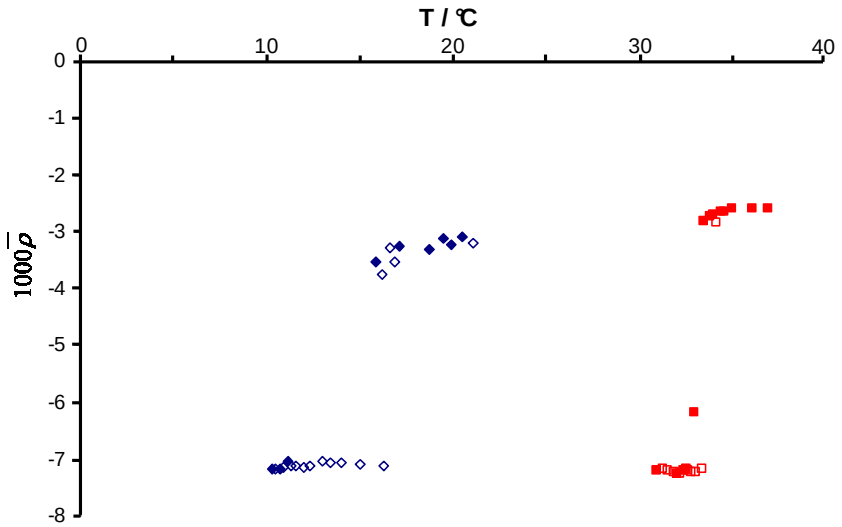

Figure 3.3 Coefficient of ellipticity as a function of temperature for mixed monolayers at the surface of 0.4 mM lyso-OPC solutions in the presence of pentadecane (diamonds) and nonadecane (squares). Open symbols denote heating cycles, closed symbols denote cooling cycles.

$C_{16}E_8$/*n*-alkane Mixed Monolayers

Of all the non-ionic surfactants studied, only mixed monolayers containing $C_{16}E_8$ showed surface freezing. Freezing transitions were found in the presence of tetradecane (19.2 °C), pentadecane (20.0 °C), hexadecane (21.0 °C) and octadecane (27.9 °C), examples of which are shown in figure 3.4.

In all cases the drop in coefficient of ellipticity upon surface freezing was approximately -2×10^{-3}, indicating the formation of only one type of frozen monolayer. The change in ellipticity is roughly double that found in the corresponding C_{16}TAB-containing type I monolayers, yet is smaller than would be expected from type II monolayer formation.

C_{16}TAB with Tetradecane:Hexadecane and Hexadecane:Octadecane Mixtures

Binary mixtures of alkanes[21-23] and alcohols[22, 24] surface freeze at the air/oil interface. Alkane mixtures with a chain length difference of less than 6 CH_2 units co-crystallise in the bulk; chain length differences larger than this cannot be tolerated in the crystal

lattice.[25] It would therefore be expected that mixed monolayers formed from binary mixtures of alkanes should also surface freeze at the air-water interface.

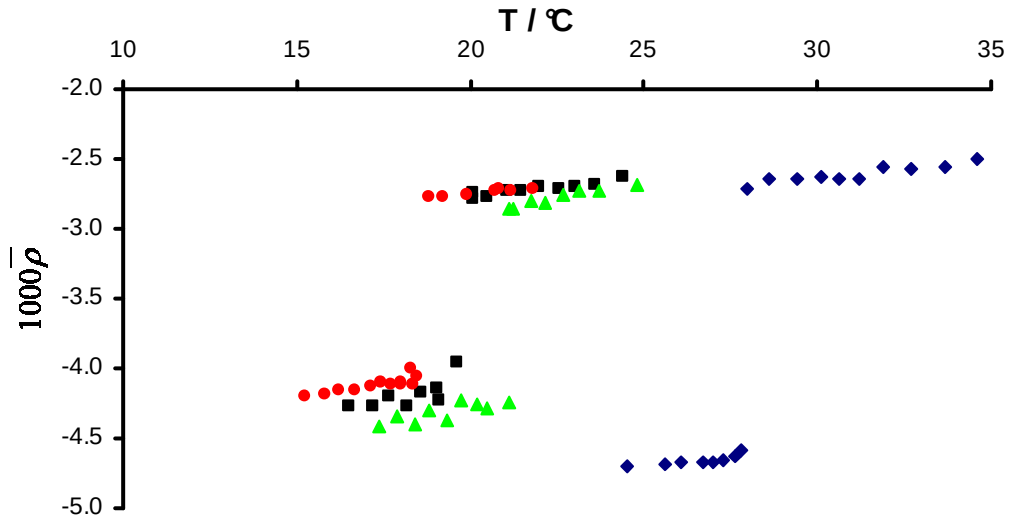

Figure 3.4 Coefficient of ellipticity as a function of temperature for mixed monolayers at the surface of a 0.1 mM $C_{16}E_8$ solution in the presence of tetradecane (circles), pentadecane (squares), hexadecane(triangles) and octadecane (diamonds).

Figure 3.5 shows the variation in coefficient of ellipticity about surface freezing transitions in ternary mixed monolayers at the air-water interface of 0.6 mM C_{16}TAB solutions with added tetradecane/hexadecane and hexadecane/octadecane. In the case of the binary mixed monolayers, tetradecane and hexadecane form type I frozen layers whilst octadecane forms a type II frozen layer. Similar behaviour was observed in the ternary mixed monolayers containing alkane mixtures, with type I behaviour observed for the type I/type I tetradecane/hexadecane mixture and type II freezing with the type I/type II hexadecane/octadecane mixture.

The transition temperatures of the ternary tetradecane/hexadecane mixed monolayers were found to vary linearly with bulk alkane composition, with excellent agreement between the measured transition temperature and a weighted average of the transition temperatures of the corresponding binary mixed monolayers (see table 3.1, section 3.3.5). The behaviour of the tetradecane/hexadecane mixture at the air-solution interface is therefore directly analogous to the behaviour of small chain length difference alkane mixtures at the air-alkane interface, with regular solution behaviour in the monolayer. The existence of a single transition temperature in all systems studied supports this conclusion.

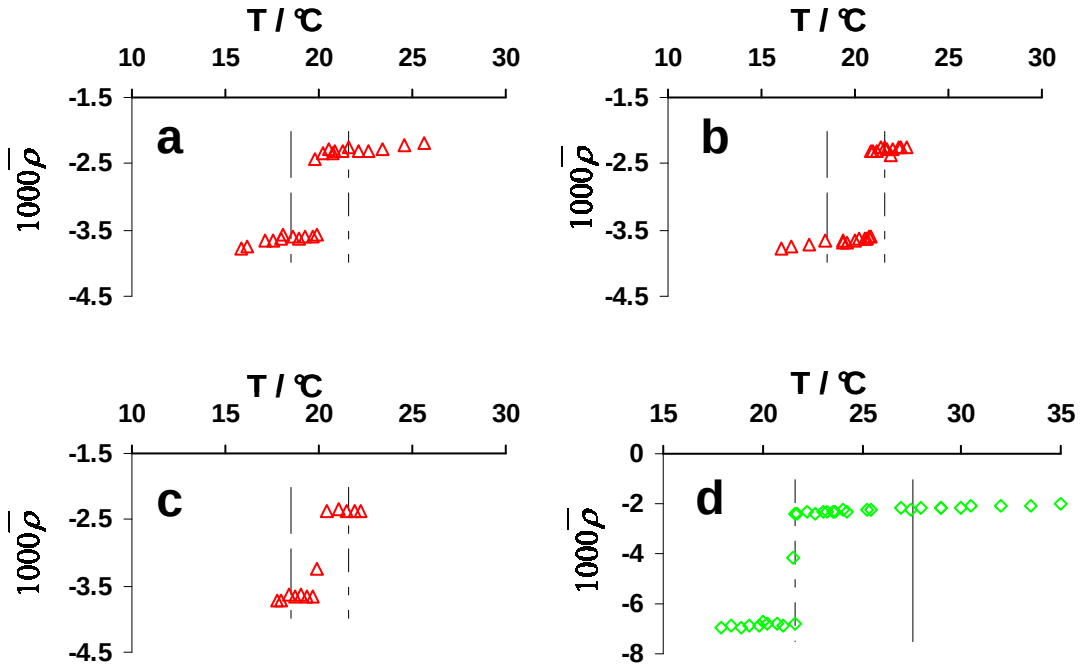

Figure 3.5 Coefficient of ellipticity as a function of temperature for mixed monolayers at the surface of a 0.6 mM C_{16}TAB solution in the presence of tetradecane:hexadecane (triangles; a 1:1, b 1:3, c 3:1) and hexadecane:octadecane (diamonds; d 1:1) binary alkane mixtures. All ratios are molecule:molecule. Long dashes, long/short dashes and continuous lines show T_s of mixed C_nTAB/pure tetradecane, hexadecane and octadecane monolayers, respectively.

The transition in the ternary hexadecane/octadecane mixed monolayer occurred at 21.7 °C. The close agreement with T_s of the binary C_{16}TAB/hexadecane monolayer is likely to be purely coincidental. Both hexadecane and octadecane surface freeze at the air-alkane interface, and so their mixtures would also be expected to surface freeze at an intermediate temperature determined by the bulk composition, with the mixture behaving ideally. In the case of a 1:1 mixture surface freezing would be expected to occur at approximately 22 °C, in excellent agreement with the observed monolayer transition temperature. This finding is entirely consistent with previously observed type II transitions in the presence of surface freezing alkane, where the monolayer transition occurs just below the neat alkane surface freezing temperature.

3.3.2 Non-Surface Freezing Systems

Surface freezing behaviour was not observed in mixed monolayers containing the zwitterionic surfactants C_{14}DAPS or C_{16}DAPS with the alkanes tridecane, tetradecane, pentadecane, hexadecane, octadecane and nonadecane. Mixed

monolayer formation was confirmed by a small, repeatable decrease in coefficient of ellipticity upon addition of alkane which indicated pseudo-partial wetting. In all cases the temperature was reduced until the added alkane lens froze, and the fact that there were no transitions at higher temperatures was evident from the original ellipticities of the bare air-solution interface. Example experiments with C_{16}DAPS/tetradecane and C_{16}DAPS/tridecane mixed monolayers are shown in figure 3.6. There is a slight discontinuity in the ellipticity of the C_{16}DAPS/tetradecane system at 12.3 °C, however no similar discontinuities were observed in any other C_nDAPS/*n*-alkane combination and so the effect in this case could have been caused by a slight drift in calibration of the ellipsometer over the extended measurement time required for the experiment. In addition, the "solid phase" ellipticity of -3×10^{-3} is rather small compared to similar transitions in C_{16}TAB monolayers (a typical liquid phase ellipticity is -2×10^{-3}, similar to that observed in C_nDAPS systems, with a drop to around -3.8×10^{-3} in the solid phase). This anomaly will be considered further in section 3.3.5 along with other modelled solid phase thicknesses.

Also included in figure 3.6 is the variation in coefficient of ellipticity of a C_{14}mal/hexadecane mixed monolayer. Again, mixed monolayer formation is confirmed by a decrease in coefficient of ellipticity upon addition of hexadecane, and no phase transition was observed over a temperature range which included the bulk alkane freezing temperature. Similar results were obtained for mixed monolayers of C_{14}mal with tetradecane, heptadecane and nonadecane.

No surface freezing was observed in ternary C_{16}TAB/pentadecane/octadecane or C_{16}TAB/tetradecane/octadecane mixed monolayers. Mixed monolayers were prepared both by adding a lens of premixed alkane to the surface and by adding successive drops of each alkane to the surface. The same result was obtained in all cases, irrespective of premixing or the order of addition of the alkanes. A range of bulk compositions were tested, between a 5:1 excess and a 1:5 deficiency of octadecane, with no phase transitions found.

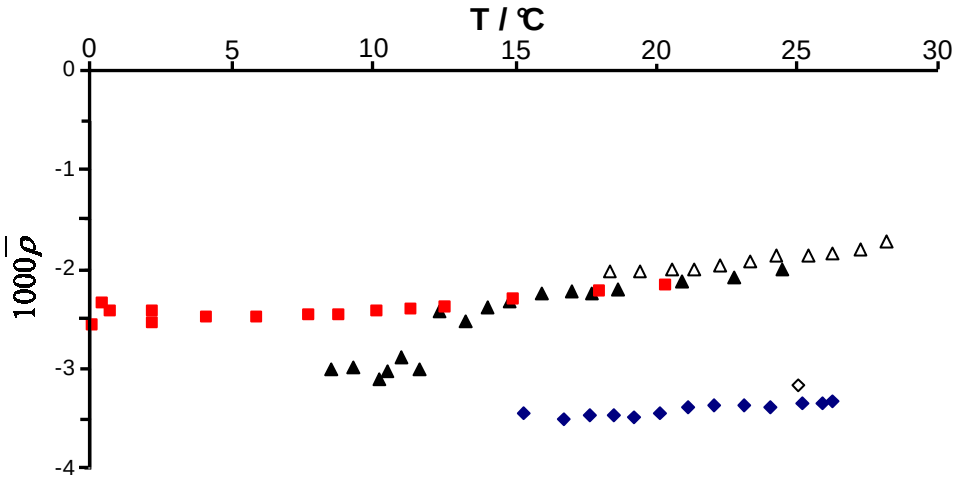

Figure 3.6 Coeeficient of ellipticity as a function of temperature for mixed monolayers of 0.006 mM C_{16}DAPS with tetradecane and tridecane (filled triangles and squares, respectively) and 0.1 mM C_{14}MAL with hexadecane (filled diamonds). Open symbols show the ellipticity of the air-solution interface in the absence of alkane.

Mixed monolayers of $C_{16}E_6$, $C_{14}E_5$, Tween 80 and Triton X-100 with a range of alkanes, in addition to $C_{16}E_8$ with eicosane, all showed anomalous behaviour. As the temperature was lowered after initial mixed monolayer formation a transition to a non-uniform thick interfacial layer occurred, reversibly, at an alkane-dependent temperature. The non-uniformity of the layer was confirmed by the lack of a stable ellipticity in all cases, and in a few cases by the appearance of a faint rainbow interference pattern on the surface. The thick layer formed at low temperatures still appeared to correspond to a pseudo-partial wetting state, as the interference colour could be seen to emanate from the position of the oil lens. The contact angle of the lens dropped to almost zero, however, and the shape of the lens became very irregular. These anomalous effects will be discussed later.

3.3.3 Origin of the *Absence* of Surface Freezing

Surface freezing in mixed monolayers of C_{16}TAB and *n*-alkanes is thought to occur as a result of the increased surface density of chains created by a wetting transition into the pseudo-partial wetting regime. The presence of surfactant chains then induces a surface freezing transition in the *n*-alkane wetting layer, forming a type I frozen monolayer. Type II bilayers are formed in instances where an alkane-like surface is created but the difference in chain length between surfactant tails and alkane chains would lead to excessive surface roughness in a frozen monolayer.

From these descriptions it might be thought that, in the absence of kinked or branched chains, the only prerequisite for a freezing transition of any type would be the initial mixed monolayer formation, with the only limiting factor being bulk freezing of the aqueous subphase (i.e. placing a lower limit on the length of alkane that can be made to surface freeze). Type II transitions would be expected to occur when a surface frozen alkane comes into contact with a mixed monolayer.

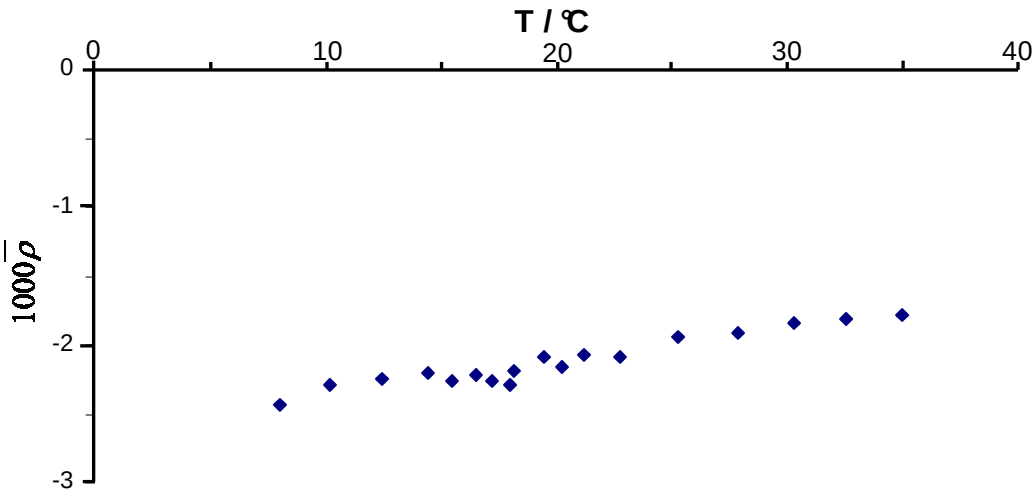

Figure 3.7 Coefficient of ellipticity as a function of temperature for mixed monolayers of C_{16}TAB with a 1:1 pentadecane:octadecane mixture.

These expectations are incorrect, however. No type II freezing is observed for mixed monolayers containing the surfactants C_{14}DAPS, C_{16}DAPS or C_{14}mal, nor for mixed C_{16}TAB/hexadecane and C_{16}TAB/pentadecane monolayers upon the addition of octadecane (or when the alkanes are added in the opposite order). The lack of type II freezing in these latter two cases is easily understood, as sufficient end-chain mismatch is required in the liquid phase to provide the correct alkane-like environment at the air-chain interface. Bulk mixtures of pentadecane and octadecane would be expected to surface freeze at the air-alkane interface, as it has been shown that shorter, non-surface freezing, alkanes can be induced to freeze in the presence of a longer chain to stabilise the structure. In the case of a mixed monolayer at the air-water interface, however, type II formation is disfavoured as a result of the entropic penalty of demixing at the surface. Type I freezing is prevented by the presence of octadecane in the monolayer, due to excess surface roughness.

In previously reported cases, it has been shown that there is no change in surface excess during a surface freezing transition, although this may not generally be the case. The ability to induce a type I transition is therefore dependent upon the capacity for additional oil uptake into the mixed monolayer. In the case of 0.6 mM C_{16}TAB/*n*-alkane systems, the area per molecule of surfactant is approximately 49 $Å^2$, compared to an area of 44 $Å^2$ at the CMC.[26] C_{14}DAPS, C_{16}DAPS and C_{14}mal were all used at concentrations above the CMC, with areas per molecule of 52.4 $Å^2$,[27] 45.5 $Å^2$,[27] and ~46 $Å^2$ (estimated from the values for C_{10}mal and C_{12}mal, and the relative insensitivity of molecular area of $C_n$mal to tailgroup length), respectively. Since all these surface excess values are similar to that of C_{16}TAB, the area per chain of surfactant at the interface is not an important factor determining the presence of surface freezing. This assertion is consistent with the observation of direct gas-solid phase transitions by Aratono *et al.*.[1] The surface excess of surfactant does have an effect on the transition temperature, however, as demonstrated by Lei *et al.*,[13] who reported freezing transitions at the tetradecane/C_{16}TAB solution interface with mole fractions of as little as 0.1. The transition temperature was found to vary linearly with surface excess, ranging from approximately 8 – 11 °C over the concentration range studied.

Thomas *et al.* have used neutron reflectivity to measure the position of dodecane chains in mixed monolayers with SDS, C_{12}TAB and $C_{12}E_5$.[28] The difference between the centres of the dodecane and surfactant tail distributions was 6 Å in C_{12}TAB monolayers, and 3 Å with SDS and $C_{12}E_5$, showing that the dodecane was further from the interface when mixed with C_{12}TAB. The presence of dodecane in C_{16}TAB monolayers was found to affect the tilt of the outer 6 carbons in the surfactant chain, but not those closer to the interface, showing a similar alkane distribution. Thomas *et al.* postulated that the alkane resides in the monolayer so as to achieve the most oil-like environment possible, and hence is intricately linked to the ability of the headgroup to shield the alkane from interfacial water molecules. The less densely packed the initial surfactant monolayer, the greater the free energy gain of alkane incorporation in the monolayer. The closer the alkane can approach the headgroup (i.e. the less repulsive the interaction with the monolayer/water interface) the greater the van der Waals enthalpic stabilisation through overlap with additional CH_2 units.

The absence of surface freezing in monolayers containing C_nDAPS and C_{14}mal must therefore result from either a low affinity for alkane incorporation or unfavourable interactions preventing them forming part of a close packed structure. In the case of C_{14}mal, the monolayers have been shown to include more interfacial water in the headgroup region than C_nE_m surfactants with the same tail structure.[29] This is attributed to the rigidity of the maltoside headgroup in comparison with the ethylene oxide headgroup. An increased water content at the monolayer/solution interface will result in a more polar, less alkane-like environment in the monolayer and thus alkane adsorption will be less favourable. VSFS experiments have also shown $C_n$mal surfactants to possess a high degree of order at the air/water interface when compared with other surfactants of similar tailgroup structure.[30] Type II freezing may therefore be disfavoured in these systems by the absence of a fluid-like environment at the interface over which surface frozen alkane can wet.

The C_nDAPS headgroup contains two charged species. In addition to providing an extremely polar environment at the monolayer-water interface, thus preventing close approach of alkane, an additional energy penalty will be incurred as a result of the inclusion of these charges in an organised lattice. Unlike C_{16}TAB solutions there are no counterions present to shield some of the electrostatic repulsion between headgroups and so this penalty becomes more severe.

3.3.4 Modelling the Solid Layer Thickness

In order to assign type I or type II behaviour to the phase transitions reported in section 3.3.1, an estimate of the solid layer thickness is necessary. Type I monolayers should give thicknesses similar to those found in C_{16}TAB/*n*-alkane mixed monolayers with alkanes between undecane and heptadecane, whereas type II monolayers will have thicknesses comparable to monolayers containing octadecane – eicosane.

The coefficient of ellipticity can be expressed as the summation of individual contributions from surface roughness, *r*, surfactant headgoups, *h*, any counterions present, *i*, and a mixed layer of surfactant and alkane chains, *c*, according to eqn. 3.3.

$$\bar{\rho}_{\exp} = \bar{\rho}_r + \bar{\rho}_h + \bar{\rho}_i + \bar{\rho}_c \tag{3.3}$$

Models for each of these individual contributions were introduced in section 2.4.1. In summary the roughness contribution scales as $\sqrt{T/\gamma}$, the headgroup and counterion contributions can be estimated using an effective medium approximation based upon an assumed structure (or rather distribution) of the headgroup layer and the debye length of the solution, respectively, and the chain contributions can be calculated using the Drude equation (eqn 3.4), modified to take into account anisotropy in the case of the solid phase (eqn. 3.5).

$$\bar{\rho}_{c,liq.} = \frac{\pi\sqrt{\varepsilon_a + \varepsilon_w}}{\lambda(\varepsilon_a - \varepsilon_w)}\left[\frac{(\varepsilon_c - \varepsilon_a)(\varepsilon_c - \varepsilon_w)}{\varepsilon_c}\right] d_{c,liq.} \tag{3.4}$$

$$\bar{\rho}_{c,sol.} = \frac{\pi\sqrt{\varepsilon_a + \varepsilon_w}}{\lambda(\varepsilon_a - \varepsilon_w)}\left[\frac{(\varepsilon_e - \varepsilon_a)(\varepsilon_e - \varepsilon_w)}{\varepsilon_e} + (\varepsilon_o - \varepsilon_e)\right] d_{c,sol.} \tag{3.5}$$

Here λ is the wavelength of the ellipsometer laser, ε_a, ε_w, ε_c, ε_e and ε_o are the dielectric constants of air, water, liquid mixed chains and the extraordinary and ordinary dielectric constants of the uniaxially anisotropic solid layer, respectively. The layer thicknesses are given by d_x.

lyso-OPC and *lyso*-PPC

At the transition temperature the roughness contribution of both the solid and liquid phases is the same, since the surface tensions must be equal. It has been shown that surface freezing of mixed monolayers is not accompanied by a large change in surface excess of surfactant,[1, 13] and therefore the counterion contribution in the case of ionic surfactants can be replaced by a constant in both phases. The headgroup structure of C_{16}TAB/*n*-alkane and $C_{16}E_8$/*n*-alkane mixed monolyers is also thought to be unchanged upon surface freezing, as shown by X-ray reflectivity[11, 31] and sum-frequency spectroscopy (see chapter 5). Therefore, it is reasonable to assume that only the chain contribution changes during the freezing transition.

In the case of *lyso*-OPC and *lyso*-PPC solid layer thickness can then be estimated from the difference in ellipticity between the solid and liquid phases without the need to model individual headgroup contributions for each surfactant used, which would involve the estimation of surface tensions and surface excesses from existing often contradictory data. The solid layer thickness is then given by

$$d_{c,sol.} = \left\{ \Delta\overline{\rho}_{\exp} \frac{\lambda(\varepsilon_a - \varepsilon_w)}{\pi\sqrt{\varepsilon_a + \varepsilon_w}} + \left[\frac{(\varepsilon_c - \varepsilon_a)(\varepsilon_c - \varepsilon_w)}{\varepsilon_c} \right] d_{c,liq.} \right\} / \left[\frac{(\varepsilon_e - \varepsilon_a)(\varepsilon_e - \varepsilon_w)}{\varepsilon_e} + (\varepsilon_o - \varepsilon_e) \right] \tag{3.6}$$

The dielectric constant of the liquid chains was estimated as that of a 1:1 mixture of alkanes corresponding to the surfactant tail length and alkane used. The anisotropic dielectric constants of the solid layer were derived from those of a behenic acid monolayer at a molecular area of 19.3 $Å^2$.[32] X-ray reflectivity has shown that the area per chain in a surface frozen mixed monolayer is 19.8 $Å^2$, and so corrected values of $\varepsilon_e = 2.32$ and $\varepsilon_o = 2.16$ were used. Both these assumptions have been shown to give good estimates of both liquid and solid layer thicknesses previously, with results verified by reflectivity studies.[9, 11] Only a single additional parameter need then be estimated in the present case, the thickness of the liquid layer.

Previous ellipsometry studies have suggested that, for a given surfactant, the liquid layer thickness is relatively insensitive to alkane chain length.[7, 9, 10] For C_{16}TAB with alkanes between undecane and eicosane the layer thickness was found to vary from 12 Å in the presence of short alkanes to about 9 Å in the presence of the longer alkanes. X-ray reflectivity studies on the same systems suggested a constant layer thickness of 11 Å, independent of *n*-alkane length. In both cases the liquid layer thickness was found to be limited by the surfactant used, with a modelled thickness of just over half the corresponding length of a fully extended surfactant tail.

The estimated liquid layer thicknesses used in the present models were based on available reflectivity and AFM data in the literature. This gave a liquid layer thickness of 13 Å for *lyso*-PPC monolayer and an estimated 14.5 Å for a *lyso*-OPC monolayer.[33] The estimate for *lyso*-OPC is taken from measurements on DOPC

bilayers, and a thicker liquid layer seems to be justified by the more negative ellipticities observed in *lyso*-OPC mixed monolayers (figures 3.2 and 3.3).

C_{16}TAB/*n*-alkane Mixtures

The layer thicknesses of the mixed monolayers containing *n*-alkane mixtures were calculated exactly as described in section 2.4.1. The Lorentz-Lorenz effective medium approximation was used to estimate the dielectric constant of the alkane mixtures based on the bulk composition. This value was then used to estimate the dielectric constant of the liquid phase mixed monolayer, assuming both components of the alkane mixture adsorbed equally to the interface.

$C_{16}E_8$/*n*-alkane

All transitions observed with $C_{16}E_8$ as surfactant exhibited type I behaviour. The headgroup contribution to the coefficient of ellipticity can be estimated using the variation in refractive index with concentration per ethylene oxide unit ($dn/dc = 0.135\,\mathrm{cm^{-3}\ g^{-1}}$) and the limiting surface excess ($3.2\times10^{-6}\,\mu\mathrm{mol\ m^{-2}}$)[34]. For the headgroup layer, the Drude equation can be written

$$\overline{\rho}_h = \frac{\pi}{\lambda}\frac{\sqrt{\varepsilon_a+\varepsilon_w}}{\varepsilon_a-\varepsilon_w}\frac{(\varepsilon_h-\varepsilon_a)(\varepsilon_h-\varepsilon_w)}{\varepsilon_h}d_h \qquad (3.7)$$

where ε_h is the dielectric constant of the headgroup layer of thickness d_h, which can be calculated using eqn 3.8.

$$\varepsilon = n^2 = \left(n_0 + c\frac{dn}{dc}\right)^2 \qquad (3.8)$$

Here n_0 is the refractive index of water, which can be estimated at the relevant temperature using eqn. 3.9. The concentration, *c*, can be estimated using the known surface excess concentration and assuming a headgroup layer thickness of 14 Å.[28] The modelled coefficient of ellipticity is actually relatively insensitive to the precise value of thickness chosen.

$$\varepsilon_{H_2O}(T) = 3.715\times10^{-8}(T/^{\circ}C)^3 - 7.803\times10^{-6}(T/^{\circ}C)^2 + 4.996\times10^{-5}(T/^{\circ}C) + 1.776 \quad (3.9)$$

The chain contribution to both the liquid and solid phases can then be calculated from the experimental coefficient of ellipticity by subtraction of the headgroup contribution and a roughness contribution (taken as the coefficient of ellipticity minus the headgroup contribution in the absence of oil, assuming a liquid phase thickness of 10 Å similar to that of C_{16}TAB/alkane mixed monolayers). The solid layer thicknesses can then be calculated from eqns. 3.4 and 3.5 in the same way as C_nTAB/C_m mixed monolayers in chapter 2.

3.3.5 Modelled Solid Thicknesses and Transition Types

Table 3.1 summarises the transition temperatures, T_s, and solid layer thicknesses calculated according to eqn. 3.6 for all the surface freezing systems detailed in the present chapter. The corresponding transitions with C_{16}TAB as surfactant are provided for comparison.

A possible transition was identified in C_{16}DAPS/tetradecane monolayers in figure 3.6. The "solid" phase thickness according to eqn. 3.6 is only 14.9 Å. Even accounting for a gross error in the estimated thickness of the liquid monolayer, there would only be a ~ 4 Å change in thickness between the high- and low-temperature phases, compared to an increase in thickness of over 8 Å in the corresponding C_{16}TAB/tetradecane system. It therefore seems likely that the change in ellipticity is either due to a change in chain tilt or fluctuations in the original measurement.

There are two distinct magnitudes of solid phase ellipticity for *lyso*-PPC/alkane mixed monolayers, highly suggestive of the presence of both type I and type II freezing. The modelled thickness of the monolayers containing tetradecane and nonadecane are slightly greater than in the same monolayers with C_{16}TAB. Although the alkyl tail lengths are the same in both surfactants, *lyso*-PPC contains an additional glycerol unit above the phosphocholine headgroup. *Lyso*-PPC therefore has the potential for a greater extended length than C_{16}TAB, and LC monolayers of DPPC are approximately 2.5 Å thicker than the fully extended length of a C_{16} alkyl chain. It should be noted that the modelled solid phase thicknesses are dependent

upon the initial choice of liquid layer thickness, which makes assumptions about the headgroup contribution to the ellipticity. It is reasonable to assume that the headgroup contribution is constant, since phosphatidylcholine headgroup structure and hydration have been shown to be invariant over a range of molecular areas, tail lengths and subsurface pH and salinity.[33]

The thickness of the type II frozen layer formed by *lyso*-PPC/octacosane is approximately equal to the sum of the extended lengths of an octacosane chain and a C_{16} alkyl chain. Assuming that the lower layer of the type II frozen phase remains unchanged, $\Delta\overline{\rho}$ yields the upper layer contribution directly, which can be modelled according to eqn. 3.5. The modelled upper layer thickness is then 34.5 Å, compared to a fully extended octacosane chain length of 36.5 Å, confirming the type II structure of the solid phase.

Lyso-OPC was chosen as a test surfactant because, containing a *cis* double bond, it is incapable of forming part of a solid monolayer. Therefore, only type II transitions should be possible with this surfactant, and this is indeed what is observed. Unusually, as was the case with C_{12}TAB and C_{14}TAB, a type II monolayer is formed with the non-surface freezing pentadecane. In this instance, the freezing transition occurs over 8.5 °C above the bulk melting point of pentadecane, a truly remarkable result as the range of surface freezing at the neat air-alkane interface is less than 3 °C, and all other type II mixed monolayer transitions reported to date have a surface freezing range of less than 1 °C (in the majority of cases occurring below the bulk alkane melting point). The observation of this novel type II transition reinforces the data of chapter 2, where it was discovered that the presence of surface frozen alkane is not required for type II solid phase formation.

Given the findings of Thomas *et al.* showing that alkanes penetrate more deeply into C_nE_m monolayers than C_nTAB monolayers, resulting in a thicker mixed monolayer, it is not surprising that $C_{16}E_8$ forms type I monolayers accommodating longer alkanes than is possible with C_{16}TAB. The transition temperatures are very similar to those with C_{16}TAB, as would also be expected from the similarity in tailgroup length. The thicker solid layer formed could be a reflection of the possibility for the ethylene oxide units closest to the tailgroup to form part of the extended solid layer, or could

simply give an indication that the frozen layer formed is more ordered, with more upright chains and fewer *gauche* defects. These observations are explored further using VSFS in chapter 5.

As would be expected, the thicknesses of the ternary C_{16}TAB/alkane mixture monolayers agree almost exactly with those of the individual alkane components for both type I and type II solid layers.

Table 3.1 *Comparison of transition temeratures, T_s, and modelled solid layer thicknesses, d_s, between phase transitions reported in this chapter with C_{16}TAB/C_n mixed monolayers reported previously.*[9]

Surfactant	C_n	T_s / °C	T_{CTAB} / °C	d_s / Å	d_{CTAB} / Å
***lyso*-PPC**	14	18.2	18.5	22.2	20.7
	19	32.8	32.8	24.1	40.4
	28	62.1		53.8	
***lyso*-OPC**	15	16.2	19.5	36.4	20.5
	19	33.4	32.8	40.2	40.4
$C_{16}E_8$	14	19.2	18.5	24.8	20.7
	15	20.0	19.5	24.7	20.5
	16	21.0	21.6	24.8	20.6
	18	27.9	27.6	24.2	38.5
C_{16}TAB	1:1 C_{14}:C_{16}	20.2	18.5 : 21.6	20.5	20.7 : 20.6
	3:1 C_{14}:C_{16}	19.0	18.5 : 21.6	20.6	20.7 : 20.6
	1:3 C_{14}:C_{16}	21.0	18.5 : 21.6	20.5	20.7 : 20.6
	1:1 C_{16}:C_{18}	22.0	21.6:27.6	40.0	20.6:38.5

3.4 Anomalous Behaviour of Non-ionic Surfactants

Mixed monolayers of the nonionic surfactants $C_{16}E_6$, $C_{14}E_5$, Tween 80 and Triton X-100 with the range of *n*-alkanes studied did not undergo first order freezing transitions. The coefficient of ellipticity did not vary linearly as in figures 3.6 and

3.7, however. Below a critical temperature, the monolayers exhibited the fully reversible formation of a thick layer at the interface in equilibrium with a low contact angle, distorted alkane lens. The same behaviour was observed in mixed monolayers of $C_{16}E_8$ and eicosane. The low temperature films formed were not of uniform thickness as evidenced by the appearance of a rainbow of interference colours at the interface in most cases. In addition, the measured ellipticity values became extremely unstable, making it impossible to record meaningful data. An example of a layer formed is given in figure 3.8, which shows pictures of a $C_{16}E_8$/eicosane mixed monolayer below and above the critical temperature of ~37 °C. The critical temperatures in all the systems studied lie between 21 and 37 °C.

It should be noted that the ellipticities measured in the presence of the thick films did not correspond to the coefficient of ellipticity. As was explained in section 2.2, the coefficient of ellipticity refers to the imaginary part of the ratio r_p / r_s at the Brewster angle. The Brewster angle is determined practically by ensuring that the real part of this ratio is zero. In the case of the anomalous low temperature monolayer behaviour in non-ionic surfactant/alkane mixtures the real signal at the Brewster angle of an air-water interface changed dramatically, indicating that the laser no longer impinged upon an air-water interface. It was not possible to measure the Brewster angle of the new low temperature surface due to the instability in both the real and imaginary parts of r_p / r_s caused by the highly non-uniform film thickness.

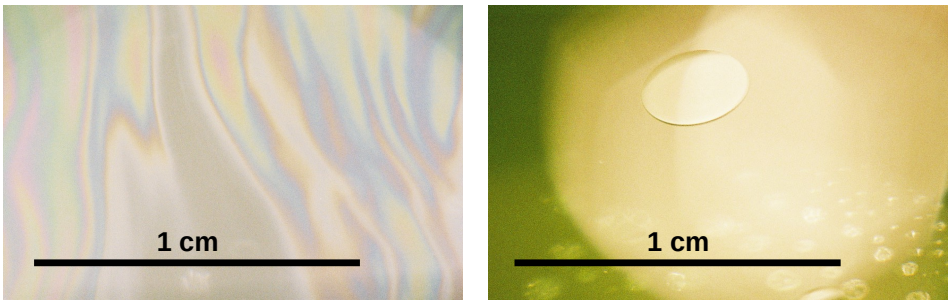

Figure 3.8 Photographs of the low (left) and high (right) temperature surfaces of a $C_{16}E_8/C_{20}$ system. Reflection in the high temperature picture is caused by the grazing angle needed to visualise the oil lens.

The low temperature surface layer appeared to have a high viscosity, particularly with $C_{16}E_6$/alkane systems where an almost opaque layer formed at the interface.

Agitation of this layer caused the reformation of individual oil lenses which then spread to reform the viscous layer.

The non-uniformity of the surface film, its viscous nature and the marked change in Brewster angle of the interface are suggestive of a reversible temperature induced wetting transition resulting in the formation of a new interface. If the layer were simply a thick wetting layer of alkane, the film would be expected to be of uniform thickness or at least to have an easily measurable, relatively fluctuation free Brewster angle. Transitions to a thicker wetting film are generally observed upon heating rather than cooling, as with short chain alkanes on brine.[35-37] That the transition observed here occurs on cooling makes it doubly unusual.

Binary mixtures of C_nE_m and water, and ternary C_nE_m/oil/water systems are known to have a rich wetting behaviour.[38] In the ternary systems, within certain composition ranges, a middle surfactant-rich phase undergoes a transition from nonwetting to complete wetting behaviour as one of two critical temperatures are approached. The appearance of this middle surfactant rich phase occurs along with oil and water continuous phases within a certain temperature range and is known as a Winsor III three phase equilibrium. For typical non-ionic surfactants the temperature range of the Winsor III zone is 20 – 35 °C,[39] which coincides with the temperature of thick layer formation observed here (although the precise temperature range varies greatly dependent upon surfactant tailgroup length). It is unlikely that Winsor III formation occurs in the surfactant/alkane/water systems in this chapter, however, as the surfactant concentrations (approximately 0.1 mM) used were far too low; typically at least 1 wt% of surfactant is needed to form a Winsor III system. The local composition at the interface will be quite different to that in the bulk, however, with a much higher surfactant concentration in the subphase. It is feasible, therefore, that the system composition close to the interface could lie within the composition range for formation of a surfactant-rich middle phase.

3.5 Conclusions

The results presented in the present chapter have shown that, although mixed monolayer formation is a ubiquitous phenomenon, surface freezing of the mixed

monolayers is neither a universal nor a general phenomenon. In cases where surface freezing does occur, the solid structures formed can be rationalised in terms of either type I or type II freezing as identified from phase transitions in C_nTAB/*n*-alkane mixed monolayers.

No evidence of phase transitions was found for the zwitterionic surfactants C_nDAPS or the sugar-based surfactant C_{14}mal. In both cases, the absence of surface freezing could be explained by unfavourable interactions between the alkane chain and surfactant headgroups, resulting in a lower uptake of alkane into the mixed monolayer and the alkane most likely residing further from the interface, reducing the enthalpic stabilisation afforded by chain overlap. The absence of phase transitions in mixed monolayers containing mixtures of surface freezing and non-surface freezing alkanes was attributed to the combined prevention of type I layer formation by the presence of long chains and the lack of sufficient end chain mismatch provided by the inclusion of short chain alkanes in the mixed monolayer.

New thin-thick transitions were reported in non-ionic surfactant/alkane/water systems which could be related to phase inversion and the formation of Winsor III three phase equilibria. The wetting phase was shown to be neither aqueous nor alkane-like in nature, lending support to the spreading of a third surfactant rich phase. Further experimentation would be required to fully understand the nature of these transitions, employing spectroscopic techniques to elucidate the composition of the wetting film and reflectivity to determine film thickness.

3.6 References

1. Matsubara, H.; Ohtomi, E.; Aratono, M.; Bain, C. D., *Journal of Physical Chemistry B* **2008,** 112, 11664.
2. Matsubara, H.; Ikeda, N.; Takiue, T.; Aratono, M.; Bain, C. D., *Langmuir* **2003,** 19, 2249.
3. Takata, Y.; Matsubara, H.; Kikuchi, Y.; Ikeda, N.; Matsuda, T.; Takiue, T.; Aratono, M., *Langmuir* **2005,** 21, 8594.
4. Aveyard, R.; Binks, B. P.; Fletcher, P. D. I.; MacNab, J. R., *Langmuir* **1995,** 11, 2515.

5. Binks, B. P.; Crichton, D.; Fletcher, P. D. I.; MacNab, J. R.; Li, Z. X.; Thomas, R. K.; Penfold, J., *Colloids and Surfaces A: Physiochemical and Engineering Aspects* **1999,** 146, 299.
6. Aratono, M.; Kawagoe, H.; Toyomasu, T.; Ikeda, N.; Takiue, T.; Matsubara, H., *Langmuir* **2001,** 17, 7344.
7. Wilkinson, K. M.; Bain, C. D.; Matsubara, H.; Aratono, M., *ChemPhysChem* **2005,** 6, 547.
8. Lu, J. R.; Li, Z. X.; Thomas, R. K.; Binks, B. P.; Crichton, D.; Fletcher, P. D. I., *Journal of Physical Chemistry B* **1998,** 102, 5785.
9. Wilkinson, K. M.; Lei, Q.; Bain, C. D., *Soft Matter* **2006,** 2, 66-76.
10. Wilkinson, K. M. Phase Transitions in Monolayers of Soluble Surfactants. University of Oxford, 2004.
11. Sloutskin, E.; Sapir, Z.; Lei, Q.; Wilkinson, K. M.; Tamam, L.; Deutsch, M.; Ocko, B. M., *Physical Review Letters* **2007,** 99, 136102.
12. Mckenna, C. E.; Knock, M. M.; Bain, C. D., *Langmuir* **2000,** 16, 5853.
13. Lei, Q.; Bain, C. D., *Physical Review Letters* **2004,** 92, 176103.
14. Sloutskin, E.; Bain, C. D.; Ocko, B. M.; Deutsch, M., *Faraday Discussions* **2005,** 129, 1.
15. Casson, B. D.; Bain, C. D., *Journal of Physical Chemistry B* **1999,** 103, 4678.
16. Casson, B. D.; Bain, C. D., *Journal of Physical Chemistry B* **1998,** 102, 7434.
17. Lenne, P.-F.; Bonosi, F.; Renault, A.; Bellet-Amalric, E.; Legrand, J. F.; Petit, J.-M.; Rieutord, F.; Berge, B., *Langmuir* **2000,** 16, 2306.
18. Gilányi, T.; Mészáros, R.; Varga, I., *Langmuir* **2000**, (16), 3200.
19. Hossain, M. M.; Islam, M. N.; Okano, T.; Kato, T., *Colloids and Surfaces A: Physiochemical and Engineering Aspects* **2002,** 205, 249.
20. Islam, M. N.; Okano, T.; Kato, T., *Langmuir* **2002,** 18, 10068.
21. Wu, X. Z.; Ocko, B. M.; Tang, H.; Sirota, E. B.; Sinha, S. K.; Deutsch, M., *Physical Review Letters* **1995,** 75, 1332.
22. Sloutskin, E.; Wu, X. Z.; Peterson, T. B.; Gang, O.; Ocko, B. M.; Sirota, E. B.; Deutsch, M., *Phyical Review E* **2003,** 68, 031065/1.
23. Sloutskin, E.; Sirota, E. B.; Kraak, H.; Ocko, B. M.; Deutsch, M., *Physical Review E* **2001,** 64, 031708.
24. Ofer, E.; Sloutskin, E.; Tamam, L.; Ocko, B. M.; Deutsch, M., *Physical Review E* **2006,** 74, 021602.
25. Small, D. M., *The Physical Chemistry of Lipids: From Alkanes to Phospholipids*. Plenum Press: New York, 1986.
26. Manning-Benson, S.; Parker, S. R. W.; Bain, C. D.; Penfold, J., *Langmuir* **1998,** 14, 990.
27. Graciani, M. d. M.; Rodriguez, A.; Munoz, M.; Moya, M. L., *Langmuir* **2005,** 21, 7161.
28. Lu, J. R.; Li, Z. X.; Thomas, R. K.; Binks, B. P.; Crichton, D.; Fletcher, P. D. I.; McNab, J. R.; Penfold, J., *Journal of Physical Chemistry B* **1998,** 102, 5785-5793.
29. Tyrode, E. C.; Johnson, C. M.; Kumpulainen, A. J.; Rutland, M.; Claesson, P. M., *Journal of the American Chemical Society* **2005,** 127, 16848.
30. Kumpulainen, A. J.; Persson, M. P.; Erikson, J. C.; Tyrode, E. C.; Johnson, C. M., *Langmuir* **2005,** 1, 305.
31. Sloutskin, E.; Sapir, Z.; Tamam, L.; Ocko, B. M.; Bain, C. D.; Deutsch, M., *Thin Solid Films* **2007,** 515, 5664-5668.
32. Paudler, M.; Ruths, J.; Riegler, H., *Langmuir* **1992,** 8, 184.

33. Yaseen, M.; Lu, J. R.; Webster, J. R. P.; Penfold, J., *Langmuir* **2006,** 22, (5825).
34. Colegate, D. M. Kinetics in Micellar Surfactant Solutions. Durham University, 2009.
35. Bertrand, E.; Dobbs, H.; Broseta, D.; Indekeu, J. O.; Bonn, D.; Meunier, J., *Physical Review Letters* **2000,** 85, 1282.
36. Bonn, D.; Pauchard, L.; Shahidzadeh, N.; Meunier, J., *Physica* **1999,** 263, 78.
37. Ragil, K.; Meunier, J.; Broseta, D.; Indekeu, J. O.; Bonn, D., *Physical Review Letters* **1996,** 77, 1532-1535.
38. Rosen, M. J., *Surfactants and Interfacial Phenomena*. 3rd ed.; Wiley-Interscience: 2004.
39. Pizzino, A.; Molinier, V.; Catte, M.; Salager, J.-L.; Aubry, J.-M., *Journal of Physical Chemistry B* **2009,** 113, 16142.

Chapter 4

ER-FTIR Spectroscopy Study of Surface Freezing at the Air/Water Interface

4.1 Introduction

This chapter introduces the theory and practice of Fourier transform infrared (FTIR) spectroscopy with particular emphasis on the study of condensed matter systems, before showing how the technique can be applied to the study of interfacial regions. A brief literature review of FTIR spectroscopy of the air-water interface (termed external reflection FTIR spectroscopy in the current research) is presented in order to demonstrate its suitability as a tool for probing monolayer systems. Two-dimensional correlation analysis, a novel analytical method that provides insight into the molecular origins of small changes within a series of multi-component spectra, is discussed and applied to the study of surface freezing at the air-water interface.

4.2 IR Spectroscopy

4.2.1 The Electromagnetic Spectrum and IR Radiation

Although modern spectroscopy is heavily reliant upon quantum mechanical descriptions of both matter and radiation, its origins as an analytical tool lie deep within the classical physics world of Newton. In his *Opticks* of 1704, Newton described experiments he had undertaken to disperse and recombine white light using prisms and lenses (interestingly, he also remarks upon both the wave- and particle-like nature of light, although he favoured the so-called *corpuscular* theory). Newton's original experiments were later carried out with much greater wavelength resolution by Fraunhofer, who noted that the well known rainbow pattern was not perfectly continuous, but rather contained several discontinuities which manifested as black lines superimposed on top of the by now familiar pattern. These lines corresponded to the image of the slit at well-defined wavelengths, and at the time were lettered alphabetically from A to H. It was much later that Kirchoff proposed that this absence of light at certain wavelengths in the spectrum of the sun was due to the absorption of that light by specific chemical species present in the solar atmosphere. Furthermore, Kirchoff proceeded to identify the chemical species responsible for each of the Fraunhofer lines through a combination of the analysis of flame spectra of common elements and, one presumes, extreme patience. It is

through this remarkable endeavour that the twin absorptions at 589.76 nm and 589.16 nm came to be known as the Sodium D lines. In effect Newton, Fraunhofer and Kirchoff (amongst others) had carried out the simplest possible spectroscopic experiment by detecting the variation in intensity of a broadband light-source with frequency after it had passed through a sample medium (in their case space and air). They had also unwittingly collected perhaps the first experimental data to explicitly require the advent of quantum mechanics in order to be fully understood.

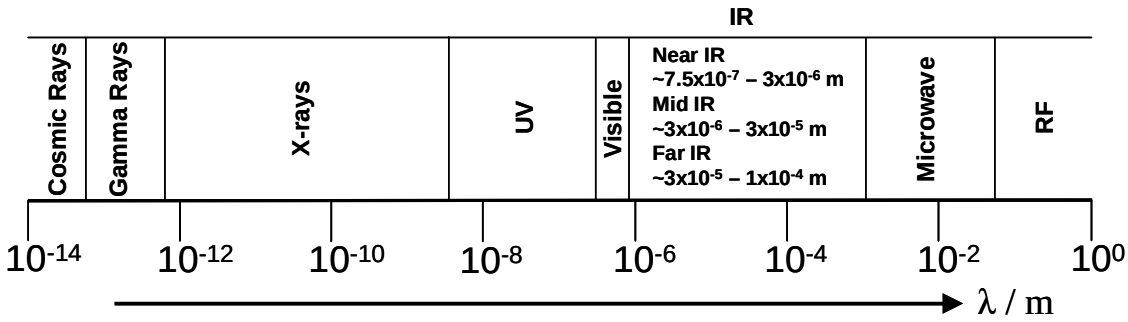

Figure 4.1 Classification of regions of the electromagnetic spectrum.

It has already been noted that the spectral lines observed by Fraunhofer are superimposed upon an otherwise continuous spectrum of radiation. Since light is now known to be a transverse waveform, consisting of oscillating electric and magnetic fields we call this the electromangnetic spectrum. Although the electromagnetic spectrum is a continuum of wavelengths, it is generally depicted as containing several distinct regions (figure 4.1). The classification of these regions is based upon the diverse physically observable effects brought about by different wavelengths of radiation. The energy, E (in J), of a given wavelength, λ (in m), of radiation is given by

$$E = \frac{hc}{\lambda} = h\upsilon = hc\tilde{\upsilon} \tag{4.1}$$

where h is Planck's constant, c is the speed of light and $\tilde{\upsilon}$ is the reciprocal wavelength (wavenumber) of the radiation (typically reported in cm^{-1}). In practice the conversion of a measured frequency or wavelength of absorption to a corresponding energy is not carried out, as historically these quantities can be measured with greater accuracy than either Planck's constant or the speed of light (although the value of the latter has since been precisely defined).

It is clear from figure 4.1 that visible light only accounts for a tiny portion of the electromagnetic spectrum. The existence of radiation with wavelengths outside the visible region was demonstrated by Herschel in 1800. Herschel dispersed white light to produce a spectrum and placed thermometers in the middle of each colour, as well as control thermometers in the dark regions beyond the red and violet. In addition to observing an increase in temperature going from violet to red, there was also a temperature increase in the thermometer placed beyond the red end of the spectrum. From this Herschel deduced that light must exist which is not visible to the human eye, whilst at the same time discovering infrared radiation. The infrared region (13300 – 10 cm^{-1}) spans the energy of vibrational transitions of molecules, with the mid-IR (4000 – 400 cm^{-1}) being of particular use as most group stretching vibrations (C=C, C=O, X-H etc.) fall within this range.

4.2.2 Vibrational Potential Wells and the Quantum Oscillator

The Simple Harmonic Oscillator

When a molecule vibrates, the periodic displacement of the atoms within that molecule leaves the centre of mass unchanged (within a laboratory reference frame, as displacement of the centre of mass is simply translation). We can therefore define a vibrational coordinate, *q*, that describes the vibrational motion of a molecule in terms of the displacement of each atom from its equilibrium position. For a diatomic molecule this can be expressed in terms of the instantaneous, *r*, and equilibrium, r_e, bond length (eqn. 4,2).

$$q = \Delta r = r - r_e \tag{4.2}$$

This vibrational coordinate can be used to describe the potential energy associated with any given vibrational motion, by solving the equation of motion for the electorns within the molecule with the positions of the nuclei fixed at various points along the vibrational coordinate (this takes advantage of the Born-Oppenheimer separation, which states that since elctronic motion is so much faster than nuclear motion the two can be treated independently). As such, the potential well of a vibration gives us the sum of the kinetic energy of the electrons and the electrostatic

energy of the nuclei at all points along the vibrational coordinate. In reality the nuclei do vibrate as well, but since this motion is much slower it remains well within the confines of the calculated potential well.

In the simplest case, the potential well can be approximated with a parabolic function of the vibrational coordinate, as in eqn. 4.3. This corresponds to the classical simple harmonic oscillator, since the restoring force is directly proportional to the vibrational coordinate and the force constant is independent of the position along the vibrational coordinate. These properties are demonstrated in eqns. 4.4 t o 4.5.

$$U_{vib} = \frac{1}{2}kq^2 \tag{4.3}$$

$$F_q = -\frac{dU_{vib}}{dq} = -kq \tag{4.4}$$

$$\frac{d^2U_{vib}}{dq^2} = k \tag{4.5}$$

The total energy of the harmonic oscillator includes a kinetic energy contribution (since the atoms within the molecule are necessarily in motion) and is given by

$$E_{vib,total} = \frac{p^2}{2\mu} + \frac{1}{2}kq^2 \tag{4.6}$$

where $p=mv$ is the instantaneous momentum of the molecule and μ is the reduced mass. The Schrödinger equation for the simple harmonic oscillator is then a second order ordinary differential equation (eqn. 4.7) that is readily solved by inserting a trial wavefunction of the form shown in eqn. 4.8 and solving for the prefactor *H(q)* (further details of this calculation can be found elsewhere[1, 2]).

$$-\frac{\hbar^2}{2\mu}\frac{\partial^2\psi_{vib}}{\partial q^2} + \frac{1}{2}kq^2\psi_{vib} = E_{vib}\psi_{vib} \tag{4.7}$$

$$\psi_{vib} = e^{-\frac{1}{2}(k\mu/\hbar^2)^{1/2}q^2}H(q) \tag{4.8}$$

Since the motion is constrained by the vibrational potential well, acceptable wavefunctions must vanish as the vibrational coordinate tends to infinity. This boundary condition leads to the quantization of the energy levels of the harmonic oscillator. The eigenvalues (energy leavels) of the harmonic oscillator are found to be evenly spaced, and are given by

$$E_{vib} = (\nu + 1/2)h\upsilon \tag{4.9}$$

where υ is the vibrational frequency, given by

$$\upsilon = \frac{1}{2\pi}\left(\frac{k}{\mu}\right)^{1/2} \tag{4.10}$$

and v is the vibrational quantum number

$$\nu = 0,1,2,3..... \tag{4.11}$$

The general form of the eigenfunctions of the simple harmonic oscillator has already been set out in eqn. 4.8. All that remains is to insert the precise form of the prefactor *H(q)*, and to add a normalisation constant to satisfy the Born interpretation of the wavefunction (i.e. that the probability of finding the molecule at any point along the vibrational coordinate is proportional to the square of the vibrational wavefunction at that point. Since the molecule must be somewhere, the normalisation constant, N_v, is required to set the integral $\left\langle \psi_{vib} \middle| \psi_{vib} \right\rangle = 1$). The resulting eigenfunctions are given by

$$\psi_{vib} = N_\nu H_\nu e^{-\frac{1}{2}(k\mu/\hbar^2)^{1/2}q^2} \tag{4.12}$$

where H_v is the Hermite polynomial of order v. The form of the first few eigenfunctions are shown in figure 4.2. An important property of the Hermite polynomials centres on the solutions of integrals of the form of eqn. 4.13, which shall be discussed later with reference to the infrared activity of any given molecular vibration.

$$\int_{-\infty}^{\infty} H_{\nu} H_{\nu'} e^{-x^2} dx = \begin{Bmatrix} 0 & \nu \neq \nu' \\ \pi^{1/2} 2^{\nu} \nu! & \nu = \nu' \end{Bmatrix} \tag{4.13}$$

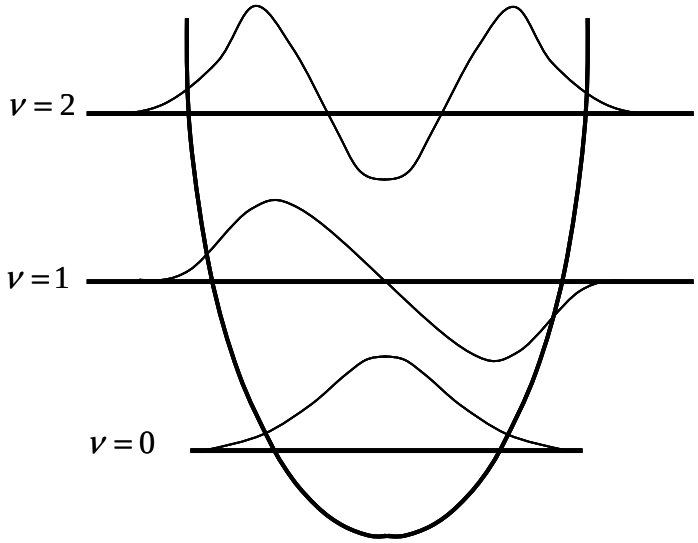

Figure 4.2 The form of the lowest three vibrational wavefunctions of the harmonic oscillator.

There are three main features that arise from the solution of the Schrödinger equation of the simple harmonic oscillator, none of which have any parallel in classical physics. Firstly, it can be seen from eqn. 4.9 that the lowest possible vibrational energy is non-zero. A consequence of this zero-point energy is that the molecule can never relax to the bottom of its potential well, and hence its constituent atoms are in constant motion. This comes about as a direct consequence of the Heisenberg uncertainty principle, which states that it is impossible to know exactly both the position and momentum of a system. The second point to make is that there is a small but finite probability of finding the vibrating molecule outside the classical bounds of its potential well. Recalling again the Born interpretation, it is possible to find the system in any region where the wavefunction is non-zero. It can be seen from figure 4.2 that the wavefuntion is, in all cases shown, non-zero beyond the walls of the harmonic potential. This phenomenon is called quantum mechanical tunnelling, and is a result of the curvature of the walls of the potential well (if the walls were infinite and vertical, tunnelling would not occur) and the extent of tunnelling depends upon the steepness of the walls. Finally, for low vibrational quantum numbers, the probability distribution of the molecule within the potential well is distinctly non-classical. The probability distribution is related to the square of

the wavefunction. Observation of figure 4.2 shows that in the case of the quantum mechanical oscillator the system is most likely to exist close to its equilibrium configuration – exactly opposite to the classical case. There are also nodes in the probability distribution of a quantum mechanical oscillator, regions *inside* the classical potential well where the probability of finding the system is zero. As the vibrational quantum number increases, the classical and quantum mechanical distributions become more similar. This is an example of the correspondence principle, where quantum and classical behaviours "merge" at high energies and long length scales.

Anharmonic Corrections to the Simple Harmonic Oscillator

The harmonic oscillator model only adequately describes vibrational motion for small deviations from the equilibrium vibrational coordinate (i.e. low vibrational quantum numbers). For more energetic vibrations, the parabolic harmonic potential well underestimates the potential at small vibrational coordinates (due to repulsive forces as atoms get close to each other) and overestimates the potential at large vibrational coordinates (as atoms become far apart). In other words, anharmonicity must be taken into account in order to describe the vibrational motion of real molecules. One way to achieve this is to recalculate the eigenvalues and eigenfunctions given in eqns. 4.9 and 4.12 using a more realistic form of the potential well. A common anharmonic potential well is described by the Morse potential (eqn 4.14).

$$U_{vib} = D_e \left(1 - e^{-\beta q}\right)^2 \tag{4.14}$$

The Morse potential implicitly introduces the dissociation energy, D_e, thus allowing bonds to break at large vibrational coordinates (dissociation is not allowed by the harmonic oscillator model). The parameter β is a constant for a given vibration which defines the tightness of curvature at the bottom of the potential well. It should be noted that, for small displacements from equilibrium, the Morse potential is well approximated by a parabolic potential. The eigenvalues of a Morse oscillator are given by

$$E_{vib} = h\upsilon(\nu + 1/2) - h\upsilon x_e(\nu + 1/2)^2 \quad (4.15)$$

where the factor υx_e describes the anharmonic correction to the energy levels, and x_e is generally small. A consequence of this anharmonic correction is that the spacing between the vibrational energy levels decreases linearly with increasing vibrational quantum number, becoming zero (i.e. a continuum of energy) at the point where the molecule dissociates. Therefore there are only a finite number of vibrational energy levels below the dissociation energy, D_e. The Morse oscillator, like the harmonic oscillator, also posses a zero-point energy, and so the actual vibrational energy required to dissociate the molecule, D_0, differs from the dissociation energy defined by the Morse potential.

Although energy levels derived using the Morse potential are useful for visualising the main features observed in real molecular systems, in practice it is better to express the energy levels of an anharmonic oscillator in terms of a power series in (v + ½), with several empirical correction factors.

4.2.3 Spectral Intensities, Linewidths and Selection Rules

The Magnitude of Absorption

The intensity of a vibrational transition is determined by the relative probabilites of the molecules within a sample absorbing or emitting radiation. Einstein derived expressions for these probabilities by considering three possible processes by which a molecule can gain or lose energy. The most intuitive of these processes is that of stimulated absorption, whereby a molecular vibration (more correctly an oscillating transition moment) couples with an oscillating electromagetic field of the correct frequency to induce a transition to a higher vibrational state. Since the coupling of vibrational transitions with oscillating electromagnetic fields is the same regardless of whether the molecule exists in the upper or lower vibrational state, this mechanism also induces the stimulated emission of radiation. These two processes are described by the Einstein *B* coefficient

$$P_{transition} = P_{12} = P_{21} = \rho(\upsilon)B \quad (4.16)$$

where the subscripts 1 and 2 refer to the lower and upper states, respectively, and the parameter $\rho(\upsilon)$ is the radiation density of the stimulating radiation. As well as these two stimulated processes, a molecule can also lose energy through spontaneous emission. In this case the molecule relaxes back to the lower state through interaction with the radiation vacuum state as described by quantum electrodynamics. Spontaneous emission is described by the Einstein *A* coeffiecient.

Combining these three processes gives us the overall probability of both absorption and emission, and the intensities of the transitions are then given by multiplication with the population of the upper and lower levels.

$$I_{emission} = N_2 h\upsilon(A + B\rho(\upsilon)) \tag{4.17}$$

$$I_{absorption} = N_1 h\upsilon B\rho(\upsilon) \tag{4.18}$$

It can then be seen that the intensity (and indeed direction) of given transition is determined by the relative populations of the upper and lower states. For a large number of molecules in thermal equilibrium the relative population densities of the various energy levels is given by the boltzmann distribution function. In the case of vibrational transitions, *kT* is much smaller than the typical difference in energy between accessible levels (the vast majority of molecules are in the vibrational ground state) and so a net absorption of radiation is observed.

Peak Linewidths

The observed wavenumber (or frequency) range of a transition is referred to as its linewidth. A number of factors contribute to the linewidth of a peak, and some of these cannot be controlled experimentaly, i.e. they are inherent to the sample and conditions being studied. For example the Heisenberg uncertainty principle requires that, in the case of a transition to an exited state with a finite lifetime, there must be an associated smearing of the energy levels associated with the transition. In fact, the extent of this smearing increases as the lifetime of the exited state becomes shorter, and so the effect of this “uncertainty” broadening is greatest for short-lived states. The process of spontaneous emission introduced earlier means that no exited state

can have an infinite lifetime, and so all spectroscopic transitions are subject to a natural linewidth that sets a lower limit on the observable resolution in the absence of other factors (instrumental resolution, data handling methods, other interactions within the sample etc.). In practice, certainly in the case of condensed matter systems, there are other mechanisms that reduce the lifetime of exited states and so lead to actual linewidths much larger than the natural linewidth. Collisional deactivation and dephasing occur as a result of collisions between molecules. Such collisions can cause a molecule to lose energy through momentum transfer to the surrounding medium, and if the molecule is in an exited state this will result in a reduction in (for example) the vibrational wavenumber. Since collisions are much more frequent in condensed samples than in dilute gases this mechanism becomes much more significant for condensed matter studies. Collisions can also cause the molecule to change its rotational state. This causes any rotational fine structure to appear as a broad linewidth in condensed phase spectra as the uncertainty broadening of each line within a spectral branch becomes large compared to the line spacing.

Another factor to consider for condensed samples is inhomogeneous broadening. Inhomogeneous broadening refers to the instantaneous position of all the molecules within a sample, and arises from the fact that at any given time these molecules will experience a range of different electronic environments due to random fluctuations in orientation, separation or mixing (in the case of a multicomponent system). This leads directly to an increased linewidth as each different orientation of a molecule (or group of molecules) will have a slightly different excitation energy, and hence each spectroscopic transition will be spread over a range of wavenumbers.

Selection Rules and “Allowed” Transitions

In order for a molecule to interact with an illuminating electromagnetic field (and therefore have an absorption spectrum) the molecule must posses a dipole oscillating at the same frequency as at least one component of that incoming radiation. This corresponds to the classical idea of a driven oscillator, whereby the driven mass only responds with any great amplitude when the driving frequency lies close to the natural frequency of the oscillator. Quantum mechanically this is expressed through the transition dipole moment, μ_{fi}. The transition moment is defined in eqn. 4.19,

where $\hat{\mu}$ is the electric dipole operator and ψ_f and ψ_i refer to the final and initial states, respectively.

$$\mu_{fi} = \left\langle \psi_f \left| \hat{\mu} \right| \psi_i \right\rangle \tag{4.19}$$

The rate of a transition is proportional to the square of the transition moment, and by comparison with the Einstein *B* coefficient in eqn. 4.18 the intensity of a transition shares this proportionality. In order for a transition to contribute to the spectrum, therefore, its transition moment must be non-zero. Through analysis of the behaviour of the transition moment it is then possible to find a set of circumstances in which a transition is allowed. The set of rules formed by such an analysis are known as the selection rules.

The gross selection rule for a vibrational transition requires that there must be a change in dipole moment during a vibration in order for it to be infrared active. This selection rule arises from the Born Oppenheimer separation. If the total wavefunctions in eqn. 4.20 are separated into a product of rotational, vibrational and electronic wavefunctions we can discard the rotational component from the present discussion as it can be separated from the electronic and vibrational components by remembering that it only depends upon the rotational coordinates of the molucule and not the molecule-fixed axis system. The dipole moment of a molecule depends upon both nuclear and electronic distributions, however, and so is a function of both the electronic and vibrational coordinates. It follows that the integral we need to consider is

$$\left\langle \psi_{ei}\psi_{vf} \left| \hat{\mu} \right| \psi_{ei}\psi_{vf} \right\rangle \neq 0 \tag{4.20}$$

where the subscripts *e* and *v* refer to the electronic and vibrational wavefunctions respectively (note that the electronic state remains the same as electronic transitions are far more energetic than vibrational transitions). The dipole moment operator can be expressed as a power series in the vibrational coordinate, *q*. If we again consider the harmonic oscillator, this becomes

$$\hat{\mu} = \mu_0 + \sum_j \left(\frac{\partial \mu_0}{\partial q_j} \right) q_j \tag{4.21}$$

where μ_0 is the equilibrium dipole moment and q is again the vibrational coordinate (here expressed as a sum over all the atoms in the molecule). The integral in eqn. 4.20 can then be re-written;

$$\left\langle \psi_{ei} \middle| \mu_0 \middle| \psi_{ei} \right\rangle \left\langle \psi_{vf} \middle| \psi_{vi} \right\rangle + \left\langle \psi_{ei} \middle| \frac{\partial \mu_0}{\partial q} \middle| \psi_{ei} \right\rangle \left\langle \psi_{vf} \middle| q \middle| \psi_{vi} \right\rangle \neq 0 \tag{4.22}$$

The first term in eqn. 4.22 necessarily vanishes due to the orthogonality of states with different vibrational quantum numbers. The second term then gives us the previously quoted gross selection rule, since the electronic component is zero unless the dipole moment changes along the vibrational coordinate. The second term on the left-hand side of eqn. 4.22 also leads to the specific selection rule for the harmonic oscillator. Recalling the form of the eigenfunctions given in eqn 4.12, and the standard integral of a Hermite polynomial in eqn. 4.13, we can see that in order to satisfy the condition $\left\langle \psi_{vf} \middle| q \middle| \psi_{vi} \right\rangle \neq 0$, the vibrational quantum number can only increase by one unit. The specific selection rule is then

$$\Delta\nu = \pm 1 \tag{4.23}$$

In the case of the anharmonic oscillator this selection rule is relaxed, due to the inclusion of higher powers of the vibrational coordinate in eqn. 4.21. In practice, this results in the appearance of weak overtone bands (corresponding to any integer change in vibrational quantum number), whose strength depends upon the extent of anharmonicity. The presence of anharmonicity also allows excitation of more than one band simultaneously. This can lead to the appearance of combination or difference bands in the spectrum. In a combination band a single photon excites two or more vibrations, increasing multiple vibrational quantum numbers to leave the molecule in an exited state unrelated to any fundamental level. A difference band appears when a molecule in a low-lying vibrational excited state absorbs a relatively low energy photon and undergoes a transition to an exited state of a completely different vibration. No new levels are created in a difference band, and so the

transitions occur at a wavenumber exactly equal to the difference between the two fundamentals involved.

The appearance of combination and overtone transitions in the spectrum leads to a third effect for an anharmonic oscillator. If an overtone, for example, has approximately the same wavenumber as another fundamental transition the overtone can become resonantly enhanced. The resonant enhancement is due to coupling between the overtone and fundamental, meaning that the strong fundamental band is now involved in both transitions. This effect is known as Fermi resonance. In some cases Fermi resonance leads to the appearance of two bands in a spectrum where only one is expected. This is a common feature in the spectra of aldehydes.[3] Fermi resonance is also relevant to the spectroscopy of alkanes, as a Fermi resonance of the CH_2 symmetric stretch appears as a broad shoulder underneath the antisymmetric stretch.[4]

4.2.4 The Vibrations of Polyatomic Molecules

Normal Modes of Vibration

Treating each atom within a molecule as a point mass, it can be seen that each mass requires three coordinates to define its position and so has three degrees of freedom. The total number of degrees of freedom for a molecule with N constituent atoms is, therefore, $3N$. However, the centre of mass of the molecule is also described by three degrees of freedom and so the molecule possesses $3N - 3$ non-translational degrees of freedom. A further number of degrees of freedom describe rotation of the molecule. For a non-linear molecule there are three mutually perpendicular axes of rotation intersecting at the centre of mass, and so rotational motion is described by three degrees of freedom (i.e. a distance, azimuthal angle and pitch are required to define the molecule relative to an arbitrary point in space). For a linear molecule this number is reduced to two, as rotation about the molecular axis does not result in the displacement of the constituent atoms. A non-linear molecule therefore has $3N - 6$ vibrational degrees of freedom, whereas for a linear molecule there are only $3N - 5$.

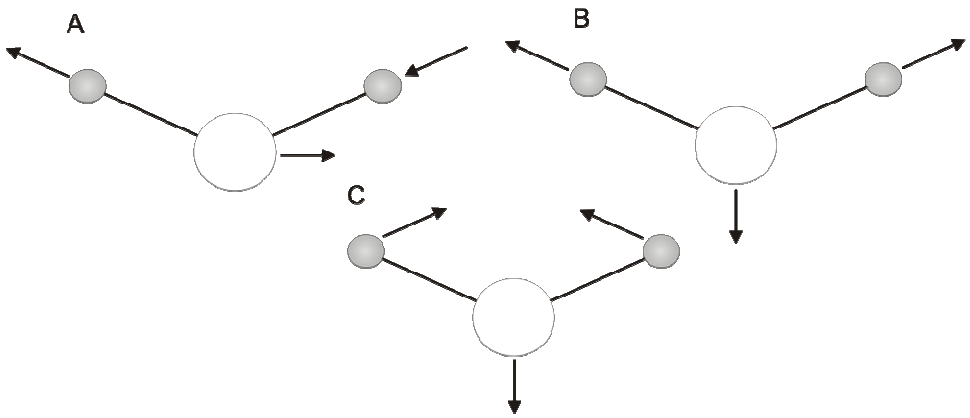

Figure 4.3 Normal modes of vibration for the water molecule. (A) Antisymmetric stretch, (B) Symmetric stretch, (C) Bend.

These vibrational degrees of freedom correspond to the so-called normal modes of the molecule. The normal modes of vibration of a molecule represent synchronous oscillations of some or all of the atoms within a molecule that do not lead to translation or rotation of the molecule as a whole (i.e. the centre of mass remains unchanged throughout the course of the vibration). Such vibrations can take the form of either stretches (deformation of bond length) or bends (deformation of bond angle) with stretches generally having the higher energy. Stretches and bends can, in turn, be categorised as either symmetric or antisymmetric (in the case of stretches) or wag, twist, scissor or rock (in the case of bends). Examples of normal modes of vibration are given in figure 4.3 for a water molecule.

Infrared Activity of Normal Modes

Although the number of normal modes of vibration a molecule possesses is determined simply by the number of constituent atoms, the number of bands in the IR spectrum is harder to deduce (even ignoring the effect of additional bands due to overtones, Fermi resonances etc.). For example, the gross selection rule requires that the dipole moment of the molecule must change during the course of a vibration in order for it to be IR active. This immediately precludes the observation of an IR spectrum for a homonuclear diatomic molecule. Further complications arise when the symmetry properties of the transition moment (eqn. 4.19) are considered. The value of the transition moment must be independent of the orientation of the molecule; or rather the value of the integral is independent of the coordinate system being used to describe it. Since the volume element of the transition moment is necessarily

invariant with orientation this fact means that the product $\psi_f \hat{\mu} \psi_i$ is required to be totally symmetric. It is therefore necessary to consider the symmetry properties of the normal modes of vibration.

The symmetry of a molecule can be classified according to the symmetry operations (rotation, reflection, inversion etc.) that leave the appearance of the molecule unchanged, i.e. only identical atoms trade positions. All such symmetry properties of a molecule serve to define the molecular point group, and the behaviour of the molecule under each of its symmetry operations is detailed by the character table of that point group. The character table contains several rows, each of which represents a symmetry species of the molecule. These symmetry species can be derived by representing each symmetry operation of the point group in matrix form and reducing any matrices which have block-diagonal form to a direct sum of two or more simpler representations. The simplest set of matrix representations (the irreducible representations of the group) gives the symmetry species of the molecule. Each normal mode of a molecule belongs to one of these symmetry species. All point groups contain at least the totally symmetric irreducible representation, where the positions of atoms remain unchanged by any symmetry operation. The product $\psi_f \hat{\mu} \psi_i$ must transform according to this totally symmetric representation in order to be non-zero, and it follows that the dipole moment must have the same symmetry as the product of the wavefunctions which describe the transition. For a fundamental transition this requirement means that the dipole moment must have the same symmetry as the excited state, as the ground state vibrational wavefunction is itself totally symmetric. The dipole moment is a vector, and so has the same symmetry properties as the *x*, *y* or *z* coordinate vectors (equivalently the three components of translational motion) and so any normal mode which shares the same symmetry species as one of these components will be IR active. More rigorously, any normal mode whose symmetry species is not spanned by *x*, *y* or *z* is Infrared inactive.

Group Frequencies and the Analytical Power of IR Spectroscopy

A polyatomic molecule can be thought of as a system of linked oscillators, where each oscillator consists of a pair of bonded atoms. In any such system the oscillators

are necessarily coupled by Newton's third law of motion, as the oscillation of one pair of atoms exerts a force on all the surrounding oscillators. If pairs of oscillators are approximated by masses connected by springs, the extent of this coupling can be visualised.

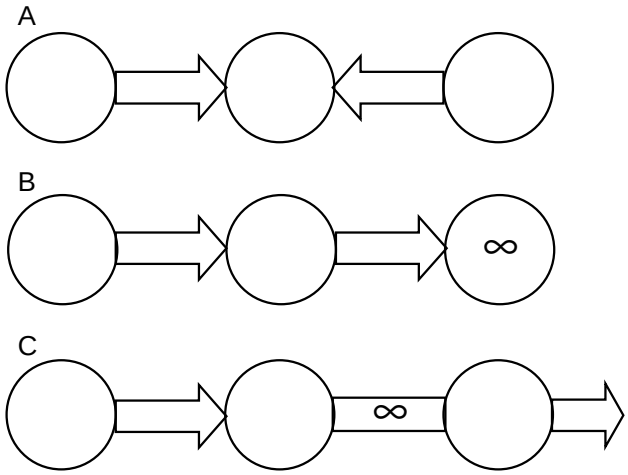

Figure 4.4 The coupling of vibrational motions is dependent upon the relative masses in the molecule. Arrows denote instantaneous direction of motion, ∞ represents an infinite mass/stiff bond.

Figure 4.4 shows a hypothetical series of oscillators representing a linear triatomic molecule. First considering the case of equal force constants and equal masses (figure 4.4a) it can be seen that in the case of a symmetric vibration no net force is exerted on the central atom, whereas for an assymetric vibration there is a periodic net force that causes the central mass to oscillate about its equilibrium position. If the central mass were made momentarily infinite and only one oscillator was driven into motion, releasing the central mass would lead to assymetric stretching behaviour as the second oscillator was driven by the first. If both oscillators were driven simultaneously and in phase, then symmetric stretching behaviour would result. Thus the two oscillators are coupled as the behaviour of one is determined by the behaviour of the other. If the system is made unsymmetrical by introducing an infinite mass (as in figure 4.4b, or equivalently a zero force constant would achieve the same effect) then the resonant frequency of one oscillator is lowered relative to the other. In this case both bond lengths distort, but the infinite mass remains stationary. In the other extreme case, the resonant frequency of one oscillator can be raised by introducing an infinite force constant (figure 4.4c, or equivalently introduce a zero mass). Now both masses move, but only one bond length distorts. These two

extreme situations serve to illustrate two approximations relevant to the vibrations of complex molecules:

1. A high frequency of incident radiation will only cause vibration of atoms directly connected to a high transition frequency oscillator in an unequal oscillator combination.

2. A low frequency of incident radiation will only cause distortion of the bond length (angle) of a low transition frequency oscillator pair in an unequal oscillator combination.

Clearly, these approximations only hold true for the extreme cases of infinite mass or infinite force constant, but it is found that the resonant frequencies of atom pairs within typical connectivities of atoms (i.e. molecules) lie sufficiently far apart that they can be considered as separate oscillators. This observation means that the IR spectra of quite complex molecules can be analysed in terms of separate contributions from individual functional groups within those molecules, thus greatly simplifying the use of IR spectroscopy both as an analytical tool and as a means of identifying unknown molecules. For example, due to its small mass, vibrations of X-H bonds are generally mechanically separate from the rest of the molecule, and tend to appear within well-defined regions of a spectrum. The same is true of double and triple bonded groups (C=C, C=N, C=O etc.) when they are connected to the rest of the molecule by averagely heavy (from an organic viewpoint) atoms such as carbon. These typical spectral ranges are known as group frequencies (technically incorrectly, as the ranges are generally quoted in wavenumbers).

4.2.5 Vibrational Spectroscopy of *n*-Alkanes

The spectral features of polyethylene and the linear *n*-alkanes are well known,[5-7] having been used as ideal systems against which to test theoretical expressions for the vibrational dynamics of chain molecules. Assignments and typical positions of the bands discussed here are summarised in table 4.1.

Initial studies on polyethylene chains concerned the calculation of low frequency skeletal vibrations.[8] These C-C stretching modes appear in the Raman spectra of

alkyl chain molecules and are useful indicators of chain order with distinct patterns of peaks corresponding to *trans*- and *gauche*- chain segments occurring in the melt, rotator and crystalline phases.[9] The position of *gauche* defects within an alkyl chain can be characterised by the peak wavenumber of methylene wagging modes.[10] Three diagnostic peaks appear in the IR spectrum relating to end-of-chain *gauche* defects, double *gauche* defects and *gauche-trans-gauche* sequences. Methylene rocking modes are weakly indicative of chain order, appearing as a progression of regularly spaced bands. Each band in the progression corresponds to a unique phase difference between the rocking of adjacent methylene units. Only certain phase differences are allowed for an all-*trans* chain, and thus if the bands can be correctly assigned an indication of the presence or absence of *gauche* defects is given. The bands described so far have been successfully used to probe conformational order in a variety of alkyl stationary phases.[10-13] Application to the monolayer systems discussed in this chapter, however, are hampered by low-wavenumber limits of detection and the presence of water vapour bands. The C-H stretching region is therefore of more practical use.

The C-H stretching region of *n*-alkanes contains four main bands. Most prominent are the methylene antisymmetric and symmetric stretches, at approximately 2925 cm^{-1} and 2850 cm^{-1}, respectively. Less intense are a pair of bands centred at 2962 cm^{-1} and 2950 cm^{-1}, representing the asymmetric vibrations of the terminal methyl groups. Two bands arise due to orientations of the transition dipole moment parallel (in-plane) and perpendicular (out-of-plane) with the chain axis. These two bands become degenerate when the rotation of the methyl group occurs on a sufficiently short timescale and the bands become sufficiently broad. Only one band is observed for the asymmetric methyl stretch in the FTIR spectra of surfactant monolayers at the air-water interface.

Table 4.1 Typical position of spectral bands in *n*-alkane spectra

Band Assignment	Description	Typical Position / cm^{-1}	Spectroscopic Technique	Effect of Ordering
υ(C-C)	*trans*-(C-C) stretch	1060, 1130	Raman	Change in relative intensities of *trans* and *gauche* bands
υ(C-C)	*gauche*-(C-C) stretch	1080	Raman	Change in relative intensities of *trans* and *gauche* bands
$\gamma_{\omega}(CH_2)$	End-*gauche* CH_2 wagging	1341	FTIR	Change in relative intensities of 1341, 1354 and 1368 cm^{-1} bands
$\gamma_{\omega}(CH_2)$	double-*gauche* CH_2 wagging	1354	FTIR	Change in relative intensities of 1341, 1354 and 1368 cm^{-1} bands
$\gamma_{\omega}(CH_2)$	*Gauche-trans-gauche* CH_2 wagging	1368	FTIR	Change in relative intensities of 1341, 1354 and 1368 cm^{-1} bands
$\delta_{\omega}(CH_2)$	CH_3 umbrella deformation	1368-1382	FTIR	Position and peak splitting dependent upon crystal form
$\gamma_{r}(CH_2)$	CH_2 rocking deformation	Progression of bands in the region 700-1000	FTIR	Band splitting dependent upon the presence of *gauche* defects.
$\gamma_{r}(CH_3)$	CH_3 rocking deformation	890	FTIR	Position and peak splitting dependent upon crystal form
d^{-}	CH_2 antisymmetric stretch	2925-2919	FTIR	Decrease in wavenumber indicates a more ordered chain
d^{+}	CH_2 symmetric stretch	2856-2850	FTIR	Decrease in wavenumber indicates a more ordered chain
r^{-}_{a}	CH_3 asymmetric stretch (in-plane of chain)	2962	FTIR	Collapses to a single band depending upon crystal structure

r^-_b	CH_3 asymmetric stretch (out-of-plane of chain)	2950	FTIR	Collapses to a single band depending upon crystal structure
r^+	CH_3 symmetric stretch	2880	FTIR	Little change
d^+(FR)	Fermi resonance interaction of d^+ with overtones of CH_2 bending modes	2900	FTIR	Little Change
r^+(FR)	Fermi resonance interaction of r^+ with overtones of CH_3 bending modes	2930	FTIR	Typically unresolved in monolayer spectra

Several less intense bands are also observed in the C-H stretching region of *n*-alkanes corresponding to the symmetric CH_3 stretch at 2880 cm^{-1}, and two Fermi resonance interactions at 2930 cm^{-1} and 2900 cm^{-1}. Snyder *et al.*[7] attributed the 2900 cm^{-1} peak to an interaction between the symmetric methylene stretch and an overtone of a methylene bending mode, whilst the peak at 2930 cm^{-1} formed a Fermi doublet with the symmetric methyl stretch after interaction with an overtone of the methyl bending modes (the peak at 2880 $cm^{-1}$was still assigned to the symmetric methyl stretching mode, however, as it contained most of the fundamental). An alternative explanation for the band at 2900 cm^{-1} has been proposed by Jordanov *et al.*[14] based on the coupling of Fermi doublets (created by the interaction of the antisymmetric methylene stretching fundamental and a methylene bending overtone) of adjacent methylene units to create a quartet of bands centred at roughly 2855 cm^{-1}, 2900 cm^{-1}, 2930 cm^{-1} and 2955 cm^{-1}. For any practical systems these peaks are not well resolved, however, and so the original description of Snyder *et al.* can be used to adequately assign peaks in spectra of chain molecules.

Of all the peaks present in the C-H stretching region, the antisymmetric and symmetric methylene stretches are most susceptible to changes in molecular conformation. The central wavenumber of both bands decreases as the number of *gauche* defects is reduced. The antisymmetric stretch is most affected, with a peak at 2925 cm^{-1} indicative of a disordered liquid-like environment whereas a peak at 2920 cm^{-1} shows the presence of all-*trans* chains. This fact has been used to study

the freezing of 1- and 2-alcohol monolayers at the air-water interface by Alonso *et al.*[15] who noted a peak shift of approximately 4 cm^{-1} upon freezing of the monolayer.

4.3 External Reflection FTIR Spectroscopy

4.3.1 Applications of ER-FTIRS

From Metal Surfaces to the Air-Water Interface

External reflection Fourier transform spectroscopy (ER-FTIRS) has been used since the 1960s as a method of surface characterisation (the technique has also collected an impressively large number of acronyms, and is referred to variously as IRAS, IRRAS, RAIRS, FT-IRRAS and IR-ERS). Initially the technique was confined to the study of organic films on metal substrates,[16-19] a purpose for which it is still routinely employed.[20-22] Early attempts to study the interactions of molecules with solid surfaces involved the deposition of monolayer or submonolayer films on the surface of metal particles dispersed within a transparent matrix placed directly in the IR beampath. In this way spectra could be obtained using the more traditional transmission geometry, although only a limited set of systems could be studied.[23-26] In particular it was impossible to study Langmuir-Blodgett films in this way, and at the time there was scant direct experimental evidence on the structure of these otherwise well characterised systems. Moreover, Langmuir-Blodgett films were known to be of great scientific and practical importance.[27] A shift to external reflection geometry was achieved by placing additional, coated, mirrors (or closely separated pairs of mirrors) in the optical beampath. Theoretical calculations showed that maximum signal was achieved at grazing-incidence.[28, 29] In this way spectra were obtained of various stearates on gold,[30] cellulose acetate on silver,[29] arachidate and docosanoic acid monolayers on aluminium to name but a few. Conformational information could be derived by comparison of relevant peak positions with the work of Snyder *et al.* described earlier with relation to bulk alkanes, a fact used by Hsu *et al.* to follow the crystallisation of amorphous perfluoroalkane films on CsI.[31]

The initial emphasis on metal substrates largely occurred as a matter of convenience, since metals have a high reflectivity and their optical properties were well

understood. Improvements in instrumentation have enabled reflectance spectra to be extracted from less reflective surfaces such as oxides, silicon and glass.[32, 33] Such improvements in detection capability and instrumental throughput ultimately led to the first successful extension of ER-FTIRS to the air-water interface by Dluhy and Cornell in 1985.[34] They identified peaks belonging to both the chain and headgroup of a Langmuir monolayer of Oleic acid at its equilibrium spreading pressure (about 30 mNm^{-1}), and were able to deduce that the acid remains protonated in the film. A quantitative analysis was published, comparing the air-metal and air-water interfaces.[35] This analysis revealed that at the air-water interface vibrations oriented both parallel and perpendicular to the interface can be observed (in contrast to the air-metal interface where only parallel bands can be seen) and this was proved by taking both s- and p-polarised spectra of a DSPC monolayer in the LC phase. In both these studies negative absorption peaks were observed. Dluhy attributed this to the behaviour of the complex refractive index of water. Mielczarski further investigated the effect of the subphase on the interpretation of reflectance spectra by considering the adsorption of cuprous ethyl xanthate to air/substrate interfaces of copper, copper sulphide and water.[36] It was demonstrated that the behaviour of the electric field components within the adsorbed layer are key in determining the position, shape and intensity of observed peaks. In particular, enhancement of the electric field within the film due to changes in the real part of the refractive index of the film as a function of wavenumber can lead to increased absorption at wavenumbers other than those expected by consideration of the behaviour of the absorption coefficient. Thus, the position of peaks in the reflectance spectrum of a thin film is dependent upon both the molecular order within the film and the optical properties of the film.

A theoretical treatment of the air/adsorbate/dielectric system was considered by Buontempo and Rice.[37] They derived expressions for the intensity of reflected IR as a function of optical parameters of the adsorbate and the thickness of the adsorbed layer, and showed that changes in orientation can be observed through changes in the dichroic ratio. The theoretical analysis was applied to Langmuir monolayers of *n*-heneicosanol in which the surface presseure had been allowed to relax to an equilibrium value.[38] It was found that at low molecular areas the chains were in a crystalline phase with all-*trans* chains, and at large molecular areas crystalline

regions coexisted with a disordered liquid phase. The average tilt angle did not change, despite a continuous reduction in *gauche*-defects.[39] In these fully relaxed systems the fatty acid behaves analogously to a smectic liquid crystal, supporting a variety of mesophases and exhibiting no true liquid phases.[40] Similar behaviour was observed for monolayers of stearyl alcohol,[41] which Hsu *et al.* found to consist of untilted chains in contrast to a perfluorinated stearyl alcohol that had a chain tilt angle of about 13°. The dichroic ratio was also considered as a measure of molecular orientation by Fina *et al.* for monolayers of sodium dodecyl sulfonate,[42] and the elucidation of molecular orientation was found theoretically to be optimised at angles of incidence close to the Brewster angle.[43]

One of the major barriers to the application of ER-FTIRS to the air-water interface is the elimination of interference due to absorption bands of the water subphase. One solution to this problem was introduced by Turlet *et al.* who adapted the established technique of PM-IRRAS for use at the air-water interface.[44] PM-IRRAS eliminates water bands directly by eliminating isotropic components of recorded spectra through measurement of the difference between s- and p-polarised spectra. The elimination of water bands allowed the observation of normal modes of the polar headgroup of deuterated arachidic acid. From these bands it was found that the headgroups existed in a symmetrical environment at the interface. Frequency shifts of CH_2 normal modes during compression of arachidic[45] and pentadecanoic[46] acid monolayers were found, indicating molecular reorganisation. Changing the pH and subphase cation concentration was found to affect the hydrogen bonding network at the interface[47] and the degree of dissociation of an arachidate monolayer.[48] The effect of cadmium ions in the subphase has also been considered for stearic acid[49] and its mixtures with stearyl alcohol[50], where an alcohol fraction of only 15% was found to reduce cadmium ion adsorption by over half. At constant area per molecule, the conformational order of alkanoic acid monolayers increases with increasing chain length, with the effect being particularly pronounced at high areas per molecule and less acidic pH.[51] Similar effects were observed in alkanoic acid ester monolayers,[52] with a change in headgroup conformation from *trans* to *gauche* upon compression with formation of an orthorhombic structure with 0° chain tilt. Qualitatively similar

results were obtained for DSPC monolayers, and in addition it was concluded that the C-O stretch of the ester group is oriented within 20° of the surface normal.

Since FTIR is a chemically specific technique, a more detailed structural analysis can be made by selective isotopic substitution. Gericke and Mendelsohn have utilised this fact to deduce that acid monolayers are significantly more ordered near the headgroup than in the tail. A comparison of tail-end perdeuterated hexadecanoic acid and hydrogenated hexadecanoic acid showed a significant red-shift in CH_2 in the case of the former at all compressions.[53] This methodology was extended to monolayers of POPC and OPPC with the same conclusion.[54]

Biological Applications – Properties of Lung Surfactant

The significant amount of work focusing on model Langmuir monolayers of simple surfactants allowed a refinement of the experimental technique of ER-FTIR on well defined systems whilst at the same time providing useful chemically specific information that would have either been inaccessible or prohibitively expensive using other techniques. Since the early 1990s there has been a shift towards the study of biologically relevant systems, particularly those which mimic the function of lung surfactant mixtures.

It has long been known that surface tension plays a role in the functioning of the lungs, and that the surface of the alveoli were coated with a mixture of phospholipids.[55] Surface pressure isotherms of such mixtures showed that the efficiency of surface tension reduction was not sufficient to account for the high surface pressures capable of being sustained by films formed from lung extracts. As a result, the role of proteins present in the lungs was investigated and four proteins were identified which associated with surfactant phospholipids. These were labelled surfactant proteins A, B, C and D (commonly abbreviated SP-X). SP-A and SP-D are hydrophilic and have been suggested to be important for defence of the lungs against infection. SP-B and SP-C are hydrophobic and are more involved in the dynamic film behaviour of the alveolar surface. Deficiency in certain lung surfactant components has been associated with various conditions and diseases, notably respiratory distress syndrome, a common problem encountered in premature infants.

A better understanding of the function of lung surfactant mixtures is necessary in order to formulate more efficient treatments for respiratory diseases.

The most abundant component of lung surfactant is the phospholipid DPPC. Dluhy *et al.* investigated the structural properties of DPPC spread films during the LE/LC phase transition. They showed a conformational change occurred during the transition, which was biphasic in nature.[56] By comparison with films of DSPC (LC at all surface pressures) and DMPC (LE at all surface pressures) the wavenumbers of CH_2 stretching bands in the DPPC spectra were shown to be excellent indicators of chain conformational order as well as monolayer phase[57] and are in agreement with the results of Snyder for bulk alkyl systems.[4-7, 58]

In order to study more directly the molecular level processes occurring within the lungs it was necessary to study complex mixtures of lipids and proteins. As a starting point, a simple binary phospholipid monolayer containing equimolar DPPC and DPPS was used.[59] Through deuteration of the acyl chains of DPPC perfect mixing was observed at all surface pressures, and both components were found to interact with calcium ions. This finding is in contrast to single component DPPC monolayers where calcium ions were found to have little effect. Further investigations into binary phospholipid monolayers revealed that, at collapse, phospholipids with more disordered acyl chains were more likely to be removed from the film (in some cases reversibly) leaving a largely single-component monolayer of the more ordered component (i.e. the component capable of sustaining a higher surface pressure) at the interface.[60] These findings seemed to provide tantalizing evidence for the so-called "squeeze-out" hypothesis whereby high surface pressures, vital to the function of the alveoli, are achieved by the reversible expulsion of certain lung surfactant components from the surface at maximum compression.[61] The logical next step was to mix SP-B and SP-C with phospholipid monolayers to see if the same "squeezing-out" occurred. In binary monolayers of DPPC and SP-B the protein is partially excluded from the surface (up to about 15%) upon compression, whereas aggregation behaviour is observed with SP-C.[61] It was therefore suggested that SP-C serves mainly to facilitate rapid spreading of DPPC *in vivo*. Comparison with earlier work on synthetic model peptides was used to suggest possible secondary structures of the

proteins in both these systems.[62] A more detailed analysis of SP-C function in the DPPC/SP-C monolayer revealed that the helix tilt angle of SP-C was significantly increased, whilst the DPPC chain-tilt was decreased, in the mixed films, suggesting that SP-C acted as a "hydrophobic lever" that disrupts the interactions between DPPC molecules, facilitating spreading, whilst also allowing the formation of tightly packed structures at high surface pressures.[63] Extension to ternary surfactant systems revealed that the addition of a natural mixture of SP-B/SP-C to mixed monolayers of DPPC/DPPG and DPPC/DOPG resulted in a decrease in order of the DPPC component, but an increase in order of the anionic phosphoglycerol component.[64] Since both DPPC and DPPG contain saturated acyl chains, these results indicate a significant difference in headgroup interaction. It was later shown[65] that both PC and PG components were excluded from the surface film at high surface pressures, and it was proposed that this surface reorganisation proceeded through the formation of local bilayer structures (most likely predominantly containing the strongly interacting DPPG/DOPG) which then nucleated the removal of both PG and PC to form larger scale multilayer structures.

Serum proteins have been identified as decreasing the function of surfactants in biological systems. Their effect on lung surfactant has therefore been considered as a model for respiratory distress syndrome. Fibrinogen adsorption to the air-water interface was found to result in only small changes in surface tension despite large changes in adsorption density.[66] Adsorbed fibrinogen contained a large fraction of water, leading to a very open, non-compact structure that limited the minimum achievable surface tension. This provides a mechanism for reduction in biological function, as proper functioning of the alveoli relies on the presence of a very low interfacial tension. Another serum protein, bovine serum albumin, was found to be stable with respect to denaturation at the air-water interface through comparison of the wavenumber of the amide-I band in monolayers of pre-denatured and natural protein.[67] The effect of fibrinogen on DPPC monolayers was considered. Competitive adsorption of bovine serum albumin and DPPC was found to be dependant upon the method of introduction of DPPC, with the effect on a spread DPPC film much lower than when both species were dispersed in the subphase.[68] In the latter case, only a very low level of DPPC adsorption occurred. In contrast,

surfactants such as DLPC[69] and sodium myristate[70, 71] were found to expel high levels of both fibrinogen and bovine serum albumin from the interface, making them suitable candidates for use in lung surfactant replacement treatments. The effect of a therapeutic agent, $(KL_4)_4K$, on monolayers of DPPC, DPPG and their mixtures was probed. The position of the carbonyl and amide bands of $(KL_4)_4K$ suggested that it caused similar effects as SP-B when inserted into the phospholipid monolayers. Although the secondary structure in these monolayers was found to be slightly different to SP-B, the position in particular of positive lysine residues caused a similarly preferential interaction with anionic DPPG, ultimately leading to the formation of multilayer structures.

Other Biological Systems

The early detection of pathogens is essential for effective antimicrobial host-defence. SP-D is known to selectively bind to lipopolysaccharides, components commonly found in bacterial cell walls. The binding is known to take place via a carbohydrate recognition domain of SP-D.[72, 73] By using a lipopolysaccharide monolayer with a model protein to mimic the action of the carbohydrate recognition domain, Mendelsohn *et al.* were able to show that the binding is likely to be non-specific in the absence of calcium ions, but that calcium-mediated binding resulted in adsorption to specific core saccharides within the monolayer.[74] The direct interaction of Intestinal Fatty Acid Binding Protein (IFABP) with membranes occurs during the intracellular uptake and transfer of fatty acids.[75] Addition of IFABP to a DMPA monolayer proceeded via a two step mechanism involving initial adsorption of IFABP to the air-water interface followed by insertion into the monolayer. IFAPB insertion was found to induce an increase in conformational order in the acyl chains of DMPA. The significance of α-helical domains in IFABP was demonstrated by considering a helixless variant, IFABP-HL, which produced a much weaker ordering effect.[76] Another protein involved in membrane transport processes is Lecithin Retinol Acyltransferase (LRAT), which is thought to be involved in the storage and mobilisation of vitamin A. A truncated version of LRAT was used to follow the hydrolysis of a DMPC monolayer.[77] The hydrolysis of organophosphorous compounds has also been studied,[78] as these are of relevance to the hydrolysis of

pesticides and nerve agents. As well as proteins that function to either disrupt or transport material across membranes, ER-FTIRS has been used to study proteins that form a functional part of membranes. Ras proteins reside within the inner leaflet of membranes and perform signalling functions.[79] It was found that model Ras proteins desorbed from membranes at only moderately high surface pressures (~30 mNm^{-1}) unless they contained two saturated alkyl chains.

The interaction of DNA with, and transport across, membranes is a key goal in the search for non-viral transfection agents for drug delivery, with particular emphasis on gene therapy. Using a combination of ER-FTIRS and x-ray diffraction, it has been found that DNA adsorption to model DMPE membranes is mediated by magnesium ions, and that the DNA appears to take up a well-ordered conformation at the interface without disturbing the packing of DMPE acyl chains.[80]

It has already been alluded to that the position of amide bands (amide-I at roughly 1650 cm^{-1} and amide-II at roughly 1550 cm^{-1}) can be used to give information about the secondary structure and orientation of proteins, and is well reported in the literature.[81, 82] These amide bands are actually rather broad features, containing contributions from various normal modes of peptides, and as such are relatively featureless when the protein is in a random conformation. The amide-I band is dominated by carbonyl stretches with two modes particularly sensitive to coupling between individual amide-I units. Well resolved peaks around 1600 cm^{-1} and 1690 cm^{-1} are indicative of an aggregated or predominantly β-sheet structure. The amide-I band is of less diagnostic use for other secondary structures, for example α-helices, as the splitting between the modes is much smaller and generally unresolvable.[83] The amide-II band is made up of a CN stretching mode and a NH bending mode, and is particularly sensitive to protonation of the peptide unit. The ratio of amide I/amide II intensities is a useful analytical tool for quantifying the tilt or orientation of peptide units. Desbat *et al.* used the position and linewidth of the amide-I band to follow the behaviour of valine gramicidin[84] (an ion-channel forming protein) and rhodopsin[85] (a membrane protein) on compression. The amide-I band of valine gramicidin was found to red-shift and sharpen on compression, suggesting a reorganisation from completely unfolded protein to a folded β-sheet structure. In

contrast, rhodopsin was found to undergo very little change in orientation upon compression, with the retention of secondary structure. Morphologies of proteins on mica have also been studied in this way.[86]

Amide-I and II bands have also been used to probe interactions between proteins and spread phospholipid films. The membrane translocation protein penetratin is capable of transpoting hydrophilic peptides into cells without damaging the cell membrane. Penetratin introduced disorder into the heagroup region of DPPC and DPPS monolayers, taking up a predominantly β-sheet formation in contrast to the native α-helix structure in the bulk.[87] In the case of DPPS the monolayer chain structure was also completely disrupted, behaviour similar to that seen as a result of the interaction of alkaline phosphatase with DPPC and DPPS.[88]

Protein unfolding at interfaces plays an important roll in the stabilisation of foams, emulsions, gels and other dispersions and is of great relevance to the food industry. By observing changes in intensity and position of amide bands, Meinders *et al.* have shown that the interfacial structure (conformation, degree of unfolding etc.) is dependent upon the method of formation of the interfacial layer.[89-91] Adsorption of egg white ovalbumin at the air-water interface results in a partially unfolded structure with a lower β-sheet fraction than in the bulk.[92] Ovalbumin has a preferential orientation at the interface, as evidenced by restricted rotational dynamics. Compression of the surface layer results in local aggregation and protein-network formation at the interface, deduced from the appearance of a shoulder at 1624 cm^{-1} in the amide-I band at large compressions (indicative of anti-parallel β-sheet formation) and a further increase in average rotational correlation time.

Interfacial hydrogen bond network formation has also been observed.[93] Monolayers of a triaminotriazine amphiphile showed a broad NH_2 scissoring absorption centred at ~1630 cm^{-1}. This mode was completely irradicated from the monolayer spectrum in the presence of barbituric acid, suggesting restriction of the conformation of the NH_2 group by hydrogen bond formation. The rigidity of the network was confirmed by the reduction in intensity and number of ring stretching vibrations in the hydrogen bonded film. Analysis of the orientation of barbituric acid in the film shows it lies in a conformation that optimises hydrogen bond angles. Interfacial hydrogen bonding

has also been observed through the physicochemical interaction of polyamines with a DPPG monolayer.[94] Introduction of polyamine caused a reduction in wavenumber of carbonyl stretching vibrations, indicative of the formation of hydrogen bonds. The magnitude of the shift in carbonyl stretching frequency increases with number of hydrogen bonds formed (i.e. with the length of the polyamine). Analysis of the PO_2 bands showed that the polyamine disrupted the packing of the DPPG monolayer. The study of such systems is important, as polyamines are present in cells *in vivo* and are their function is known to be related to the proliferation of cancerous cells.

Langmuir-Blodgett films of alcohol dehydrogenase (ADH) on gold can be used as biosensors to detect the presence of ethanol.[22] Caseli *et al.* showed that ADH could be succesfully transferred to a gold substrate, but that the transfer efficiency was enhanced when a binary mixed monolayer of ADH and DMPA was used. Using PM-IRRAS it was possible to follow the formation of a Gibbs monolayer of ADH at the air-water interface by observing how the amide-I and amide-II intensity evolved with time. The amide-I band showed two distinct peaks at all times, corresponding to α-helices and β-sheets. The ratio of these two peaks remained constant throughout adsorption, suggesting little or no change in orientation occurred. The introduction of ADH into solution beneath a pre-formed DMPA monolayer results in an increase in surface pressure due to ADH incorporation into the surface layer. The ADH incorporated into the DMPA monolayer contains a greater fraction of α-helical structure than at the neat air-water interface, although again the structure does not change as adsorption progresses. The Langmuir-Blodgett mixed films on gold were found to be capable of detecting ethanol with a sensitivity of better than 10 ppb.

Application to Soluble Surfactant Systems

By following the incorporation of ADH in real time, Caseli *et al.* were essentially performing a simple experiment on the adsorption kinetics of the soluble surfactant ADH to a bare water surface and to a surface saturated with DMPA. The adsorption kinetics of *n*-nonyl-β-D-glucopyranoside were studied in a similar way.[95] By following the intensity and peak position of OH and CH_2 bands, Meister *et al.* were able to observe sudden changes in layer thickness and conformation of surfactant tails. These sudden structural changes in the adsorbed layer were claimed to be

consistent with the formation of surface micelles during the adsorption process, a phenomenon proposed in earlier literature.[96] Initially, the hydrocarbon tails took up a preferential horizontal orientation at the interface. When sufficient molecules had adsorbed, they could form 2D clusters (or surface micelles), maintaining the horizontal chain orientation. At some later point the surface becomes saturated with these micelles (this is referred to as a granular phase elsewhere[97]), and a sharp rearrangement takes place to an upright conformation. The central wavenumber of the CH_2 bands support this conformational analysis.

Kinetic studies such as those described above are useful for studying relatively slow adsorption processes, but suffer from the major drawbacks of poor temporal resolution and ill-defined hydrodynamics. A way of circumventing these problems is to study adsorption kinetics under steady-state conditions rather than in real time. In this way, longer acquisition times can be used allowing more detailed information to be obtained for adsorption at well defined surface ages closer to $t = 0$. Using an Overflowing Cylinder (OFC) to create a continually expanding steady-state surface, Campbell *et al.* were able to quantify in detail the dynamic adsorption behaviour of CTAB,[98] $C_{10}E_8$,[99] APFN[100] and their mixtures[101] by following changes in CH_2 or CF_2 peak intensities with bulk surfactant concentration. A chemometric method of data analysis, Target Factor Analysis (TFA), was utilised in order to enhance the quantification of the dynamic surface excess at low surface coverage (through the elimination of "noise" components within a spectral dataset) and to aid the deconvolution of overlapping features in the spectra. Such deconvolution was found to be necessary to separate spectral signals arising from bulk and adsorbed surfactant.[102] For the mixed surfactant systems, three different behaviours were observed. Ideal mixing at the interface occurred over a wide range of bulk compositions for mixtures of CTAB/$C_{10}E_8$, whereas non-ideal mixing well explained by regular solution theory was found in mixtures of APFN/$C_{10}E_8$. No mixing at the interface was observed for the cationic-anionic CTAB/APFN mixture when either component was present in excess. Co-adsorption did occur, however, exclusively at equimolar bulk composition. Due to the oppositely charged headgroups CTAB and APFN interacted strongly in the bulk solution, forming vesicles. These vesicles diffused considerably more slowly than either surfactant monomer, and so an excess

of either component prevented vesicle adsorption through the formation of an electrostatic barrier at the interface. The dynamic adsorption properties of an oppositely charged polymer-surfactant mixture of poly(dmdaac)/SDS have also been investigated using the OFC.[103] Here again, bulk complexation was found to affect the surface properties, which could be explained by the diffusion-controlled adsorption of polymer/surfactant complexes of constant composition for SDS concentrations up to charge neutralisation. At higher SDS concentrations SDS alone adsorbed.

ER-FTIRS has also been used to study equilibrium properties of soluble surfactant systems. The first such study was reported by Fina *et al.* who showed that the surface excess and orientation of sodium dodecyl sulphonate (SDSn) remained constant throughout the linear region of the adsorption isotherm.[104] Similar studies have been carried out using SDS, although extended to probe the whole adsorption isotherm.[105] In this case it was found that the conformational order of the SDS tail increased with increasing concentration up to about 3 mM, after which the SDS monolayer was in a constant liquid crystalline state, although it should be noted that contributions from bulk surfactant were ignored. At all concentrations the conformational order of the SDS monolayer was found to be higher than in monomeric or micellar SDS in the bulk solution. Furthermore, the liquid crystalline state was maintained at the interface at all temperatures down to and below the Krafft point, despite the crystallisation of SDS in the bulk solution.[106] Adsorption from mixtures of SDS and SDSn, at a 1:1 molar ratio, leads to a homogeneous monolayer that is enriched in SDS.[107] Similar synergistic adsorption was observed for mixtures of sodium myristate and myristic acid.[108] Kawai *et al.* reported unusual adsorption behaviour from mixtures of SDS and cetyl pyridinium chloride (CPC).[109] The composition of the surface layer was independent of bulk SDS mole fraction, with the evolution of a novel multilayer structure at long times from solutions containing intermediate mole fractions of SDS.

The structure of ethylene glycol mono-*n*-dodecyl ether was probed using a combination of PM-IRRAS spectra at the air-water interface and infrared transmission and reflectance measurements of transferred films of Au. From the position of CH_2 stretching and bending vibrations it was deduced that the alkyl chains in the tailgroup adopted an all *trans* conformation in a crystalline

environment.[110] Using the complex refractive indices derived from reflectance measurements it was suggested that the chains have a tilt of 21° to the surface normal and a chain twist of 56° relative to the water subphase. Water-soluble poly(ethylene oxide) polymers, end capped with fluorinated helices, orient at the air-water interface with the fluorinated chains highly ordered and normal to the interface. This ordering extends into the poly(ethylene oxide) backbone, resulting in a more ordered surface layer than with uncapped polymer.

The oriented growth of crystals, common in biological systems, led to interest in template-directed crystallisation beneath surfactant films. The first ER-FTIRS study of this phenomenon was carried out by Ahn *et al.* who showed reorganisation of the monolayer on polymerisation.[111] Spread monolayers of poly(acrylic acid) and Stearic acid were found to promote the crystallisation of L-asparagine monohydrate, although the films did not nucleate specific growth of any single crystal face.[112] Crystallisation of DL-aspartic acid beneath nylon 6 films has likewise been studied.[113] DL-aspartic acid inserted into the nylon 6 film, ultimately comprising half of the material at the surface. Surface crystals of DL-aspartic acid were also formed, but on a limited scale relative to the overall surface concentration of the acid.

Since the pioneering work of Dluhy and Cornell,[34] ER-FTIRS has been applied to the study of a diverse range of chemical systems, prompting several reviews of the technique.[114-116] Molecular recognition and self assembly of urea beneath a barbituric acid monolayer,[117] changes in the structure of photochromic monolayers under differing light conditions,[118] the study of novel gemini surfactants[119] and the formation of hybrid gold-surfactant monolayers for use in a range of molecular-electronic devices[120] represent but a few examples of the other systems investigated using this powerful technique.

4.3.2 Physical Basis of ER-FTIRS

In a traditional transmission IR spectroscopy experiment, the transmittance, T, is related to the molar absorption coefficient, ε, and the absorbance, A, by the Beer-Lambert law.[2]

$$\log \frac{I}{I_0} = \log T = -\varepsilon c_n l = -A \tag{4.24}$$

Here I and I_0 are the transmitted and incident intensities, respectively, c_n is the concentration of the sample and l is the path length after which the transmittance is measured.

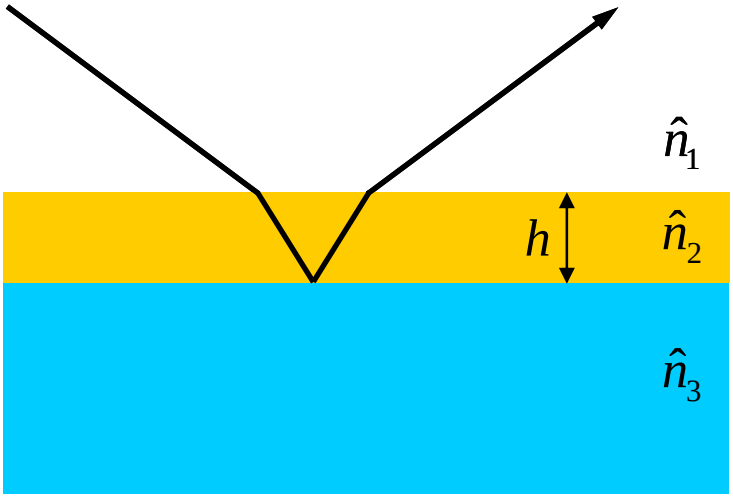

Figure 4.5 An isotropic slab model used to calculate the reflectivity of a three layer system comprising air, a monolayer of thickness h and water.

In the case of external reflection FTIR spectroscopy, the measured quantity is the reflectivity, R, of the surface. The reflectivity can be related to ε through the application of the Fresnel equations, introduced in section 1.3.2. The surface can be modelled as a system of three homogeneous, isotropic layers as illustrated by figure 4.5. If the refractive indices are taken to be n_1, $\hat{n}_2$ and $\hat{n}_3$ (where $\hat{n}_x = n_x + ik_x$) and the monolayer has thickness $h = z_2 - z_1 = \Delta z$, then the overall reflectivity of the system can be described by

$$R_{123,m} = \left|\hat{r}_{123,m}\right|^2 = \frac{\hat{r}_{12,m}^{\ 2} + \hat{r}_{23,m}^{\ 2} + 2\hat{r}_{12,m}\hat{r}_{23,m}\cos 2\beta}{1 + \hat{r}_{12,m}^{\ 2}\hat{r}_{23,m}^{\ 2} + 2\hat{r}_{12,m}\hat{r}_{23,m}\cos 2\beta} \tag{4.25}$$

where $\hat{r}_{ab,m}$ represents the complex amplitude reflection coefficient of m polarised light at the ab interface and $\beta = \left(2\pi / \lambda\right)\hat{n}_2 h \cos\hat{\theta}_2$ describes the phase change of a wave reflected through the layer (i.e. that passes through it twice) and λ is the

wavelength in vacuo. Eqn. 4.25 therefore relates the observed reflectivity to the complex refractive index of the monolayer.

Equation 4.24 can be derived by considering the sum of all waves reaching the detector after multiple reflections at the interface, for example in the case of s-polarised light;[121]

$$\begin{aligned}\hat{r}_{123,s} &= r_{12} + t_{12}r_{23}t_{21} + t_{12}r_{23}{}^{2}r_{21}t_{21} + t_{12}r_{23}{}^{3}r_{21}{}^{2}t_{21} + ...\\ \hat{r}_{123,s} &= r_{12} + t_{12}r_{23}t_{21}(1 + r_{23}r_{21} + r_{23}{}^{2}r_{21}{}^{2} + ...)\\ \hat{r}_{123,s} &= r_{12} + \frac{t_{12}r_{23}t_{21}}{1 - r_{23}r_{21}}\end{aligned} \tag{4.26}$$

In eqn. 4.26, r_{xy} and t_{xy} are the Fresnel coefficients of reflection and transmission, respectively, for the relevant interface. Substitution of expressions for r_{xy} and t_{xy} (see section 1.2.3) into eqn. 4.26 gives the Fresnel coefficient of reflection for the three-layer system.

$$\hat{r}_{123,s} = e^{2iq_1z_1}\frac{\hat{r}_{12,m} + \hat{r}_{23,m}e^{2iq_2\Delta z}}{1 + \hat{r}_{12,m}\hat{r}_{23,m}e^{2iq_2\Delta z}} \tag{4.27}$$

In eqn. 4.27, $q_n = (2\pi / \lambda)\hat{n}_n \cos\theta_n$, and represents the surface-normal momentum transfer at each interface within the monolayer. The reflectivity of the interface is given by the square of the Fresnel coefficient, yielding the result quoted in eqn. 4.25. An identical expression for p-polarised light can be derived in the same way.

The Kramers-Kronig relations link the real and imaginary parts of analytical functions. The calculation of the real part of the refractive index from the imaginary part can be given by;

$$n(\bar{\nu}) - n_\infty = \frac{2}{\pi}P\int_0^\infty \frac{k(\bar{\nu}')}{\bar{\nu}'^2 - \bar{\nu}^2}\,d\bar{\nu}' \tag{4.28}$$

Here n_∞ is the refractive index in the case where the material does not absorb and $\bar{\nu}$ is the wavenumber. The symbol *P* denotes that the Cauchy principal value at the

pole, i.e. the singularity at $\tilde{\nu} = \tilde{\nu}'$, is excluded from the integration. The imaginary part can be calculated using eqn. 4.29, derived from the Beer-Lambert law.

$$k = \frac{\lambda}{4\pi} \varepsilon c_n \tag{4.29}$$

Equation 4.25 can be used to calculate model reflectivity curves for the air-water (R_0) and air-monolayer-water (R_s) interfaces, which can then be used to derive model ER-FTIR spectra on a scale of normalised intensity $\Delta R / R_0$, where $\Delta R = R_s - R_0$. Values for the complex refractive index of water were taken from ATR-IR spectra in the range 4000-1500 cm^{-1} by Bertie *et al.*.[122] The refractive index of a saturated monolayer of CTAB was modelled by modifying the refractive index of hexadecane, $n_{2,\infty} = 1.41$,[123] with four Lorentzian oscillators using the dispersion relation,[124]

$$\hat{\varepsilon}_r = (n + ik)^2 = \varepsilon_{r,\infty} - \sum_m \frac{a^2}{\tilde{\nu}'^2 - \tilde{\nu}^2 + i\tilde{\nu}\gamma} \tag{4.30}$$

where *a* is the amplitude of the oscillator, $\tilde{\nu}'$ is its central wavenumber and γ is the linewidth. The parameters used in eqn. 4.30 were derived from fitting of a subtracted monolayer spectrum of 1 mM CTAB with a thickness of 1 nm, and are summarised in table 4.2.

Table 4.2 *Peak fitting parameters used in the modelling of reflectivity of the air-monolayer-solution system.*

Peak	A	B	C	D
$\tilde{\nu}'$ / cm^{-1}	2961	2924	2891	2854
a / cm^{-1}	46.6	115.6	36.5	74.8
γ / cm^{-1}	12.8	19.3	26.1	12.8

To consider the effect of bulk surfactant, the refractive index of water was modified using the Lorentz-Lorenz effective medium approximation taking into account the volume fractions of water (ψ_{water}) and surfactant ($\psi_{surfactant}$).

$$\frac{\hat{n}_3^{\,2}-1}{\hat{n}_3^{\,2}+2}=\varphi_{water}\frac{\hat{n}_{water}^{\,2}-1}{\hat{n}_{water}^{\,2}+2}+\psi_{surfactant}\frac{\hat{n}_{surfactant}^{\,2}-1}{\hat{n}_{surfactant}^{\,2}+2} \qquad (4.31)$$

Figure 4.6 shows the wavenumber-dependent variation in the real and imaginary parts of the oscillator modified refractive index of CTAB. The variation in *n* around a vibrational band is dispersive-shaped, whilst the variation in *k* is peak-shaped.

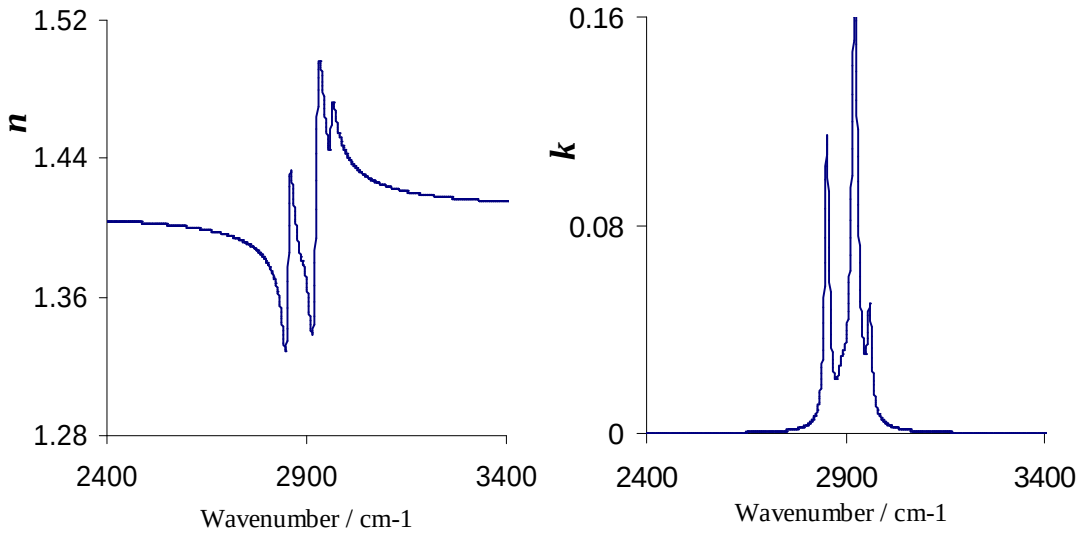

Figure 4.6 Real, left, and imaginary, right, parts of the oscillator modified refractive index of a model C_{16}TAB layer of 1 nm thickness.

Subtracted monolayer spectra sit on highly curved baselines in the C-H region due to the anti-reflection properties of organic thin films. The refractive index of the CTAB film lies between that of the incident and reflecting air and water, resulting in a loss of intensity on multiple reflections within the film. For the analysis of real experimental spectra, therefore, a method of baseline subtraction has to be applied as described in section 4.5.3. The appearance of this baseline curvature can be seen in figure 4.7, along with the effect of increasing bulk surfactant concentration. The modelled spectra from the surface of a 1 mM CTAB solution shows that the majority of the signal results from the variation in *k*, and so absorption bands in ER-FTIR spectra are predominantly peak shaped. With increasing bulk surfactant concentration, however, the contribution from variation in *n* can become significant, as can be seen from the modelled spectrum from the surface of a 10 mM CTAB solution, where significant dispersive contributions further complicate the curvature of the baseline. The contributions of bulk surfactant, therefore, are largely dispersive-

shaped, and in sufficiently severe cases can lead to apparent peak shifts in recorded spectra, as demonstrated by the peak at approximately 2920 cm^{-1} in figure 4.7.

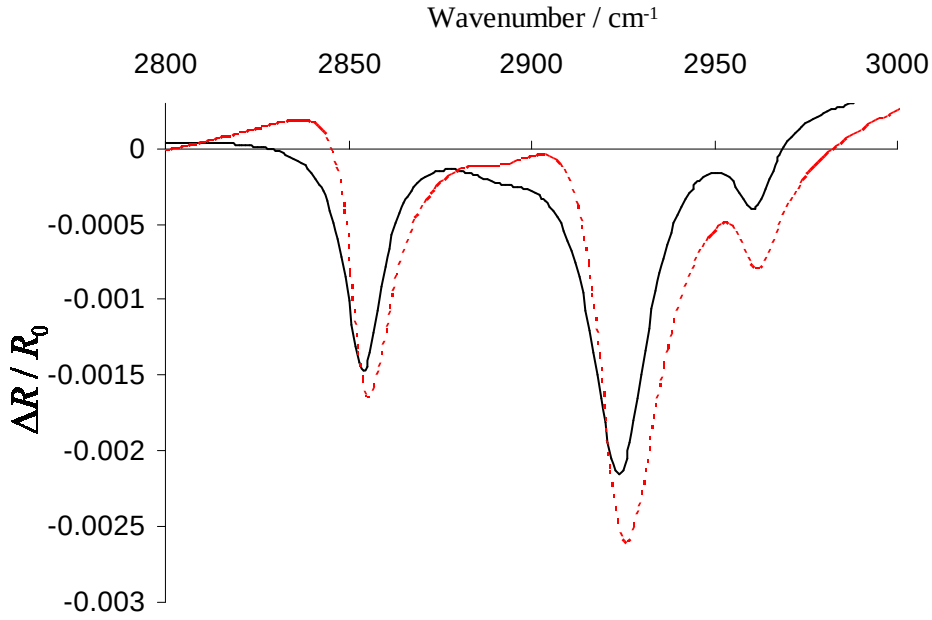

Figure 4.7 Modelled subtracted monolayer spectra for a saturated CTAB monolayer, 10 Å thickness, above (solid line) 1 mM bulk surfactant and (dashed line) 10 mM bulk surfactant.

Mielczarski showed that the maximum values of $\Delta R / R_0$ for peaks in a p-polarised spectrum are obtained close to the Brewster angle.[36] Figure 4.8 also shows the variation in reflectivity for p- and s-polarised light (3000 cm^{-1}) as a function of angle of incidence, however, where it can be seen that the reflectivity of p-polarised light is very low close to Brewster angle. Practically this has been shown to reduce the signal-to-noise ratio for p-polarised spectra close to the Brewster angle.[125] It is therefore more appropriate to use a lower angle of incidence, in the range 30-40°, where the signal-to-noise ratio for s-polarised spectra is also optimised. Experimentally, however, the angle of incidence used is determined by the optical layout, resulting in an angle of incidence of 50° being used throughout this chapter (see section 4.5.2).

Since the peaks in ER-FTIR spectra have their origins in the variations in the real and imaginary parts of the refractive index of both the monolayer and solution about a vibrational band – which modify the Fresnel reflection coefficients and therefore in turn the overall reflectivity of the interface – the technique is best described as a form

of spectroscopic reflectometry rather than a traditional absorption spectroscopy. The following section describes an analytical technique, 2D correlation analysis, which can be used to further enhance the potential of ER-FTIR as a tool for studying monolayer systems.

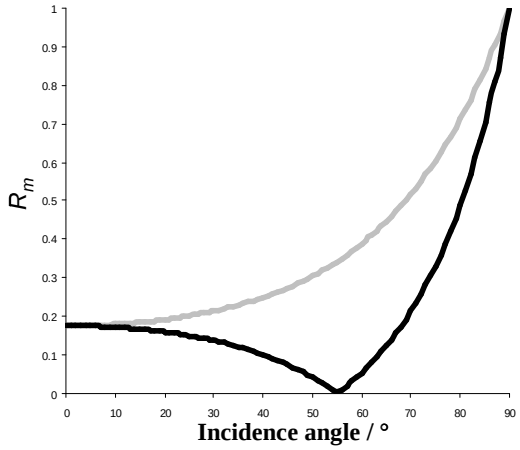

Figure 4.8 The reflectivity curves for s- (grey) and p- (black) polarised light (at 3000 cm^{-1}) as a function of incidence angle.

4.4 Two-Dimensional Correlation Spectroscopy

The concept of enhancing resolution by obtaining spectra as a function of two independent spectral axes, and therefore spreading peaks over a second spectral dimension, has been commonplace in the field of NMR spectroscopy for several decades.[126] A 2D NMR spectrum is generated from the double Fourier transform of a set of time-domain spectra collected whilst a series of pulses of radio frequency radiation are applied to the sample. These pulses act as a periodic and well-defined external perturbation and the resulting 2D spectrum gives information about the coupled relaxation of nuclei between pulses. The direct application of such a pulse-based procedure to the field of optical spectroscopy was initially hampered by the relative timescales of the relaxation processes involved, as the nuclear relaxation probed by NMR is a much slower process than the vibrational relaxation studied by, for example, IR spectroscopy. In recent years, however, improvements to femtosecond laser systems have allowed such "conventional" 2D-IR experiments to become more commonplace.[127] Although the analytical technique of 2D correlation spectroscopy introduced in this section uses many of the same mathematical concepts

as 2D NMR (indeed the field emerged from a consideration of the mathematical background of 2D NMR spectroscopy) the physical basis of the two techniques is different. Whilst 2D-NMR experiments generally investigate intramolecular coupling between nuclei in order to gain insight into the connectivity of a molecule, 2D correlation IR experiments are concerned with larger scale changes involving groups of atoms, such as chemical reactions or molecular rearrangements.

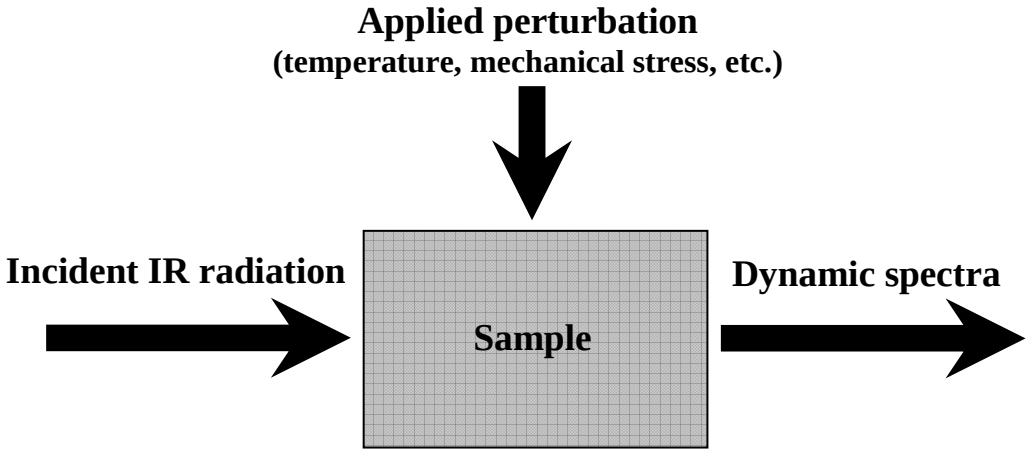

Figure 4.9 Schematic of a 2D-IR experiment.

The fundamental requirement for the production of a 2D correlation spectrum is the application of an external perturbation (for example temperature, pressure etc.) which produces a change in the spectral response of the system (figure 4.9). Spectra are then collected as a function of this external perturbation and a cross-correlation analysis is applied to the perturbation-domain data set. In the late 1980s a novel approach was introduced by Noda that allowed mathematical concepts from 2D NMR to be applied to optical spectroscopy.[128-130] An external perturbation in the form of a sinusoidally varying strain was applied to polymer films containing a binary mixture of two immiscible polymers, low density polyethylene and atactic polystyrene. It was found that the molecular level reorganisation of the two polymers was completely uncorrelated, as expected from such an immiscible (and therefore phase-separated) blend. These findings represented a significant leap in the application of 2D correlation methodologies to optical spectroscopy, and indeed there has been a large body of research that utilises the original sinusoidal perturbation-based approach as set out by Noda.[131, 132] This approach is only effectively implemented when the spectral response varies sinusoidally (i.e. a linear

spectral response to a perturbation with a sinusoidal waveform), however, and so a new, generalised 2D correlation spectroscopy was developed to allow the effects of a much wider range of external perturbations (temperature, pressure, concentration etc.) of any arbitrary waveform to be studied.[133]

4.4.1 Generalised 2D Correlation Spectroscopy

A set of spectra obtained according to the general scheme outlined in figure 4.9 can be converted to a dynamic spectrum, upon which the 2D correlation analysis is performed. The dynamic spectrum of a system, derived from a set of spectra collected as a function of external perturbation *t* between T_{min} and T_{max}, is defined as[131]

$$\tilde{y}(\upsilon,t) = \begin{cases} y(\upsilon,t) - \overline{y}(\upsilon,t) & T_{\min} \le t \le T_{\max} \\ 0 & t < T_{\min}, t > T_{\max} \end{cases} \tag{4.32}$$

where $y(\upsilon,t)$ is the perturbation induced variation in spectral intensity and $\overline{y}(\upsilon,t)$ is known as the reference spectrum. The form of the reference spectrum is not specified, and is largely a matter of convenience depending upon the particular application. The most commonly used reference spectrum is the average (static) spectrum of the system, but could equally well be chosen as the spectrum observed at a fixed reference point such as the initial or final state of the system. The reference spectrum can also be set equal to zero, although this can lead to the appearance of extra peaks that can complicate the appearance of the asynchronous spectra. The average spectrum is used as reference throughout this thesis.

The 2D correlation concept is then to quantitatively compare spectral intensity variations for all pairs, υ_1 and υ_2, of spectral variables along the perturbation coordinate *t*. The 2D correlation spectrum is then formally expressed as

$$X(\upsilon_1,\upsilon_2) = \left\langle \tilde{y}(\upsilon_1,t) \cdot \tilde{y}(\upsilon_2,t) \right\rangle \tag{4.33}$$

where $\left\langle \ \right\rangle$ denotes the use of a cross-correlation function (see eqn. 4.35, below). The correlation intensity, $X(\upsilon_1,\upsilon_2)$, is then a measure of the relative similarity or dissimilarity in the intensity changes at the two spectral variables υ_1 and υ_2.

The specific choice of correlation function, and the manipulation of the correlation intensity, is somewhat arbitrary. It turns out to be both simple and convenient to treat the 2D correlation spectrum as a complex function.[134, 135]

$$X(\upsilon_1,\upsilon_2) = \Phi(\upsilon_1,\upsilon_2) + i\Psi(\upsilon_1,\upsilon_2) \tag{4.34}$$

In this way, the 2D correlation intensity is split into two orthogonal components. The synchronous correlation intensity, $\Phi(\upsilon_1,\upsilon_2)$, contains information about the overall similarity or coincidence between changes observed at pairs of spectral variables, whereas the asynchronous correlation intensity, $\Psi(\upsilon_1,\upsilon_2)$, contains information about the relative dissimilarity or out-of-phase character of the spectral changes.

The generalised 2D correlation function is defined as

$$\Phi(\upsilon_1,\upsilon_2) + i\Psi(\upsilon_1,\upsilon_2) = \frac{1}{\pi(T_{\max} - T_{\min})}\int_0^\infty \tilde{Y}_1(\omega)\cdot\tilde{Y}_2^*(\omega)d\omega \tag{4.35}$$

where $\tilde{Y}_1(\omega)$ is the forward Fourier transform of $\tilde{y}(\upsilon_1,t)$ and ω is its Fourier frequency component of the spectral variation along the external perturbation *t*. Likewise, $\tilde{Y}_2^*(\omega)$ is the conjugate Fourier transform of $\tilde{y}(\upsilon_2,t)$. Both $\tilde{Y}_1(\omega)$ and $\tilde{Y}_2^*(\omega)$ can be expressed in terms of real and imaginary components of the respective Fourier transforms, where the real components are even functions and the imaginary components are odd functions. The υ-dependence of the Fourier transforms has been omitted for clarity in the proceeding equations.

$$\tilde{Y}_1(\omega) = \int_{-\infty}^{\infty}\tilde{y}(\upsilon_1,t)e^{-i\omega t}dt = \tilde{Y}_1^{\mathrm{Re}}(\omega) + i\tilde{Y}_1^{\mathrm{Im}}(\omega) \tag{4.36}$$

$$\tilde{Y}_2^*(\omega) = \int_{-\infty}^{\infty} \tilde{y}(\upsilon_2, t) e^{+i\omega t} dt = \tilde{Y}_2^{\mathrm{Re}}(\omega) - i\tilde{Y}_2^{\mathrm{Im}}(\omega) \tag{4.37}$$

All that is required in order to generate the synchronous and asynchronous 2D correlation spectra, therefore, is to perform the appropriate Fourier transforms of the measured dynamic spectrum as set out by eqn. 4.31.

The terms dynamic, asynchronous and synchronous have been retained from the origins of 2D correlation in the framework of statistical time-series analysis where the perturbation *t* is assumed to be the passage of time. In the same way that the nature of this perturbation is not limited to such purely chronological forms, the probe used can originate from any form of spectroscopy, including those from x-ray and neutron scattering studies and even to other fields such as mass spectrometry or chromatography. The generalised 2D correlation method has also been applied to NMR spectra,[136, 137] showing that the technique has grown out of its origins and become well established in its own right.

4.4.2 Cross Correlation Analysis

Having introduced the central tenets of generalised 2D correlation analysis it is useful to consider some concepts of classical statistical cross-correlation analysis to reveal the significant crossover between the two formalisms and discover why the arbitrary choice of correlation function in eqn. 4.34 proves to be particularly useful.

The classical cross-correlation function between distinct dynamic intensity variations observed with the progression of *t* between T_{min} and T_{max} is given by[138]

$$C(\tau) = \frac{1}{T_{\max} - T_{\min}} \int_{T_{\min}}^{T_{\max}} \tilde{y}(\upsilon_1, t) \cdot \tilde{y}(\upsilon_2, t+\tau) dt \tag{4.38}$$

where τ is the correlation time. The cross-correlation function compares the time-dependence of two functions shifted by a constant τ. The Fourier transform of such a convolution integral is given by the product of the Fourier transforms of the individual functions and so the cross spectrum, $S(\omega)$ (i.e. the Fourier transform of eqn. 4.38), is given by

$$S(\omega) = \frac{\tilde{Y}_1^*(\omega) \cdot \tilde{Y}_2(\omega)}{T_{\max} - T_{\min}} = \phi_\omega(\upsilon_1, \upsilon_2) - i\psi_\omega(\upsilon_1, \upsilon_2) \tag{4.39}$$

The real and negative imaginary components of the cross spectrum are referred to as the cospectrum and the quad-spectrum, respectively, where the term spectrum refers to the Fourier domain representation of the time-dependent intensities. The co- and quad-spectra can be expressed in terms of the real and imaginary components of the Fourier transforms in eqn. 4.35.

$$\phi_\omega(\upsilon_1, \upsilon_2) = \frac{1}{T_{\max} - T_{\min}} \left[\tilde{Y}_1^{\mathrm{Re}}(\omega) \cdot \tilde{Y}_2^{\mathrm{Re}}(\omega) + \tilde{Y}_1^{\mathrm{Im}}(\omega) \cdot \tilde{Y}_2^{\mathrm{Im}}(\omega) \right] \tag{4.40}$$

$$\psi_\omega(\upsilon_1, \upsilon_2) = \frac{1}{T_{\max} - T_{\min}} \left[\tilde{Y}_1^{\mathrm{Im}}(\omega) \cdot \tilde{Y}_2^{\mathrm{Re}}(\omega) - \tilde{Y}_1^{\mathrm{Re}}(\omega) \cdot \tilde{Y}_2^{\mathrm{Im}}(\omega) \right] \tag{4.41}$$

By inspection of eqn. 4.35, it can be seen that the synchronous and asynchronous 2D correlation spectra are related to the cospectrum and quad-spectrum, respectively, by

$$\Phi(\upsilon_1, \upsilon_2) = \frac{1}{\pi} \int_0^\infty \phi_\omega(\upsilon_1, \upsilon_2) d\omega \tag{4.42}$$

$$\Psi(\upsilon_1, \upsilon_2) = \frac{1}{\pi} \int_0^\infty \psi_\omega(\upsilon_1, \upsilon_2) d\omega \tag{4.43}$$

Thus it can be seen that the cospectrum and quad-spectrum are the Fourier components of the synchronous and asynchronous 2D correlation spectra. The cross-correlation function and the 2D correlation intensity are therefore related, and this fact can be used to greatly simplify the calculation of the synchronous and asynchronous correlation spectra.

Synchronous Correlation Spectrum

The Wiener-Khintchine theorem is used to relate the cross-correlation of a pair of functions and the Fourier transforms of those functions as shown in eqn. 4.44, where $Y^*(\omega)$ and $G(\omega)$ are Fourier transforms of $f(t)$ and $g(t)$ in a similar fashion to eqns. 4.35 – 4.37.

$$\left\langle f(t)\cdot g(t)\right\rangle = \int_{-\infty}^{\infty} f(t)\cdot g^{*}(t+\tau)d\tau = \int_{-\infty}^{\infty} Y^{*}(\omega)\cdot G(\omega)e^{i\omega t}d\omega \qquad (4.44)$$

This allows eqn. 4.38 to be re-written as

$$C(\tau) = \frac{1}{2\pi(T_{\max}-T_{\min})}\int_{-\infty}^{\infty} \tilde{Y}_{1}^{*}(\omega)\cdot\tilde{Y}_{2}(\omega)e^{i\omega\tau}d\omega \qquad (4.45)$$

which, for $\tau = 0$, reduces to

$$C(0) = \frac{1}{2\pi(T_{\max}-T_{\min})}\int_{-\infty}^{\infty} \tilde{Y}_{1}^{*}(\omega)\cdot\tilde{Y}_{2}(\omega)d\omega \qquad (4.46)$$

Only the real component of eqn. 4.46 is non-zero, as the imaginary component of a Fourier transform is an odd function. Therefore,

$$C(0) = \frac{1}{\pi(T_{\max}-T_{\min})}\mathrm{Re}\left\{\int_{0}^{\infty} \tilde{Y}_{1}^{*}(\omega)\cdot\tilde{Y}_{2}(\omega)d\omega\right\} \qquad (4.47)$$

Eqn. 4.47 is identical to the real part of eqn. 4.35, and is therefore equivalent to the synchronous correlation spectrum. The synchronous correlation spectrum can then be computed directly from the cross-correlation function with $\tau = 0$, avoiding the use of Fourier transforms, as given in eqn. 4.48.

$$\Phi(\upsilon_{1},\upsilon_{2}) = \frac{1}{T_{\max}-T_{\min}}\int_{T_{\min}}^{T_{\max}} \tilde{y}(\upsilon_{1},t)\cdot\tilde{y}(\upsilon_{2},t)dt \qquad (4.48)$$

Asynchronous Correlation Spectrum

It is also possible to circumvent the use of Fourier transforms in the calculation of asynchronous correlation spectra, by making use of the Hilbert transform, defined in eqn. 4.49 for the analytical function $g(t)$.

$$h(t) \equiv \frac{1}{\pi}P\int_{-\infty}^{\infty}\frac{g(t')}{t'-t}dt' \qquad (4.49)$$

Here P indicates the use of the Cauchy principal value of the integral is taken. The Hilbert transform is similar to the Kramers-Kronig transformation introduced earlier.

Closer inspection of the Hilbert transform shows that it can be considered as the integral of a convolution of the functions $g(t)$ and $1/t$. The Fourier transform of the Hilbert transform is therefore related to the product of the Fourier transforms of these two functions by

$$H(\omega) = \int_{-\infty}^{\infty} h(t)e^{-i\omega t}dt = \frac{1}{\pi}\int_{-\infty}^{\infty}\frac{1}{t}e^{-i\omega t}dt \cdot \int_{-\infty}^{\infty} g(t)e^{-i\omega t}dt \tag{4.50}$$

In turn, the Fourier transform of the Hilbert transform and of the function $g(t)$ (denoted as $G(\omega)$) are related by the signum function, whose value is either -1, 0 or +1 dependent upon whether ω is greater than, equal to or less than zero.

$$\begin{aligned} H(\omega) &= i\,\mathrm{sgn}(\omega)\cdot G(\omega) \\ H(\omega) &= \begin{cases} -G^{\mathrm{Im}}(\omega) + iG^{\mathrm{Re}}(\omega) & \omega > 0 \\ 0 & \omega = 0 \\ G^{\mathrm{Im}}(\omega) - iG^{\mathrm{Re}}(\omega) & \omega < 0 \end{cases} \end{aligned} \tag{4.51}$$

The Hilbert transform therefore causes a phase shift of magnitude $\pi/2$ in the Fourier components of a function $g(t)$, and hence the two functions are orthogonal.

This orthogonality can be used to produce a simplified expression for the asynchronous correlation spectrum through the introduction of an orthogonal spectrum, $\tilde{x}(\upsilon_2, t)$ such that

$$\tilde{x}(\upsilon_2, t) \equiv \frac{1}{\pi} P\int_{-\infty}^{\infty}\frac{\tilde{y}(\upsilon_2, t')}{t' - t}dt' \tag{4.52}$$

The cross-correlation function between the dynamic and orthogonal spectra is then given by

$$D(\tau) = \frac{1}{T_{\max} - T_{\min}}\int_{T_{\min}}^{T_{\max}} \tilde{y}(\upsilon_1, t)\cdot\tilde{x}(\upsilon_2, t+\tau)dt \tag{4.53}$$

Eqn. 4.53 can be expressed, as before, in terms of the Fourier transforms of the dynamic and orthogonal spectra, as shown in eqn. 4.54.

$$D(\tau) = \frac{1}{2\pi(T_{\max} - T_{\min})} \int_{-\infty}^{\infty} \tilde{Y}_1^*(\omega) \cdot \tilde{X}_2(\omega) e^{i\omega\tau} d\omega \tag{4.54}$$

Setting the correlation time equal to zero and applying the relation in eqn. 4.57 recasts eqn. 4.54 in terms of the dynamic spectrum alone.

$$\begin{aligned} D(0) &= \frac{i}{2\pi(T_{\max} - T_{\min})} \int_{-\infty}^{\infty} \operatorname{sgn}(\omega) \tilde{Y}_1^*(\omega) \cdot \tilde{Y}_2(\omega) d\omega \\ D(0) &= \frac{1}{2\pi} \int_{-\infty}^{\infty} i \operatorname{sgn}(\omega) S(\omega) d\omega \end{aligned} \tag{4.55}$$

Comparison of eqns. 4.55, 4.39 and 4.51 then leads to a direct expression for the asynchronous correlation function, showing the asynchronous correlation intensity to be the *t*-average of the product of the dynamic and orthogonal spectra at υ_1 and υ_2.

$$\Psi(\upsilon_1, \upsilon_2) = \frac{1}{T_{\max} - T_{\min}} \int_{T_{\min}}^{T_{\max}} \tilde{y}(\upsilon_1, t) \cdot \tilde{x}(\upsilon_2, t) dt \tag{4.56}$$

4.4.3 Computation of 2D Correlation Spectra

The elimination of the need for Fourier transforms in the calculation of both the synchronous and asynchronous spectra greatly simplifies the practical computation of 2D correlation spectra. In addition, the integral equations presented thus far are converted into discrete summations of cross-correlated pairs to account for a discrete data set of *m* points along the perturbation axis *t* during the measurement interval (eqns. 4.57). As a result, it is instructive to think of the dynamic spectrum as a matrix, where each column gives the dynamic change at a given υ along the perturbation axis (eqn. 4.58).

$$\begin{aligned} \Phi(\upsilon_1, \upsilon_2) &= \frac{1}{m-1} \sum_{j=1}^{m} \tilde{y}_j(\upsilon_1) \cdot \tilde{y}_j(\upsilon_2) \\ \Psi(\upsilon_1, \upsilon_2) &= \frac{1}{m-1} \sum_{j=1}^{m} \tilde{y}_j(\upsilon_1) \cdot \tilde{x}_j(\upsilon_2) \end{aligned} \tag{4.57}$$

$$Y = \begin{pmatrix} \tilde{y}(\upsilon_1, t_1) & \tilde{y}(\upsilon_2, t_1) & ..... & \tilde{y}(\upsilon_n, t_1) \\ \tilde{y}(\upsilon_1, t_2) & \tilde{y}(\upsilon_2, t_2) & ..... & \tilde{y}(\upsilon_n, t_2) \\ ..... & ..... & ..... & ..... \\ \tilde{y}(\upsilon_1, t_m) & \tilde{y}(\upsilon_2, t_m) & ..... & \tilde{y}(\upsilon_n, t_m) \end{pmatrix} \tag{4.58}$$

The synchronous correlation between intensity changes along *t* for two spectral variables υ_x and υ_y is then given by the product of two dynamic spectrum matrix elements and the whole synchronous correlation spectrum is simply a table of variance and covariance between vectors in the dynamic spectral matrix, i.e. the covariance matrix as given by eqn. 4.59.

$$\Phi_{\upsilon\upsilon} = \frac{1}{m-1} Y^T Y \tag{4.59}$$

Likewise, the asynchronous spectrum is obtained by multiplying the dynamic spectrum matrix (eqn. 4.58) with its orthogonal counterpart, obtained through the use of the Hilbert-Noda transformation matrix, *N*, as

$$\Psi_{\upsilon\upsilon} = \frac{1}{m-1} Y^T N Y \tag{4.60}$$

where *NY* gives the orthogonal spectrum and

$$N = \begin{pmatrix} 0 & 1 & 1/2 & .... \\ -1 & 0 & 1 & .... \\ -1/2 & -1 & 0 & .... \\ .... & .... & .... & .... \end{pmatrix} \tag{4.61}$$

By computing the 2D correlation spectra in this manner only elementary calculations need be performed, avoiding the use of complex number calculations as are required by fast Fourier transform algorithms. It has been demonstrated that this direct Hilbert transform method gives the most efficient computational method for a dynamic spectrum produced from up to 128 individual data sets.[139]

Pre-treatment of Data

It has been demonstrated by several authors[140-145] that various artefacts can be introduced into 2D correlation spectra by random fluctuations in the original data set. As a result, different methods of spectral pre-treatment have been used to remove these artefacts caused by non-specific intensity changes, including baseline correction methods,[140, 145] normalisation,[140] spectral deconvolution[146] and the statistical smoothing of data by techniques such as principal component analysis.[144] In all cases the appearance of the 2D correlation spectra were greatly simplified by the pre-treatment, especially the asynchronous spectra which are particularly sensitive to the small uncorrelated fluctuations associated with random noise. However, the noise levels and background fluctuations were, in all cases, much greater than those encountered in the present study and so no extra pre-treatment of data was employed other than that described in section 4.5.3.

All 2D correlation spectra presented in this thesis were calculated using the program 2D shige, kindly made freely available by Shigeaki Morita at Kwansei Gakuin University, Japan.

4.4.4 Properties of 2D Correlation Spectra

Synchronous 2D Correlation Spectrum

The intensity of the synchronous correlation spectrum provides a measure of the similarity in the variation of spectral intensity at two separate points as the external perturbation is applied. As such, peaks appearing in the synchronous spectrum arise from spectral bands whose intensity changes simultaneously or coincidentally through the course of the measurement.

An example of a synchronous 2D correlation spectrum is shown in figure 4.10, where shaded regions symbolise negative correlation intensity. Synchronous spectra are always symmetrical with respect to the diagonal $\upsilon_1 = \upsilon_2$. The 2D spectrum shown here is made up from four separate peaks, located at 2750 cm^{-1}, 2850 cm^{-1}, 2950 cm^{-1} and 3050 cm^{-1}. The presence of four *autopeaks* (at coordinates [2750,

2750], [2850, 2850] etc.) located along the diagonal confirms this fact, as the intensity change of a single peak is necessarily simultaneously correlated with itself. Since the synchronous correlation intensity has been shown to be a measure of the overall similarity of the spectral intensity change at any given set of coordinates, it follows that the magnitude of the autopeaks represents the susceptibility of that particular spectral region to change under the applied perturbation. Moreover, this means that autopeaks must always be positive.

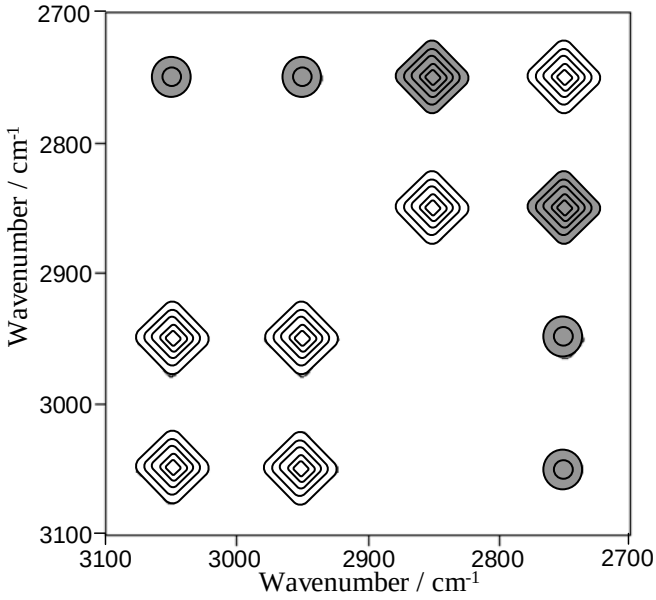

Figure 4.10 Example of a synchronous 2D correlation spectrum made up from four bands centred at 2750, 2850, 2950 and 3050 cm^{-1} respectively. Shaded areas indicate regions of negative correlation intensity.

In addition to the presence of diagonal autopeaks, synchronous correlation spectra contain cross-peaks located at off-diagonal coordinates. Correlation squares, such as those observable in figure 4.10, can be drawn between pairs of autopeaks and symmetrically positioned crosspeaks. The presence of these correlation squares indicates a synchronicity or concurrence in the spectral changes occurring at the positions of the pair of autopeaks that make up the square. In the example shown in figure 4.10, therefore, the spectral bands at 2750 cm^{-1} and 2850 cm^{-1} are synchronously correlated, as are the bands at 2950 cm^{-1} and 3050 cm^{-1}. Whilst the sign of the autopeaks is necessarily positive, synchronous crosspeaks may be either positive or negative, with the sign of a pair of crosspeaks giving information about the relative directions of the intensity changes of two bands. In the present example,

positive crosspeaks indicate that the bands at 2950 cm^{-1} and 3050 cm^{-1} change intensity in the same direction, whilst negative crosspeaks between the bands at 2750 cm^{-1} and 2850 cm^{-1} indicate that one band increases in intensity as the other decreases. It should be noted, however, that there is no indication as to the absolute direction of any intensity change, only the relative directions between each correlated pair.

Asynchronous 2D Correlation Spectrum

Peaks in an asynchronous 2D correlation spectrum arise from sequential or successive changes in spectral intensity, and therefore asynchronous spectra contain only crosspeaks as shown in figure 4.11. Asynchronous correlation spectra are always antisymmetric with respect to the diagonal $\upsilon_1 = \upsilon_2$. It is again possible to draw correlation squares between pairs of crosspeaks and the positions on the diagonal corresponding to autopeaks in the synchronous spectrum. In the example shown, correlation squares indicate asynchronous correlation between bands at 2750 cm^{-1} and 2950 cm^{-1}, 2750 cm^{-1} and 3050 cm^{-1}, 2850 cm^{-1} and 2950 cm^{-1} in addition to 2850 cm^{-1} and 3050 cm^{-1}.

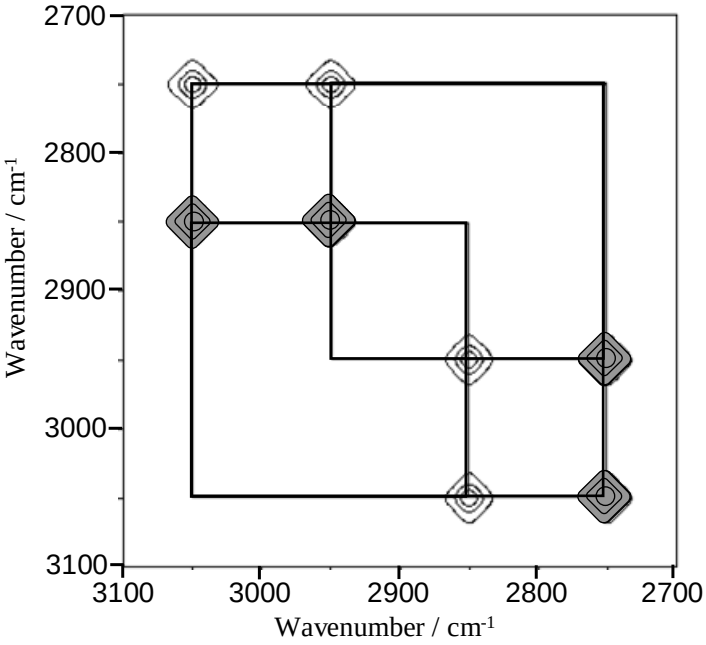

Figure 4.11 Example asynchronous correlation spectrum based on the same four bands as in figure 4.10.

It is apparent from figure 4.11 that asynchronous correlation spectra are typically much more complicated to analyse than the corresponding synchronous spectra, largely due to the absence of autopeaks. This feature is useful, however, as an aid to identifying highly overlapped bands whose response is out of phase under the influence of an external perturbation since crosspeaks will be present even for bands with very similar positions. Such situations arise, for example, in mixtures where each component contains similar functional groups. 2D correlation spectroscopy is ideally suited, therefore, to the study of mixtures of alkyl-chain surfactants and *n*-alkanes.

The sign of crosspeaks in asynchronous correlation spectra can be used to deduce the sequential order of spectral events, using a set of empirical rules, sometimes referred to as Noda's rules;[129]

1. A positive synchronous crosspeak, in conjunction with a positive asynchronous crosspeak at coordinates (υ_1, υ_2) indicates that the intensity change at υ_1 occurs first.

2. A positive synchronous crosspeak in conjunction with a negative asynchronous crosspeak at coordinates (υ_1, υ_2) indicates that the intensity change at υ_2 occurs first.

3. A negative synchronous crosspeak in conjunction with a positive asynchronous crosspeak at coordinates (υ_1, υ_2) indicates that the intensity change at υ_2 occurs first.

4. A negative synchronous crosspeak in conjunction with a negative asynchronous crosspeak at coordinates (υ_1, υ_2) indicates that the intensity change at υ_1 occurs first.

These rules can then be used to assign an order to the spectral changes in the examples shown in figs. 4.10 and 4.11, where we find that the changes at 2950 cm^{-1} and 3050 cm^{-1} occur predominantly after those at 2750 cm^{-1} and 2850 cm^{-1}. Care

must be taken when applying Noda's rules since the asynchronous spectra produced from raw spectra containing even a moderate number of highly overlapped peaks can contain contradictory features that preclude such a simple analysis. These considerations are discussed in section 4.4.5, and again in section 4.6 in the context of present results.

4.4.5 Properties of 2D Correlation Spectra Containing Features Other Than Simple Intensity Changes

As has been noted, the application of Noda's rules for analysing 2D correlation spectra are only reliable if the spectral variations are fairly monotonic and are confined to simple changes in intensity. Exceptions arise when more complicated features are present in the basis data set, such as peak shifts and band broadening commonly effected when an external perturbation changes the physical environment of the system under study, for example during a phase transition. In such instances the simple relationship between spectral bands and correlation peaks breaks down and it becomes necessary to use spectral simulations to avoid the over-interpretation of multiple correlation peaks. Fortunately, many of the complex patterns observed in 2D correlation spectra are highly characteristic of particular changes in the underlying dynamic spectrum and so provide a readily identifiable fingerprint that greatly aids the subsequent analysis of such correlation spectra. Of particular relevance are the following four scenarios:

1. Peak shifts caused by a single band of constant intensity changing position.
2. Peak shifts of a single band coupled with a change in intensity.
3. Peak shifts brought about by the disappearance of one band concurrently with the appearance of a second band of similar central wavenumber.
4. Broadening or narrowing of a single band.

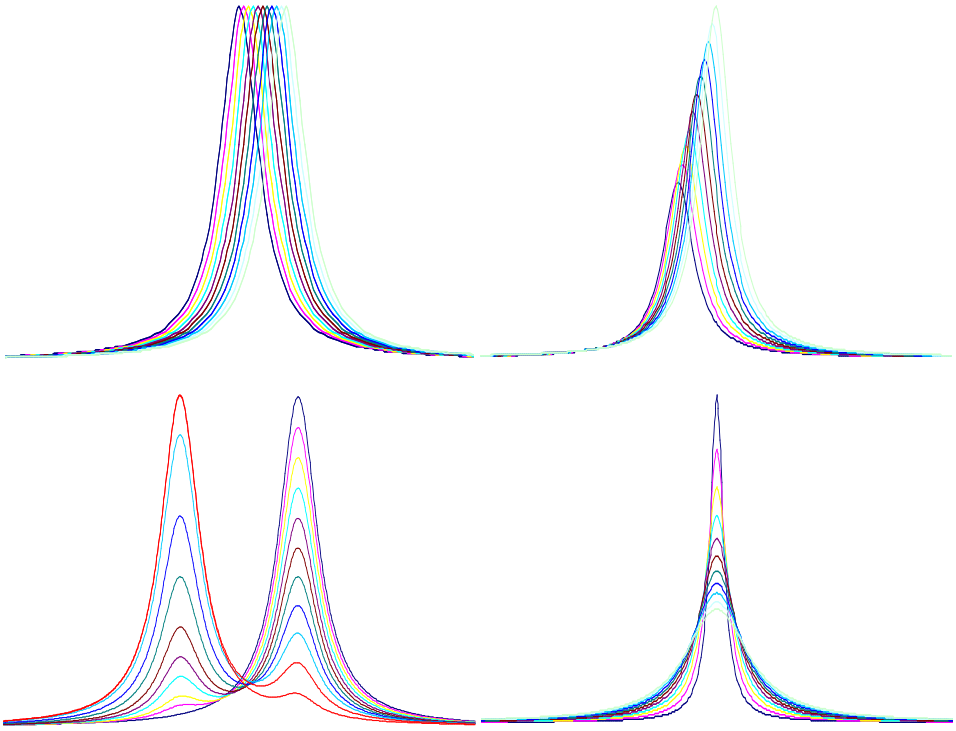

Figure 4.12 Lorentzian curves used to simulate 2D correlation spectra of a single band shifting (top left), a single band shifting coupled with an increase in intensity (top right), two bands changing intensity in opposite directions (bottom left, note the lack of isosbestic point. This is due to the requirement that both peaks change intensity with different waveforms, otherwise no peaks appear in the asynchronous spectrum) and a single band broadening (bottom right).

In order to demonstrate the 2D correlation patterns created by these four effects, four sets of simulated spectra were created (see figure 4.12) following a similar treatment to Noda,[131] Dluhy *et al.*[147] and Czarnecki,[142] amongst others. The corresponding synchronous and asynchronous correlation spectra are shown in figure 4.13. It should be noted that all the simulated 2D correlation spectra shown were calculated with increasing overall intensity. If the calculation were repeated with decreasing overall intensity, the signs of peaks in the asynchronous spectra would be reversed.

In the case of a single band undergoing a peak shift, characteristic four-fold and two-fold symmetric patterns are produced in the synchronous and asynchronous spectra, respectively. In the case with an accompanying change in intensity these characteristic patterns are elongated along the diagonal towards the higher intensity end of the peak shift. The four-lobed pattern in the synchronous spectrum is centred

approximately at coordinates along the diagonal corresponding to the peak maximum of the average spectrum. The elongated butterfly-like pattern in the asynchronous spectrum provides the best indication that the pattern is created by a single peak, as well as the clearest example of why Noda's sequence rules cannot be directly applied since the asynchronous cross peaks span both positive and negative regions of the synchronous spectrum. The pair of crosspeaks close to the diagonal are typically much more intense than the outlying pair, which are easily overlooked in real spectra where other higher intensity peaks may also be present. Intriguingly, the appearance of both synchronous and asynchronous spectra is little changed by the magnitude of the peak shift and so the patterns observed are purely diagnostic and have little analytical value. The origin of this effect probably lies in the normalisation step preceding calculation of the correlation spectra.

In contrast, the asynchronous spectrum created by two separate bands changing intensity in opposite directions contains a single pair of crosspeaks centred at coordinates that approximately correspond to the peak positions of the two constituent bands. The synchronous spectrum is very similar to that of a single band shifting, demonstrating that the asynchronous spectrum has far greater diagnostic value.

The patterns created by a single band broadening are more complex again than those related to band shifts. The large autopeak in the synchronous spectrum often dominates the less intense outlying peaks, and so again the asynchronous spectrum is more indicative of broadening. The asynchronous spectrum resulting from the broadening of a band is distinguished from the above cases by the presence of a rotated four-leaf-clover pattern close to the diagonal.[148, 149] Such a four lobed pattern is not unique, however, and can be confused with the existence of multiple overlapped bands, the effects of which tend to dominate the appearance of 2D correlation spectra. The main indication of the presence of broadening effects, therefore, is the appearance of pairs of symmetrical extended peaks parallel with the spectral axes.

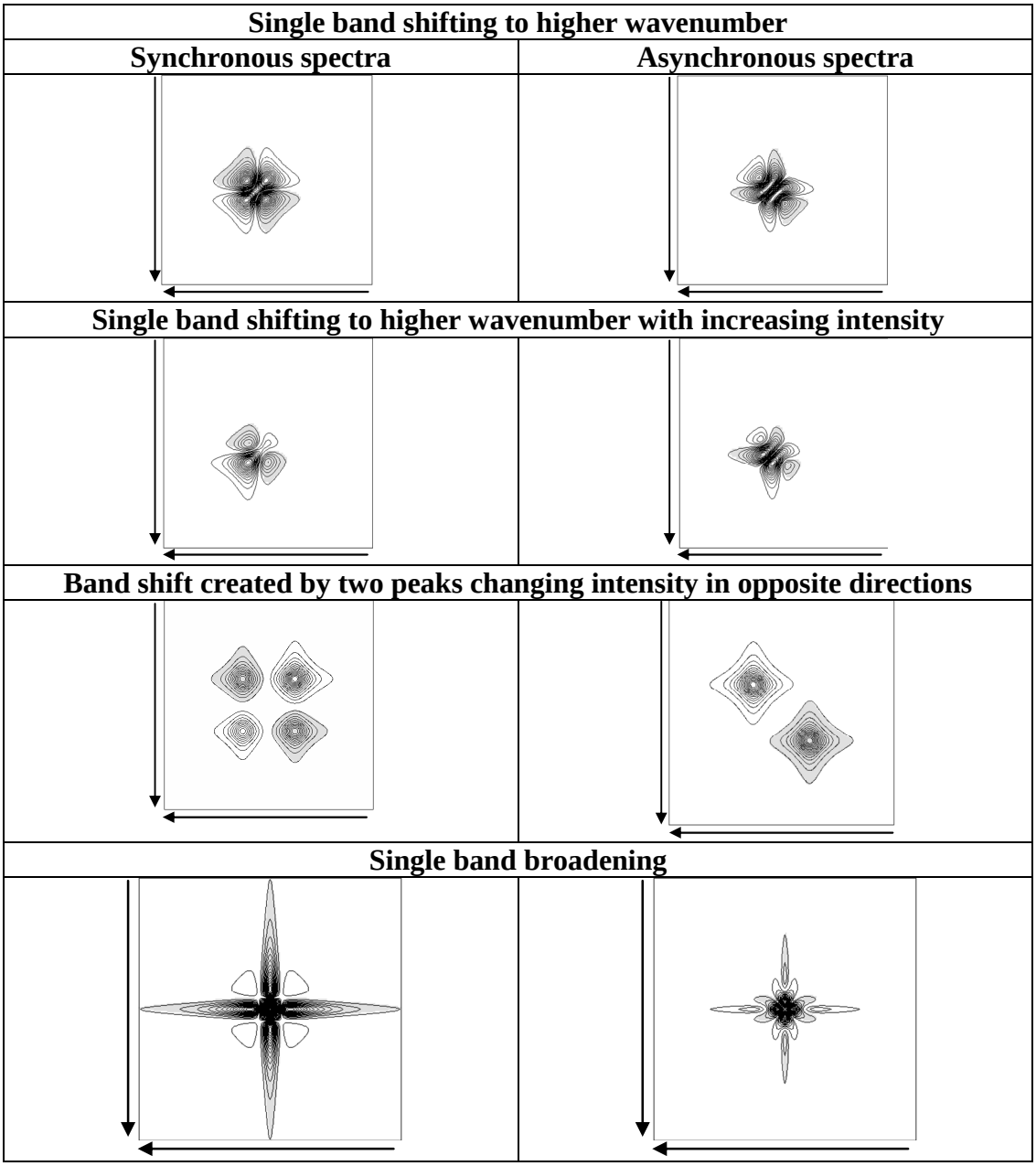

Figure 4.13 Simulated synchronous and asynchronous 2D correlation spectra derived from the spectra shown in figure 4.12. Arrows indicate the direction of increasing wavenumber.

Empirical adaptations of Noda's rules have been set out for these more complex cases. In the example of a single band shifting position, the direction of the shift can be deduced from the sign of the elongated crosspeak just above the diagonal. If this peak is negative, then the shift is to a higher wavenumber. The sequential order of intensity changes in the case of two separate bands is also given by the sign of the crosspeak above the diagonal in the asyncronous spectrum. A negative crosspeak indicates that the intensity change of the higher wavenumber band occurs largely

after the change in the lower wavenumber band. Broadening can be distinguished from narrowing by considering the sign of the vertical pair of extended peaks in the asynchronous spectrum. A negative pair of crosspeaks is indicative of band broadening. Applying these rules to the example spectra of figure 4.13 leads to the correct observations that the single band shifts to higher wavenumber, the lower wavenumber band increases in intensity most rapidly and the single band is indeed broadening.

The application of these rules to real experimental data is generally complicated by the appearance of additional crosspeaks as a result of the presence of a large number of bands in the original spectra. In fact, the number of bands need not be that large; since each individual band can contribute up to four crosspeaks, the asynchronous correlation of just two bands gives a total of up to sixteen crosspeaks, giving the 2D spectra a very complex appearance. It is perhaps more appropriate to use physically reasonable spectral simulations, therefore, than to apply rules based on idealised situations. A good example was provided by Kim *et al*.,[150] who demonstrated that the shifting and broadening of just two bands (typical of the electronic spectrum of an organic dye) can lead to a range of increasingly complex and beautiful patterns that cannot be properly interpreted in terms of the above rules.

4.4.6 Practical Applications of 2D Correlation Spectroscopy

In addition to providing much of the mathematical framework for the calculation of 2D correlation spectra Noda, often in collaboration with Ozaki, has produced a number of demonstrations of the applicability of generalised 2D correlation spectroscopy to a variety of practical systems,[151-156] as well as periodic reviews detailing advances in the technique.[157-159] A particularly elegant and simple example of the application of Noda's rules involved the deposition of dissolved polystyrene to form a film during the evaporation of a volatile solvent system containing methyl ethyl ketone and toluene. Only weak synchronous correlation was found between the three components, whilst all three were strongly asynchronously correlated. These findings implied that the changes in concentration of each component were independently controlled by either the volatility of the solvent or solubility in the case of polystyrene. The fact that weak synchronous correlation was found, despite

the essentially uncorrelated behaviour of the system, could be due in part to subtly changing interactions as the composition of the solution changed with time, but more likely reflects that even for intensity changes with very different rates and waveforms there will often be some component of the Fourier-domain frequency common to all species. This will be reflected by the appearance of weak crosspeaks in the synchronous spectrum unless other higher intensity crosspeaks are present which dominate (this is also the origin of the two weakly negative regions in figure. 4.10). Analysis of the signs of crosspeaks in both synchronous and asynchronous spectra revealed that changes in methyl ethyl ketone bands occurred largely before changes in toluene bands (as expected from the relative volatilities of the two components) and polystyrene was deposited gradually throughout the course of evaporation. An important point regarding the interpretation of sequential order information is highlighted by the evaporation study, as the concentration (and therefore spectral intensity) of each component clearly changes at all times during the measurement. It is therefore more appropriate to consider the order of events as revealed by Noda's rules as relating to relative rates of change averaged over the whole measurement interval, or in terms of the half-times or half-intensities of the spectral changes as discussed by Jai *et al.*,[160] rather than as sequential stages for most real-world applications.

The effects of temperature and pressure on semicrystalline polyethylene, known to have a complex structure consisting of crystalline lamellae suspended in a liquid-like amorphous matrix, has been studied using 2D correlation spectroscopy.[161] The appearance of the IR spectrum is determined by the relative proportions of the crystalline and amorphous phases. 2D correlation as a function of temperature and pressure allowed bands relating to the amorphous phase and distinct axes of the crystal lamellae to be distinguished and the melting and pre-melting processes to be studied for both polyethylene and nylon-12.[153, 154] Asynchronous correlations between the amorphous band and crystalline bands revealed pre-melting to occur at temperatures as much as 90° below the melting point in a process very similar to that of normal melting. In addition, it was found that the true amorphous state does not appear until well above the reported melting point. Melting could also be induced by applying pressure, and in this case melting was shown to be preceded by the

uncoiling of crystal lamellae. This conclusion was supported by the appearance of negative crosspeaks in the synchronous spectrum, revealing contrary intensity changes in bands corresponding to different crystalline axes.

Generalised 2D correlation spectroscopy has also been applied to the study of various other inter- and intramolecular reorganisation effects instigated by external stimuli. Palmer, Chao *et al.* realised that the reorientation of liquid crystals by electric fields could be thought of in much the same way as the reorganisation of polymer structures under mechanical stress.[162-164] The absence of crosspeaks correlating the dipolar "head" region, containing stiff biphenyl groups, with the flexible alkyl "tail" of the model nematic liquid crystal 5CB showed that the reorientation occurred in two stages when an electric field was either applied or withdrawn from the sample. Strong asynchronous crosspeaks between the alkyl and biphenyl groups showed that reorganisation of the tail was much slower than the head when a field was applied to an isotropic sample, whereas it was the thermal motion of the alkyl tail that dragged the molecules into a disordered state when the field was removed. Ozaki *et al.* elucidated sub-molecular level information about composition-dependent structural changes in ethylene-vinyl acetate copolymers using 2D Raman correlation spectroscopy.[165] The supramolecular disordering of the system with increasing vinyl acetate content was found to be caused by a shortening of all *trans*-methylene segments which disrupted packing in crystalline lamellae. This study complemented earlier Raman studies on the same system where only phenomenological conclusions could be drawn.[166] The dissociation of hydrogen bonds by increasing the temperature of pure liquid *N*-methylacetamide was found to involve the sequential dissociation of clusters of decreasing size.[167] The presence of clusters with distinct size ranges was revealed by the presence of multiple crosspeaks in the amide I and amide II regions of the asynchronous correlation spectra which corresponded to distinct but highly overlapped (and therefore unresolved) peaks in the raw spectra which disappeared at different rates as the temperature was raised. This system was also studied using an interesting modification of the 2D correlation technique, 2D heterospectral correlation.[152]

2D heterospectral correlation differs from the generalised 2D correlation method described so far in that two independent dynamic spectra are correlated with each other, rather than a single dynamic spectrum being correlated with itself. The two dynamic spectra may be generated from any pair of complementary spectral probes under the same external perturbation. In the example above, 2D IR-Raman correlation spectroscopy was used to complement the original 2D-IR studies to further aid band assignments in the *N*-methylacetamide system and demonstrate the potential of the modified approach. It should be noted that the mathematical formalisms and calculation of 2D heterospectral correlation spectra are identical to those described in sections 4.4.1 to 4.4.3, with the simple replacement of $\tilde{y}(\upsilon_2, t)$ with $\tilde{z}(\upsilon_2, t)$, where $\tilde{z}$ denotes the use of a second spectral index. The differing physical origins of spectral bands, however, means that all peaks in heterospectral correlation spectra, even in the synchronous spectrum, are technically crosspeaks as autocorrelation cannot take place between distinct datasets. In addition to applications involving traditionally complementary spectral probes, such as IR/Raman, IR/NIR[168, 169] and UV-vis/NIR the 2D heterospectral method can be applied to completely different techniques such as IR/ESR[170] or IR/SAXS.[171]

Another novel application of the 2D correlation method, related in some ways to 2D heterospectral analysis, is the so-called sample-sample correlation spectroscopy formulated by Ozaki *et al.*.[172] In contrast to variable-variable correlation spectroscopies which correlate changes in spectral bands along the perturbation axis, sample-sample correlation spectroscopy is applied to a transposed dataset to reveal changes in the sample at different extents of perturbation along the spectral variable. This process is most simply understood by considering the matrix approach of section 4.4.3, where a simple transposition of the spectral data matrix **Y** gives the synchronous spectra as

$$\Phi_{ss} = \frac{1}{n-1} YY^T \tag{4.62}$$

where the suffix *ss* denotes sample-sample, *n* (the number of spectral variables) replaces *m* (the number of perturbations over which the dataset was obtained) and the association product is now used rather than the dispersion product.

Traditional 2D-NIR spectroscopy was used alongside sample-sample correlation spectroscopy to study phase transitions in oleic acid from the liquid crystal structure to a true isotropic liquid phase.[173] Wavenumber-wavenumber correlation showed the breaking of hydrogen bonded dimers with increasing temperature by the disappearance of splitting of OH bands, whilst the sample-sample spectra demonstrated unequivocally the existence of two distinct transitions at 32 °C and 55 °C by the appearance of two distinct discontinuities in synchronous correlation intensity at these two temperatures. A similar study has been carried out on water,[174] suggesting that between 6 °C and 80 °C two major species are present with stronger and weaker hydrogen bonds, respectively. The idea of sample-sample correlation has recently been extended to take into account multiple independent perturbations, such as concentration and temperature, so the effects of two interrelated perturbations can be correlated with each other on a wavenumber-wavenumber plot.[175] In a multiple perturbation 2D correlation analysis, two external perturbations are applied simultaneously to the sample and synchronous and disrelation (an approximation of the asynchronous spectrum) spectra are calculated that contain the effects of both perturbations. Additional crosspeaks in the multiple perturbation correlation spectra appear at spectral coordinates whose behaviours are linked under the influence of both perturbations. This new kind of analysis could prove particularly useful for the determination of the effectiveness of industrial formulations.

Two dimensional correlation analysis has been applied to a variety of surface and interfacial systems, with much of the work to date summarised in a review by Dluhy *et al*..[176] The pressure-dependent behaviour of a DPPC monolayer at the air-water interface was studied in a series of papers to elucidate the nature of the liquid expanded to liquid condensed phase transition.[147, 177] Spectral simulations were used in conjunction with polarised ER-FTIR spectra to discriminate between a two-phase model in which a more ordered species (lower wavenumber methylene peaks) appeared at the expense of a less ordered species and single phase model with a

gradual peak shift. It was found that the whole pressure range studied was not adequately described by either of these models alone, and that it was instead more appropriate to consider two separate pressure intervals. In the low pressure regime, incorporating the LE/LC phase boundary, the two-phase model accounts well for the experimental 2D spectra indicating that the LE/LC transition is indeed biphasic. At higher pressures, however, an additional peak shift was found to occur within the LC phase, attributed to intramolecular reorganisation as surface pressure was increased. In this instance, the data were best represented by a single phase model indicating a small simple peak shift. These subtle effects were only revealed after normalisation of the raw spectra to account for changes in surface density, however, and therefore could be caused by random baseline fluctuations, the effect of which can be magnified when genuine intensity changes are removed. A similar study was carried out on the gel-to-liquid crystalline phase transition of a DPPC bilayer.[178] Simulated spectra indicated that the mechanism of the bilayer phase transition was somewhere between that of the two-phase and single phase models. In this case, however, the intensity changes in the two-phase model were linear and occurred at the same rate (albeit in opposite directions). Such linear intensity changes are known not to produce meaningful asynchronous correlation intensities,[134] casting doubt over the models used.

Aratono *et al.* used 2D correlation ER-FTIR spectroscopy to study the analogous LE/LC phase transition during the adsorption of $C_{12}E_1$. They followed the adsorption both as a function of time during dynamic evolution of surface tension and as a function of subphase concentration, with both approaches yielding identical spectra, independent of normalisation. The asynchronous correlation spectra clearly showed the splitting of the symmetric and antisymmetric methylene stretching bands into two components, and therefore that the transition was a first-order, two-phase process.

It has already been noted that Noda's rules for the sequential order of spectral events are better interpreted in terms of relative rates of change. Dluhy and Elmore proposed a modified βv-correlation approach to account for the relative phases of change semi-quantitatively without relying on signs of crosspeaks in the original correlation spectra.[179] This new method involved the introduction of a new

parameter, the effective phase angle β_e, against which relative phase lags between real spectral components can be compared. A βv-correlation analysis is carried out by performing an asynchronous cross-correlation of a dynamic spectrum with a set of model sinusoidal functions that differ only in phase angle β, and have the general form

$$f(\beta) = \sin(k\phi + \beta) \tag{4.63}$$

where ϕ is chosen such that each model function describes one-quarter of a sinusoidal cycle and k is an integer. The asynchronous correlation is then formally described by

$$\Psi(\upsilon, \beta) = \frac{1}{m-1} \sum_{j=0}^{m-1} f(\upsilon, n_j) \cdot \sum_{k=0}^{m-1} N_{jk} \cdot \sin(k\phi + \beta) \tag{4.64}$$

where m is the total number of spectra, $f(\upsilon, n_j)$ is the measured spectral dataset and N_{jk} is the Hilbert-Noda transformation matrix. The effective phase angle, β_e, is then defined as

$$\beta_e = \beta_{\max} + 90^\circ \tag{4.65}$$

This definition ensures that the phase angle and effective phase angle are the same when the signal variation has a constant sinusoidal frequency.

As an example, model βv-correlation spectra were calculated for a set of simulated spectra containing two peaks, centred at 2850 cm^{-1} and 2950 cm^{-1}, increasing in intensity with identical waveforms. Figure 4.14 A shows the βv-correlation spectrum of the model system when the phase lag between the two peaks is zero. In this case the intensity change in both peaks is seen to have the same effective phase angle, approximately -90° taken from the maximum of the positive correlation peaks, indicating that the spectral changes occur exactly in phase as expected. If the intensity change in the band at 2950 cm^{-1} is delayed relative to the change at 2850 cm^{-1} (whilst still retaining the same waveform), a lag will appear in the relative phase angles of the two bands. This effect can be seen in figure 4.14 B, where the higher

wavenumber band now has a reduced effective phase angle of approximately -115°. In the case of the first-order phase transitions reported in this thesis the increase in spectral intensity should occur simultaneously for all components as the system freezes, and so a *βv*-correlation analysis should resemble that shown in figure 4.14 A.

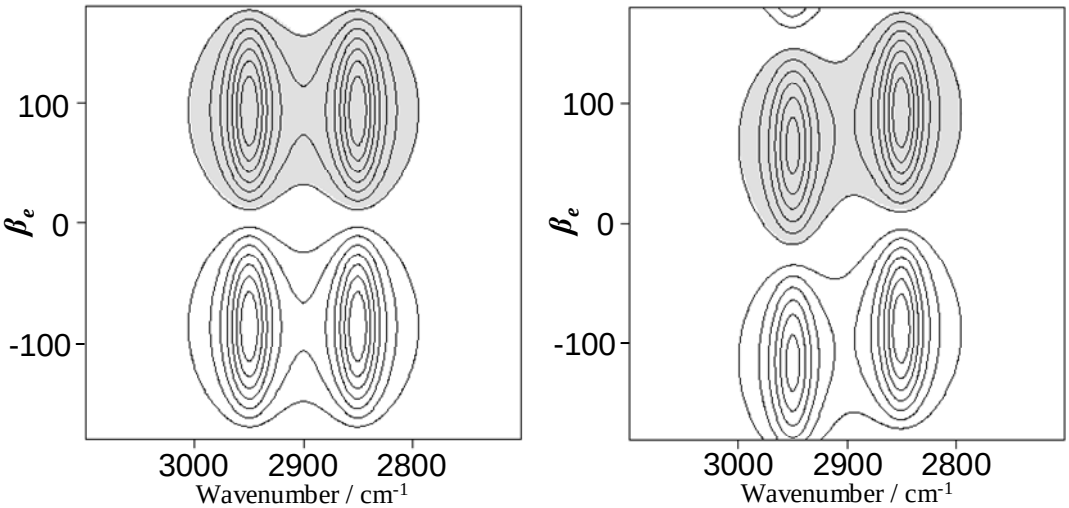

Figure 4.14 Model βv-correlation spectra calculated from two independent peaks increasing in intensity at the same rate. Left, changes perfectly in phase. Right, with a phase lag introduced into the higher wavenumber band.

βv-correlation analysis has been used to analyse the rotator transition of nonadecane,[179] the structural dynamics of ideal and nonideal binary phospholipid mixtures at the air-water interface[180] and the mechanisms of interaction of phospholipid monolayers with dissolved antibiotic.[181] The concept has recently been extended to allow the use of any arbitrary trial function through the use of a global phase angle.[182, 183] The approach is formally similar to that described above, only the form of the trial function can change to incorporate exponential, quadratic, etc. intensity variations.

Further interfacial applications of 2D correlation spectroscopy include the conformation of mixed phospholipid-peptide monolayers,[184] the adsorption of *β*-lactoglobulin[185] and thermal behaviour of spin-coated copolymer films.[186]

The advencement of non-linear optical techniques based on pulsed laser excitations has allowed ultrafast 2D spectroscopic studies to be undertaken that are formally identical to the well established pulse-based approaches common to 2D NMR. These techniques have allowed the study of various dynamic phenomena, such as the

structures of benzophenone[187] and liquid formamide,[188] water diffusion in biodegradeable plastics,[189] the solvation of water in acetonitrile[190] and even the interfacial structure of a dodecanol monolayer.[191]

4.5 Experimental Methods and Materials

4.5.1 The FTIR Spectrometer

The Michelson Interferometer

An interferometer is a device that generates an interference pattern from incoming radiation in a well defined way. In essence this is achieved by splitting the incoming light into several sources, with a known (or measurable) optical path length difference between them. A simplistic example of an interferometer is Young's famous double slit experiment, where two light sources (i.e. the slits) with a fixed optical path length difference were allowed to interfere. In this case the optical path length difference was determined by the distance between the slits, resulting in the familiar interference pattern upon recombination. In order to gain information from a wide range of incident frequencies, it is necessary to use an interferometer with an adjustable optical path length difference. A simple solution to this problem was provided by Michelson in the late 1800s (who was attempting to measure changes in the speed of light in different directions), and the interferometers used in modern FTIR spectrometers are based upon his original design.

The Michelson interferometer is a dual-beam device that uses a beamsplitter to divide incoming radiation into two beams which are later recombined after reflection from two mutually perpendicular mirrors (figure 4.15). Upon recombination the two beams interfere and are partially reflected to the detector and partially transmitted back towards the source, with the intensity of the reflected and transmitted beams dependent upon the optical path length difference between the two arms of the interferometer. By allowing one mirror to move, thus creating a variable optical path length difference, an oscillating intensity will be observed at the detector characteristic of the incident light source. The optical path length difference is

commonly called the retardation, δ, and a plot of measured intensity as a function of retardation gives the interferogram of the light source.

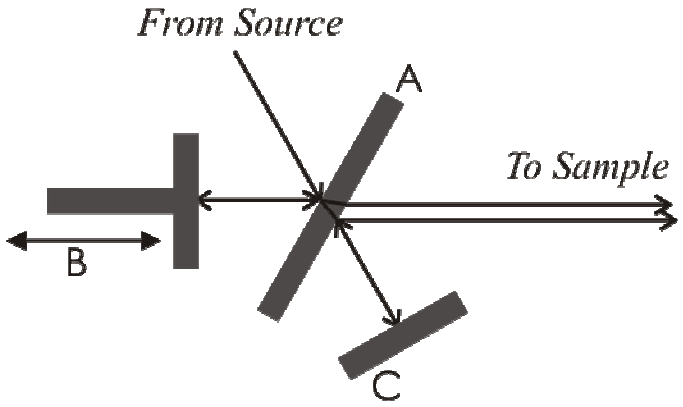

Figure 4.15 Schematic of the Michelson interferometer showing the beamsplitter (A), moving mirror (B) and fixed mirror (C).

In the limiting case of a monochromatic light source the intensity is simply a sinusoidal function of retardation, with maxima when $\delta = n\lambda$ and minima when $\delta = (n + 1/2)\lambda$. More generally, the intensity as a function of retardation is given by[192]

$$I(\delta) = 0.5I(\bar{\nu})[1 + \cos 2\pi\bar{\nu}\delta] \tag{4.66}$$

where $I(\bar{\nu})$ is the intensity of the source emitting radiation of wavenumber $\bar{\nu}$. The dc component of the intensity in unimportant for spectroscopic measurements, and the term interferogram usually refers to only the ac component of eqn. 4.65. Various instrumental parameters can also be accounted for, such as wavelength-dependent behaviour of the beamsplitter, non-linear response of detectors and any filters applied to the signal before detection. In this case, an extra wavelength-dependent correction factor, $H(\bar{\nu})$ must be added to account for these effects (eqn. 4.66). The parameter $B(\bar{\nu})$ describes fully a source of wavenumber $\bar{\nu}$ after modification by the components of the spectrometer.

$$I(\delta) - 0.5I(\bar{\nu}) = 0.5I(\bar{\nu})H(\bar{\nu})\cos 2\pi\bar{\nu}\delta = B(\bar{\nu})\cos 2\pi\bar{\nu}\delta \tag{4.67}$$

When a source emits more than one wavenumber of radiation, the measured interferogram is the product of interferograms corresponding to each wavenumber of radiation emitted by the source. In the case of sharp line sources the envelope of the

interferogram repeats at regular intervals, much like the beats heard when two musical instruments play slightly out of tune. This fact was utilised by Michelson to deduce that the red Balmer line in the spectrum of hydrogen was a doublet, as he could only resolve the envelope and not the high frequency structure[193] of the interferogram. As the lines broaden the envelope of the interferogram decays exponentially rather than repeating infinitely, and will decay very rapidly for a broadband source since all the sine waves contributing to the interferogram are in phase only at the point of zero retardation. In the case of a continuous source, the interferogram in eqn. 4.66 can be represented as an integral function of the incident wavenumber, and likewise the spectrum can be represented as an integral function of the interferogram;

$$I(\delta) - 0.5I(\overline{\nu}) = \int_{-\infty}^{+\infty} B(\overline{\nu}) \cos 2\pi\overline{\nu}\delta \cdot d\overline{\nu} \tag{4.68}$$

$$B(\overline{\nu}) = \int_{-\infty}^{+\infty} [I(\delta) - 0.5I(\overline{\nu})] \cos 2\pi\overline{\nu}\delta \cdot d\delta \tag{4.69}$$

Here, the interferogram ($I(\delta) - 0.5I(\overline{\nu})$) and the spectrum ($B(\overline{\nu})$) form a cosine Fourier transform pair, relating the distance (or time) domain measurement of δ to the wavenumber (or frequency) domain of the spectrum. Implicit in eqn. 4.27 is the fact that, in order to achieve infinitely high spectral resolution, the interferogram must be recorded over an infinite range of retardations, and hence an infinite motion of the moving mirror. This is clearly impossible, and so it is instructive to consider how severely the incomplete acquisition of an interferogram affects the spectral resolution.

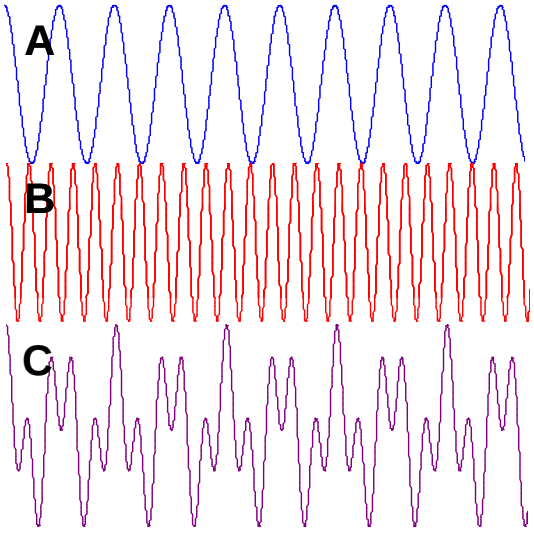

Figure 4.16 Superposition of waves A and B to give trace C.

Considering the simple case where a line source emits a doublet of radiation with a separation of $\Delta\bar{\nu}$ wavenumbers, the interferogram will consist of a superposition of two cosine waves as shown in figure 4.16.[192] The two waves are in phase at the point of zero retardation, become exactly out of phase when $\delta = 0.5(\Delta\bar{\nu})^{-1}$, and are back in phase after a retardation of $(\Delta\bar{\nu})^{-1}$; the envelope of the interferogram has a wavelength equal to the separation of the two lines. If the interferogram is recorded over a smaller range of retardations, it is impossible to unambiguously extract both component waves. This simple analysis serves to illustrate the correct conclusion that the spectral resolution is inversely proportional to the range of retardation measured, and hence to the distance travelled by the moving mirror. If the mirror moves at a fixed speed then the acquisition time of an interferogram (that is, the time per scan) is proportional to the resolution of the measurement. Both these facts have implications for the signal-to-noise ratio of recorded spectra, as the noise per spectrum is proportional to the square of both the acquisition time per scan at fixed resolution, and the resolution for a fixed acquisition time.

The Apodization Function

As well as limiting resolution, a consequence of measuring incomplete interferograms is to introduce unwanted and unrealistic features into the resulting

spectra. This is due to the fact that any truncation of the interferogram must be reproduced by the Fourier transform, which in practice introduces baseline oscillations around spectral peaks. The appearance of these unwanted features can be reduced by applying a smoothing function to the interferogram that gradually reduces the intensity to zero at the point of maximum measured retardation. The process of smoothing is known as apodization and the smoothing function is the apodization function, $A(\delta)$.

Table 4.3. The effect of common apodization functions on spectral appearance

Apodization Function	FWHM increase / %	Appearance
Boxcar $A(\delta) = \begin{cases} 1 & -\delta_{\max} \le \delta \le \delta_{\max} \\ 0 & \delta < -\delta_{\max}, \delta > \delta_{\max} \end{cases}$	0	Large sidelobes up to 15% of peak intensity Positive and negative baseline fluctuation over a large wavenumber range
Triangular $A(\delta) = \begin{cases} 1 - \left\lvert \frac{\delta}{\delta_{\max}} \right\rvert & -\delta_{\max} \le \delta \le \delta_{\max} \\ 0 & \delta < -\delta_{\max}, \delta > \delta_{\max} \end{cases}$	48	Only positive sidelobes Baseline fluctuations occur over a small wavenumber range
Happ-Genzel $A(\delta) = \begin{cases} a + b\cos\frac{\delta\pi}{2\delta_{\max}} & -\delta_{\max} \le \delta \le \delta_{\max} \\ 0 & \delta < -\delta_{\max}, \delta > \delta_{\max} \end{cases}$	51	Sidelobe intensity reduced to 0.8% of peak intensity Baseline oscillations spread over a wide wavenumber range

The effect of apodization on the appearance of the interferogram increases as $\delta \to \delta_{\max}$. Information about rapid changes of intensity in the frequency domain are contained at large retardations, and so sharp lines appear broadened by apodization. More generally apodization decreases spectral resolution by reducing the contribution of points in the interferogram far from the point of zero retardation, thus effectively reducing the maximum retardation measured. It is therefore necessary to weigh up the effective reduction in resolution with the degree of removal of baseline

oscillations when choosing an apodization function. As a result there have been a large number of proposed apodization functions, and which to use is in many cases a matter of personal preference. Different functions can produce subtly different effects, however, and a comparison of three common apodization functions (boxcar, triangular and Happ-Genzel) is presented in table 4.3.[194]

Practical Interferometry

The discussion so far has been limited to the case of a coherent collimated light source. In reality IR radiation is produced by a broadband, incoherent and un-collimated source (due to the finite size of the source), which leads to divergence of the incoming beam as it passes through the interferometer. As a result of this divergence, light impacts the various optical components of the interferometer at a range of angles and hence the actual retardation produced by a given position of the moving mirror is not single-valued but is smeared-out by additional interference effects of the divergent light source. To achieve high spectral resolution it is therefore necessary to reduce this divergence, practically accomplished by focusing the beam through an aperture before it enters the interferometer.

In order to record an interferogram on a computer the data must be digitised, a process that involves discretization of the measured intensities. In any practical system this also results in finite sampling of the interferogram at discrete values of the retardation. The continuous Fourier transform in eqn. 4.27 is then replaced by a discrete Fourier transform, sampled at regular intervals during movement of the mirror. If x is the sampling interval (in terms of the position of the moving mirror, such that $kx = \delta$ where k is an integer), and $I_\lambda(k)$ is the intensity of the interferogram at the k^{th} sampling point the discrete Fourier transform of N sampled points can be expressed as;

$$B(\overline{\nu}_n) = I_\lambda(0) + 2\sum_{k=1}^{N-1} I_\lambda(k)\cos 2\pi\overline{\nu}_n kx \quad \overline{\nu}_n = \overline{\nu}_1, \overline{\nu}_2, \ldots, \overline{\nu}_{N-1} \tag{4.70}$$

It can be seen, therefore, that a large number of computations are necessary to calculate a spectrum acquired over any reasonable wavenumber range. In order to cut

down the number of calculations required, and hence drastically increase the maximum rate of data acquisition, Cooley and Tukey devised the fast Fourier Transform (FFT) algorithm.[195] The algorithm works by expressing the discrete Fourier transform of eqn. 4.28 in exponential form using the Euler relation, then factorising the resulting matrix (eqn. 4.28 must be performed for each wavenumber in the spectrum individually) using the symmetry properties of the $e^{-i2\pi}$ function. The FFT algorithm works most efficiently when the total number of sampled points, *N*, is a power of 2. To ensure this is the case, additional data points of zero intensity can be added to the interferogram at $\pm\delta_{max}$. These additional points will have no effect on the appearance of the spectrum since the intensity of the interferogram has already been defined to be zero at extreme δ by the apodization function. It is also possible to enhance the digital resolution of the spectrum by doubling the number of sampled points through the addition of more zeros. This is known as zero-filling.

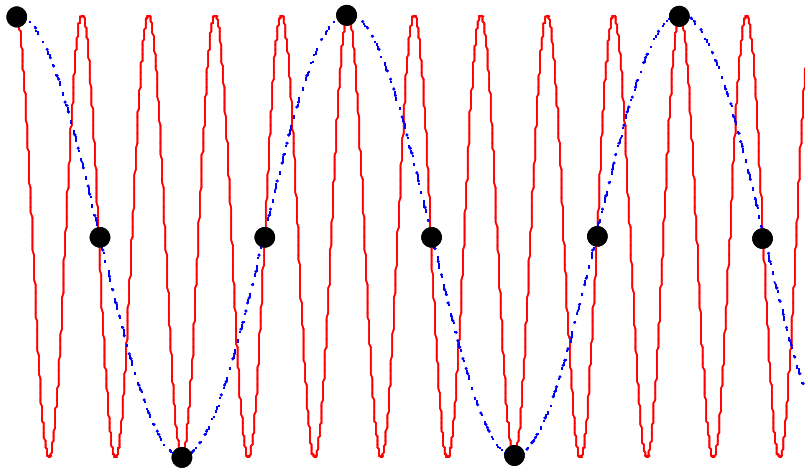

Figure 4.17 Undersampling (dots) of a cosine wave (solid line) to yield a detected wave of lower frequency (dashed line).

The actual sampling rate employed by the interferometer is determined by the bandwidth (i.e. wavenumber range) being measured. The Nyquist criterion states that, in order to unambiguously record an oscillating signal, the sampling rate must be at least twice that of the highest frequency component of the signal.[196] Practical examples of the effect of this criterion can be seen in video footage of helicopter blades or the spokes of car wheels, where as the car accelerates the wheels appear to rotate backwards, then stand still as the rotational frequency approaches and then matches the film capture rate. In most practical interferometers, the retardation is

measured using the well defined interferogram of a monochromatic light source as described earlier (eqn. 4.24). A reference 633 nm He-Ne laser beam is passed through the interferometer, and the intensity of the signal after the beamsplitter is measured using a photodiode array. After subtraction of the constant dc signal, an output cosine wave is produced that periodically has zero intensity; whenever $\delta = (n + 1 / 4)\lambda_{He-Ne}$. If the interferogram is sampled at each of these so-called zero-crossing points (i.e. with twice the frequency of the wave, or every $0.5\lambda_{He-Ne}$ cm), the Nyquist limited spectral bandwidth is roughly 0 – 15800 cm^{-1}. A consequence of sampling at less than this rate is the aliasing of higher wavenumber (or, equivalently, frequency) peaks to lower values. Such undersampling of a high frequency wave is illustrated in figure 4.17. The problem of aliasing can be overcome if any unwanted frequencies are filtered from the signal before it reaches the detector. A bandpass filter can be used to restrict the detected frequencies, or the choice of a detector with only limited response outside the spectral region of interest. If a bandpass filter is employed, restrictions on the sampling frequency are relaxed and the acquisition time can be reduced by measuring over a smaller spectral bandwidth.

4.5.2 Layout of the Optical Bench

The arrangement of the internal spectrometer components described in the previous section, the external sampling and alignment components and the sample stage are shown in figures 4.18 – 4.19. The optical bench was initially designed for the study of dynamic adsorption at the air-water interface by Dr. Richard Campbell in his PhD thesis at Oxford University.[125] In the present research the optical bench has been modified to include a new sample alignment procedure and to accommodate a temperature controlled, sealed sample cell (shown schematically in figure 4.20).

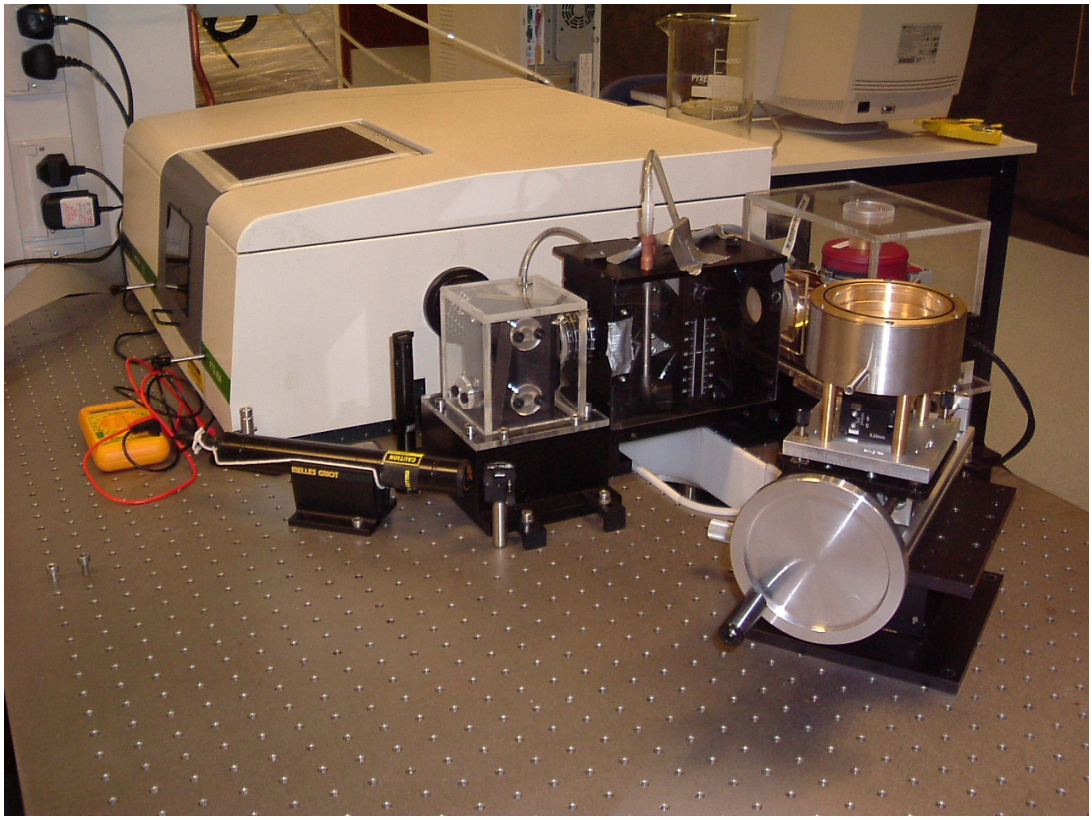

Figure 4.18 The optical bench, including spectrometer, VeeMax, alignment laser and sealed sample cell.

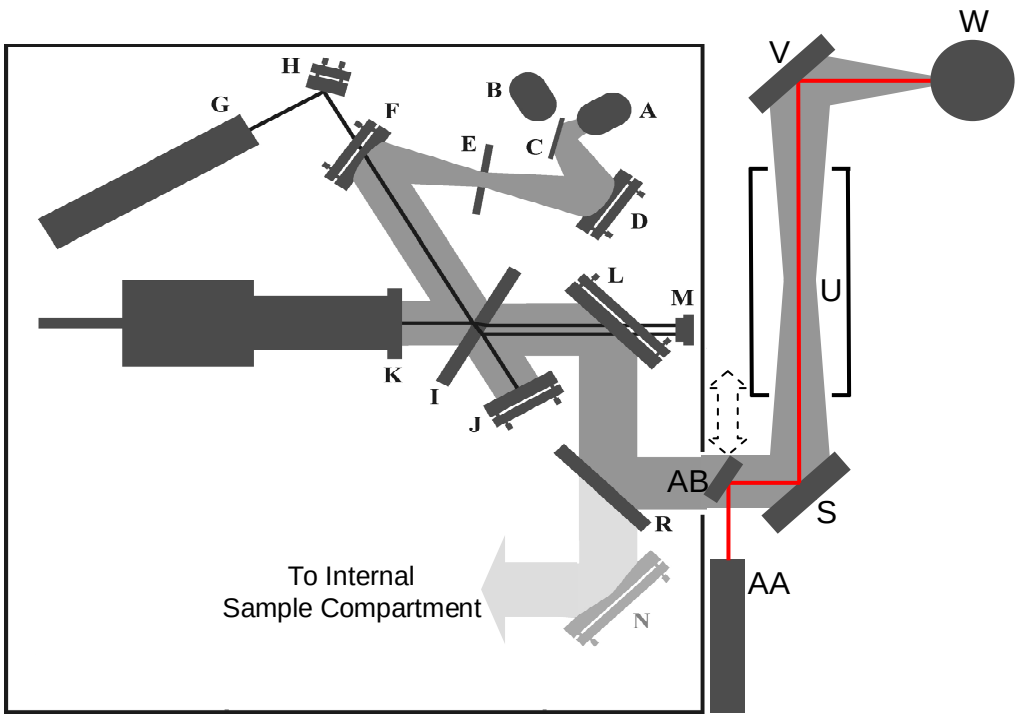

*Figure 4.19 Schematic diagram of the Bio-rad FTS 40A spectrometer. Adapted with kind permission from Dr. R. Campbell.[125] Components in red show the position of alignment laser, **AA**, and removable mirror, **AB**, used in the present alignment.*

The IR source (figure 4.19, **A**) produces a diverging, incoherent beam of radiation which is focused by mirror (**D**) through an aperture (**E**) and collimated by a spherical mirror (**F**), before entering the Michelson interferometer (**I – K**, see figure 4.15). The reference He-Ne laser beam (**G**) is introduced via a hole in the centre of mirror **F** and passes to the photodiode detector array (**M**) through a similar hole in the centre of mirror **L**. The beam is then diverted into the external beampath by a plane pop-up mirror (**R**) and focused to the centre of the sample compartment (**U**) by a parabolic mirror (**S**). Sample compartment (**U**) is a commercial specular reflection accessory (VeeMax II, Pike Technologies) that focuses the incoming IR beam onto the sample surface and is adjustable over a range of incidence angles (30° to 80°). The VeeMax was designed for the study of solid surfaces, but here is inverted to cause a single reflection from the air-water interface. The temperature controlled sample cell seals against the baseplate of the VeeMax, and a calcium fluoride window isolates the interior of the cell from the VeeMax chamber. The calcium fluoride window is tilted at an angle of approximately 5° to prevent reflections from its surface reaching the detector. A consequence of the inclusion of the calcium fluoride window is a reduction in the incidence angle range of the VeeMax, resulting in a working range of the optical bench of 30-60°. The sample height can be adjusted using the vertical translation stage (Standa, 5 mm travel) as shown in figure 4.20. On exiting the VeeMax the beam is focused onto the detector (**W**) by an elliptical mirror (**V**). All the optical components in the external beampath are mounted on anodised aluminium baseplates to maintain constant height of the IR beam.

4.5.3 Experimental Details

Spectrometer Hardware

All spectra presented in this thesis were recorded using a Bio-rad FTS 40A FTIR spectrometer. The choice of source, beamsplitter and detector were guided by the desire to focus on the C-H and C-D stretching regions, and so were chosen to optimise performance in the mid-IR. A water-cooled ceramic source was used, emitting radiation between 7500 – 75 cm^{-1}, in combination with a KBr beamsplitter (7500 – 400 cm^{-1}) coated to provide 50 % transmittance and reflectance and a liquid

nitrogen cooled mercury-cadmium-telluride detector (6000 – 600 cm^{-1}). In practice, the working range of the spectrometer was limited by the calcium fluoride window, with a low wavenumber cut-off at roughly 850 cm^{-1}, although poor signal-to-noise limits this to 1100 cm^{-1}. A combination of aluminium and gold coated mirrors were used, ensuring high reflectivity throughout the whole spectral range. In cases where polarised IR spectra were recorded an automatic polariser (Pike Technologies) was placed before the VeeMax.

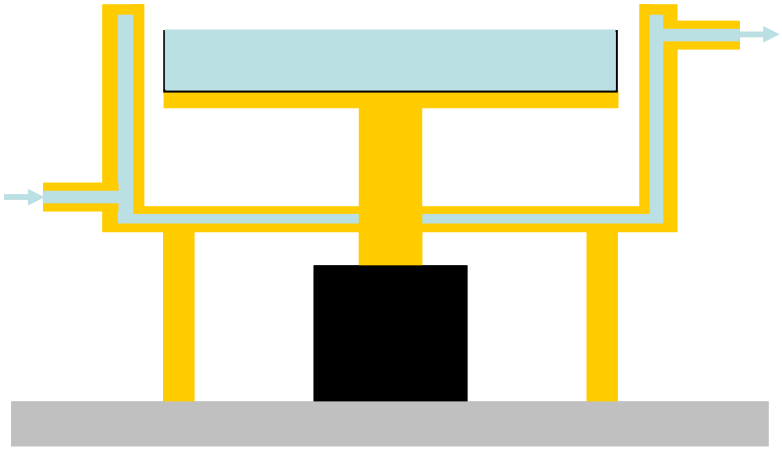

Figure 4.20 Schematic of the temperature controlled, sealed cell used in this research (note the seal is made against the lower surface of the VeeMax accessory).

Alignment Procedures

Interferometer alignment is achieved in two ways. Dynamic alignment is performed continuously during a scan, using piezoelectric mounts to adjust the tilt of the fixed mirror. This ensures that the sinusoidal variation in intensity of the He-Ne laser detected by each of the three photodiodes is locked in phase at all times, resulting in good long-term stability of the interferometer. At the beginning of each experimental run, the orientation of the beamsplitter and fixed mirror is adjusted by the spectrometer software in order to maximize the throughput of radiation and optimize interferogram symmetry. An initialization scan is taken automatically before each measurement to accurately find the point of zero retardation. During a scan the retardation is measured through a process of fringe counting. The maximum intensity of the He-Ne laser is measured and from this the zero-crossing intensity is calculated, effectively calibrating the fringe positions.

Sample alignment is achieved using an external alignment He-Ne laser and removable plane mirror (**AA** and **AB** in figure 4.19). The mirror (**AA**) is mounted on a rail with secure endstops to allow for reproducible positioning, and is placed so as to reflect the alignment laser (**AA**) centrally along the external beampath of the spectrometer during sample alignment. In this way the laser beam is focused at the centre of the sample cell. The reflection is then used to maintain a constant sample height during an experiment. This is important since the throughput of the spectrometer is sensitive to both the position of the sample relative to the focus of the IR beam and the amount of water vapour present in the beampath. Matching throughput is essential in order to record spectra with flat baselines free from interference effects.

Spectral Parameters and Processing

Spectra were recorded at 4 cm^{-1} resolution with either 250 (kinetic, approximately 100 s acquisition time) or 2500 (static, approximately 900 s acquisition time) co-added scans. Triangular apodization was used in all cases, with an undersampling ratio of 2 and no zero-filling. Double-sided interferograms were collected to reduce the effects of interferogram asymmetry.

The spectrum of a water surface is dominated by dispersive features arising from variation in the real part of the refractive index of water close to the O-H stretching and H-O-H bending regions (3600-3100 cm^{-1} and 1650 cm^{-1}, respectively). As a result of this, monolayer peaks are completely obscured in the raw spectra and must be extracted by a subtraction process. This involves the collection of a spectrometer background spectrum, a water reflectance background spectrum and a sample reflectance spectrum.

ER-FTIR spectra are typically reported in terms of the normalised reflectivity of the surface, $\Delta R / R_0$. The spectrometer background was acquired as a reflectance spectrum from a gold surface. All subsequent spectra were normalised to this gold reference to remove the effect of wavenumber dependent responses from the spectrometer components (due to non-linear response of the detector or material adsorbed onto the optical components, for example). The water background provides

a reflectance spectrum, R_0, free from adsorbed species. This can then be subtracted from a sample reflectance spectrum, R_s, to give the effect of adsorbed surfactant in the difference spectrum $\Delta R = R_s - R_0$. The spectrometer records these reflectance spectra in absorbance units, A_x, and so the reference and sample spectra are given by

$$A_0 = -\log R_0 \tag{4.71}$$

$$A_s = -\log R_s = -\log(R_0 + \Delta R) \tag{4.72}$$

In order to extract the surfactant peaks, the difference between these two absorbance spectra is taken

$$A_s - A_0 = -\log\left(\frac{R_0 + \Delta R}{R_0}\right) = -\log\left(1 + \frac{\Delta R}{R_0}\right) \tag{4.73}$$

Since $\ln x = 2.3 \log x$, and $\Delta R / R_0 \ll 1$, eqn. 4.31 can be simplified to yield the subtracted monolayer spectrum in the desired form.

$$\frac{\Delta R}{R_0} = -2.3(A_s - A_0) \tag{4.74}$$

Ideally the subtraction process would lead directly to a set of monolayer peaks on a flat baseline. In practice a significant amount of curvature remains in the subtracted spectra due to the antireflective properties of the monolayer and small changes in spectrometer throughput caused by either imperfect matching of sample heights or changing curvature of the liquid surface between reference and sample spectra. In order to remove the curvature, a quartic polynomial function was fitted to the baseline using at least five points in each of the ranges 3000-3150 cm^{-1} and 2600-2800 cm^{-1} for the C-H stretching region or 2350-2500 cm^{-1} and 2000-2100 cm^{-1} for the C-D stretching region.

Materials

Hexadecyl trimethylammonium bromide (CTAB, Sigma >99%) was recrystalized three times from a mixture of acetone and ethanol. Fully deuterated CTAB (*d*-

CTAB) was supplied by Dr. R. K. Thomas and recrystalized twice before use. The *n*-alkanes hexadecane (Sigma, 99%) and eicosane (sigma 99%) were purified by passing through a column of activated basic alumina.

All glassware was soaked in a dilute solution of alkaline detergent (Borer 15PF, Borer Chemie) and rinsed copiously before use.

4.6 Results

2D ER-FTIR Spectra of Surface Freezing Transitions

Figures 4.21 and 4.22 show two sets of subtracted monolayer spectra obtained as a function of time upon cooling through the surface freezing transition of mixed monolayers of CTAB with hexadecane (C_{16}, T_s=21.6 °C) and eicosane (C_{20}, T_s= 36.9 °C), type I and type II transitions, respectively. Samples were cooled at a rate of 1.5 °C per hour to ensure equilibrium was maintained throughout, and a surfactant concentration of 0.6 mM was used. Both surfactant and alkane were hydrogenated, and therefore peaks in these spectra contain information about both components of the mixed monolayer. The spectra were taken using unpolarised IR, and so are dominated by signal from the s-component.

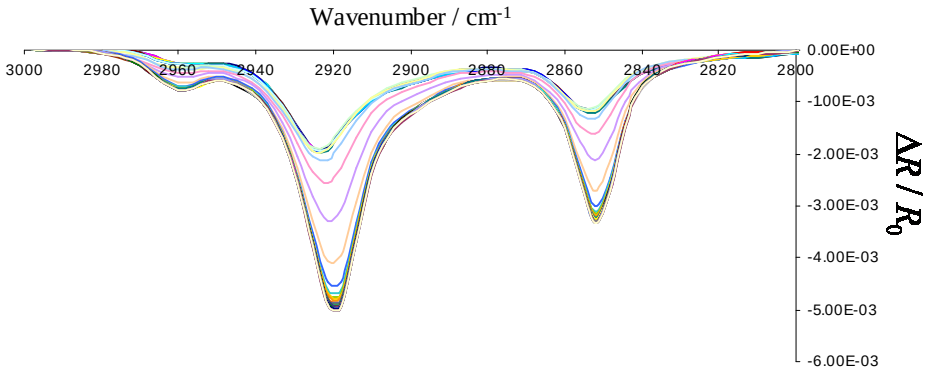

Figure 4.21 Subtracted monolayer spectra following the surface freezing transition of a CTAB + C_{16} mixed monolayer. Unpolarised IR, 250 scans per spectrum, 53° angle of incidence. Cooling rate 1.5 °/hour.

In both systems, the overall intensity increases dramatically through the course of the measurement, as expected from an increase in surface density on freezing. Mean spectra from the liquid and solid phases of both systems were fitted with multiple Voigt profiles using fitting software Fityk 0.8.9. An example fit of a mean solid

phase spectrum from the CTAB/C_{16} mixed monolayer system is shown in figure 4.23.

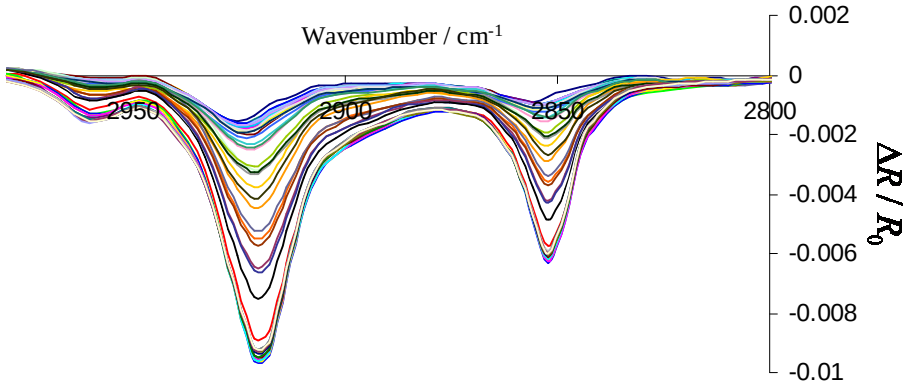

Figure 4.22 Subtracted monolayer spectra following the surface freezing transition of a CTAB + C_{20} mixed monolayer. Unpolarised IR, 250 scans per spectrum, 53° angle of incidence. Cooling rate 1.5 °/hour.

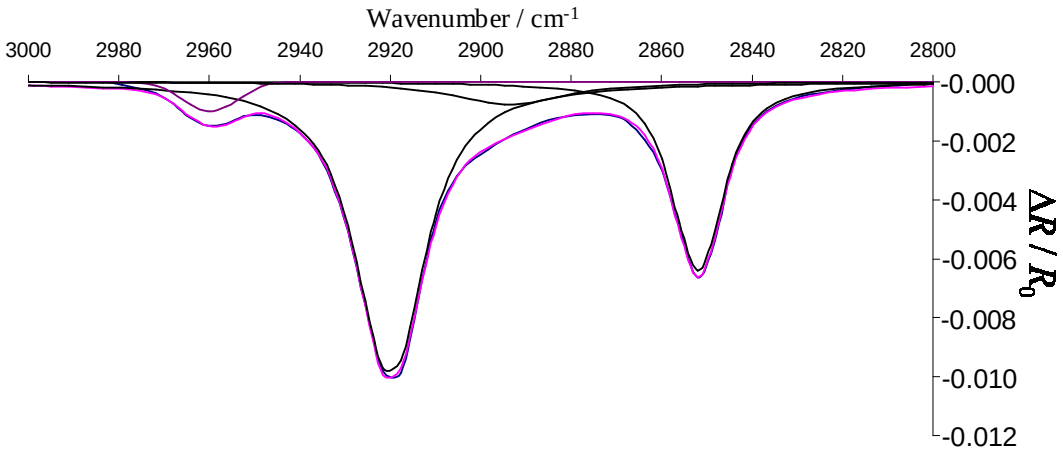

Figure 4.23 Subtracted monolayer spectrum of a mixed monolayer of CTAB and C_{16} in the solid phase, fitted using a four peak model. Fit parameters are summarised in table 4.4.

Four peaks were used to fit the mean spectra, corresponding to the antisymmetric and symmetric CH_2 stretches – at approximately 2920 cm^{-1} and 2851 cm^{-1}, respectively – the antisymmetric CH_3 stretch at about 2960 cm^{-1} and a wider peak centred at roughly 2900 cm^{-1} to take into account the broad central features of the spectra caused by the symmetric CH_3 stretch and a Fermi resonance involving the symmetric CH_2 stretch. The peak assignments, peak positions and peak areas found by the fitting procedure are given in table 4.4 (the broad peak at ~2900 cm^{-1} has been

omitted as only the contribution to the total area of the C-H stretching region is useful).

For both the type I and type II transitions, a clear red shift in position of the methylene stretching bands indicates an increase in order of alkyl chains at the interface and the elimination of *gauche* defects. The magnitude of the shift for the symmetric band is smaller than that of the antisymmetric band, as noted in similar studies on insoluble monolayers.[147, 177, 197] The liquid state peak positions for CTAB/C_{20} mixed monolayers are at higher wavenumbers than the corresponding peaks in the CTAB/C_{16} case, suggesting that the former exhibits a more disordered liquid state. This observation is in agreement with X-ray reflectivity,[198] ellipsometry,[199] and neutron reflectivity[200] measurements which show that the extent of alkane adsorption into the mixed monolayer decreases with increasing alkane chain length, and that alkane inclusion causes a partial ordering of the surfactant alky tail at the end nearest the interface. The solid phase of the type II CTAB/C_{20} frozen monolayer also appears slightly less ordered than the type I CTAB/C_{16} monolayer, since it contains contributions from a liquid-like lower layer as well as a layer of surface frozen alkane.

The relative difference in intensity between the solid and liquid phases can be used to give an estimate of the composition of the mixed monolayer. Deutsche *et al.* used X-ray diffraction to show that the area per chain in a surface frozen mixed monolayer of CTAB and C_{16} is 19.8 $Å^2$.[198] Surface tension measurements suggest that the surface excess of surfactant does not change upon freezing,[201] and so from an estimate of the surface excess of CTAB in the solid phase it is possible to characterise the composition of the system in both the liquid and solid phases. A reasonable approximation for the surface excess of CTAB is to use a value of 3.38 $\mu molm^{-2}$ measured by neutron reflection for a 0.6 mM CTAB solution at 25 °C.[202] If changes in orientation are ignored, and the oscillator strength is assumed to remain constant upon freezing, the ratio of intensities I(liquid)/I(solid) can be used to estimate the surface excess of chains in the liquid phase. The composition in both phases can then be estimated by direct subtraction of the CTAB surface excess, to give a molar ratio (surfactant %:alkane %) of 88:12 in the liquid phase and 40:60 in the solid phase for

the type I CTAB/C_{16} mixed monolayer, an increase in C_{16} mole fraction of 48% in the solid phase. The liquid phase composition is in excellent agreement with that previously reported by Matsubara *et al.* (85:15 surfactant:oil).[203]

Table 4.4 Spectral parameters obtained by fitting in figure 4.23

Peak Assignment	**Peak Centre / cm^{-1}**	**Area (to 3 d.p.) / cm^{-1}**
Liquid Phase CTAB + C_{16}		0.105
Symmetric CH_2	2853.2	.034
Antisymmetric CH_2	2923.9	.043
Antisymmetric CH_3	2960.1	.002
Solid Phase CTAB + C_{16}		0.228
Symmetric CH_2	2851.9	0.063
Antisymmetric CH_2	2920.0	0.139
Antisymmetric CH_3	2960.0	0.018
Liquid Phase CTAB + C_{20}		0.078
Symmetric CH_2	2853.8	.025
Antisymmetric CH_2	2925.5	0.046
Antisymmetric CH_3	2960.6	0.001
Solid Phase CTAB + C_{20}		0.437
Symmetric CH_2	2852.6	0.114
Antisymmetric CH_2	2920.7	0.273
Antisymmetric CH_3	2960.5	0.015

The intensity change during type II freezing is larger than that for type I freezing. This is in accord with the different structures of the frozen layers. A type I frozen layer consists of a frozen mixed monolayer, and so requires sufficient alkane to bring the overall area per chain down to 19.8 $Å^2$. On the other hand, type II freezing involves bilayer formation, where a fresh closely packed layer is added on top of the existing mixed monolayer. Enough new material is required, therefore, to produce a complete layer of chains with molecular area 19.8 $Å^2$. The intensity change of the type II CTAB/C_{20} system can be rescaled to give a relative intensity change for a hypothetical "CTAB/C_{16}" type II bilayer by considering an intensity change per CH_2 unit (based on the assumption that the increase in adsorbed amount in the frozen layer is solely attributable to the alkane). When this is done, it is found that the intensity change for type II freezing is approximately double that for type I freezing. Above it was shown that the intensity change for a type I transition corresponded to a 48% percent increase in C_{16} mole fraction. An intensity change twice as large would correspond to double this effect, i.e. a mole fraction of 96%, which is approximately a complete surface frozen monolayer. Since the formation of a complete frozen monolayer is the requirement for a type 2 transition it can be seen that the relative intensity changes reported above are in agreement with the structures proposed for type I and type II frozen layers.

Although it is clear that a peak shift coupled with an overall intensity change takes place upon surface freezing of type I and type II mixed monolayers, the broad nature of condensed phase peaks prevents resolution of individual contributions from the liquid and solid phases, and therefore any elucidation of the mechanisms of the two freezing transitions.

Mixed Monolayers of CTAB and C_{16}

To gain insight into the molecular level processes taking place during surface freezing, the two sets of dynamic spectra shown in figures 4.21 and 4.22 were used to calculate 2D correlation spectra. Figure 4.24 shows synchronous and asynchronous correlation spectra for the type I transition of a CTAB/C_{16} mixed monolayer as the temperature was lowered from 23 °C to 20 °C (the transition temperature for this system is 21.6 °C). Two strong autopeaks appear in the

synchronous correlation spectrum at 2918 cm^{-1} and 2852 cm^{-1}, and these are assigned to the antisymmetric and symmetric CH2 stretches, respectively. The presence of a third, weak autopeak at 2960 cm^{-1} is implied by the appearance of four crosspeaks at (2960 cm^{-1}, 2918 cm^{-1}) and (2960 cm^{-1}, 2852 cm^{-1}), as well as at the reflected coordinates, which clearly form correlation squares with the two strong autopeaks. This third autopeak can be assigned to the antisymmetric CH_3 stretch. In addition, the pair of crosspeaks at (2918 cm^{-1}, 2852 cm^{-1}) and (2852 cm^{-1}, 2918 cm^{-1}) form a correlation square between the two main autopeaks. All the crosspeaks are positive, indicating a general synchronous increase in intensity through the course of the freezing transition, in full agreement with the 1D spectra in figure 4.21.

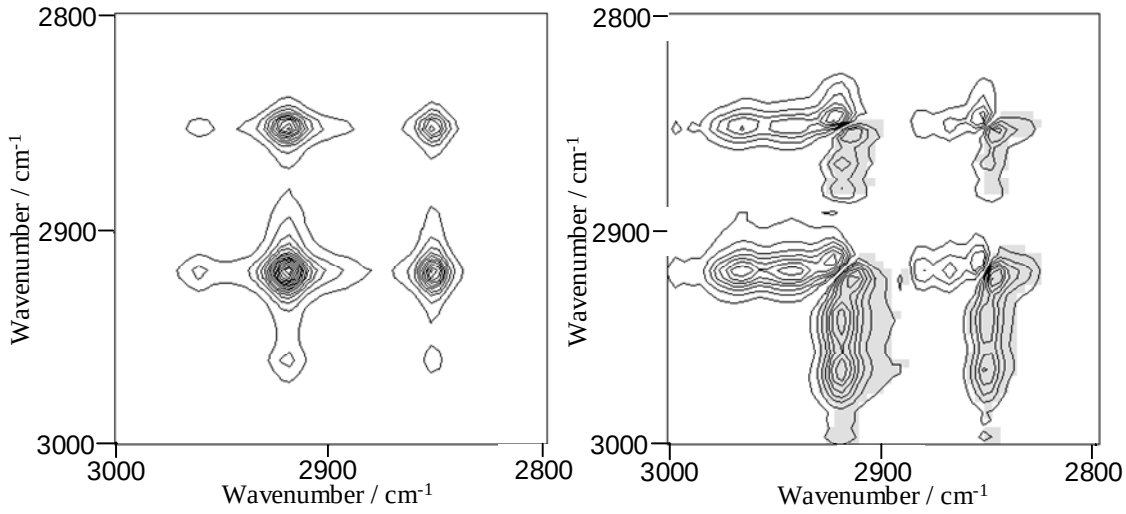

Figure 4.24 2D ER-FTIR correlation analysis of surface freezing for $C_{16}TAB$ + C_{16} mixed monolayers. (Left) Synchronous correlation spectrum. (Right) Asynchronous correlation spectrum.

The asynchronous 2D correlation spectrum can be separated into two sets of crosspeaks. The four positive/negative pairs of peaks centred at (2918 cm^{-1}, 2918 cm^{-1}), (2852 cm^{-1}, 2852 cm^{-1}), (2918 cm^{-1}, 2852 cm^{-1}) and (2852 cm^{-1}, 2918 cm^{-1}) show the existence of some asynchronous correlation between the symmetric and antisymmetric CH_2 stretching regions during the course of the transition, and are highly suggestive that the bands in the original spectra contain contributions from two highly overlapped components. The major remaining crosspeaks show asynchronous correlation between the antisymmetric CH_3 stretch and the two main autopeaks from the synchronous spectrum, i.e. the methyl and

methylene stretching bands are asynchronously correlated. In fact, as shown most clearly by the two asynchronous crosspeaks at (2964 cm^{-1}, 2918 cm^{-1}) and (2941 cm^{-1}, 2918 cm^{-1}), the CH_3 band is resolved into two components in the asynchronous correlation spectrum, corresponding to the r^- antisymmetric stretch (2964 cm^{-1}) and a Fermi resonance involving the r^+ mode (2941 cm^{-1}). The weaker crosspeaks around the centre of the asynchronous spectrum show asynchronous correlation between peaks at 2880 cm^{-1} and 2870 cm^{-1} with the methylene bands. It is likely that these peaks can be assigned to the symmetric methyl stretch (2870 cm^{-1}) and a Fermi resonance interaction between the symmetric CH_2 stretch and an overtone of a low wavenumber CH_3 deformation mode (2880 cm^{-1}). The peaks could also originate from random uncorrelated fluctuations in the baselines. Asynchronous correlation spectra are more susceptible to noise in this manner as random noise is, by its very nature, generally uncorrelated to any real spectral variation. The absence of other asynchronous peaks in the same region, however, suggests that the peak assignment is sound.

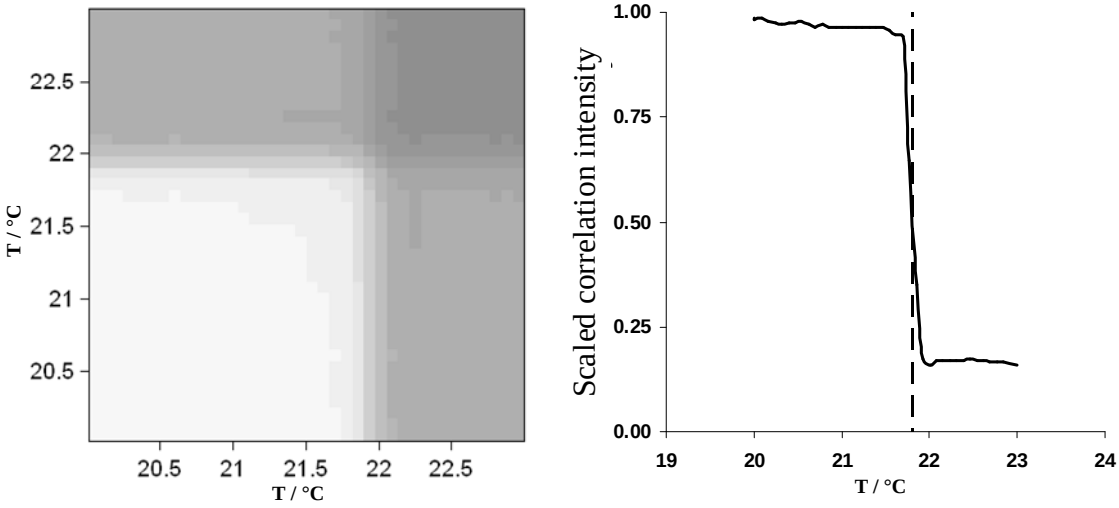

Figure 4.25 Left, sample-sample correlation plot for surface freezing of a C_{16}TAB + C_{16} mixed monolayer. Shading denotes planes of equal correlation intensity. Right, slice spectrum along the T_1=T_2 diagonal, clearly showing a single phase transition temperature at 21.7 °C (dashed line).

Figure 4.25 shows a sample-sample correlation plot of the type I freezing transition of a mixed monolayer of C_{16}TAB and C_{16}. There are two main plateaus in correlation intensity defined by the surface freezing temperature. Moving along the diagonal defined by T_1=T_2, a sudden change in intensity is reached at the point T_1=T_2=21.7

°C, in excellent agreement with the expected transition temperature of 21.6 °C, as measured by elipsometry.

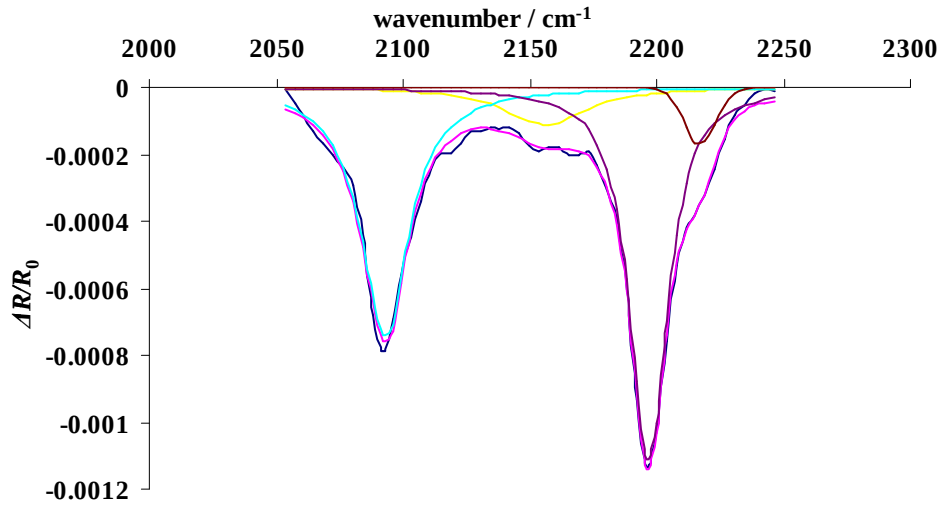

Figure 4.26 Subtracted monolayer spectrum in the C-D stretching region of a d-CTAB/h-C_{16} mixed monolayer in the solid phase.

In order to investigate each component of the C_{16}TAB/C_{16} mixed monolayer, spectra were taken from a mixed monolayer of deuterated C_{16}TAB (*d*-CTAB) and hydrogenated hexadecane (*h*-C_{16}), cooled from 20 °C to 17 °C. Surface freezing temperatures have previously been found to be reduced by approximately 3 °C when either component is deuterated,[204] and indeed ellipsometry showed that T_s=18.6 °C for the *d*-CTAB/*h*-C_{16} system. Figure 4.26 shows a representative spectrum of the C-D stretching region in the solid phase. The bands at 2088 cm^{-1} and 2196 cm^{-1} correspond to the symmetric and antisymmetric CD_2 stretches, respectively, and the shoulder at 2240 cm^{-1} to the CD_3 antisymmetric stretch. The corresponding asynchronous correlation spectra in the C-D and C-H stretching regions are shown in figure 4.27. Heterospectral correlation between the C-D and C-H regions contained no useful information due to the higher levels of noise contained in the C-D spectra, particularly in the liquid phase (the higher levels of noise are a result of close proximity to water bands).

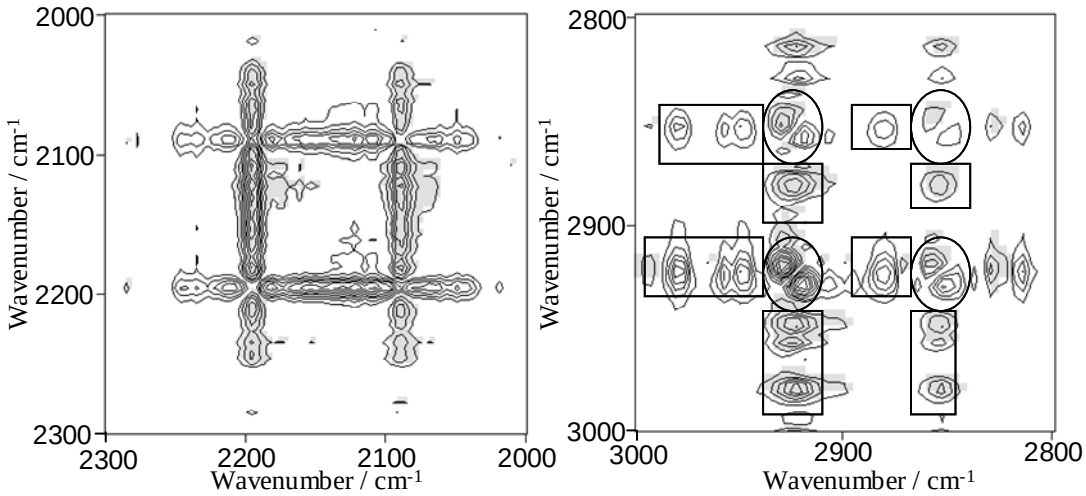

Figure 4.27 Asynchronous 2D correlation plots for the surface freezing of a mixed monolayer of d-CTAB and h-C_{16}. Left, C-D stretching region representing CTAB contributions. Right, C-H stretching region representing C_{16} contributions.

The form of the asynchronous correlation spectra for both *d*-CTAB and *h*-C_{16} components are very similar to that shown earlier for the fully hydrogenated mixed monolayer, and notably share the same general features implying that both surfactant and alkane undergo the same reorientation processes upon freezing. The asynchronous correlation spectrum in the C-D region contains long ridges parallel to the wavenumber axes. These are solely due to increased baseline fluctuations in the C-D region,[140] which is bounded by a strong atmospheric CO_2 absorption and a band structure due to the water bending mode causing background matching and subtraction to be particularly difficult in this region. Nevertheless, a set of four positive/negative pairs of crosspeaks centred at (2196 cm^{-1}, 2196 cm^{-1}), (2088 cm^{-1}, 2088 cm^{-1}), (2196 cm^{-1}, 2088 cm^{-1}) and (2088 cm^{-1}, 2196 cm^{-1}) form a diagnostic correlation pattern which suggests that the CD_2 stretching modes of the raw spectra contain contributions from two components. These coordinates correspond to those of autopeaks in the synchronous correlation spectrum of the C-D stretching region (not shown), and clearly originate from the symmetric (2088 cm^{-1}) and antisymmetric (2196 cm^{-1}) CD_2 stretches. Asynchronous correlation between the asymmetric CD_3 stretch and the CD_2 bands is shown by the two positive crosspeaks at (2240 cm^{-1}, 2196 cm^{-1}) and (2240 cm^{-1}, 2088 cm^{-1}) as well as the two negative peaks situated at the reflected coordinates.

The asynchronous spectrum in the C-H region, relating changes in the alkane component, C_{16}, during the transition contains a quartet of positive/negative peaks centred at (2921 cm^{-1}, 2921 cm^{-1}), (2852 cm^{-1}, 2852 cm^{-1}), (2921 cm^{-1}, 2852 cm^{-1}) and (2852 cm^{-1}, 2921 cm^{-1}). For clarity they have been circled in figure 4.27. The crosspeaks resulting from asynchronous correlation between the r^- and r^+_{FR} are highlighted by rectangles. Additional peaks are an artefact caused by the relatively low surface excess of alkane in the liquid phase (see earlier) which leads to a greater noise contribution from these spectra. The wavenumber positions of all peaks are the same, to within 0.5 cm^{-1} (i.e. the resolution of the plot), as those found in the fully hydrogenated system in figure 4.24, with the exception of the d^- mode which appears at a higher wavenumber. This observation implies that the alkane and surfactant components within the liquid layer might possess different levels of order, or have different bandwidths.

Mixed monolayers of C_{16}TAB and C_{20}

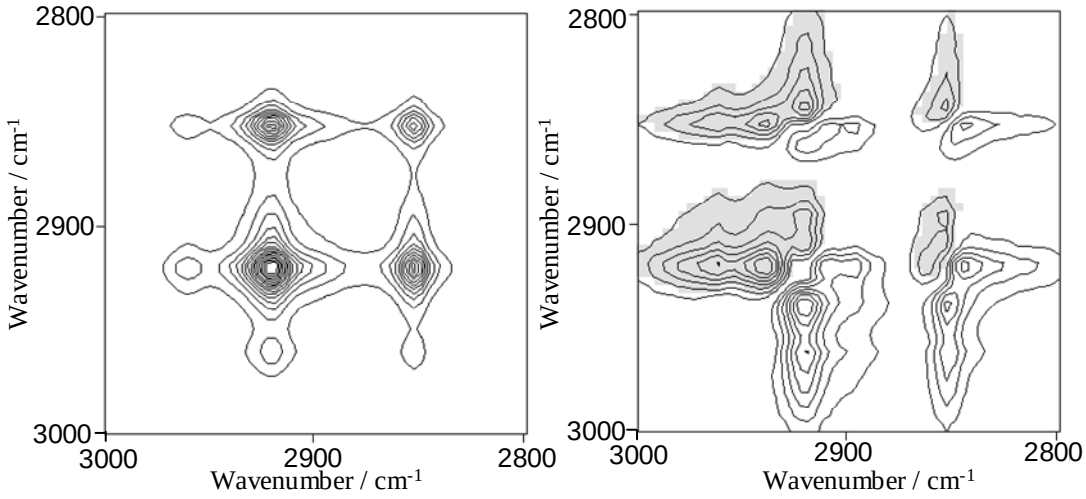

Figure 4.28 2D ER-FTIR correlation analysis of surface freezing for C_{16}TAB + C_{20} mixed monolayers. (Left) Synchronous correlation spectrum. (Right) Asynchronous correlation spectrum.

Synchronous and asynchronous 2D correlation spectra for a type II C_{16}TAB/C_{20} mixed monolayer (T_s=36.9 °C) are shown in figure 4.28. The correlation spectra were calculated from a set of dynamic spectra collected as the sample was cooled from 38 °C to 36 °C. Both components of the monolayer were hydrogenated, and so the correlation spectra contain information from changes in both components during

the transition. Strong autopeaks are located at 2918 cm^{-1} and 2852 cm^{-1}, with a weak autopeak implied at 2960 cm^{-1}. Positive crosspeaks between each of these autopeaks demonstrate a general synchronised increase in intensity of all bands in the C-H stretching region as the monolayer freezes. The asynchronous correlation spectra contains weak pairs of positive/negative crosspeaks centred at 2918 cm^{-1} and at 2852 cm^{-1}, as well as two pairs forming the corners of a correlation square at (2918 cm^{-1}, 2852 cm^{-1}) and (2852 cm^{-1}, 2918 cm^{-1}). This set of four pairs of crosspeaks suggests that multiple overlapped components make up the antisymmetric and symmetric methylene stretching bands of the raw spectra. The most intense crosspeaks are those relating to the methyl stretches, r^- and r^+_{FR}, situated at (2918 cm^{-1}, 2941 cm^{-1}), (2918 cm^{-1}, 2961 cm^{-1}) and their reflections. These crosspeaks – along with slightly weaker peaks at (2852 cm^{-1}, 2941 cm^{-1}) and (2852 cm^{-1}, 2961 cm^{-1}) – indicate an asynchronous correlation between both the methyl stretches and the antisymmetric and symmetric methylene stretches. Qualitatively similar results were obtained for a DTAB/C_{16} mixed monolayer, which also exhibits type II freezing with a transition temperature of 16 °C.[204] The 2D correlation spectra obtained for a mixed monolayer of DTAB and C_{16} are shown in figure 4.29. Mixed monolayers of C_{16}TAB and deuterated eicosane have been shown to form type II solid phases by ellipsometry (see chapter 5), although surface freezing could not be observed by ER-FTIR.

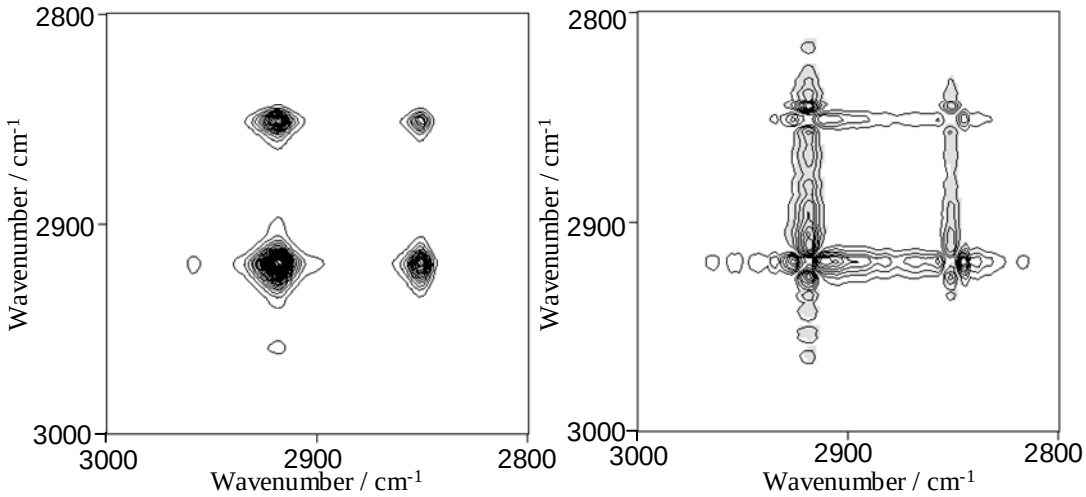

Figure 4.29 2D ER-FTIR correlation analysis of surface freezing for DTAB + C_{16} mixed monolayers. (Left) Synchronous correlation spectrum. (Right) Asynchronous correlation spectrum.

In terms of the patterns and positions of crosspeaks, the asynchronous correlation spectra of the type I and type II systems are fairly similar. There are differences in the signs of these peaks, however, with the signs of peaks in the type II asynchronous spectra exactly opposite those in the type I asynchronous spectra. It is possible that this points to a difference in the mechanism by which the transitions take place. A combination of spectral simulations and semi-quantitative βv-correlation analysis was employed to probe possible differences between the two transitions.

Model 2D Correlation Spectra Based on Simulated Spectra

The concept of using spectral simulations to aid the interpretation of real 2D correlation spectra was introduced in section 4.4.5. The results of these simulations should be applied with care, however, as subtle changes to the input spectra can produce marked differences to the calculated spectra. As an example, figure 4.30 shows simulated 2D correlation spectra recreated from the model described by Elmore *et al.* to distinguish between a true two-phase system and a simple peak shift during the LE/LC transition of a DPPC monolayer.[147] The simulated spectra on which the model is based are shown in figure 4.31, although the overlapped peaks effect has been exaggerated for clarity.

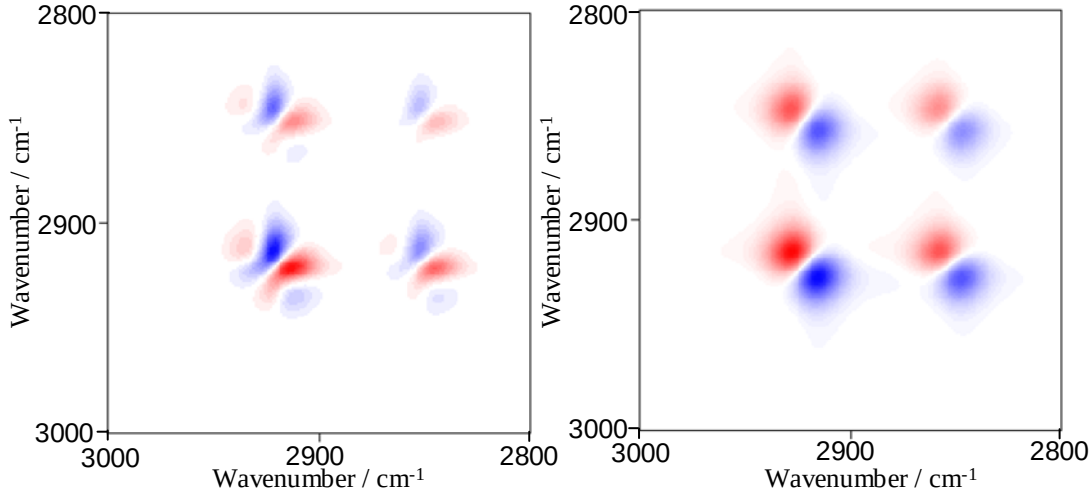

Figure 4.30 Simulated asynchronous 2D correlation spectra based on model spectra as decribed by Elmore et al.[147, 177] for (left) a peak shifting model and (right) an overlapped peaks model. Blue and red indicate regions of negative and positive correlation intensity, respectively.

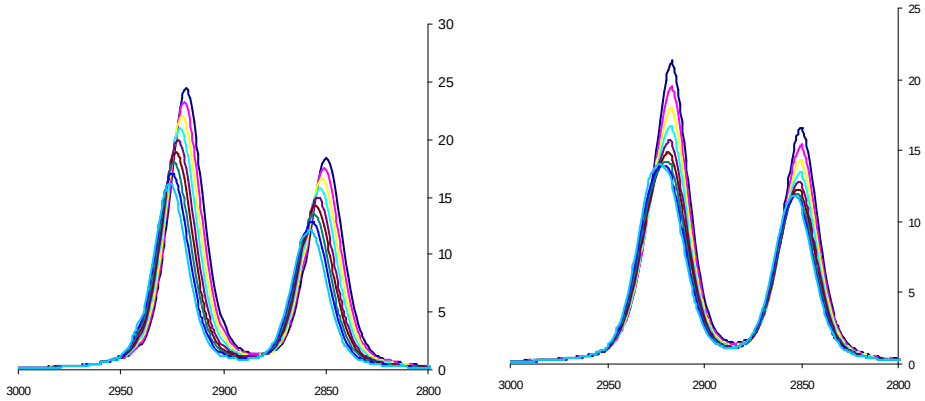

Figure 4.31 Model spectra used in the calculation of the 2D correlation plots shown in figure 4.30. Left, peak shifting model. Right, overlapped peaks model.

The difference between the two extreme cases shown in figure 4.30 is very clear. A peak shift results in a complex structure in the asynchronous correlation spectrum, with distinctive curvature present in crosspeaks close to the diagonal. In contrast, the overlapped peaks model produces a simple pattern consisting of doublets of opposite sign and no curvature. The peak positions of a pair of doublets close to the diagonal approximates to the positions of the two overlapped peaks in the original spectra. This approximation gets worse as the constituent peaks get closer together, however, and the coordinates in the asynchronous spectrum always overestimate the real separation.

The presence of pairs of doublets, or the absence of peak curvature, should not be taken as proof of the existence of two highly overlapped bands in the raw spectra, however. In the example above, the change in peak position is not only sufficiently clear in the simulated spectra to be seen without the aid of 2D correlation analysis, the magnitude of the peak shift is great enough to ensure that all the model spectra are not subsumed under the envelope of the most intense spectra, i.e. a slight "shoulder" appears to the naked eye. This situation does not arise in the spectra reported in this chapter, where the overall peak shifts are sufficiently small that when the spectra are overlaid the envelope of the most intense peak contains all other peaks within it. In this situation, a slightly modified set of patterns are produced in the 2D correlation spectra of a simulated dataset.

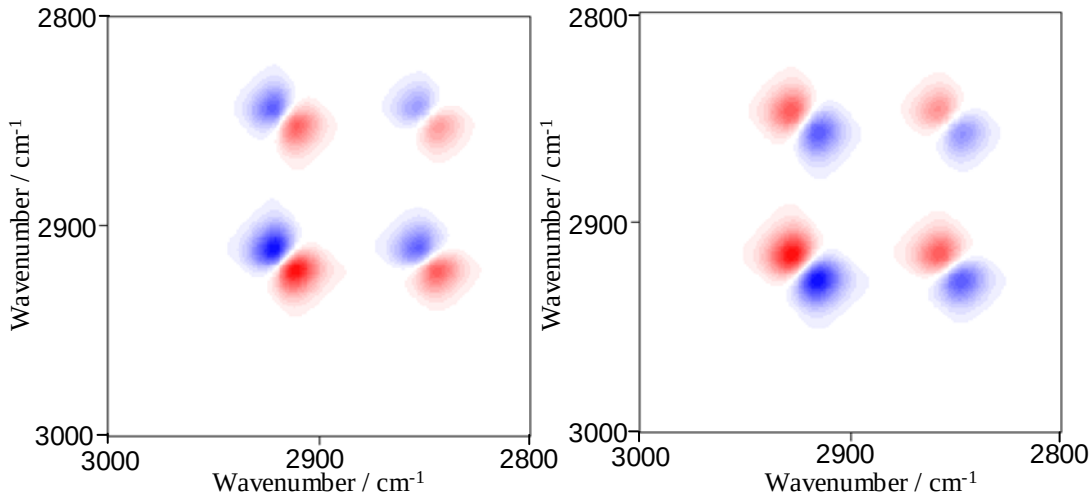

Figure 4.32 Model asynchronous 2D correlation spectra for (left) a peak shifting model and (right) an overlapped peaks model in the case of a small overall peak shift.

The model asynchronous correlation spectra shown in figure 4.32 were calculated from simulated spectra containing two peaks with lineshapes which were 50% Gaussian and 50% Lorentzian in character. The overall peak shift is approximately 1 cm^{-1} in both cases, although it should be noted that the same patterns are produced regardless of peak shift/separation (provided the constraint on the envelope of the most intense peak is satisfied). In fact, the patterns were retained down to a separation of 1×10^{-3} cm^{-1}, the smallest separation tested.

The model spectra shown in figure 4.32 demonstrate unequivocally the importance of modelling when analysing complex 2D correlation spectra, even in cases which seem to display well-published peak patterns. The only differences, in many cases, between a system containing two overlapped peaks and one showing a simple peak shift are the signs of the peaks in the 2D spectra. In such cases the order in which the spectra are inputted is of paramount importance, as signs are also reversed depending on whether a general increase or decrease in intensity is being followed. In this respect, the calculation and modelling of 2D correlation spectra is much like peak fitting – slightly different absolute results may be obtained by different researchers but the same general trends will be observed provided the analyses are internally consistent.

Figure 4.33 shows spectral simulations of the C-H stretching region using an overlapped peaks model. A "three peak" model was constructed using overlapped bands centred at 2920 cm^{-1} and 2924 cm^{-1} for the antisymmetric CH_2 stretch, 2855 cm^{-1} and 2853 cm^{-1} for the symmetric CH_2 stretch and 2960 cm^{-1} for the antisymmetric CH_3 stretch. The use of these peaks alone recreates the peak positions of all major synchronous and asynchronous correlation peaks observed for both type I and type II freezing, apart from those relating to the asynchronous correlation of methyl and methylene stretching bands. In order to model these effects, two extra peaks were added at 2964 cm^{-1} and 2941 cm^{-1} to represent a liquid phase asymmetric CH_3 stretch and a Fermi resonance component whose presence is implied by the experimental 2D correlation spectra. The intensities of these peaks were decreased monotonically throughout the dataset, being replaced by a single asymmetric methyl stretch centred at 2960 cm^{-1} in the solid-phase simulated spectra.

The 2D asynchronous spectra calculated using this model are shown in figures 4.34 and 4.35, alongside the asynchronous correlation spectra for type I freezing of the $C_{16}TAB/C_{16}$ system and type II freezing of the $C_{16}TAB/C_{20}$ system, respectively. There is excellent agreement between the simulated and experimental spectra in figure 4.34, sufficient to justify a phase-coexistence model for the type I transition.

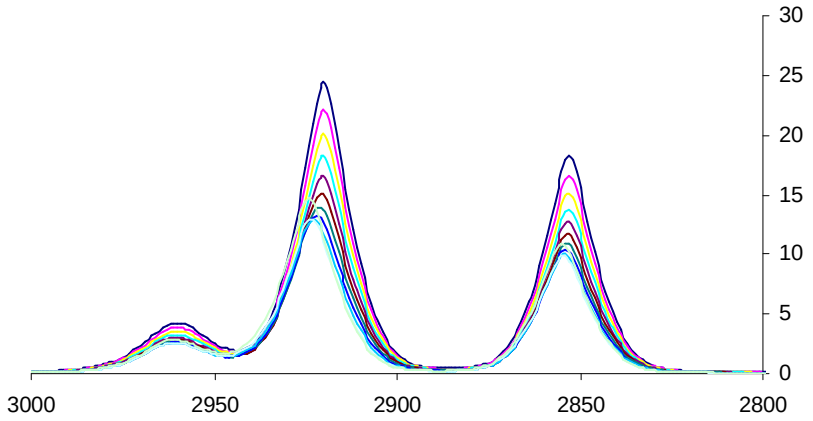

Figure 4.33 Simulated spectra based on a "three peak overlapped" model used for the calculation of trial 2D correlation spectra representing surface freezing transitions.

A purely overlapped peaks model does not account for type II freezing of a $C_{16}TAB/C_{20}$ mixed monolayer, however. As noted earlier, although the peak positions in the experimental synchronous and asynchronous correlation spectra agree to within the resolution of the plot for both $C_{16}TAB/C_{16}$ and $C_{16}TAB/C_{20}$ mixed monolayers, the peak signs in the asynchronous spectra are reversed. Based on the modelling presented here, this finding equates to a different pattern of intensity changes for each transition.

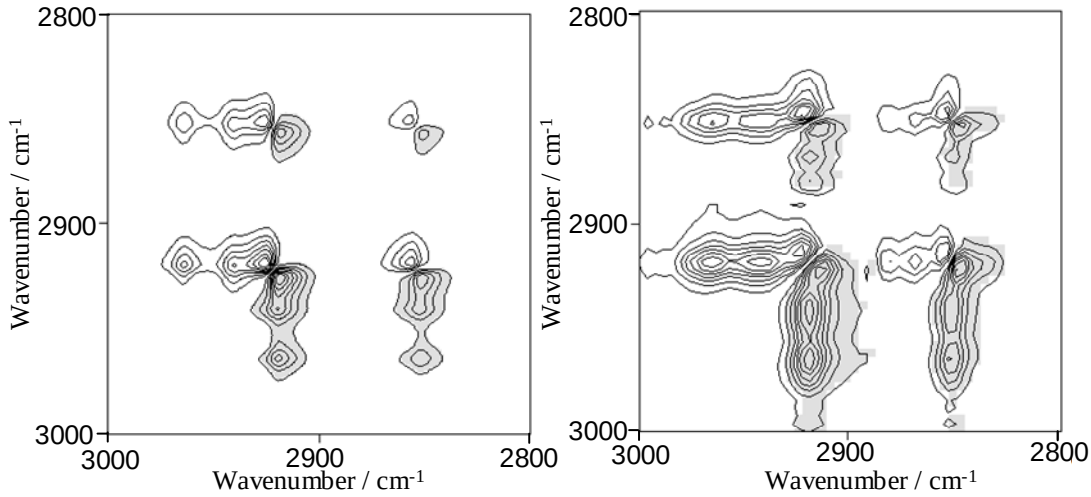

Figure 4.34 Left, asynchronous 2D correlation spectrum calculated from the simulated spectra shown in figure 4.33. Right, asynchronous correlation spectrum for type I surface freezing of a $C_{16}TAB/C_{16}$ mixed monolayer.

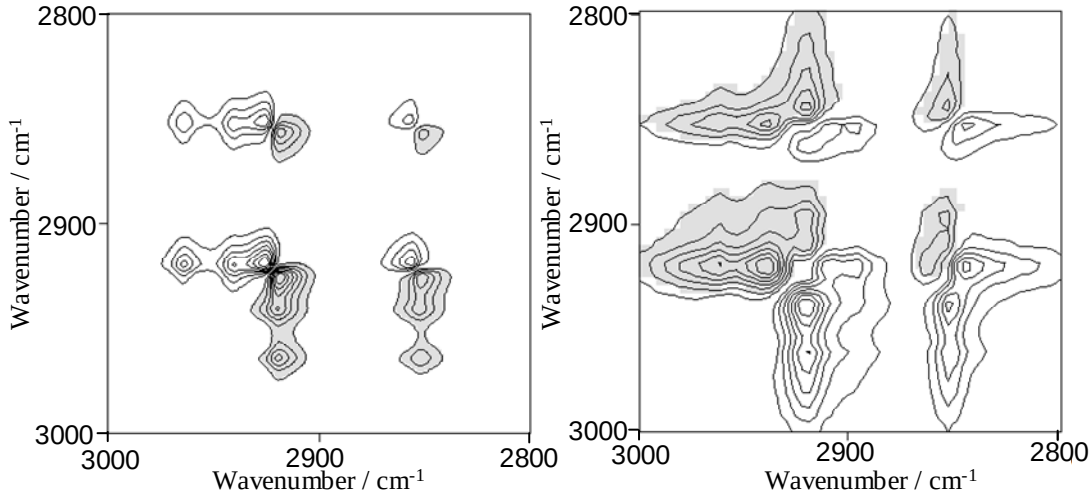

Figure 4.35 (Left) Asynchronous 2D correlation spectrum calculated from the simulated spectra shown in figure 4.33. (Right) Asynchronous correlation spectrum for type II surface freezing of a $C_{16}TAB/C_{20}$ mixed monolayer.

Figure 4.36 shows an asynchronous correlation spectrum calculated using a peak shifting model for the type II transition. The magnitude of the peak shift was set as the difference between the two components in the original overlapped peaks model. The peak shifting model qualitatively recreates the features of the experimental spectrum, including peak signs, with the important exception that the maximum correlation intensity occurs for the pair of peaks centred about the position of the antisymmetric CH_2 stretching band. In the experimental spectrum the maximum correlation intensity relates to the methyl stretching bands, and the intensity of the bands relating solely to methylene stretches are relatively weak. It is probable, therefore, that the majority of the intensity changes in the original experimental spectra take place entirely synchronously. A model is proposed, therefore, in which a small intensity increase accompanies a peak shift, followed by a rapid increase in intensity at constant peak position. The results of this "modified peak shift" simulation are shown in figure 4.37. The modified peak shift model accounts well for both the peak positions and relative intensities of the experimental spectrum, suggesting it could represent a valid description of the type II transition.

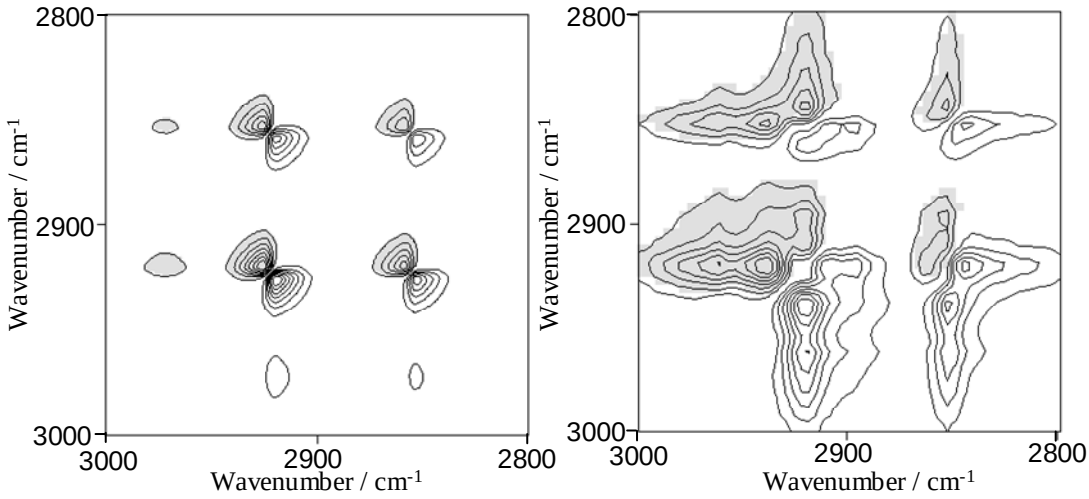

Figure 4.36 (Left) Modelled asynchronous correlation spectrum based on a peak shifting simulation. (Right) Experimental type I asynchronous spectrum of a C_{16}TAB/C_{16} mixed monolayer.

In order to determine whether the sequential orders of intensity change suggested for type I and type II freezing transitions are reasonable, βv-correlation analysis was carried out for both systems. The results of this analysis are shown in figure 4.38. The β_e values are all very similar, both within and between datasets. These results

show that intensity increases in the methyl and methylene bands occur coincidentally and with the same phase for all bands during both type I and type II freezing transitions. Furthermore, the peak positions in the *βv*-correlation plots correlate to the more ordered alkyl phase. These findings are consistent with a concerted increase in intensity caused by the appearance of a more ordered structure, and as such support (or at least do not rule out) the sequence of intensity changes revealed by the simulated spectra.

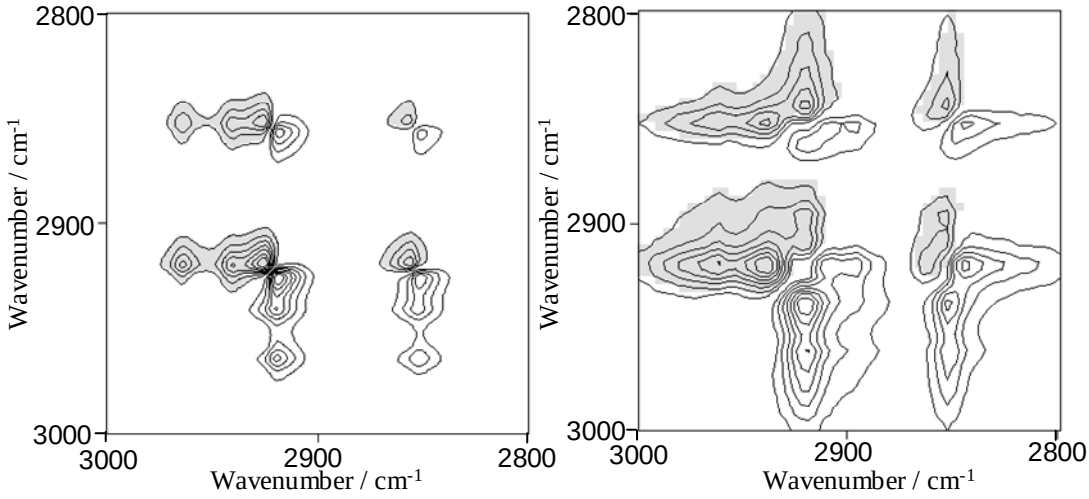

Figure 4.37 (Left) Modelled asynchronous correlation spectrum based on a "modified peak shifting" simulation. (Right) Experimental type II asynchronous spectrum of a $C_{16}TAB/C_{20}$ mixed monolayer.

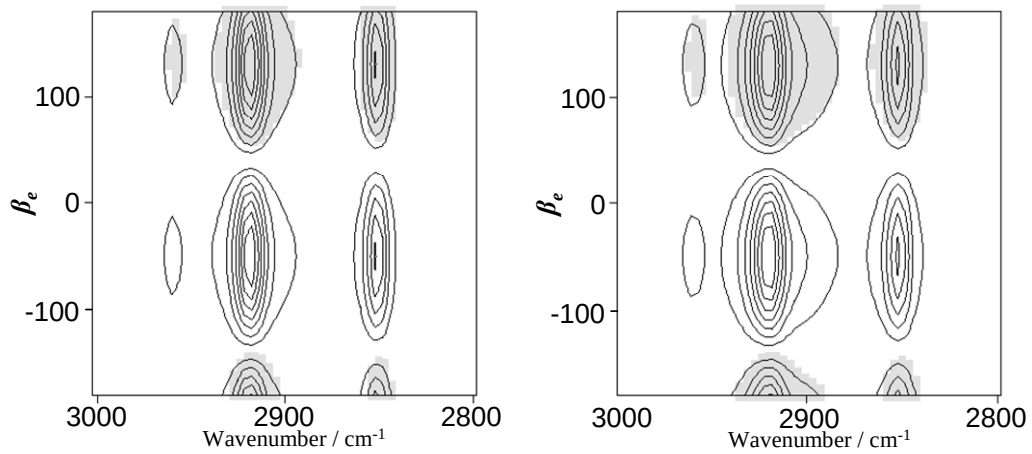

Figure 4.X3 βv-correlation analysis plots for the surface freezing of(left) a type I $C_{16}TAB/C_{16}$ mixed monolayer and (right) a type II $C_{16}TAB/C_{20}$ mixed monolayer.

4.7 Summary

In this chapter, a combination of 2D correlation techniques have been used to probe the structural dynamics of mixed monolayers of surfactant and alkane during surface freezing. Spectral simulations suggest different behaviours for type I and type II freezing. The implications of this finding will be discussed in the context of ellipsometry evidence from chapters 2 and 3 in the conclusions, chapter 6. Vibrational sum-frequency spectroscopy (VSFS) has been applied to complement the ER-FTIR data, and is presented in the next chapter.

4.8 References

1. Levine, I. N., *Quantum Chemistry*. 5th ed.; Prentice Hall: 2000.
2. Atkins, P. W.; Friedman, R. S., *Molecular Quantum Mechanics*. 3rd ed.; Oxford University Press: 1997.
3. Colthup, N. B.; Daly, L. H.; Wiberley, S. E., *Introduction to Infrared and Raman Spectroscopy*. 3rd ed.; Academic Press: 1990.
4. Macphail, R. A.; Strauss, H. L.; Snyder, R. G.; Elliger, C. A., *Journal of Physical Chemistry* **1984,** 88, 334.
5. Snyder, R. G., Infrared and Raman Spectra of Polymers. In *Methods of Experimental Physics: Polymers*, 1 ed.; Fava, F. A., Ed. Academic Press: New York, 1980; Vol. 16A.
6. Snyder, R. G.; Strauss, H. L.; Elliger, C. A., *Journal of Physical Chemistry* **1982,** 86, 5145-5150.
7. Macphail, R. A.; Strauss, H. L.; Snyder, R. G.; Elliger, C. A., *Journal of Physical Chemistry* **1984,** 88, 334-341.
8. Liang, C. Y.; Krimm, S.; Sutherland, G. B. B. M., *Journal of Chemical Physics* **1956,** 25, 543-548.
9. Suranga, P. A.; Wickramarachchi, R.; Spells, S. J.; de Silva, D. S. M., *Journal of Physical Chemistry B* **2007,** 111, 1604-1609.
10. Venkataraman, N. V.; Vasudevan, S., *Journal of Physical Chemistry B* **2001,** 105, 1805-1812.
11. Srinivasan, G.; Neumann-Singh, S.; Muller, K., *Journal of Chromatography A* **2005**, (1074), 31-41.
12. Gorce, J.-P.; Spells, S. J.; Zeng, X.-B.; Ungar, G., *Journal of Physical Chemistry B* **2004,** 108, 3130-3139.
13. Sander, L. C.; Lippa, K. A.; Wise, S. A., *Analytical and Bioanalytical Chemistry* **2005,** 382, 646-668.
14. Jordanov, B.; Tsankov, D.; Korte, E. H., *Journal of Molecular Structure* **2003,** 651-653, 101-107.
15. Alonso, C.; Blaudez, D.; Desbat, B., *Chemical Physics Letters* **1998,** 284, 446-451.
16. Francis, S. A.; Ellison, A. H., Infrared Spectra of Monolayers on metal mirrors. *Journal of the Optical Society of Ameria* **1959,** 49, (2), 131-138.

17. Greenler, R. G., Infrared Study of Adsorbed Molecules on Metal Surfaces by reflection Techniques. *The Journal of Chemical Physics* **1966,** 44, (1), 310-315.
18. Greenler, R. G., Reflection Method fro Obtaining the Infrared Spectrum of a Thin Layer on a Metal Surface. *The Journal of Chemical Physics* **1969,** 50, (5), 1963-1968.
19. Hsu, S. L.; Reynolds, N.; Bohan, S. P.; Strauss, H. L.; Snyder, R. G., Structure, Crystallization and Infrared Spectra of Amorphous Perfluoro-n-alkane Films Prepared by Vapour Condensation. *Macromolecules* **1990,** 23, 4565-4575.
20. Richter, L. J.; Yang, C. S.-C.; Wilson, P. T.; Hacker, C. A.; van Zee, R. D.; Stapleton, J. J.; Allara, D. L.; Yao, Y.; Tour, J. M., Optical Characterisation of Oligo(phenylene-ethynylene) SAMs on Gold. *Journal of Physical Chemistry B* **2004,** 108, 12547-12559.
21. Scheuing, D. R., *Fourier Transform Infrared Spectroscopy in Colloid and Interface Science*. ACS: 1990.
22. Caseli, L.; Perinotto, A. C.; Viitala, T.; Zucolotto, V.; Oliveira, O. N., Jr., Immobilization of ADH in phospholipid films to detect ethanol. *Langmuir* **2009,** 25, 3057-3061.
23. Eischens, R. P.; Francis, S. A.; Pliskin, W. A., *Journal of Physical Chemistry* **1956,** 60, 194.
24. Pliskin, W. A.; Eischens, R. P., *Journal of Chemical Physics* **1956,** 24, 482.
25. Yang, A. C.; Garland, C. W., *Journal of Physical Chemistry* **1957,** 61, 1504.
26. Eischens, R. P.; Pliskin, W. A., *Advances in Catalysis*. Academic Press, inc.: New York, 1957; Vol. IX.
27. Gaines, G. L., *Insoluble Monolayers at the Liquid-Gas Interface*. Wiley and Sons: New York, 1966.
28. Greenler, R. G., *Journal of Chemical Physics* **1966,** 44, 310.
29. Greenler, R. G., *Journal of Chemical Physics* **1969,** 50, 1963.
30. Francis, S. A.; Ellison, A. H., *Journal of the Optical Society of America* **1959,** 49, 131.
31. Hsu, S. L.; Reynolds, N.; Bohan, S. P.; Strauss, H. L.; Snyder, R. G., *Macromolecules* **1990,** 23, 4565.
32. Brunner, H.; Mayer, U.; Hoffmann, H., *Applied Spectroscopy* **1997,** 51, 209.
33. Blaudez, D.; Buffeteau, T.; Desbat, B.; Fournier, P.; Ritcey, A.-M.; Pézolet, M., *Journal of Physical Chemistry* **1998,** 102, 99.
34. Dluhy, R. A.; Cornell, D. G., *Journal of Physical Chemistry* **1985,** 89, 3195.
35. Dluhy, R. A., *Journal of Physical Chemistry* **1986,** 90, 1373.
36. Mielczarski, J. A., *Journal of Physical Chemistry* **1993,** 97, 2649.
37. Buontempo, J. T.; Rice, S. A., *Journal of Chemical Physics* **1993,** 98, 5825.
38. Buontempo, J. T.; Rice, S. A., *Applied Spectroscopy* **1992,** 46, 725.
39. Buontempo, J. T.; Rice, S. A.; Karaborni, S.; Siepmann, J. I., *Langmuir* **1993,** 9, 1604.
40. Buontempo, J. T.; Rice, S. A., *Journal of Chemical Physics* **1993,** 98, 5835.
41. Buontempo, J. T.; Rice, S. A., *Journal of Chemical Physics* **1993,** 99, 7030.
42. Tung, Y.-S.; Gao, T.; Rosen, M. J.; Valentini, J. E.; Fina, L. J., *Applied Spectroscopy* **1993,** 47, 1643.
43. Fina, L. J.; Tung, Y.-S., *Applied Spectroscopy* **1991,** 45, 986.
44. Blaudez, D.; Buffeteau, T.; Cornut, J. C.; Desbat, B.; Escafre, N.; Pézolet, M.; Turlet, J. M., *Applied Spectroscopy* **1993,** 47, 869.

45. Gericke, A.; Michailov, A. V.; Huhnerfuss, H., *Vibrational Spectroscopy* **1993,** 4, (335).
46. Sinnamon, B. F.; Dluhy, R. A.; Barnes, G. T., *Colloids and Surfaces A: Physiochemical and Engineering Aspects* **1999,** 146, 49.
47. Johann, R.; Vollhardt, D.; Möhwald, H., *Colloids and Surfaces A: Physiochemical and Engineering Aspects* **2001,** 182, 311.
48. Le Calvez, E.; Blaudez, D.; Buffeteau, T.; Desbat, B., *Langmuir* **2001,** 17, 670.
49. Sakai, H.; Unemura, J., *Chemistry Letters* **1993**, 2167.
50. Kim, T. Y.; Ahn, D. J., *Material Science and Engineering C* **2004,** 24, 205-208.
51. Gericke, A.; Hühnerfuss, H., *Jounal of Physical Chemistry* **1993,** 97, 12899-12908.
52. Gericke, A.; Hühnerfuss, H., *Ber. Bunsenges. Phys. Chem.* **1995,** 99, 641-650.
53. Gericke, A.; Mendelsohn, R., *Langmuir* **1996,** 12, 758-762.
54. Gericke, A.; Moore, D. J.; Erukulla, R. K.; Bittman, R.; Mendelsohn, R., *Journal of Molecular Structure* **1996,** 379, 227-239.
55. Creuwels, L. A. J. M.; van Golde, L. M. G.; Haagsman, H. P., *Lung* **1997,** 175, 1-39.
56. Mitchell, M. L.; Dluhy, R. A., *Mikrochimica Acta* **1988,** I, 349-352.
57. Mitchell, M. L.; Dluhy, R. A., *Journal of the American Chemical Society* **1998,** 110, 712-718.
58. Macphail, R. A.; Snyder, R. G.; Strauss, H. L., *Journal of Chemical Physics* **1982,** 77, 1118-1137.
59. Flach, C. R.; Brauner, J. W.; Mendelsohn, R., *Biophysical Journal* **1993,** 65, 1994-2001.
60. Pastrana-Rios, B.; Flach, C. R.; Brauner, J. W.; Mautone, A. J.; Mendelsohn, R.,
Biochemistry **1994,** 33, 5121-5127.
61. Pastrana-Rios, B.; S., T.; Keough, K. M. W.; Mautone, A. J.; Mendelsohn, R., *Biophysical Journal* **1995,** 69, 2531-2540.
62. Flach, C. R.; Brauner, J. W.; Taylor, J. W.; Baldwin, R. C.; Mendelsohn, R., *Biophysical Journal* **1994,** 67, 402-410.
63. Gericke, A.; Flach, C. R.; Mendelsohn, R., *Biophysical Journal* **1997,** 73, 492-499.
64. Dluhy, R. A.; Ping, Z.; Faucher, K.; Brockman, J. M., *Thin Solid Films* **1998,** 327-329, 308.
65. Brockman, J. M.; Wang, Z.; Notter, R. H.; Dluhy, R. A., *Biophysical Journal* **2003,** 84, 326.
66. Hernández, E. M.; Franses, E. I., *Colloids and Surfaces A: Physiochemical and Engineering Aspects* **2003,** 214, 249.
67. McClellan, S. J.; Franses, E. I., *Colloids and Surfaces B: Biointerfaces* **2003,** 28, 63.
68. Wen, X.; Frasnes, E. I., *Colloids and Surfaces A: Physiochemical and Engineering Aspects* **2001,** 190, 319.
69. Phang, T.-L.; Frasnes, E. I., *Journal of Colloid and Interface Science* **2004,** 275, 477.

70. Hernández, E. M.; Phang, T.-L.; Wen, X.; Frasnes, E. I., *Journal of Colloid and Interface Science* **2002,** 250, 271.
71. McClellan, S. J.; Frasnes, E. I., *Colloids and Surfaces B: Biointerfaces* **2003,** 30, 1.
72. Wright, J. R., *Nature Reviews Immunology* **2005,** 5, 58-68.
73. Crouch, E. C., *Respiratory Research* **2000,** 1, 93-108.
74. Wang, L.; Brauner, J. W.; Mao, G.; Crouch, E.; Seaton, B.; Head, J.; Smith, K.; Flach, C.; Mendelsohn, R., Interaction of SP-D with Lipopolysacharide. *Biochemistry* **2008,** 47, 8103-8113.
75. Hsu, K. T.; Storch, J., *Journal of Biological Chemistry* **1996,** 271, 13317-13323.
76. Wu, F.; Corsico, B.; Flach, C.; Cistola, D. P.; Storch, J.; Mendelsohn, R., *Biochemistry* **2001,** 40, 1976-1983.
77. Brussieres, S.; Buffeteau, T.; Desbat, B.; Breton, R.; Salesse, C., *Biochimica et Biophysica Acta* **2008,** 1778, 1324-1334.
78. Zheng, J.; Desbat, B.; Rastogi, V. K.; Shah, S. S.; DeFrank, J. J.; Leblanc, R. M., *Biomacromolecules* **2006,** 7, 2806-2810.
79. Meister, A.; Nicolini, C.; Waldmann, H.; Kulhmann, J.; Kerth, A.; Winter, R.; Blume, A., *Biophysical Journal* **2006,** 91, 1388-1401.
80. Gromelski, S.; Brezesinski, G., *Physical Chemistry Chemical Physics* **2004,** 6, 5551-5556.
81. Miyazawa, T.; Blout, E. R., Infrared Spectra of Polypeptides in various conformations: Amide I and I bands. *Journal of the American Chemical Society* **1961,** 83, 712-719.
82. Hiramatsu, H.; Kitagawa, T., FTIR approaches on amyloid fibril structure. *Biochimica et Biophysica Acta* **2005,** 1753, 100-107.
83. DeFlores, L. P.; Ganim, Z.; Nicodemus, R. A.; Tokmakoff, A., Amide I-II Spectroscopy Provides Enhanced Protein Secondary Structure Sensitivity. *Journal of the American Chemical Society* **2009,** 131, 3385-3391.
84. Lavoie, H.; Blaudez, D.; Vaknin, D.; Desbat, B.; Ocko, B. M.; Salesse, C., Properties of valine gramicidin A in monolayers at the air-water interface. *Biophysical Journal* **2002,** 83, 3558-3569.
85. Lavoie, H.; Desbat, B.; Vaknin, D.; Salesse, C., Structure of rhodopsin in monolayers at the air-water interface. *Biochemistry* **2002,** 41, 13424-13434.
86. Yamada, K.; Tsuboi, Y.; Itaya, A., AFM observation of fibroin on mica substrates. *Thin Solid Films* **2003,** 440, 208-216.
87. Bellet-Amalric, E.; Blaudez, D.; Desbat, B.; Graner, F.; Gauthier, F.; Renault, A., Interaction of penetratin protein and a phospholipid monolayer. *Biochimica et Biophysica Acta* **2000,** 1467, 131-143.
88. Ronzon, F.; Desbat, B.; Chauvet, J.-P.; Roux, B., Behaviour of GPI-anchored protein in phospholipid monolayers. *Biochimica et Biophysica Acta* **2002,** 1560, 1-13.
89. Meinders, M. B. J.; van den Bosch, G. G. M.; de Jongh, H. H. J., IRRAS, a new tool in food science. *Trends in Food Science and Technology* **2000,** 11, 218-224.
90. Martin, A. H.; Meinders, M. B. J.; Bos, H. J.; Cohen Stuart, M. A.; van Tillet, T., Conformational aspects of proteins at air-water interfaces. *Langmuir* **2003,** 19, 2922-2928.
91. Meinders, M. B. J.; Van den Bosch, G. G. M.; de Jongh, H. H. J., *European Biophysics Journal* **2001,** 30, 256-267.

92. Kudryashova, E. V.; Meinders, M. B. J.; Visser, A. J. W. G.; van Hoek, A.; de Jongh, H. H. J., *European Biophysics Journal* **2003,** 32, 553-562.
93. Huo, Q.; Dziri, L.; Desbat, B.; Russel, K. C.; Leblanc, R. M., *Journal of Physical Chemistry B* **1999,** 103, 2929-2934.
94. Berdycheva, O.; Desbat, B.; Vaultier, M.; Saint-Pierre-Chazalet, M., *Chemistry and Physics of Lipids* **2003,** 125, 1-11.
95. Meister, A.; Kerth, A.; Blume, A., Adsorption kinetics of pyranoside. *Journal of Physical Chemistry B* **2005,** 109, 6239-6246.
96. Israelachvili, J., *Intermolecular and Surface Forces*. 2nd ed.; Academic Press: 1991.
97. Kumpulainen, A. J.; Persson, M. P.; Eriksson, J. C.; Tyrode, E. C.; Johnson, C. M., surface micelles. *Langmuir* **2005,** 21, 305-315.
98. Campbell, R. A.; Parker, S. R. W.; Day, J. P. R.; Bain, C. D., CTAB. *Langmuir* **2004,** 20, 8740-8753.
99. Campbell, R. A.; Bain, C. D., C10E8. *Vibrationnal Spectroscopy* **2004,** 35, 205-211.
100. Sekine, M.; Campbell, R. A.; Valkovska, D. S.; Day, J. P. R.; Curwen, T. D.; Martin, L. J.; Holt, S. A.; Eastoe, J.; Bain, C. D., APFN. *Physical Chemistry Chemical Physics* **2004,** 6, 5061-5065.
101. Day, J. P. R.; Campbell, R. A.; Russel, O. P.; Bain, C. D., Mixtures. *Journal of Physical Chemistry C* **2007,** 111, 8757-8774.
102. Campbell, R. A.; Day, J. P. R.; Bain, C. D., Separation of bulk abd adsorbed. *Applied Spectroscopy* **2005,** 59, 993-1001.
103. Campbell, R. A.; Ash, P. A.; Bain, C. D., *Langmuir* **2007,** 23, 3242-3253.
104. Tung, Y.-S.; Gao, T.; Rosen, M. J.; Valentini, J. E.; Fina, L. J., *Applied Spectroscopy* **1993,** 47, 1643-1650.
105. Kawai, T.; Kamio, H.; Kon-No, K., *Langmuir* **1998,** 14, 4964-4966.
106. Kawai, T.; Kamio, H.; Kondo, T.; Kon-No, K., *Journal of Physical Chemistry B* **2005,** 109, 4497-4500.
107. Prosser, A. J.; Frasnes, E. I., *Langmuir* **2002,** 18, 9234-9242.
108. Wen, X.; Lauterbach, J.; Frasnes, E. I., *Langmuir* **2000,** 16, 6987-6994.
109. Kawai, T.; Yamada, K.; Kondo, T., 2008. *Journal of Physical Chemistry C* 112, 2040-2044.
110. Islam, M. N.; Ren, Y.; Kato, T., *Langmuir* **2002,** 18, 9422-9428.
111. Ahn, D. J.; Berman, A.; Charych, D., *Journal of Physical Chemistry* **1996,** 100, 12455-12461.
112. Cooper, S. J., *Langmuir* **2002,** 18, 3749-3753.
113. Jamieson, M. J.; Cooper, S. J.; Miller, A. F.; Holt, S. A., *Langmuir* **2004,** 20, 3593-3600.
114. Mendelsohn, R.; Brauner, J. W.; Gericke, A., *Annual Reviews of Physical Chemistry* **1995,** 46, 305-334.
115. Blaudez, D.; Buffeteau, T.; Desbat, B.; Turlet, J. M., *Current Opinion in Colloid and Interface Science* **1999,** 4, 265-272.
116. Bain, C. D.; Greene, P. R., *Current Opinion in Colloid and Interface Science* **2001,** 6, 313-320.
117. Weck, M.; Fink, R.; Ringsdorf, H., *Langmuir* **1997,** 13, 3515-3522.
118. Kawai, T.; Hane, R.; Ishizaka, F.; Kon-No, K., *Chemistry Letters* **1999,** 5, 375-376.

119. Walsh, C. B.; Wen, X.; Frasnes, E. I., *Journal of Colloid and Interface Science* **2001,** 233, 295-305.
120. Pang, S.; Tetsuya, O.; Tomoyuki, W.; Kondo, T.; Kawai, T., *Journal of Colloid and Interface Science* **2005,** 285, 634-639.
121. Lekner, J., *Theory of Reflection*. Matinus Nijhoff Publications: 1987.
122. Bertie, J. E.; Ahmed, M. K.; Eysel, H. H., *Journal of Physical Chemistry* **1989,** 93, 2210.
123. Lide, D. R., *CRC Handbook of Chemistry and Physics*. 74th ed.; CRC Press: Boca Raton: 1993.
124. Losurdo, M.; Bruno, G.; Irene, E. A., *Journal of Applied Physics* **2003,** 94, 4923-4929.
125. Campbell, R. A. External Reflection FTIR Spectroscopy of Surfactants at the Dynamic Air-Water Interface. University of Oxford, Oxford, 2005.
126. Ernst, R. R.; Bodenhausen, G.; Wakaun, A., *Principles of Nuclear Magnetic Resonance in One and Two Dimensions*. Oxford University Press: 1987.
127. Woustersen, S.; Hamm, P., *Journal of Physics - Condensed Matter* **2002,** 14, R1035.
128. Noda, I., *Bulletins of the American Physical Society* **1986,** 31.
129. Noda, I., *Applied Spectroscopy* **1990,** 44.
130. Noda, I., *Journal of the American Chemical Society* **1989,** 111.
131. Noda, I.; Ozaki, Y., *Two-Dimensional Correlation Spectroscopy*. Wiley: 2004.
132. Noda, I.; Dowrey, A. E. M., C., *Applied Spectroscopy* **1993,** 47, 1317-1323.
133. Noda, I., *Applied Spectroscopy* **1993,** 47, 1329.
134. Ekgasit, S.; Ishida, H., *Applied Spectroscopy* **1995,** 49, (9), 1243-1253.
135. Noda, I.; Dowrey, A. E.; Marcott, C.; Story, G. M.; Ozaki, Y., *Applied Spectroscopy* **2000,** 54, (7), 236A-248A.
136. Eads, C. D.; Noda, I., *Journal of the American Chemical Society* **2002,** 124, 1111-1118.
137. Hu, B. W.; Zhou, P.; Noda, I.; Ruan, Q. X., *Journal of Physical Chemistry B* **2006,** 110, 18046-18051.
138. Hannan, E. J., *Multiple Time Series*. Wiley, New York: 1970.
139. Noda, I., *Applied Spectroscopy* **2000,** 54.
140. Czarnecki, M. A., *Applied Spectroscopy* **1999,** 53, 1392-1397.
141. Jung, Y. M., *Vibrational Spectroscopy* **2004,** 36, 267-270.
142. Czarnecki, M. A., *Applied Spectroscopy* **1998,** 52, 1583-1590.
143. Berry, R. J.; Ozaki, Y., *Applied Spectroscopy* **2002,** 56.
144. Jung, Y. M.; Shin, H. S.; Kim, S. B.; Noda, I., *Applied Spectroscopy* **2002,** 56.
145. Czarnik-Matusewicz, B.; Murayama, K.; Tsenkova, R.; Ozaki, Y., *Applied Spectroscopy* **1999,** 53.
146. Czarnik-Matusewicz, B.; Murayama, K.; Wu, Y.; Ozaki, Y., *Journal of Physical Chemistry B* **2000,** 104.
147. Elmore, D. L.; Dluhy, R. A., *Colloids and Surfaces A: Physiochemical and Engineering Aspects* **2000,** 171, 225-239.
148. Huang, H.; Malkov, S.; Coleman, M.; Painter, P., *Macromolecules* **2003,** 36, 8148-8155.
149. Huang, H.; Malkov, S.; Coleman, M.; Painter, P., *Macromolecules* **2003,** 36.

150. Kim, H.; Jeon, S.-J., *Bulletins of the Korean Chemical Society* **2001,** 22, 807-815.
151. Noda, I.; Liu, Y.; Ozaki, Y., *Journal of Physical Chemistry* **1996,** 100, 8665-8673.
152. Noda, I.; Liu, Y.; Ozaki, Y., *Journal of Physical Chemistry* **1996,** 100, 8674-8680.
153. Noda, I.; Story, G. M.; Marcott, C., *Vibrational Spectroscopy* **1999,** 19, 461-465.
154. Ozaki, Y.; Liu, Y.; Noda, I., *Macromolecules* **1997,** 30, 2391-2399.
155. Noda, I.; Dowrey, A. E.; Marcott, C.; Story, G. M.; Ozaki, Y., *Applied Spectroscopy* **2000,** 54, 264A.
156. Noda, I.; Liu, Y.; Ozaki, Y.; Czarnecki, M. A., *Journal of Physical Chemistry* **1995,** 99, 3068-3073.
157. Noda, I.; Dowrey, A. E.; Marcott, C., *Applied Spectroscopy* **1993,** 47, 1317-1323.
158. Noda, I., *Vibrational Spectroscopy* **2004,** 36, 143-165.
159. Ozaki, Y.; Noda, I., *Progress in 2D Correlation Spectroscopy*. American Institute of Physics: New York, 2000.
160. Jai, Q.; Wang, N. N.; Yu, Z. W., *Applied Spectroscopy* **2009,** 63, 344-353.
161. Noda, I.; Story, G. M.; Marcott, C., *Vibrational Spectroscopy* **1999,** 19, 461.
162. Palmer, P. A.; Manning, C. J.; Chao, L. J.; Noda, I.; Dowrey, A. E.; Marcott, C., *Applied Spectroscopy* **1991,** 45, 12.
163. Gregoriou, V. G.; Chao, L. J.; Toriumi, H.; Palmer, P. A., *Chemical Physics Letters* **1991,** 179, 491.
164. Fuji, A.; Palmer, P. A.; Chen, P.; Jiang, E. Y.; Chao, L. J., *Mikrochimica Acta* **1997,** 14, 599.
165. Ren, Y.; Shimoyama, M.; Ninomiya, T.; Matsukawa, K.; Noda, I.; Ozaki, Y., *Applied Spectroscopy* **2000,** 53, 919-926.
166. Strobl, G. R.; Hagedorn, W., *Journal of Polymer Science: Polymer Phyisics Edition* **1978,** 16, 1181.
167. Noda, I.; Liu, Y.; Ozaki, Y., *Jounal of Physical Chemistry* **1996,** 100, 8665-8673.
168. Awichi, A.; Tee, E. M.; Srikanthan, G.; Zhao, W., *Applied Spectroscopy* **2002,** 56, 897.
169. Czarnecki, M. A.; Wu, P.; Siesler, H. W., *Chemical Physics Letters* **1998,** 283, 326.
170. Choi, H. C.; Jung, Y. M.; Noda, I.; Kim, S. B., *Journal of Physical Chemistry B* **2003,** 107, 5806.
171. Noda, I., *Macromolecular Chemistry* **1990,** 1, 89.
172. Sasic, S.; Muszynski, A.; Ozaki, Y., *Journal of Physical Chemistry A* **2000,** 104, 6380-6387.
173. Sasic, S.; Muszynski, A.; Ozaki, Y., *Journal of Physical Chemistry A* **2000,** 104, 6388-6394.
174. Segtnan, V. H.; Sasic, S.; Isaksson, T.; Ozaki, Y., *Analytical Chemistry* **2001,** 73, 3153-3161.
175. Shinzawa, H.; Morita, S.-I.; Awa, K.; Okada, M.; Noda, I.; Ozaki, Y.; Sato, H., *Applied Spectroscopy* **2009,** 63, 501-506.
176. Dluhy, R. A.; Shanmuckh, S.; Morita, S.-I., *Surface and Interface Analysis* **2006,** 38, 1481-1496.

177. Elmore, D. L.; Dluhy, R. A., *Applied Spectroscopy* **2000,** 54, 956-962.
178. Nabet, A.; Auger, M.; Pezolet, M., *Applied Spectroscopy* **2000,** 54, 948-954.
179. Elmore, D. L.; Dluhy, R. A., *Journal of Physical Chemistry B* **2001,** 105, 11377-11386.
180. Elmore, D. L.; Shanmuckh, S.; Dluhy, R. A., *Journal of Physical Chemistry A* **2002,** 106, 3420-3428.
181. Shanmuckh, S.; Dluhy, R. A., *Vibrational Spectroscopy* **2004,** 36, 167-177.
182. Morita, S.-I.; Shanmuckh, S.; Ozaki, Y.; Dluhy, R. A., *Applied Spectroscopy* **2006,** 60, 1279-1284.
183. Morita, S.-I.; Shanmuckh, S.; Dluhy, R. A., *Journal of Molecular Structure* **2006,** 799, 48-51.
184. Shanmuckh, S.; Biswas, N.; Waring, A. J.; Walther, F. J.; Wang, Z.; Chang, Y.; Notter, R. H.; Dluhy, R. A., *Biophysical Chemistry* **2005,** 113, 233-244.
185. Czarnik-Matusewicz, B.; Murayama, K.; Wu, Y.; Ozaki, Y., *Journal of Physical Chemistry B* **2000,** 104, 7803-7811.
186. Ji, H.; Kim, S. B.; Noda, I.; Jung, Y. M., *Spectrochimica Acta Part A: Molecular and Biomolecular Spectroscopy* **2009,** 71, 1873-1876.
187. Sett, P.; Chowdhury, J.; Mallick, P. K., *Journal of Molecular Structure* **2009,** 929, 200-206.
188. Lina, M.; Chelli, R.; Volkov, V. V.; Righini, R., *Journal of Chemical Physics* **2009,** 130, 204518.
189. Yang, H. X.; Sun, M.; Zhou, P., *Polymer* **2009,** 50, 1533-1540.
190. Jansen, T. I. C.; Cringins, D.; Pshenichnikov, M. S., *Journal of Physical Chemistry A* **2009,** 113, 6250-6265.
191. Bredenbeck, J.; Ghosh, A.; Smits, M.; Bonn, M., *Journal of the American Chemical Society* **2008,** 130, 2152-2153.
192. Griffiths, P. R.; de Haseth, J. A., *Fourier Transform Infrared Spectroscopy*. John Wiley & Sons: 1986.
193. Michelson, A. A., *Studies in Optics*. University of Chicago Press: 1927.
194. Rabolt, J. F.; Bellar, R., Apodization. *Applied Spectroscopy* **1980,** 35, 132-135.
195. Cooley, J. W.; Tukey, J. W., **1965,** 19, 297-301.
196. Johnston, S. F., *Fourier Transform Infrared, a constantly evolving technology*. 1st ed.; Ellis Horwood: 1991.
197. Alonso, C.; Blaudez, D.; Desbat, B.; Artzner, F.; Berge, B.; Renault, A., *Chemical Physics Letters* **1998,** 284, 446-451.
198. Sloutskin, E.; Sapir, Z.; Bain, C. D.; Lei, Q.; Wilkinson, K. M.; Tamam, L.; Deutsch, M., *Physical Review Letters* **2007,** 99, 136102.
199. Wilkinson, K. M.; Lei, Q.; Bain, C. D., *Soft Matter* **2006,** 2, 66-76.
200. Binks, B. P.; Crichton, D.; Fletcher, P. D. I.; MacNab, J. R.; Li, Z. X.; Thomas, R. K.; Penfold, J., *Colloids and Surfaces A: Physiochemical and Engineering Aspects* **1999,** 146, 299.
201. Lei, Q.; Bain, C. D., *Physical Review Letters* **2004,** 92, 176103.
202. Manning-Benson, S.; Parker, S. R. W.; Bain, C. D.; Penfold, J., *Langmuir* **1998,** 14, 990.
203. Matsubara, H.; Ikeda, N.; Takiue, T.; Aratono, M.; Bain, C. D., *Langmuir* **2003,** 19, 2249.
204. Wilkinson, K. M. Phase Transitions in Monolayers of Soluble Surfactants. University of Oxford, 2004.

Chapter 5

VSFS Study of Surface Freezing at the Air/Water Interface

5.1 Introduction

Vibrational Sum-Frequency Spectroscopy (VSFS) is an intrinsically surface sensitive technique and, moreover, the intensity of peaks in sum-frequency spectra are indicative of molecular ordering, orientation and adsorption density at the surface. VSFS is thus a useful experimental tool for the study of phases and phase transitions at interfaces. The technique is also inherently complementary to both FTIR and Raman spectroscopy. Where the intensity of a band in an FTIR spectrum, for example, is dependent upon the absolute number of bonds present which contribute to that band, the intensity of a band in a sum-frequency spectrum is determined largely by symmetry considerations at the interface. A particularly useful consequence for the present study is that VSF spectra of all-*trans* alkyl chain molecules are dominated by methyl stretches, whilst the corresponding FTIR spectra are dominated by methylene stretches. The origin of this observation will be discussed later.

Bain *et al.* have used VSFS to study thermal phase transitions in monolayers of medium chain length alcohols on water.[1, 2] It was found that the monolayers displayed a high degree of order even in the liquid phase but that the proportion of *gauche* defects decreased upon monolayer freezing, accompanied by a sudden increase in surface density. These findings correlate well with PM-IRRAS experiments carried out by Berge *et al.*. Surface freezing transitions in mixed monolayers of SDS with dodecanol, C_nTAB with dodecanol, and C_{16}TAB with tetradecane have also been studied by VSFS.[3-5] In all cases selective deuteration of surfactant and oil was used to confirm that both components of the mixed monolayer become more ordered below the freezing transition. Experiments were carried out on a D_2O subphase to eliminate interfacial water bands which could complicate the appearance of the spectra. To date, VSFS has only been used to study type I surface freezing transitions.

Since VSFS is a chemically specific technique, the structure of different areas of a molecule can be studied by targeting different spectral regions. The headgroup structure of SDS monolayers as a function of bulk SDS concentration and salinity

has been studied in this manner, and was found to remain constant irrespective of ionic strength or molecular area at the interface.[6]

The ordering of interfacial water molecules by both cationic and anionic surfactants has also been observed.[7] A marked enhancement of background water signal with increasing surfactant concentration was attributed to the ordering of several layers of water molecules as the electrostatic field at the interface increased. More subtle hydration behaviour takes place in the case of nonionic surfactant headgroups at the air-water interface. Many of the characteristic phenomena associated with nonionic surfactants (such as the existence of a cloud point and temperature-induced phase inversions in microemulsion systems, for example) occur as a result of these complex, temperature-dependent, interactions. VSFS has been used to probe the hydration state of a variety of nonionic surfactant headgroups.[8, 9] Surfactants studied included those, such as sugar-based maltosides and glucosides, whose headgroups are rigid and form ordered structures at the air-water interface as well as poly(ethylene oxide) surfactants whose headgroups are flexible and remain disordered upon adsorption. In all cases, irrespective of headgroup order, a strong structuring of interfacial water was effected by adsorption of nonionic surfactant.

The aim of this chapter is to utilise the unique features of VSFS to address a number of facets of surface freezing that are not yet fully understood. Recent X-ray reflectivity data have suggested a possible change in headgroup orientation in the frozen phase of type I C_{16}TAB/*n*-alkane,[10] which should cause a change in interfacial water structure. Previous VSFS studies of these systems have eliminated water bands through the use of a D_2O subphase, and so it has not as yet been possible to observe directly any change in interfacial water structure. The appearance of type I and type II freezing transitions has been attributed to the chain length difference between surfactant tailgroups and *n*-alkane chains. Current rationalisations of type II frozen bilayer structures describe a liquid-like mixed alkane/surfactant monolayer wet by a surface frozen alkane monolayer. If this is the case, only the alkane component should order during the freezing transition.

In addition to an extension of existing VSFS studies on type I C_{16}TAB/hexadecane mixed monolayers, data are presented for two novel systems: a type II

C_{16}TAB/eicosane mixed monolayer and a type I $C_{16}E_8$/octadecane mixed monolayer. The former system is of interest as to date only type I frozen monolayers have been studied using VSFS, whilst the latter explores a tailgroup/*n*-alkane chain combination that exhibits type II freezing with C_{16}TAB as surfactant.

5.2 Acknowledgement

All spectra presented in this chapter were obtained and produced under the supervision of Dr. Eric Tyrode at the Royal Institute of Technology (KTH), Stockholm.

5.3 Vibrational Sum Frequency Spectroscopy

VSFS is a non-linear spectroscopic technique, which utilises incident radiation of comparable magnitude to the internal electric field of a molecule. In such situations, the electronic response of a molecule is not directly proportional to the strength of an applied field and higher order terms in the expansion of the dipole moment must be taken into account, hence the term non-linear (eqn. 5.1).

$$\mu = \mu_0 + \alpha.E + \beta \cdot E \cdot E + ... \tag{5.1}$$

Here the dipole in the absence of any field is given by μ_0, α is the polarisability of the molecule, β the hyperpolarisability and E the applied electric field. All these quantities are tensors, with β a third-rank tensor; β is represented by a three-dimensional array.

In condensed phase studies it is usual to consider the polarisation induced per unit volume of material, **P**, which takes the same form as eqn. 5.1 with α and β replaced by $\chi^{(1)}$ and $\chi^{(2)}$, the first- and second-order susceptibility tensors (eqn. 5.2).

$$\mathbf{P} = \varepsilon_0(\chi^{(0)} + \chi^{(1)} \cdot E + \chi^{(2)} \cdot E \cdot E + ...) \tag{5.2}$$

VSFS uses two pulsed lasers, one fixed in the visible (ω_{vis}) and the other tuneable in the IR (ω_{ir}), overlapped both spatially and temporally at the interface to produce the non-linear response. As a result of the non-linear optical response, light is reradiated by the sample not only at the frequency of the incident radiation but also at additional frequencies corresponding to the modulation of higher-order (in this case second-order) polarisations. Frequency doubled radiation, corresponding to $2\omega_{vis}$ and $2\omega_{ir}$, is emitted along with the two linear combinations $(\omega_{vis} + \omega_{ir})$ and $(\omega_{vis} - \omega_{ir})$. Light reradiated with frequency $(\omega_{vis} + \omega_{ir})$ is the sum-frequency signal, detected during a VSFS experiment, and which gives the technique its name.

The angle at which the sum-frequency beam is emitted is related to the angles of incidence of the visible and IR beams, and can be readily calculated by considering the conservation of momentum of radiation parallel with the surface (eqn. 5.3).

$$\omega_{SF} \sin\theta_{SF} = \omega_{vis} \sin\theta_{vis} + \omega_{IR} \sin\theta_{IR} \tag{5.3}$$

The intensity of the generated sum-frequency signal is proportional to the square of the $(\omega_{vis} + \omega_{ir})$ component of the second-order term in eqn. 5.2.

$$I_{SF} \propto \left|\chi^{(2)}\right|^2 I_{vis} I_{IR} \tag{5.4}$$

The key factor in determining the intensity of the observed sum-frequency signal, therefore, is the form of the second-order susceptibility, $\chi^{(2)}$, which is proportional to the orientation-averaged molecular hyperpolarisability, $\langle\beta\rangle$, and the number density of molecules, *N* (eqn.5.5).

$$\chi^{(2)} = \frac{N}{\varepsilon_0} \langle\beta\rangle f \tag{5.5}$$

Here the factor *f* takes into account the local electric field experienced by each molecule, which will be different to the overall electric field of the incident radiation due to the induced dipoles of neighbouring molecules. The presence of the orientation-averaged hyperpolarisability in eqn. 5.5 gives rise to the sensitivity of

VSFS to the degree of molecular-level order present in a sample. In the case where pairs of molecules have the same net orientation, contributions to $\langle\beta\rangle$ are additive. Contributions from molecules with opposing orientations cancel, and therefore a more ordered sample gives rise to a stronger SF signal.

The intrinsic surface sensitivity of VSFS arises from the symmetry properties of $\chi^{(2)}$, which changes sign under the inversion operation. The majority of bulk materials are centrosymmetric, with identical properties irrespective of inversion, and so the equality in eqn. 5.6 can only be satisfied when $\chi^{(2)}_{ijk} = 0$. Hence, sum-frequency signal can, in general, only be generated from molecules residing in non-centrosymmetric environments such as those at the interface between two bulk media.

$$\chi^{(2)}_{ijk} = -\chi^{(2)}_{-i-j-k} \tag{5.6}$$

Application of perturbation theory leads to a general expression for the molecular hyperpolarisability in the vicinity of a molecular vibration (eqn. 5.7).

$$\beta = \frac{\alpha\mu}{2(h/2\pi)(\omega_{IR} - \omega_0 - i\Gamma)} \tag{5.7}$$

In eqn. 5.7 α is the Raman transition dipole moment, μ is the IR transition dipole moment and Γ is a parameter describing the linewidth of a vibration of frequency ω_0. This relation reveals two important features of sum-frequency spectra. Firstly, in order for β, and hence the intensity of the generated sum-frequency signal, to be non-zero, a vibrational transition must be both IR and Raman active. Secondly, the sum-frequency signal reaches a maximum when the incident IR beam is resonant with a molecular vibration. Scanning the tuneable IR laser through a frequency range of interest therefore yields a vibrational spectrum of the sample.

Four different polarisation combinations can be used to probe elements of the susceptibility, *SSP*, *PPP*, *SPS* and *PSS* (where the letters *P* and *S* refer to p and s polarisation, respectively, and the order denotes the polarisations of sum-frequency, visible and IR in order). Spectra taken in these polarisations give information about

vibrational modes with preferential orientation along different axes with respect to the interface, and hence give complementary information. By far the most useful polarisation combination for this project is *SSP*, which contains information about the methyl and methylene stretching modes and gives an indication of the presence or absence of *gauche* defects. Examples of this are given in section 5.3.1.

5.3.1 Vibrational Sum-Frequency Spectra of *n*-Alkanes

The position and assignment of peaks in the sum-frequency spectra of *n*-alkanes are identical to those previously discussed in chapter 4.2.5 in relation to the underlying IR and Raman bands from which the sum-frequency response is generated. The relevant mode assignments, along with approximate peak wavenumbers are summarised in table 5.1.

In the case of IR and Raman spectroscopy, it is the central wavenumber of these peaks that provides structural information. By contrast, in sum-frequency spectra the absolute intensity of peaks gives the information about ordering and orientation of the bonds giving rise to that peak. For example, IR and Raman spectra of *n*-alkanes are dominated by methylene stretches due to the large number of these groups in a typical alkane. In an all-*trans* chain, however, each C-C unit contains a centre of inversion and so contributions to β from methylene units either side of this centre cancel and no SF signal is generated. This symmetry is broken when chains contain *gauche* defects, however, and methylene stretches will appear. As a result, the relative intensities of d^+ and r^+ modes in *SSP* spectra give an indication of the fraction of gauche defects present in alkyl chains at an interface. *PPP* and *SPS* spectra are dominated by the presence or absence a single strong peak assigned to the asymmetric methyl stretch, centred at approximately 2965 cm^{-1}. The presence of a strong band indicates a highly ordered, approximately vertical orientation of chains at the interface. These features are demonstrated in figure 5.1 using spectra obtained from the surface of liquid *n*-hexadecane at 20 °C. The strongest peak in the *SSP* spectrum is that of the symmetric methylene stretch, d^+, with only a relatively weak symmetric methyl stretch. Coupled with a weak r^- peak in the *PPP* spectrum this is indicative of an interfacial layer containing a significant proportion of *gauche*

defects, as would be expected from the liquid nature of the *n*-hexadecane surface at 20 °C.

Table 5.1 CH stretching modes of *n*-alkanes

Mode	Description	Approximate wavenumber / cm^{-1}
D^+	CH_2 symmetric stretch	2850
$D^+\omega$	Terminal CH_2 symmetric stretch	2853
R^+	CH_3 symmetric stretch	2870
D^+_{FR}	Fermi resonance involving CH_2 symmetric stretch	2890
d^-	CH_2 antisymmetric stretch	2920
R^+_{FR}	Fermi resonance involving CH_3 symmetric stretch	2930
r_b^-	Out-of-plane component of CH_3 antisymmetric stretch	2950
r_a^-	In-plane component of CH_3 antisymmetric stretch	2960

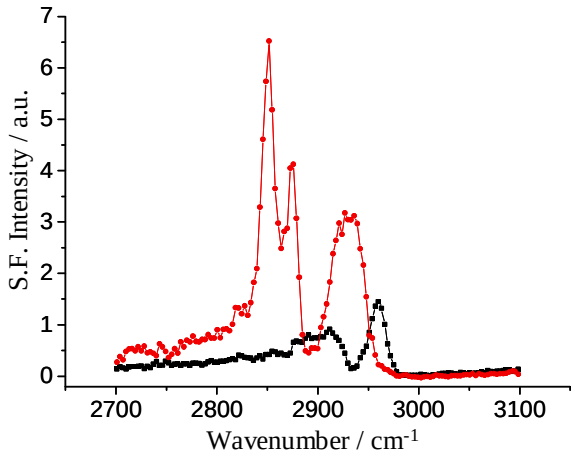

Figure 5.1 Sum-frequency spectra of the surface of liquid n-hexadecane. Red line indicates SSP, black line indicates PPP polarisations.

5.4 Experimental Methods and Materials

5.4.1 The Sum-Frequency Spectrometer

All the spectra presented in this chapter were acquired using the sum-frequency spectrometer at KTH in Stockholm, the details of which have been extensively described elsewhere.[11, 12] Only a brief summary is presented here.

A Nd:YAG pumping laser (Ekspla, PL2143A/20) is used to produce a pulsed laser beam at 1064 nm. The pulse length is approximately 24 ps with a rate of 20 Hz and an average energy of 40 mJ. The pulsed beam is used to pump an optical parameter generator/amplifier (OPG/OPA, LaserVision) to generate fixed visible (532 nm) and tuneable IR (3 – 12 μm) beams which in turn are used to generate the sum-frequency signal. The generated beams are directed toward the sample such that they overlap spatially and temporally at the interface at angles of 55° (visible) and 63° (IR), resulting in the creation of a sum-frequency signal at approximately 56° (dependent upon IR wavelength according to eqn. 5.3).

The sum frequency signal is spatially filtered to ensure there is no interference from the reflected visible and IR beams and then optically filtered by a notch filter, bandpass filter and monochromator before detection by a PMT.

Figure 5.2 shows the geometry of the IR, visible and sum-frequency beams at the sample surface. Although most of the path length before the sample is contained in a dry air purged container, some of the beam necessarily passes through the more humid laboratory atmosphere. In order to account for fluctuations in IR beam power due to water vapour absorption, a portion of the incident IR beam passes through the sample cell without reflection from the sample surface. The variation in intensity of this signal with time is then used to normalise total IR throughput. The intensity of the visible beam is monitored in a similar way, but is much less affected by environmental conditions.

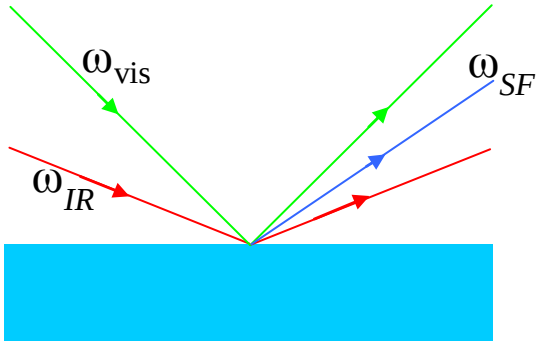

Figure 5.2 Schematic of a VSFS experiment.

The sample is contained in a glass cell sealed with o-rings and teflon stoppers. The beams enter and leave the cell through CaF_2 windows, transparent in the IR. The temperature of the sample is controlled by immersion of the sample cell in a water bath whose temperature is regulated by a heating coil connected to a second water bath in order to minimise vibrations of the sample surface by water circulation. The temperature is measured by a thermocouple housed inside a glass capillary and is recorded as spectra are taken. The sample height can be changed without removing the sample, and so experiments at different temperatures are readily accomodated.

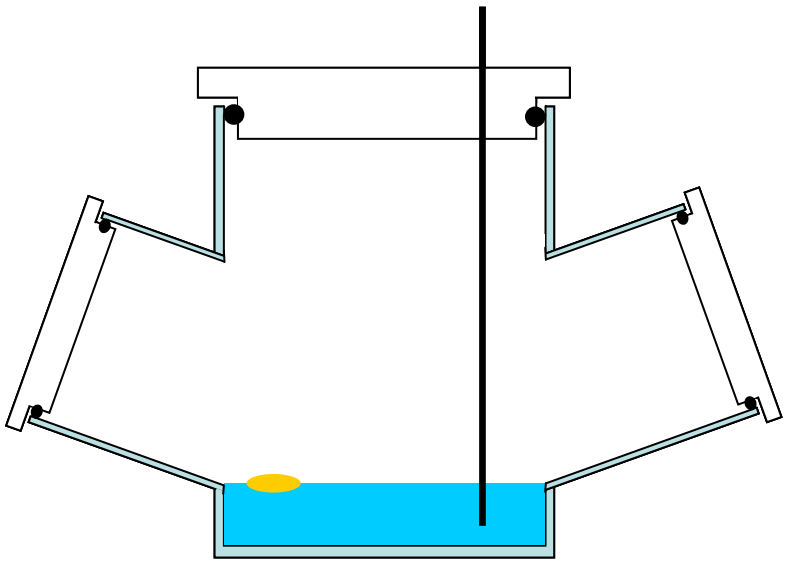

Figure 5.3 Cross-section of the sealed VSFS sample cell. The cell was placed in a thermostated water bath during measurements.

5.4.2 Materials

The cationic surfactant C_{16}TAB (Sigma, 99.9 %) was recrystallised three times from a mixture of acetone and ethanol. Deuterated C_{16}TAB (*d*-CTAB) was provided by Dr. R. K. Thomas and recrystallised twice before use from the same mixture. $C_{16}E_8$

(99.9%) was purchased from Nikko chemicals Japan, and was used as received. The oils *n*-hexadecane (Sigma, 99.5%), *n*-dodecane (Sigma, 99.5%) and *n*-eicosane (Sigma, 99%) were purified by passing through a column of activated neutral alumina immediately prior to use.

All glassware was soaked in a dilute solution of Decconex (Borer Chemicals) for several hours and rinsed copiously with MilliQ water before use.

5.5 Results

5.5.1 C_{16}TAB Monolayers in the Absence of *n*-alkane

Figure 5.4 shows sum-frequency spectra of a 0.6 mM C_{16}TAB monolayer at the air-water interface in the absence of oil. The appearance of these spectra is similar to the *n*-hexadecane spectra discussed in section 5.2.1. The relative strengths of the symmetric methylene and methyl bands in the *SSP* spectrum (in face, the d^+ is more intense than the r^+ band) indicates a high proportion of *gauche* defects, and this is supported by the appearance of only a weak asymmetric methyl band in the *SPS* and *PPP* spectra. As has been demonstrated previously, then, C_{16}TAB monolayers appear highly disordered at the air-water interface.[13]

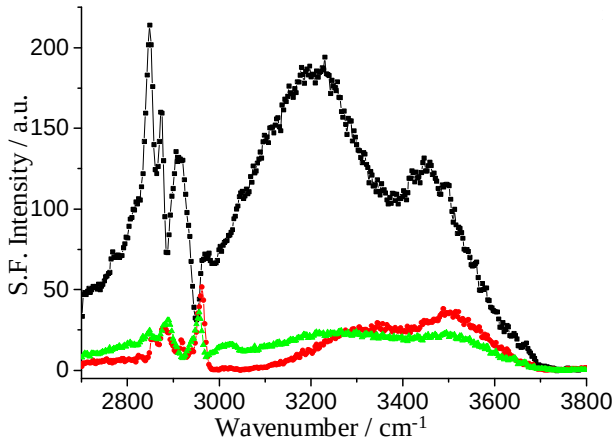

Figure 5.4 SSP (black), SPS (green) and PPP (red) polarised sum-frequency spectra of a 0.6 mM C_{16}TAB monolayer at the air-water interface at 20 °C.

The broad spectral features in the OH stretching region, ~3000 – 3700 cm^{-1}, give information about the interfacial water structure perturbed by the presence of TAB^+

headgroups in the monolayer. Details of the SF spectra of water have been presented elsewhere,[14, 15] so only a brief description is given here. The central wavenumber of OH stretching modes are sensitive to the hydrogen bonding network present, with a red-shift of several hundred wavenumbers between gas phase molecules and tetrahedrally coordinated water molecules found in ice. In the present case, the absence of any sharp feature around 3705 cm^{-1} indicates there are no "free" OH bonds at the interface in the presence of C_{16}TAB, as is the case for both the bare water surface and in the presence of some simple surfactants. The presence of two distinct, broad absorbances in the *SSP* spectrum can be reconciled with the presence of hydrogen-bonded water in so-called "ice-like" and "liquid-like" environments in the interfacial region, although this interpretation is not universally accepted. Any change in headgroup structure will be manifested by a sudden change in the appearance of this spectral region at the transition temperature, and so in this present work the features in the OH stretching region are purely diagnostic.

Similar spectra were recorded at several temperatures in the range 10 – 40 °C. A small (<10 %) decrease in surface excess with increasing temperature was implied by an overall decrease in sum-frequency intensity. This is in agreement with simple ellipsometry measurements. No structural differences were observed either in the monolayer or interfacial water with changing temperature, however, and so results within this temperature range presented here from systems with different surface freezing temperatures are fully comparable.

5.5.2 Type I Freezing: C_{16}TAB in the Presence of *n*-Hexadecane

Comparison of *SSP* polarised spectra of C_{16}TAB both with and without *n*-hexadecane (figs. 5.4 and 5.5) shows that the addition of oil induces a small but noticeable decrease in the number of *gauche* defects at the interface, even in the high-temperature liquid phase. This effect is observed more by a change in the relative intensities of the methylene and methyl symmetric stretching bands than a direct comparison of intensities, as the arbitrary units are not necessarily comparable between experiments due to fluctuations in laser power from day to day. In the case of the mixed monolayer the most intense peak is that of the symmetric methyl stretch, whereas in the pure C_{16}TAB spectrum the methylene peak is most intense.

As noted previously, the ratio of intensities of these two peaks gives a good indication of the proportion of *gauche* defects present in the chains, and hence the mixed monolayer contains fewer *gauche* defects and therefore a higher degree of order. The *PPP* polarised spectra support this conclusion; the antisymmetric methyl stretch is relatively more intense than the symmetric methyl stretch in the mixed monolayer spectrum than in the pure C_{16}TAB spectrum.

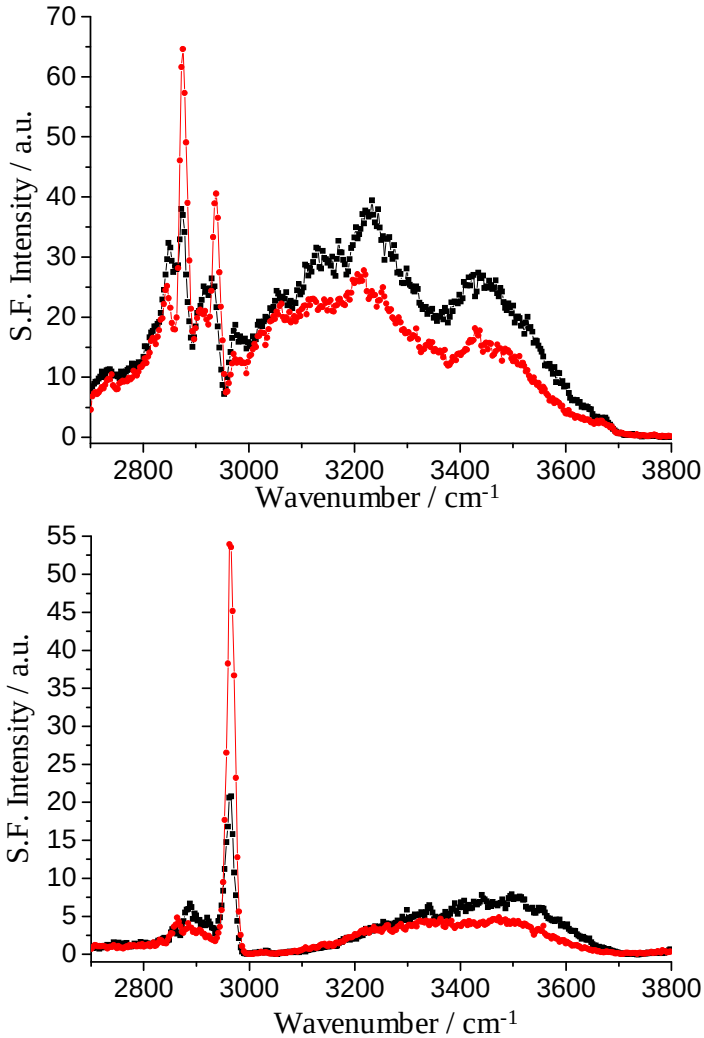

Figure 5.5 Sum-frequency spectra of a mixed monolayer of 0.6 mM C_{16}TAB and n-hexadecane at the air water interface in the solid (red, 20 °C) and liquid (black, 23.4 °C). Top, SSP polarisation. Bottom, PPP polarisation.

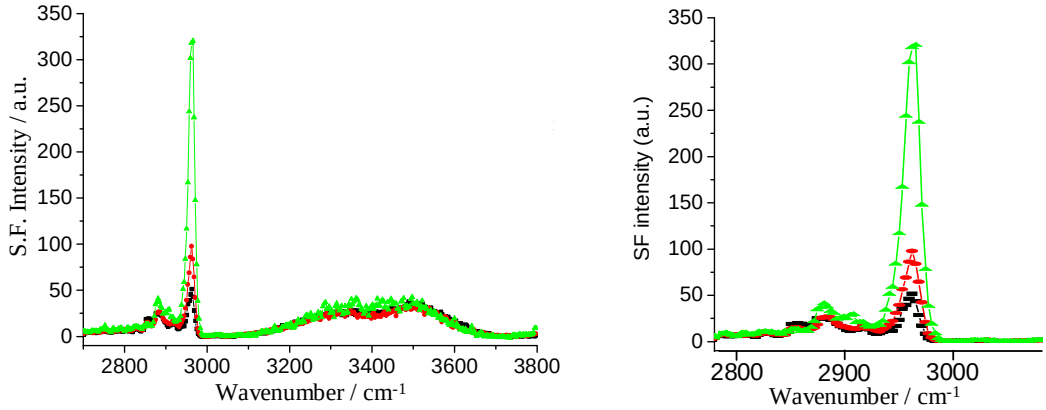

Figure 5.6 PPP polarised spectrum of 0.6 mM C_{16}TAB (black, 20 °C), 0.6 mM C_{16}TAB with n-dodecane in the liquid phase (red, 12 °C) and solid phase (green, 5.9 °C). Right, Expanded view of the 2800 – 3000 cm^{-1} region.

Below the surface freezing temperature the ordering of chains at the interface is even more evident, with a roughly twofold increase in intensity of the r^+ mode accompanied by a marked decrease in intensity of the d^+ mode in the *SSP* spectrum. In addition, the intensity of the asymmetric methyl stretch (r^-) in the *PPP* spectrum increases by almost three times upon surface freezing. Both these findings indicate the formation of a highly ordered solid phase with all-*trans* chains, in agreement with previous VSFS[5] and X-ray reflectivity[10] studies on type I C_{16}TAB/*n*-alkane mixed monolayers. The X-ray reflectivity data of Sloutskin *et al.*[10] implied that a small but significant change in the electron density profile of the headgroup layer accompanied surface freezing of type I systems, in turn suggesting a change in water structure at the interface. Although the OH stretching region of the solid and liquid phase *SSP* spectra in figure 5.5 are not identical, the differences are small and within the error of the measurement. In cases where interfacial water structure has been shown to change, the intensities of the component water bands vary by at least an order of magnitude.[7-9] It is reasonable, therefore, to suggest that, although the surface excess of surfactant may change slightly, no change in either water or headgroup layer structure takes place during surface freezing. This conclusion is consistent with surface tension experiments showing there is no change, within error, in surface excess of surfactant upon surface freezing.[16, 17]

Experiments were also carried out on a mixed monolayer of C_{16}TAB and *n*-dodecane to assess potential differences in structure between type I frozen monolayers where

the *n*-alkane chain length varies relative to that of the C_{16}TAB. Figure 5.6 shows *PPP* spectra of this system in both the liquid and solid phases, and is indicative that similar solid phase structures are formed regardless of *n*-alkane chain length.

5.5.3 Type II Freezing: C_{16}TAB in the Presence of *n*-Eicosane

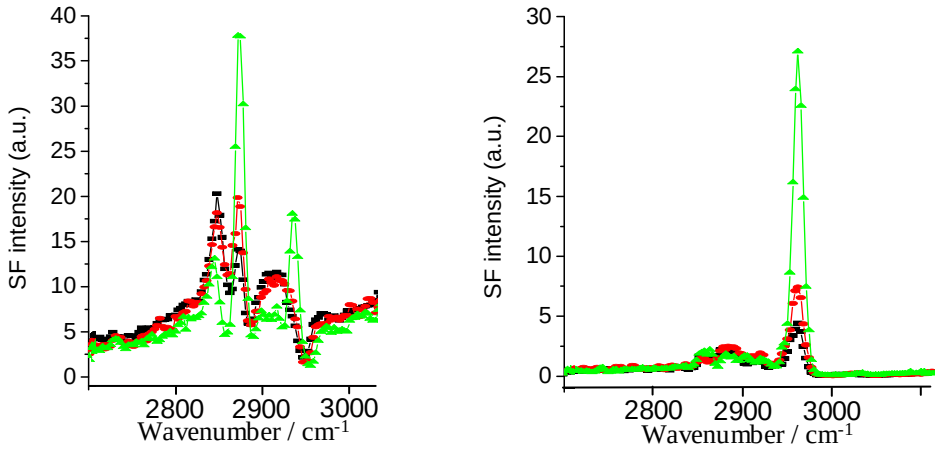

Figure 5.7 Sum-frequency spectra of a mixed monolayer of 0.6 mM C_{16}TAB and n-eicosane in the liquid (red, 39.5 °C) and solid (green, 36.5 °C) phases. Left, SSP polarisation. Right, PPP polarisation. Black data are from a 0.6 mM C_{16}TAB monolayer in the absence of oil for comparison.

Spectra of the liquid and solid phases of type II C_{16}TAB/*n*-eicosane mixed monolayers are shown in fig. 5.7. The spectra in both phases are similar in appearance to the type I C_{16}TAB/*n*-hexadecane spectra in section 5.4.2. A sharp increase in intensity of the r^+ band in the surface frozen layer accompanied by a decrease in intensity of the d^+ band in the *SSP* spectra, as well as the appearance of a sharp r^- band in the solid phase *PPP* spectrum confirms the presence of a highly ordered solid phase. The liquid phase contains a higher fraction of *gauche* defects compared to the type I mixed monolayers, as evidenced by a roughly 1:1 ratio of r^+:d^+ intensities, although the monolayers are still more ordered than those of pure C_{16}TAB. A possible explanation for this lies in variations in the extent of adsorption of different chain lengths of *n*-alkane at the air-solution interface. The mole fraction of *n*-alkane in the mixed monolayer decreases with increasing alkane chain length, limiting the ability of the longer *n*-alkanes to affect the surfactant tailgroup structure at the interface.

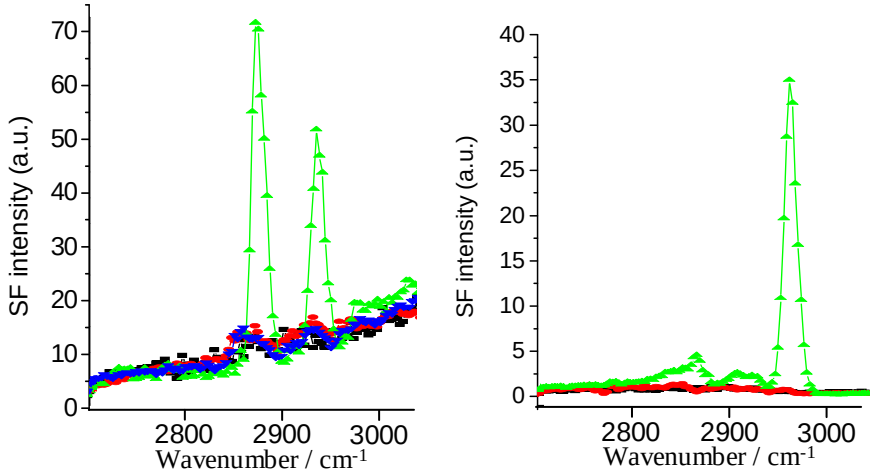

Figure 5.8 Sum-frequency spectra of a mixed monolayer of 0.6 mM d-CTAB and n-eicosane in the liquid (red and blue, 39.9 and 40.5 °C) and solid (green, 36.8 °C) phases. Left, SSP polarisation. Right, PPP polarisation. Black data are from a 0.6 mM d-CTAB monolayer in the absence of oil for comparison.

Up to this point, the presented spectra have included contributions from both surfactant and alkane, since both components have been hydrogenated. In order to isolate structural changes occurring in the *n*-eicosane component, the experiment was repeated replacing hydrogenated C_{16}TAB with fully deuterated *d*-CTAB. The resulting spectra are shown in fig. 5.8. The paucity of alkane adsorption in the liquid phase monolayer can be readily appreciated from the extremely low signal level from C-H stretches, also consistent with the view that the alkane has no preferred orientation in the liquid monolayer. In the solid phase, a very strong r^+ band in the *SSP* spectrum suggests an all-*trans* arrangement of the *n*-eicosane chain, and in fact no methylene modes are present in the spectra. An all-*trans* alkane chain is centrosymmetric, however, and so no sum-frequency signal is expected. This apparent inconsistency has been observed previously by Sefler *et al.*[18] in sum-frequency spectra of the neat eicosane surface below its surface freezing temperature. The presence of a sum-frequency response despite the presence of a centre of symmetry has been proposed to result from the incomplete cancellation of signals from the opposing methyl groups.[5] The rationale behind this explanation stems from the different local electric fields at the air/monolayer and monolayer/water interfaces which causes the electric dipole approximation to break down. The appearance of the solid phase spectra are very similar to those taken from the *n*-eicosane/*h*-C_{16}TAB

system, supporting the bilayer model introduced in chapter 1. Experiments were also carried out using *h*-C_{16}TAB/*d*-eicosane. No change in spectra were observed upon cooling, implying that C_{16}TAB does not become ordered during the transition. This will be discussed further in section 5.5.

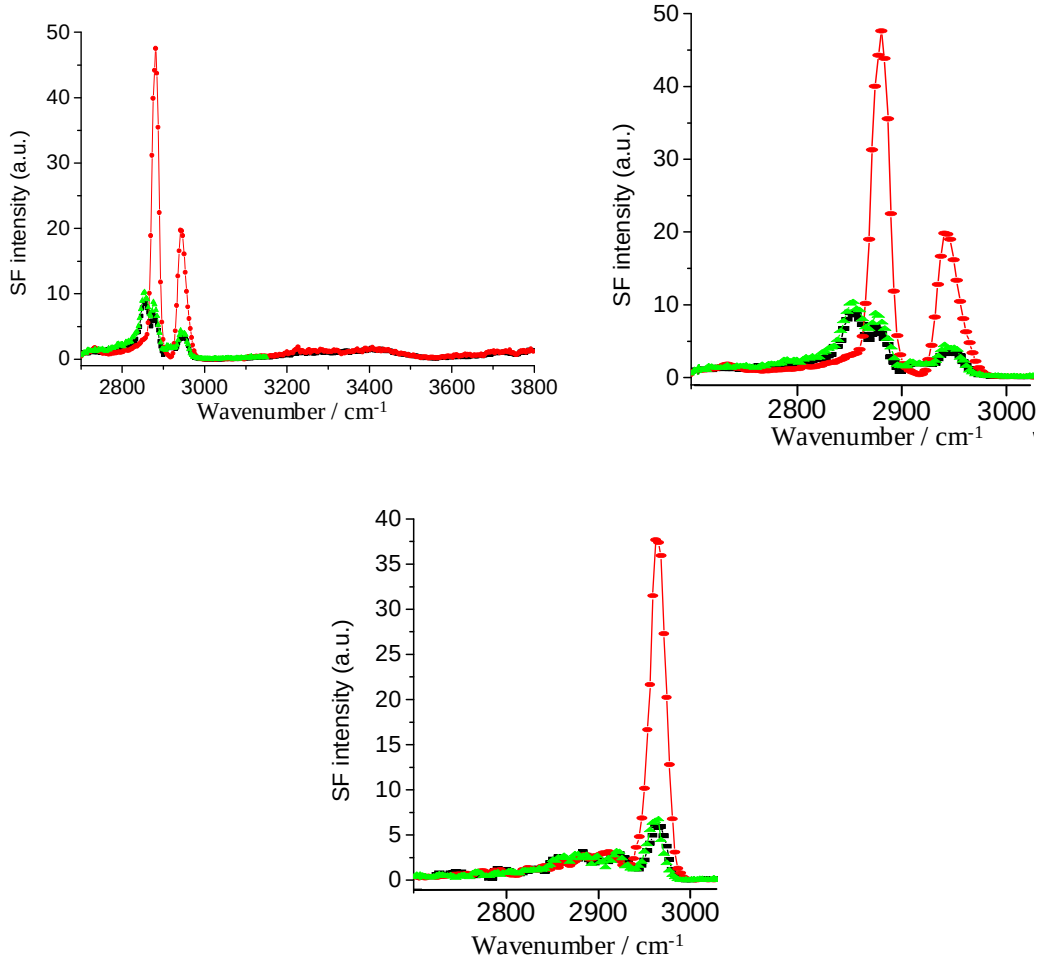

Figure 5.9 Sum-frequency spectra of a mixed monolayer of 1 mM $C_{16}E_8$ and n-octadecane in the liquid (green,32.2 °C) and solid (red, 29.4 °C) phases. Above left, SSP polarisation. Above right, SSP polarisation, expanded in the range2800 – 3000 cm^{-1}. Bottom, PPP polarisation. Black data are from a 1 mM $C_{16}E_8$ monolayer in the absence of oil for comparison.

5.5.4 Type I Freezing: $C_{16}E_8$ in the Presence of *n*-Octadecane

In contrast to mixed monolayers with C_{16}TAB, ellipsometry data suggest *n*-octadecane forms a type I surface frozen monolayer at the air/$C_{16}E_8$ solution interface. Figure 5.9 shows sum-frequency spectra of both the solid and liquid phases of $C_{16}E_8$/*n*-octadecane mixed monolayers. The r^+ mode in the *SSP* spectra increases

fivefold through the freezing transition, with the d^+ mode becoming virtually unobservable. Similarly in the *PPP* and *SPS* spectra, the r^- mode increases in intensity dramatically in the solid phase. The solid nature of the low temperature phase is confirmed by these findings, and moreover the miniscule d^+:r^+ ratio indicates that the frozen layer contains fewer *gauche* defects than corresponding type I frozen monolayers formed from C_{16}TAB/alkane mixtures. The OH stretching bands are much weaker in the presence of non-ionic $C_{16}E_8$ than in the presence of ionic surfactants. This is due to the greater ability of a charged headgroup to induce a preferred orientation in interfacial water molecules, and also the disordered nature of the oxyethylene headgroup.

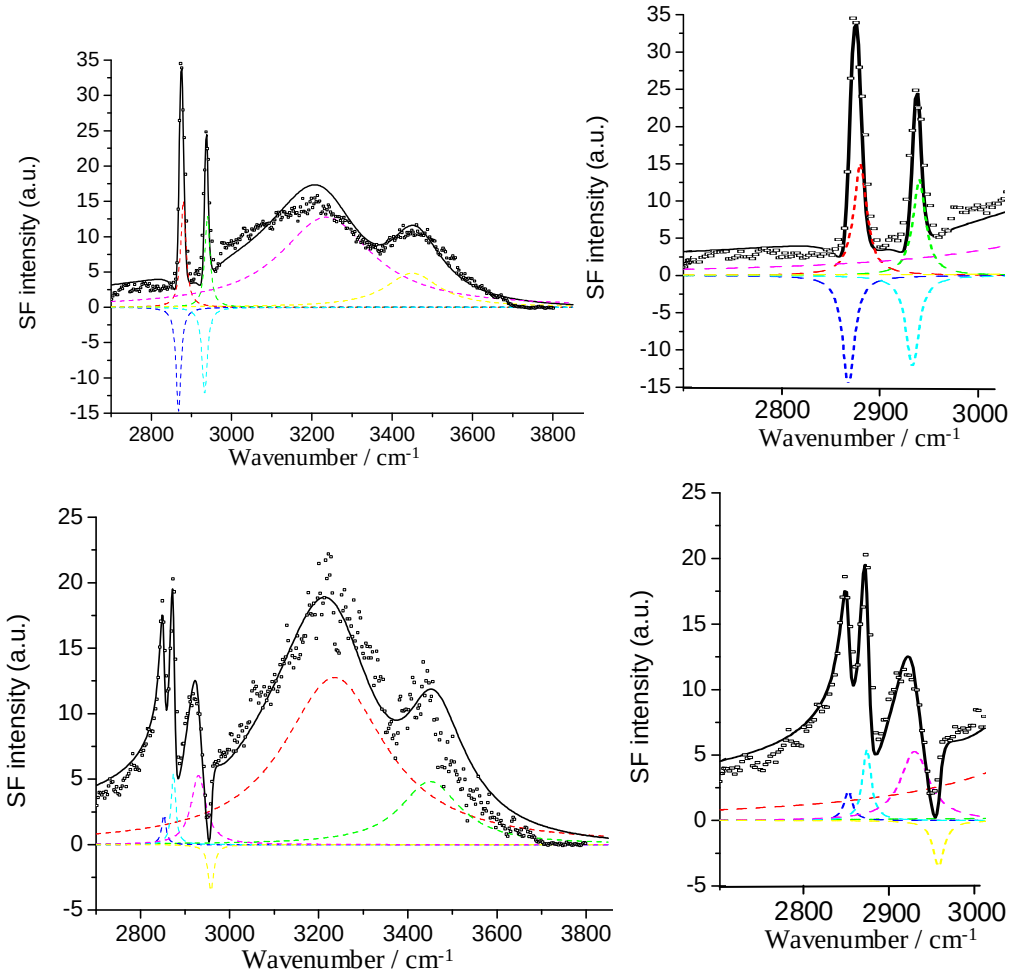

Figure 5.10 Top left, fitted solid phase SSP spectrum of d-CTAB/n-eicosane monolayer, with expanded view of C-H region top right. Bottom left, liquid phase SSP spectrum of h-C_{16}TAB/n-eicosane monolayer, with expanded view of the C-H region bottom right. Points represent experimental spectra, modelled spectra shown by solid lines.

5.6 Comparison with Previous Results

5.6.1 Type II Freezing

Based on ellipsometry and X-ray reflectivity data type II monolayers are thought to exhibit a bilayer structure in which a surface frozen layer of all-*trans* alkane chains wet the air-monolayer interface above a liquid mixed monolayer containing both surfactant and alkane. It should be possible, therefore, to reproduce accurately the solid phase *SSP* spectrum of the fully hydrogenated C_{16}TAB/*n*-eicosane system in figure 5.7 from a combination of the corresponding liquid phase spectrum and the solid phase spectrum in the presence of deuterated C_{16}TAB (fig. 5.8).

Figures 5.10 and 5.11 show the fitted solid and liquid phase spectra and their summation, respectively. Peaks were fitted with Lorentzian line shapes according to eqn. 5.8. It was necessary to fit the r^+ band of the solid phase *d*-CTAB/*n*-eicosane spectrum with two peaks of opposite phase separated by approximately 10 cm^{-1} to account for contributions from methyl groups at the air-frozen layer and frozen layer-liquid layer interfaces, with the air-layer group having the higher frequency. Such a fitted separation is consistent with the findings found by Davies *et al.* in Langmuir-Blodgett multilayers on gold for methyl groups pointing towards air and alkane environments, although the separation is smaller in their case.[19] The fully hydrogenated solid phase *SSP* spectrum modelled in this way correlates extremely well with the experimentally measured spectrum, fully supporting the bilayer model structure of type II frozen layers (figure 5.11).

$$I_{SF}(\omega_{IR}) = \left| A_{NR} + \sum_n \frac{A_n}{\omega_n - \omega_{IR} - i\Gamma_n} \right| \qquad (5.8)$$

The sum-frequency data is also fully consistent with the ER-FTIR data presented in chapter 4. In the case of ER-FTIR it was shown that the increase in surface excess of chains during a type II freezing transition was greater than the increase in surface excess during a type I transition, and further that this increase in surface excess is fully accounted for by the formation of a complete solid alkane monolayer. Both spectroscopic techniques, therefore, show that only the alkane component is involved

structurally in a type II transition and that the lower leaflet of the solid phase bilayer remains liquid-like.

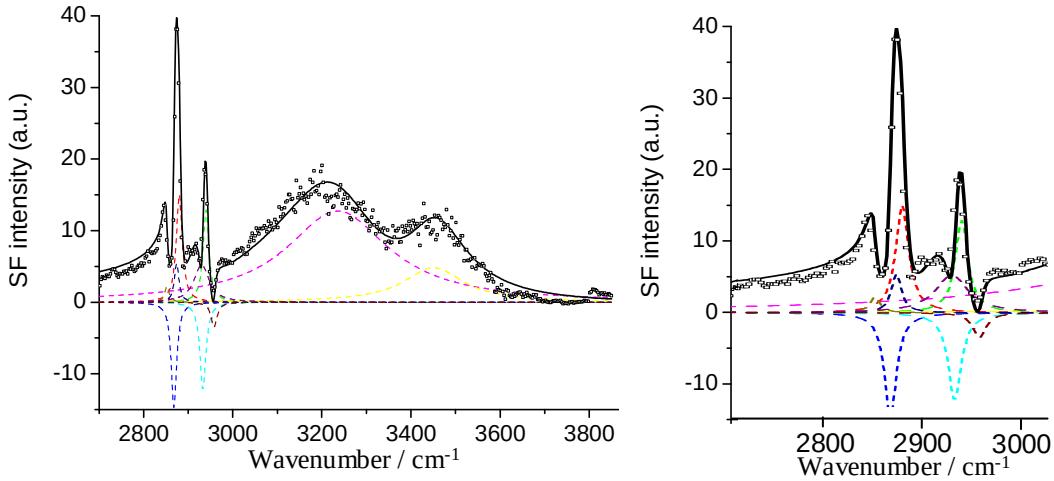

Figure 5.11 Modelled fully hydrogenated solid phase SSP spectrum of a C_{16}TAB/n-eicosane mixed monolayer, solid line, compared to the experimentally measured spectrum, points.

5.6.2 Chain Length Dependence of Surface Freezing

Detailed ellipsometry studies[5, 20] have revealed that the occurrence of type I or type II surface freezing is dependent on the chain length difference between the surfactant tailgroup and the *n*-alkane chain. In the case of the series of cationic surfactants, C_nTAB, the crossover from type I to type II behaviour is generally found to occur when the *n*-alkane chain is two methylene units longer than the tailgroup (see chapter 2). This behaviour can be explained by the unfavourable van der Waals attractions that would exist if the difference in length of the extended, all-*trans* chains were too great in the solid phase. Superficially, then, the $C_{16}E_8$/*n*-octadecane system might be expected to form a type II solid phase. The fact that a type I transition is found for this system suggests that some mechanism exists to reduce the end-chain mismatch between surfactant and alkane. Two possibilities are apparent; either the octadecane artificially shortens itself by the introduction of extra kinks in the alkyl chain or the alkane more closely approaches the headgroup region of the mixed monolayer. The first of these possibilities can be discounted immediately as the sum-frequency spectra in figure 5.9 indicate that the chains in the $C_{16}E_8$/*n*-octadecane solid phase are in fact more ordered and contain fewer defects than those in type I solid phases

formed with C_nTAB surfactants. If the alkane were to reside partially in the headgroup region then some ordering of the headgroup would be expected to take place during the freezing transition. There is no evidence of a change in water structure in the *SSP* spectra, however, which would accompany any ordering of headgroup ethylene units. The most likely explanation for the appearance of type I behaviour, therefore, is that a weak net attraction exists between ethylene glycol fragments in the headgroup layer and the octadecane, a reasonable assumption given the solubility of PEG-based surfactants in oil, which counteracts the imiscibility of alkane and water. The terminal methyl group could then sit closer to the monolayer-solution interface, and hence interact more fully with the surfactant tail in the solid phase resulting in a greater degree of chain order. This explanation is consistent with the neutron data of Thomas *et al.*[21] which showed that the mean separation between surfactant tailgroups and alkane chains was lower in mixed monolayers of dodecane and $C_{12}E_5$ than in the corresponding monolayers with $C_{12}TAB$, although no information was obtained regarding the structure of the $C_{12}E_5$ headgroup in the mixed monolayers.

5.7 Conclusion

This chapter has shown how a combination of spectroscopic techniques can be used to confirm directly interfacial structures inferred from other techniques. The first sum-frequency spectra of type II monolayers have been presented, and shown to be fully consistent with the proposed bilayer structure. Spectra on the novel $C_{16}E_8$/*n*-octadecane system have confirmed the existence of a true solid phase that is somewhat more ordered than the $C_{16}TAB$ counterparts, and demonstrated the importance of the nature of the surfactant headgroup in determining the extent of overlap between sufactant and alkane chains.

5.8 References

1. Braun, R.; Casson, B. D.; Bain, C. D., *Chemical Physics Letters* **1995,** 245, 326-334.
2. Casson, B. D.; Braun, R.; Bain, C. D., *Faraday Discussions* **1996,** 104, 209-229.
3. Casson, B. D.; Bain, C. D., *Journal of Physical Chemistry B* **1998,** 102, 7434-7441.

4. Casson, B. D.; Bain, C. D., *Journal of Physical Chemistry B* **1999,** 103, 4678-4686.
5. Wilkinson, K. M.; Lei, Q.; Bain, C. D., *Soft Matter* **2006,** 2, 66-76.
6. Johnson, C. M.; Tyrode, E. C., *Physical Chemistry Chemical Physics* **2005,** 7, 2635-2640.
7. Gragson, D. E.; McCarty, B. M.; Richmond, G. L., *Journal of the American Chemical Society* **1997,** 119, 6144-6152.
8. Tyrode, E. C.; Johnson, C. M.; Kumpulainen, A. J.; Rutland, M.; Claesson, P. M., *Journal of the American Chemical Society* **2005,** 127, 16848-16859.
9. Tyrode, E. C.; Johnson, C. M.; Rutland, M.; Claesson, P. M., *Journal of Physical Chemistry C* **2007,** 111, 11642-11652.
10. Sloutskin, E.; Sapir, Z.; Tamam, L.; Ocko, B. M.; Bain, C. D.; Deutsch, M., *Thin Solid Films* **2007,** 515, 5664-5668.
11. Tyrode, E. C. Vibrational Sum Frequency Spectroscopy Studies at the Air-Liquid Interface. Royal Institute of Technology, Stockholm, 2005.
12. Johnson, C. M.; Tyrode, E. C.; Baldelli, S.; Rutland, M. W.; Leygraf, C., *Journal of Physical Chemistry B* **2005,** 109, 321-328.
13. Campbell, R. A.; Parker, S. R. W.; Day, J. P. R.; Bain, C. D., CTAB. *Langmuir* **2004,** 20, 8740-8753.
14. Du, Q.; Superfine, R.; Freysz, E.; Shen, Y. R., *Physical Review Letters* **1993,** 70, 2313-2316.
15. Richmond, G. L., *Chemical Reviews* **2002,** 102, 2693-2724.
16. Matsubara, H.; Ohtomi, E.; Aratono, M.; Bain, C. D., *Journal of Physical Chemistry B* **2008,** 112, 11664.
17. Lei, Q.; Bain, C. D., *Physical Review Letters* **2004,** 92, 176103.
18. Sefler, G. A.; Du, Q.; Miranda, P. B.; Shen, Y. R., *Chemical Physics Letters* **1995,** 235, 347.
19. Holman, J.; Davies, P. B.; Nishida, T.; Ye, S.; Neivandt, D. J., *Journal of Physical Chemistry B* **2005,** 109, 18723-18732.
20. Wilkinson, K. M. Phase Transitions in Monolayers of Soluble Surfactants. University of Oxford, 2004.
21. Lu, J. R.; Li, Z. X.; Thomas, R. K.; Binks, B. P.; Crichton, D.; Fletcher, P. D. I.; McNab, J. R.; Penfold, J., *Journal of Physical Chemistry B* **1998,** 102, 5785-5793.

Chapter 6

Discussion and Conclusions

6.1 Introduction

In the preceding chapters, a range of ellipsometric and spectroscopic data have been presented which give insight into the phenomenological and structural characteristics of surface freezing transitions in mixed monolayers of oil and surfactant at the air-water interface. In particular, new transitions have been reported which are not entirely consistent with the current theories proposed by Sloutskin *et al.*,[1-3] as type II behaviour has now been observed in the presence of alkanes that do not exhibit surface freezing at the neat air-alkane interface. In addition, both ellipsometry and 2D-FTIR simulations suggest that type II freezing occurs *via* a two-step mechanism. These findings will be discussed further in section 6.3. Section 6.2 considers existing data on type I freezing systems and discusses the effect of surfactant on type I/type II crossover. The main conclusions of this thesis are then brought together in section 6.4.

6.2 Type I Behaviour

Table 6.1 summarises the transition temperatures, T_s, and solid layer thicknesses, d_s, observed. Type I transitions are indicated by light grey shading. In all cases, the solid thickness is similar to the length of the fully extended surfactant tail and the variation in layer thickness with *n*-alkane chain length is relatively weak. These findings reinforce previous ellipsometry[4] and X-ray reflectivity studies where it was noted that the solid layer thickness is dominated by the surfactant component of the mixed monolayer, suggesting little extension of the alkane above the surfactant tails.

The FTIR data for $C_{16}TAB/C_{16}$ type I monolayers presented in chapter 4 were shown to be consistent with earlier estimates of the composition of solid and liquid mixed monolayers, and the magnitude of peak shifts upon freezing were similar to those observed previously in neat alcohol monolayers at the air-water interface by Alonso *et al.*.[5] A 2D-FTIR analysis of spectra recorded as a function of temperature was consistent with a “phase coexistence” model as expected for a first order phase transition.

Table 6.1 Transition temperature (°C), type (type I light grey, type II dark grey) and solid layer thickness (Å) of systems reported in this thesis

	C_{12}	**C_{13}**	**C_{14}**	**C_{15}**	**C_{16}**	**C_{17}**	**C_{18}**	**C_{19}**	**C_{20}**	**C_{28}**
C_{12}TAB			T_s = 1.6 d_s = 31.5	T_s = 9.2 d_s = 31.8	T_s = 16.0 d_s = 31.1	T_s = 22.3 d_s = 22.5	T_s = 27.7 d_s = 33.1	T_s = 32.9 d_s = 34.5	T_s = 36.9 d_s = 34.7	
C_{14}TAB	T_s = 0.2 d_s = 16.2		T_s = 7.6 d_s = 17.9	T_s = 10.6 d_s = 33.8	T_s = 17.3 d_s = 34.5	T_s = 23.4 d_s = 34.8	T_s = 27.7 d_s = 34.1	T_s = 32.8 d_s = 35.5	T_s = 35.4 d_s = 35.8	
C_{16}TAB	T_s = 10.2 d_s = 17.4	T_s = 14.2 d_s = 17.7	T_s = 18.5 d_s = 19.4	T_s = 19.5 d_s = 19.3	T_s = 21.6 d_s = 19.3	T_s = 22.9 d_s = 18.7	T_s = 27.6 d_s = 36.8	T_s = 32.8 d_s = 38.6	T_s = 36.9 d_s = 38.8	
$C_{16}E_8$			T_s = 19.2 d_s = 24.8	T_s = 20.0 d_s = 24.7	T_s = 21.0 d_s = 24.8		T_s = 27.9 d_s = 24.2			
***lyso*-PPC**			T_s = 18.2 d_s = 22.2					T_s = 32.8 d_s = 24.1		T_s = 62.1 d_s = 53.8
***lyso*-OPC**				T_s = 16.2 d_s = 36.4				T_s = 33.4 d_s = 40.2		
C_{18}TAB			T_s = 20.1 d_s = 20.7		T_s = 24.3 d_s = 22.2				T_s = 36.8 d_s = 39.7	

Although the VSFS spectra presented in chapter 5 suggest that the headgroup structure remains unchanged by surface freezing, the ability of the headgroup to interact with alkane does have an effect on the chain length difference required to cause a crossover from type I to type II behaviour. The surfactants C_{16}TAB, $C_{16}E_8$ and *lyso*-PPC all have 16 carbon tailgroups, but the crossover to type II behaviour does not occur at the same alkane chain length (or indeed at all in the case of $C_{16}E_8$, as discussed in chapter 3). In the presence of octadecane, C_{16}TAB monolayers form a type II solid phase whereas $C_{16}E_8$ and *lyso*-PPC monolayers remain as type I systems in the presence on octadecane and nonadecane, respectively. Both $C_{16}E_8$ and *lyso*-PPC headgroups contain chain-like structural elements that could stabilise a longer alkane chain in a type I frozen monolayer by allowing end chain mismatch to be shared at both the air-chain and chain-headgroup interfaces, thereby maximising favourable van der Waals interactions between the chains. In contrast, end-chain mismatch in mixed monolayers containing C_{16}TAB is confined to the air-chain interface, since it is less favourable for the alkane to penetrate the headgroup region, and hence a smaller chain length difference is required to destabilise a type I frozen layer, as protrusion of all-*trans n*-alkane segments beyond the surfactant tails would lead to unfavourable van der Waals interactions. This observation is similar to the bulk freezing behaviour of alkane mixtures, where alkanes with a chain length difference of six CH_2 units or less will co-crystallise.[6] Again, in the bulk end-chain mismatch can be shared between both ends of the chain and so larger chain length differences can be tolerated.

6.3 Type II Behaviour

In all the previously reported cases the crossover to type II behaviour occurred when the type I monolayer freezing temperature fell below the surface freezing temperature of the neat air-alkane interface. It was therefore proposed that type II freezing involved wetting of a liquid-like mixed monolayer by surface frozen alkane.[7, 8] The effect of end chain mismatch discussed above is to introduce an increased number of *gauche* defects at the air-chain interface. The appearance of the air-chain interface in the liquid phase will then be similar to that of the neat alkane interface in the liquid state, allowing a solid alkane

layer to wet a mixed monolayer in contact with a reservoir of surface frozen alkane, leading to a bilayer structure as shown in figure 6.1.

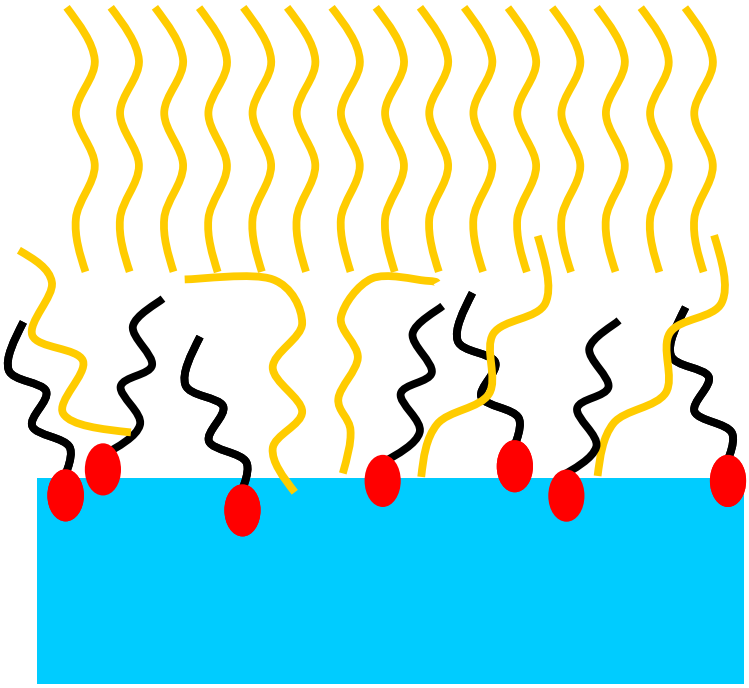

Figure 6.1 Schematic structure of a type II frozen phase, with a solid upper layer of frozen alkane on top of a liquid-like mixed monolayer.

If type II freezing were driven by a wetting transition of surface frozen alkane, the monolayer and air-alkane transition temperatures might be expected to be similar. In fact, the monolayer transitions are at temperatures roughly 1 °C below the reported alkane surface freezing transitions. Even taking into account slight variations in the surface freezing range of alkanes (due to varying levels of impurity, for example) the fact that type II freezing occurs with a negative ΔT in the case of $C_{12}TAB/C_{16}$ mixed monolayers (i.e. below the bulk melting point of hexadecane, although the reported surface freezing temperature of neat hexadecane is also below the bulk melting point)[9] implies that, in some cases at least, phase transitions at the two interfaces are not coincident. This finding demonstrates the importance of long-range dispersion interactions at the interface, which are much less favourable for a mixed monolayer on a water subphase than for surface frozen alkane at the air/alkane interface.

In addition, the transitions found in C_{12}TAB/C_{15}, C_{12}TAB/C_{14} and C_{14}TAB/C_{15} systems have shown that type II freezing can take place in the presence of a non-surface freezing alkane. Therefore, the formation of type II frozen layers must either be more complex than a simple wetting transition or the presence of surfactant somehow influences the surface phase behaviour of the oil lens. This latter possibility is unlikely in the extreme, as it would involve penetration of the air-alkane interface by charged surfactant molecules. It is also unlikely that the alkane-solution interface plays any part in the freezing transitions, as phase transitions occur in only a limited number of cases at the liquid-liquid interface (although fewer systems have been studied). The type II freezing transitions in the C_{14}TAB/C_{15} and the *lyso*-OPC systems are of particular interest, as they take place above (8.5 °C above in the case of *lyso*-OPC) the bulk melting point of pentadecane and so represent thermodynamically stable type II phases formed by a non-surface freezing oil. In contrast, the type II frozen layers formed by C_{12}TAB in the presence of tetradecane and pentadecane may be only metastable relative to a liquid monolayer and frozen alkane lens, as evidenced by the negative values of ΔT (very negative in the case of tetradecane), although the surface frozen layers might be only marginally unstable at the air/alkane interface and so small energy terms could provide sufficient stabilization above a liquid monolayer. Such marginal instability of a surface frozen tetradecane layer was demonstrated by Lei *et al.* at the tetradecane/C_{16}TAB solution interface, where it was found that very small mole fractions of surfactant (less than 0.1) could facilitate surface freezing.

The bilayer structure shown in figure 6.1 has been unequivocally demonstrated by a combination of ellipsometry and X-ray reflectivity.[3, 4, 8] The intensity changes observed in ER-FTIR spectra upon surface freezing, presented in chapter 4, are consistent with this structural model. 2D-FTIR data, however, are not consistent with either a first-order "phase coexistence" model or a simple wetting of the liquid mixed monolayer by surface frozen alkane. Figure 6.2 shows both the experimental asynchronous 2D-FTIR spectrum (for the C_{16}TAB/C_{20} mixed monolayer system) and a modelled 2D-FTIR spectrum based upon a two-step mechanism with initial formation of a more ordered intermediate followed by a first-order phase transition from this intermediate state (details of the

model can be found in section 4.6). Support for such a transient intermediate was provided by time-resolved ellipsometry measurements of the type II $C_{18}TAB/C_{20}$ mixed monolayer, shown in figure 6.3, upon cooling through the transition temperature. A clear plateau can be seen at an intermediate ellipticity, with a value close to that expected from type I frozen layer formation. No such transiently stable intermediates were directly observed in any other type II system, although their existence is strongly implied by 2D-FTIR of both the $C_{16}TAB/C_{20}$ and $C_{12}TAB/C_{16}$ systems shown in chapter 4.

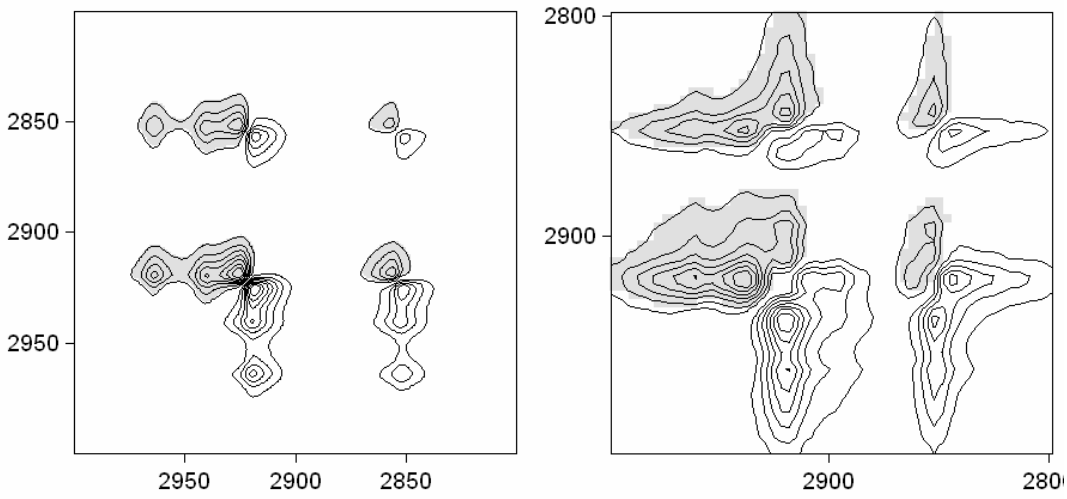

Figure 6.2 (Left) Asynchronous 2D correlation spectrum calculated using a two-step transition pathway. (Right) Experimental asynchronous correlation spectrum for type II surface freezing of a CTAB/C_{20} mixed monolayer.

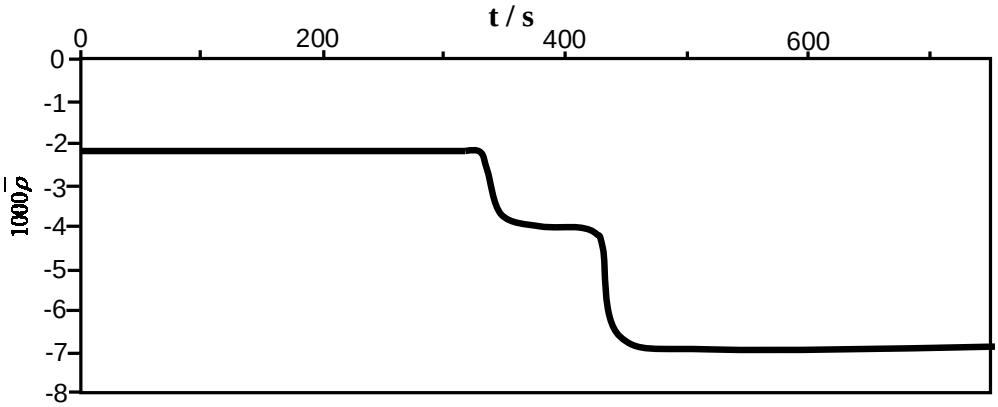

Figure 6.3 Coefficient of ellipticity as a function of time as the temperature of a $C_{18}TAB/C_{20}$ mixed monolayer was lowered through the transition temperature.

A possible explanation for such a two step mechanism is provided within the framework of classical nucleation theory, taking into account the fundamentally dynamic nature of the nucleation process. The Ostwald step rule states that a phase transition will occur *via* a metastable intermediate if such an intermediate exists which is closer in free energy to the initial state of the system than the thermodynamically stable final state. Thus, the crystal phase that is nucleated first is that which has the lowest free energy barrier of formation. This observation is in contrast to the basic principle of macroscopic thermodynamics that the phase formed during a transition is the one with the lowest free energy.

Classical nucleation theory treats nuclei as compact spherical objects. The free energy of a nucleus is then size dependent, with a negative bulk contribution determined by the difference in chemical potential between the two phases and a positive surface term due to the creation of an interface between the phases. At small droplet radii the surface term dominates and the free energy of nucleation is unfavourable. Above a critical radius the volume term becomes dominant and the nuclei grow spontaneously into the new bulk phase. The same concepts can be used for 2D surface phase transitions by considering circular nuclei and the associated line tension. The free energy of formation of a nuclei of radius r can be described by equation 6.1, where γ_l is the line tension, $\Delta\mu$ the difference in chemical potential between the two phases and A_m the area per mole at the interface.

$$\Delta G = 2\pi r\gamma_l - \frac{\pi r^2}{A_m}\Delta\mu \qquad (6.1)$$

In order to consider the impact of equation 6.1 on nucleation in type II systems, the nature of a nucleus formed both within (type I nucleus) and above (type II nucleus) the mixed monolayer must be considered, as shown schematically in figure 6.4. Due to the more alkane-like environment, the line tension of a nucleus formed within the monolayer will be lower than for a nucleus formed above the monolayer. The first term in equation 6.1 is therefore more favourable for formation of a nucleus of type I phase.

The energy barrier for type I nucleus formation will be lower than for type II nucleus formation, and so the phase transition could be expected to proceed *via* a metastable type I phase. The data in figures 6.2 and 6.3 support this assertion. In the case of a $C_{18}TAB/C_{20}$ mixed monolayer, a type I phase is stable with respect to the liquid phase and metastable with respect to a type II phase. The 2D-FTIR data suggests that this could be true for other systems as well, such as $C_{12}TAB/C_{15}$ or $C_{14}TAB/C_{15}$, and whether or not a transient type I phase is actually observed depends upon the nucleation kinetics of the type II layer. The nucleation kinetics of type II layer formation will be largely determined by transport of alkane to the interface, and so will be slower for longer alkanes. In this sense, a precursor type I phase could act as a local reservoir for the excess alkane needed for type II freezing.

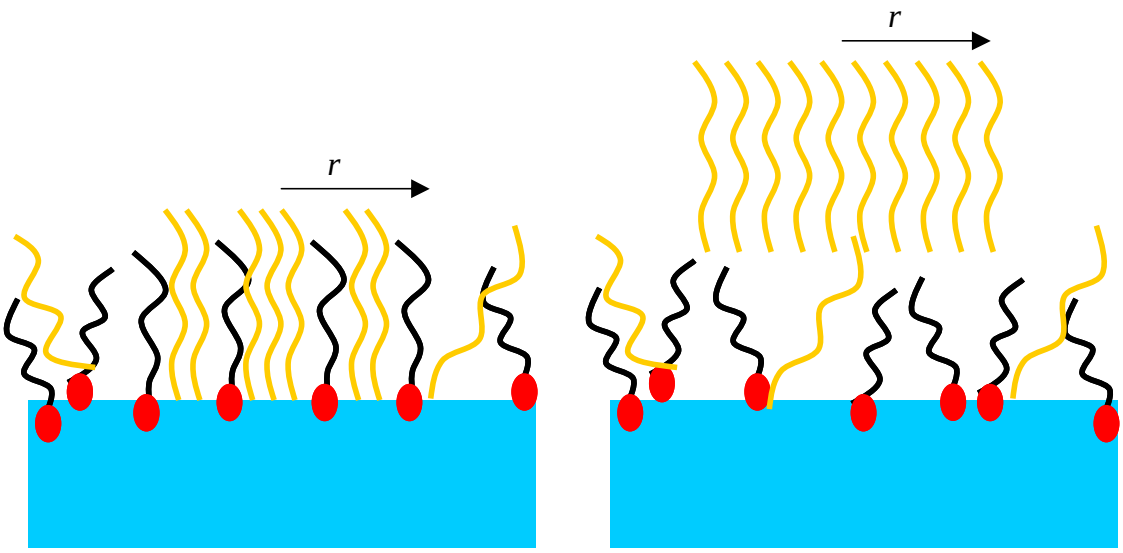

Figure 6.4 Nucleus formation within (left) and above (right) a mixed monolayer.

6.4 Conclusions

The data presented in this thesis have shown both type I and type II surface freezing to be general, although not universal, phenomena for a range of surfactant/alkane systems. The unusual wetting behaviour exhibited by mixed monolayers containing the surfactants Triton X-100, $C_{16}E_6$, $C_{16}E_8$ and Tween 20 is thought to be caused by the formation of a Winsor III surfactant-rich phase at the air-water interface as the

temperature is lowered, driven by the high local concentration of the surfactants at the interface and depletion effects from the bulk.

It was shown that type II frozen monolayers can be formed in the absence of surface frozen alkane, in contrast with existing ideas about the formation of these phases. In the case of *lyso*-OPC/C_{15} mixed monolayers the resulting type II phase is remarkably stable. 2D-FTIR and ellipsometry data showed that the formation of type II frozen monolayers could occur in a two-step process, *via* a transient type I phase, in agreement with classical nucleation theory and Ostwald's step rule. Formation of a metastable type I phase could account for the unusual type II behaviour, as it provides a mechanism of transport of alkane to the interface.

6.5 References

1. Ofer, E.; Sloutskin, E.; Tamam, L.; Ocko, B. M.; Deutsch, M., *Physical Review E* **2006,** 74, 021602.
2. Sloutskin, E.; Sapir, Z.; Lei, Q.; Wilkinson, K. M.; Tamam, L.; Deutsch, M.; Ocko, B. M., *Physical Review Letters* **2007,** 99, 136102.
3. Sloutskin, E.; Sapir, Z.; Tamam, L.; Ocko, B. M.; Bain, C. D.; Deutsch, M., *Thin Solid Films* **2007,** 515, 5664-5668.
4. Wilkinson, K. M.; Lei, Q.; Bain, C. D., *Soft Matter* **2006,** 2, 66-76.
5. Alonso, C.; Blaudez, D.; Desbat, B.; Artzner, F.; Berge, B.; Renault, A., *Chemical Physics Letters* **1998,** 284, 446.
6. Small, D. M., *The Physical Chemistry of Lipids: From Alkanes to Phospholipids*. Plenum Press: New York, 1986.
7. Wilkinson, K. M. Phase Transitions in Monolayers of Soluble Surfactants. University of Oxford, 2004.
8. Sloutskin, E.; Sapir, Z.; Bain, C. D.; Lei, Q.; Wilkinson, K. M.; Tamam, L.; Deutsch, M., *Physical Review Letters* **2007,** 99, 136102.
9. Hayami, Y.; Findenegg, G. H., *Langmuir* **1997,** 13, 4865.